Non-Fermi Liquid Behaviour in Uranium-Based Heavy-Fermion Compounds

ACADEMISCH PROEFSCHRIFT

ter verkrijging van de graad van doctor
aan de Universiteit van Amsterdam
op gezag van de Rector Magnificus
prof. dr J. J. M. Franse,
ten overstaan van een door het college voor promoties ingestelde
commissie, in het openbaar te verdedigen in de Aula der Universiteit
op dinsdag 26 september 2000, te 12.00 uur

door

Pedro Miguel de Lemos Correia Estrela

geboren te Lissabon, Portugal

Amsterdam, 2000

Promotor: prof. dr F. R. de Boer

Co-promotor: dr A. de Visser

Commissie: prof. dr P.F. de Châtel
prof. dr J.J.M. Franse
prof. dr M. Godinho (Universidade de Lisboa)
dr E.H. Brück
dr G.J. Nieuwenhuys (Universiteit Leiden)

The work described in this thesis was partially financed by the European Commission through a Marie Curie Fellowship and was carried out at the

Van der Waals - Zeeman Instituut
Universiteit van Amsterdam
Valckenierstraat 65
1018 XE Amsterdam
The Netherlands

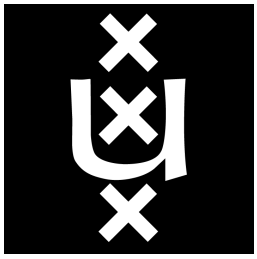

where a limited number of copies of this thesis is available.

ISBN: 90-5776-051-7

Non-Fermi liquid behaviour in uranium-based heavy-fermion compounds

Contents

1. Introduction

1.1. Scope

"Condensed matter physics has been surprisingly fertile in giving rise to new and unexpected phenomena, associated very often with new ground states of the electronic system. Many of them lurk at the fringes of interest until they are received into the Church of Physics by baptism with a name, and the latest such addition is provided by what are now called *heavy-fermion* materials". This sentence, written by B.R. Coles [1] more than a decade ago in the introduction of a review paper on heavy-fermion compounds, can now be used in the introduction of this thesis by simply replacing the term *heavy-fermion* by *non-Fermi liquid*.

Landau's Fermi liquid theory has been outstandingly successful in describing the low-temperature properties of normal and heavy-fermion metals. However, in the past decade an increasing number of heavy-fermion systems has been reported to show strong deviations from Fermi liquid behaviour at low temperatures. This so called non-Fermi liquid (NFL) behaviour is generally believed to represent a new type of ground state of metals, thus challenging both theorists and experimentalists to properly describe this new behaviour [2]. This represents the main motivation for the work described here.

Different mechanisms leading to NFL behaviour have been proposed. Some of these mechanisms are based on the physics of quantum phase transitions, while others are based on local Fermi liquid descriptions. NFL materials can normally be grouped into one of these two

classes of mechanisms. Up to now, a theoretical model which yields an universal description of NFL behaviour is not available. Crystallographic disorder, which is present in most NFL materials, is expected to play an important role in modelling certain types of NFL behaviour, however its precise influence is far from being understood. The lack of a full theoretical understanding of NFL behaviour asks for careful and detailed studies of the low-temperature properties of heavy-fermion compounds exhibiting NFL behaviour.

In the course of this thesis work, several systems exhibiting NFL behaviour were studied. Among them, U_2Pt_2In appeared to be the most interesting system and a detailed study of its electronic, thermal and magnetic properties was carried out. Although U_2Pt_2In is a "difficult" material from the metallurgical point of view, it is the first stoichiometric uranium-based compound discovered to exhibit NFL behaviour at ambient pressure. U_2Pt_2In is a promising compound to study NFL behaviour because: i) it is a stoichiometric compound, thus the physics might not be dominated by disorder; ii) the observation of NFL behaviour at ambient pressure, enables the use of a wide range of experimental techniques. These points, together with the availability of samples in a single-crystalline form, yield the motivation to study U_2Pt_2In extensively.

Hopefully, this thesis will serve as a reference work to NFL behaviour in heavy-fermion compounds. No definite answer as to the origin of the observed NFL behaviour is given. Actually, considering the state of the art of NFL physics, no definite answer *can* be given at present. The experimental results presented here are discussed in terms of possible mechanisms, yielding strong indications for collective (as in quantum criticality) or single-ion (as in local Fermi liquid descriptions) phenomena.

1.2. Outline

Throughout this thesis, the discussion of the results runs in parallel with the presentation and analysis of the experimental data. A general discussion of the physical properties and/or a summary of the results is given at the end of each chapter.

A brief introduction to heavy-fermion compounds and Fermi liquid theory, as well as an overview of the relevant models that predict NFL properties is given in Chapter 2. In this chapter, a short overview of materials exhibiting NFL behaviour is given as well.

A description of the experimental techniques used throughout this work can be found in Chapter 3. As most of these experimental techniques and set-ups have been described extensively elsewhere, the presentation is kept relatively short. However, the high-pressure technique, used in Chapters 6 and 7, and the muon spin relaxation and rotation (μSR) technique, used in Chapters 5 and 7, are described in more detail.

In Chapter 4, an introduction to the U_2T_2X family of compounds is given and a Doniach phase diagram is constructed for the families with X=In and Sn. In the case of U_2Pt_2In, measurements of the magnetization, resistivity, magnetoresistance, specific heat, specific heat in field and thermal expansion are presented, analysed and discussed. The data presented in this chapter undoubtedly establish the NFL character of U_2Pt_2In.

Zero-, longitudinal- and transverse-field μSR spectra taken on U_2Pt_2In are discussed in Chapter 5. These experiments served to confirm the absence of static magnetic order in U_2Pt_2In. In the NFL regime, pronounced magnetic fluctuations are found.

Chapter 6 deals with resistivity measurements on U_2Pt_2In under hydrostatic pressure, as well as with Th-doping studies. Results of the recovery of a Fermi liquid state in U_2Pt_2In under pressure and the possible emergence of magnetic ordering in Th-doped U_2Pt_2In are presented. For comparison, the suppression under pressure of magnetism in U_2Pd_2In was studied. A discussion in terms of the Doniach phase diagram is given. In addition, magnetization measurements are presented for several compounds of the U_2T_2X family in order to investigate their location in the Doniach diagram.

Besides the U_2T_2X family, several other uranium intermetallic systems exhibiting NFL behaviour were studied. Namely, $U_3Ni_3Sn_4$ was studied by means of specific heat, resistivity (under pressure) and μSR experiments, $U(Pt_{1-x}Pd_x)_3$ by means of μSR experiments and $URh_{1/3}Ni_{2/3}Al$ by means of resistivity measurements. The results are presented in Chapter 7 in a collection of published (or submitted for publication) articles.

Some concluding remarks are made in Chapter 8.

Several abbreviations are introduced in this thesis. A list is presented in Table 1.1.

Table 1.1 - List of abbreviations used in this work.

AF	AntiFerromagnetism	QCP	Quantum Critical Point
CW	Curie-Weiss	QKE	Quadrupolar Kondo Effect
EPMA	Electron Probe MicroAnalysis	RE	Rare Earth
FC	Field Cooled	RKKY	Rudermann-Kittel-Kasuya-Yosida
FL	Fermi Liquid	RT	Room Temperature
FM	FerroMagnetism	SBF	Symmetry Breaking Field
GPS	General Purpose Spectrometer	SC	SuperConductivity
HF	Heavy Fermion	SCR	Self-Consistent Renormalization
HTSC	High-Temperature SuperConductivity	SDW	Spin Density Wave
INS	Inelastic Neutron Scattering	SEM	Secondary Electron Microscopy
LDA	Local Density Approximation	SG	Spin Glass
LF	Longitudinal Field	SMAF	Small-Moment AntiFerromagnetism
LMAF	Large-Moment AntiFerromagnetism	SQUID	Superconducting QUantum Interference Device
LTF	Low Temperature Facility	TCKE	Two-Channel Kondo Effect
MCW	Modified Curie-Weiss	TEM	Transmission Electron Microscopy
MORE	Muons On REquest	TF	Transverse Field
MR	MagnetoResistance	XRD	X-Ray Diffraction
NFL	Non-Fermi Liquid	ZF	Zero Field
NMR	Nuclear Magnetic Resonance	ZFC	Zero Field Cooled
OFHC	Oxygen-Free High Conductivity	μ-s.s.	Muon Stopping Site
PSI	Paul Scherrer Institute	μSR	Muon Spin Relaxation or Rotation

References

1. B.R. Coles, Contemp. Phys. 28 (1987) 143.
2. Proc. ITP Conference on Non-Fermi Liquid Behaviour in Metals, Santa Barbara, 1996, in J. Phys.: Condens. Matter 8 (1996) 9675 ff.

2. Non-Fermi liquid behaviour in heavy-fermion compounds

2.1. Heavy-fermion compounds and Fermi liquid theory

Heavy-fermion (HF) systems are predominantly found in cerium and uranium compounds where the 4*f*- and 5*f*-electron states are relatively close to the Fermi level. Near room temperature (RT), the *f*-moment sublattice has properties resembling those of weakly (Curie-Weiss) interacting magnetic moments. The electronic transport properties are dominated by incoherent scattering of the conduction electrons by the local moments. As the temperature is lowered, local-moment behaviour gives way to electronic properties that are consistent with those of a narrow band of conduction electrons. The crossover temperature is the coherence temperature T_{coh}.

In Landau's theory of Fermi liquids (FL), a one-to-one mapping of non-interacting electron states to interacting electron states is assumed close to the Fermi energy. If the interactions are turned adiabatically, the states can be described in terms of quasiparticles, which have an enhanced effective mass due to interactions with other quasiparticles in the surrounding medium.

At sufficiently low temperatures (much lower than the Fermi temperature), a useful tool to describe the thermodynamic properties of a system with itinerant electrons is the effective mass

of the electrons. In normal metals, the effective mass m^* is of the order of the free-electron mass m_e, while in heavy-fermion systems m^* can attain values as large as $10^3\, m_e$.

A single quasiparticle has an energy

$$\varepsilon_{\boldsymbol{k}}^0 = \frac{\hbar^2 k_F}{2m^*}(|\boldsymbol{k}| - k_F) \quad , \tag{2.1}$$

where $\boldsymbol{k}$ is the wave-vector and $k_F = (3\pi^2\rho_e)^{1/3}$ is the Fermi wave-vector (ρ_e is the number of electrons per unit volume). This expression defines the effective mass m^*. When a quasiparticle is added to the system, it will have an energy

$$\varepsilon_k = \varepsilon_{\boldsymbol{k}}^0 + \frac{1}{\Omega}\sum_{k'} f(k,k')\,\delta n(k') \quad , \tag{2.2}$$

where Ω is the volume of the system and $f(k,k')$ is the quasiparticle interaction function. From this, it follows that the energy of the added quasiparticle is not just the bare quasiparticle energy $\varepsilon_{\boldsymbol{k}}^0$, but also depends on the presence of other quasiparticles. $\delta n(k)=1$ represents an excited quasiparticle and $\delta n(k)=-1$ an excited quasi-hole. Notice that k denotes $(\boldsymbol{k},\sigma)$ with σ the spin index ($\uparrow$ or $\downarrow$). The function $f(k,k')$ can be transformed into spin-symmetric and spin-antisymmetric functions:

$$\begin{cases} f(\boldsymbol{k}\uparrow,\boldsymbol{k}'\uparrow) = f^s(\boldsymbol{k},\boldsymbol{k}') + f^a(\boldsymbol{k},\boldsymbol{k}') \\ f(\boldsymbol{k}\uparrow,\boldsymbol{k}'\downarrow) = f^s(\boldsymbol{k},\boldsymbol{k}') - f^a(\boldsymbol{k},\boldsymbol{k}') \end{cases} . \tag{2.3}$$

A restriction of the Fermi-liquid theory is that all involved particles have a momentum very close to the Fermi surface: $|\boldsymbol{k}| \approx |\boldsymbol{k}'| \approx k_F$. The $f^{a,s}$ functions can then be expanded in a series of Legendre polynomials P_L:

$$f^{a,s}(\boldsymbol{k},\boldsymbol{k}') = \sum_{L=0}^{\infty} f_L^{a,s} P_L(\cos\theta) \tag{2.4}$$

with $\cos\theta = (\boldsymbol{k}\cdot\boldsymbol{k}')/k_F^2$. A dimensionless form of the coefficients $f_L^{a,s}$ is given by the Landau parameters

$$F_L^{a,s} = \frac{m^* k_F}{\pi^2\hbar^2} f_L^{a,s} \quad . \tag{2.5}$$

The thermodynamic and response functions of the electronic liquid can now be calculated and shown to be smooth functions of temperature. The density of states at the Fermi energy is given by

$$N(0) = \frac{m^* k_F}{\pi^2 \hbar^2} \quad , \tag{2.6}$$

where the effective mass of the quasiparticles m^* is related to the bare mass m_e by a symmetric Landau parameter

$$\frac{m^*}{m_e} = 1 + \frac{F_l^s}{3} \quad . \tag{2.7}$$

The temperature independent Pauli susceptibility has the form

$$\chi = \frac{\mu_0 \mu_B^2 \, m^* k_F}{\pi^2 \hbar^2} \frac{1}{1 + F_0^a} \tag{2.8}$$

with F_0^a an antisymmetric Landau parameter. χ is enhanced with respect to the Pauli susceptibility of the non-interacting system by a factor $m^*/m_e(1+F_0^a)$.

The specific heat c_V in the FL theory is given by

$$\frac{c_V}{T} = \gamma = \frac{m^* k_F \, k_B^2}{3\hbar^2} \quad , \tag{2.9}$$

which is enhanced with respect to the specific heat of the non-interacting system by a factor m^*/m_e. Therefore, the specific-heat coefficient gives direct information about the effective mass m^*. The Wilson ratio R_W relates the Pauli susceptibility to the electronic specific-heat coefficient

$$R_W = \frac{\pi^2 k_B^2}{3\mu_0 \mu_B^2} \frac{\chi}{\gamma} = \frac{1}{1 + F_0^a} \quad . \tag{2.10}$$

In the case of a non-interacting system, $R_W = 1$.

The electrical resistivity behaves as

$$\rho = \rho_0 + AT^2 \quad , \tag{2.11}$$

where ρ_0 is the residual resistivity due to impurities and defects and A is a constant.

The FL theory gives a good description of the low-temperature properties of metals (above any magnetic or superconducting transition). In heavy-fermion compounds, the high-temperature local-moment behaviour gives way to a low-temperature coherent state where the FL theory is valid with a strongly enhanced effective mass m^*. The specific heat, susceptibility and resistivity follow the temperature dependencies $c(T) = \gamma T$, $\chi(T) = \text{const}$ and $\rho(T) = \rho_0 + AT^2$, respectively. Values of the Wilson ratio in the range 2-5, as normally found in HF systems, can be accounted for by a negative Landau parameter F_0^a. The coefficient A is related to γ by the empirical Kadowaki-Woods relation: $A/\gamma^2 \sim 10\ \mu\Omega\text{cmK}^2\text{mol}^2\text{J}^{-2}$ [1].

Within the FL theory, spin fluctuations in the HF system give rise to a correction term in the specific heat of the form $c(T) = \gamma T + \delta T^3 \ln(T/T^*)$, where T^* is a characteristic spin-fluctuation temperature.

Most HF compounds exhibit the Kondo effect [2], manifested in measurements of the electrical resistivity from room temperature down to low temperatures. The Kondo Hamiltonian describes the exchange interaction of a single magnetic impurity (with spin **S**) with a conduction electron (with spin **s**):

$$\mathcal{H} = -2J\,\mathbf{s}\cdot\mathbf{S} \quad . \tag{2.12}$$

For a negative coupling parameter J, the impurity spin is completely compensated at low temperatures and a Kondo singlet is formed. As a result, the resistivity obeys a $-\ln(T/T_K)$ behaviour. The binding energy of a Kondo singlet is

$$k_B T_K \propto \frac{1}{N(0)} \exp\left(-\frac{1}{JN(0)}\right) \quad . \tag{2.13}$$

HF materials may be considered as Kondo lattices with a periodic array of magnetic "impurities". In Kondo lattices, scattering at low temperatures may be coherent, resulting in a fast drop of the resistivity (as the temperature is lowered) and a T^2 behaviour at the lowest temperatures. In general, the compensation of the *f*-moments by means of the Kondo effect leads to the formation of a non-magnetic ground state.

On the other hand, antiferromagnetic interactions between the *f*-moments are provided via the conduction electrons by the Rudermann-Kittel-Kasuya-Yosida (RKKY) interaction. This interaction tends to form a magnetic ground state in HF systems. The energy associated with the RKKY interaction is

$$k_B T_{RKKY} \propto J^2 N(0) \quad . \tag{2.14}$$

Considering the scales defined by T_K and T_{RKKY}, Doniach proposed that the low-temperature ground state of the system is a direct consequence of the competition between the Kondo scattering and the RKKY interaction [3]. A (Doniach) phase diagram can then be constructed (Figure 2.1) [i]. Heavy-fermion compounds are in general located close to the magnetic

[i] Strictly speaking, the Doniach phase diagram is of the form T/W versus J/W. However, for HF compounds and close to the magnetic instability, external parameters like pressure and doping will more effectively influence the exchange-coupling parameter J than the bandwidth W. Therefore, and also for simplicity, $T(J)$ diagrams will be used throughout this work.

instability, where the competition between the Kondo effect and the RKKY interaction is most important.

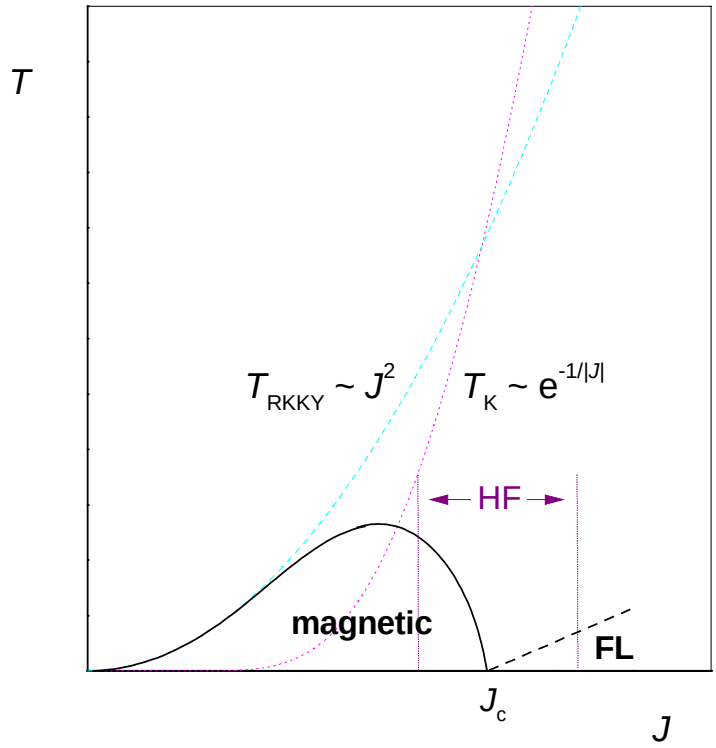

Figure 2.1 - Doniach phase diagram (FL = Fermi liquid, HF = heavy fermion). The dotted lines represent T_{RKKY} and T_K. The full line represents the ordering temperature and the dashed line the temperature below which FL behaviour is attained.

Reviews on heavy-fermion compounds are given in Refs. 4 and 5. The Fermi-liquid theory is extensively described in Refs. 6 and 7.

2.2. Non-Fermi liquid behaviour

During the past decade, a new class of heavy-fermion systems that exhibit strong deviations from Fermi-liquid theory has attracted much interest [8]. These *non-Fermi liquid* (NFL) materials are U-, Ce- and Yb-based intermetallics that, with a few exceptions, have been doped with a non-magnetic element. The main macroscopic properties related to NFL behaviour are a diverging specific heat divided by temperature ($c/T \sim -\ln(T/T_0)$ or $c/T \sim \gamma_0 - \alpha T^{1/2}$), a

diverging magnetic susceptibility ($\chi \sim 1\text{-}bT^{\beta}$ or $\chi \sim -\ln(T/T_0)$) and a non-quadratic electric resistivity ($\rho \sim aT^{\alpha}$ with $\alpha < 2$ and a can be positive or negative).

The divergency of c/T is the hallmark of NFL behaviour. Within the FL theory, a temperature dependent coefficient γ that diverges as $T \to 0$ would imply a diverging density of states at the Fermi level. Therefore, FL theory cannot be applied in its simple form. This is why the name *non-Fermi liquid* was fist given to this behaviour. Nevertheless, in some cases, models based on a local FL description can account for this new behaviour.

At present, no theoretical models are at hand which yield an universal description of NFL behaviour. However, a common starting point may be found in the physics of quantum critical points. This results from the recognition that NFL properties emerge at or close to the magnetic instability in a typical Doniach phase diagram for HF compounds (Figure 2.2).

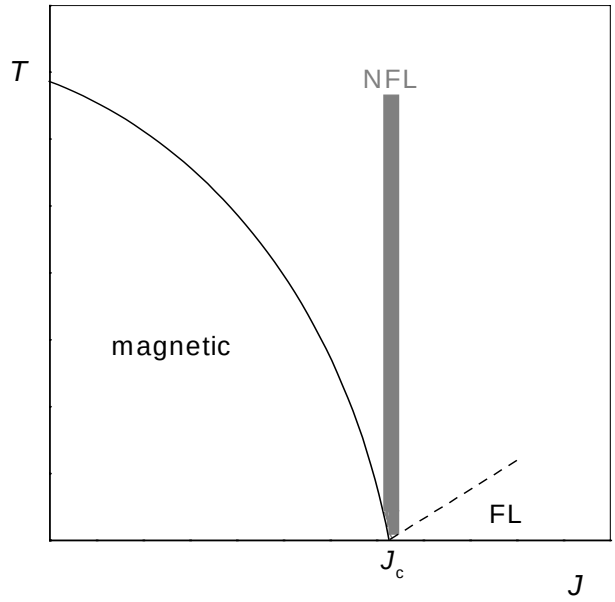

Figure 2.2 - NFL region close to a magnetic instability for HF systems.

Within the Doniach phase diagram, magnetism vanishes when the single-ion Kondo scattering becomes more important than the RKKY interaction. In renormalization group language, antiferromagnetism (AF) and FL behaviour can be considered as two competing fixed points. As the temperature is lowered, the system evolves from the high-temperature local-moment behaviour to one of these fixed points, as represented in the flow diagram in Figure 2.3. The trajectories represented correspond to different values of T_K/T_{RKKY}. When a material is tuned to the critical value of T_K/T_{RKKY}, it is forced to evolve to the quantum critical point (QCP) [9].

The existence of an antiferromagnetic QCP implies that the two fixed points (AF and FL) are linked by a new unstable fixed point. For a wide range of materials, T_K/T_{RKKY} is close to its critical value. These materials will evolve towards the FL or AF fixed points, passing close to the new fixed point. Over a large temperature range their properties, excitations and interactions will be dominated by the physics of this QCP.

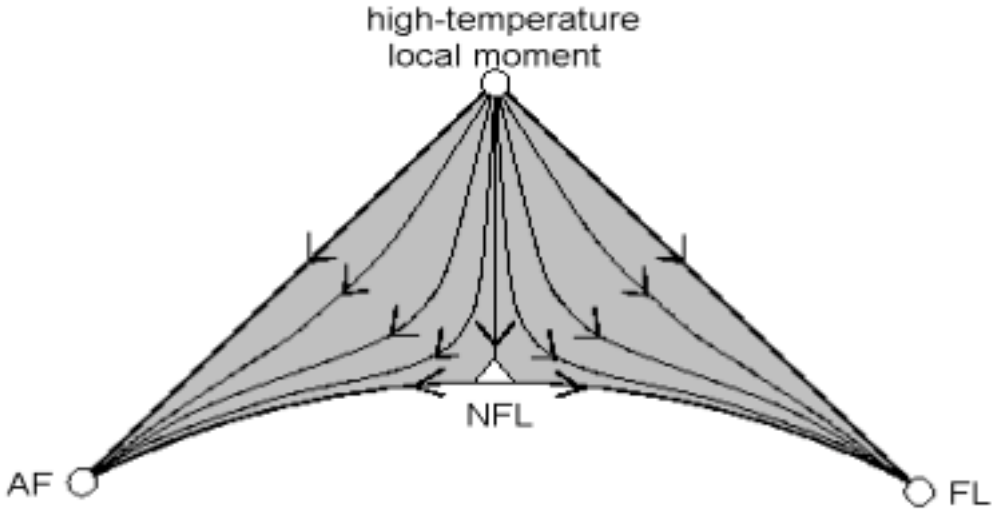

Figure 2.3 - Schematic flow diagram for the Kondo lattice. Taken from Ref. 9.

However, since a number of *f*-systems exhibiting NFL properties does not seem to be at a QCP, other models have been put forward in order to describe the microscopic mechanisms that lead to NFL behaviour. Single-ion Kondo models have been applied, with relative success. Also models have been proposed where disorder plays a crucial role, as a number of NFL systems are chemically-substituted or diluted compounds and, therefore, disordered.

The most relevant routes that have been proposed to lead to non-Fermi liquid behaviour in *f*-electron systems are:

i) a two-channel Kondo effect [10], where the *f*-electron impurity spin is overscreened by the spins of the conduction electrons, giving rise to an antiferromagnetic superexchange interaction with electrons off the impurity site (see Section 2.3.1);

ii) a distribution of Kondo temperatures [11], where the Kondo effect on each *f*-electron impurity sets a different temperature scale, resulting in a broad range of effective Kondo temperatures; averaging over such a distribution gives rise to thermodynamic properties which follow the NFL expressions (see Section 2.3.2);

iii) a proximity to a QCP [12], where a magnetic or superconducting phase transition occurs at $T = 0$ K (either spontaneously or the transition might be tuned to 0 K by an external parameter, like hydrostatic or chemical pressure); here, the thermodynamic properties are determined by collective modes corresponding to fluctuations of the order parameter in the vicinity of the critical point (see Section 2.3.3);

iv) a Griffiths phase model [13] where, due to disorder, magnetic clusters appear in the paramagnetic phase close to a QCP (see Section 2.3.4).

NFL properties have also been found in *d*-transition-metal systems. For instance, Ni_xPd_{1-x} has a ferromagnetic QCP at $x = 0.025$ [14]. The specific heat, resistivity and magnetic susceptibility strongly deviate from the standard FL behaviour and can be fully accounted for by a proximity to a ferromagnetic QCP (see Section 2.3.3).

NFL behaviour may also be found in one-dimensional (1D) systems, where it is described theoretically by the Luttinger liquid model [15]. In these 1D systems, the electron-electron interaction is much stronger than in a FL, which may lead to spin-charge separation [16]. Quantum wires [17] and some organic 1D conductors [18] have been described as Luttinger liquids.

The normal state of high-T_c cuprates is also known to exhibit properties that deviate strongly from FL behaviour. A so-termed marginal-Fermi liquid model [19] has been proposed as a phenomenological approach to the behaviour of high-temperature superconductors. Here, it is assumed that the spin and charge susceptibilities have an unusual form, in that they are approximately momentum independent and vanish linearly in ω/T for low frequencies. In contrast, spin and charge of a FL are strongly momentum dependent and have a low-frequency behaviour that becomes independent of temperature as $T \to 0$. This assumption gives rise to a scattering rate linear in temperature and an effective mass that diverges logarithmically as the Fermi energy is approached.

2.3. Routes to non-Fermi liquid behaviour

2.3.1. Multichannel Kondo effect

As mentioned before, within the usual single-channel Kondo effect, the physics of an *f*-electron system can be described by a local version of Landau's FL theory [20]. However, a simple modification of this model can produce NFL behaviour: the multichannel Kondo effect [10].

In the overcompensated multichannel Kondo model, M identical spin-½ conduction bands exchange-couple to a single-impurity spin S_I with the condition $M/2 > S_I$, so that there are more conduction spins than needed to fully compensate the impurity.

In the simplest case of the S_I=½ two-channel Kondo effect (TCKE) [21], the impurity spin is overcompensated by the presence of two conduction spins ½. The resulting spin of the ground state will be ½ and an antiferromagnetic superexchange will be generated with electrons off the impurity site. In renormalization group language, the kinetic energy introduced by this superexchange interaction makes the strong-coupling ($J\to\infty$) fixed point unstable, since at this fixed point the kinetic energy is zero. This maps the effective model back to the weak-coupling (J=0) limit. However, the weak-coupling fixed point is unstable due to the Kondo effect. Thus both weak- and strong-coupling limits are unstable. Therefore, a non-trivial fixed point at intermediate coupling must exist [22].

This non-trivial fixed point gives rise to a degenerate ground state and a NFL energy spectrum. The extra specific-heat coefficient and spin susceptibility per mole of impurity diverge for $T\to 0$ as [23]

$$\frac{c(T)}{T} = -\frac{A'}{T_K}\ln\frac{T}{bT_K} + B' \qquad (2.15a)$$

$$\chi(T) \sim -\frac{1}{T_K}\ln\frac{T}{b_\chi T_K} \quad , \qquad (2.15b)$$

where $A' = 0.251\mathrm{R}$, $b = 0.41$, b_χ is of the order of 1 and B' is a temperature independent electronic or crystal-field background in c/T. The resistivity, on the other hand, behaves as [24]

$$\rho(T) \sim 1 - a\left(\frac{T}{T_K}\right)^{1/2} \quad , \tag{2.15c}$$

where a is of the order of 1. However, while the logarithmic divergence of c/T and χ appears for $T < 0.5T_K$, $\rho \sim 1\text{-}aT^{1/2}$ should be observable only for $T < 0.05T_K$ [10]. In the intermediate temperature range $0.05T_K < T < T_K$, $\rho \sim 1\text{-}aT$.

The two channels of conduction spin and the impurity have an effective spin ½. Therefore, the degeneracy of the impurity spin is never lifted, unlike in the ordinary Kondo problem. This residual degeneracy manifests itself in a net residual entropy of ½Rln2 per mole impurity. This residual entropy can be recovered by e.g. an external magnetic field [10], which will lift the degeneracy.

For the quadrupolar multichannel Kondo effect (QKE) [25], where the electrical quadrupolar moment of the *f*-ion interacts with the conduction electrons and their spins provide the two channels, the susceptibility does not diverge logarithmically but as

$$\chi(T) = \chi(0)\left[1 - b'\left(\frac{T}{T_K}\right)^{1/2}\right] \tag{2.16}$$

with $b' \sim 1$.

2.3.2. Kondo disorder model

A distribution of Kondo temperatures T_K can arise if a material has large disorder. Around each single magnetic impurity, antiferromagnetically coupled to conduction electrons (assuming an effective spin-½ impurity magnetic moment), the Kondo effect will occur at a different value of T_K. Averaging over such a distribution can produce thermodynamic and transport properties with NFL-like dependencies due to the broad range of effective Fermi temperatures. Essentially, the unquenched moments contribute to the NFL physics.

In this scenario, a NFL state is generated as a consequence of the interplay of disorder and strong correlations. The main idea of this model is that moderate bare disorder in a lattice model of localized moments is magnified due to the strong local correlations between the *f*-moments and the conduction electrons. In particular, a broad distribution of local energy scales (Kondo temperatures) is generated. A few local sites with very low Kondo temperatures are unquenched

at low temperatures and dominate the thermodynamics and transport, giving rise to a dilute gas of low-lying excitations above the disordered metallic ground state. The presence of these unquenched moments leads to the formation of a NFL phase [11].

In $UCu_{5-x}Pd_x$ (x = 1, 1.5), Cu NMR studies revealed the presence of a strong inhomogeneous broadening of the NMR line width [26]. This broadening can be explained within the Kondo disorder model assuming a collection of completely uncorrelated spins, each coupled to the conduction-electron bath by a Kondo-coupling constant $N(0)J$, which is allowed to be randomly distributed in the sample. This distribution is supposed to originate from the local disorder induced by Pd substitution at the Cu sites. The thermodynamic response is then calculated by taking an average over the response of a single Kondo spin with a distribution of coupling constants. Because of the exponential dependence of T_K on $N(0)J$, a broad distribution of Kondo temperatures results, as shown in Figure 2.4.

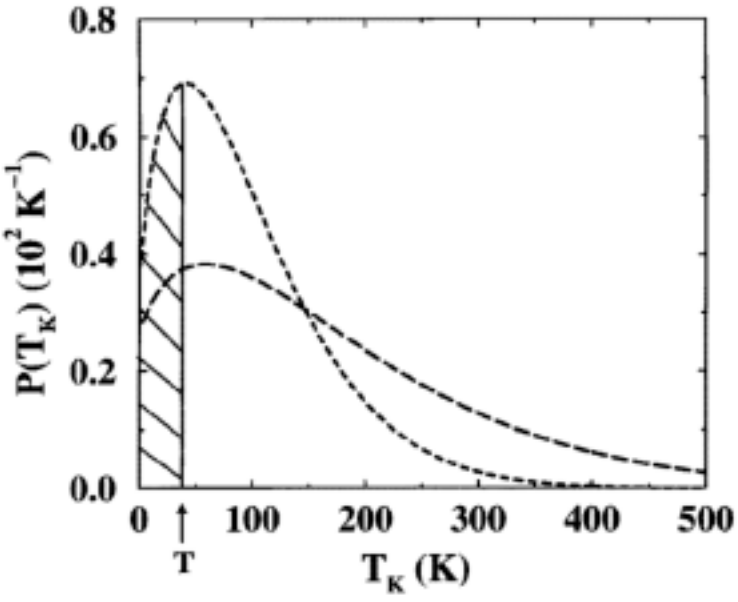

Figure 2.4 - Distribution of Kondo temperatures in UCu_4Pd (dashed line) and in $UCu_{3.5}Pd_{1.5}$ (dotted line). The shaded area below T represents the low-T_K spins which remain unquenched at that temperature. Taken from Ref. 11.

The Kondo disorder model also leads to an incoherent nature of the transport properties with sufficient disorder strength. Due to local Kondo physics at each *f*-site, the effective disorder generated from a bare distribution of local *f*-shell parameters is strongly renormalized up to scales of the order of the conduction electron bandwidth. Although clean systems have low resistivities due to the onset of coherence at low temperature, moderate amounts of *f*-element

disorder are capable of destroying this low-temperature coherence, leading to characteristic incoherent Kondo scattering behaviour.

The predictions of the model for the specific heat, susceptibility and resistivity are [11]

$$c(T) \sim -T \ln(T/T_0) \quad (2.17a)$$

$$\chi(T) \sim -\ln(T/T_0) \quad (2.17b)$$

$$\rho(T) \sim 1 - aT \quad . \quad (2.17c)$$

2.3.3. Proximity to a quantum critical point

A quantum critical point (QCP) occurs when a critical point such as that associated with a ferro- or antiferromagnetic transition is tuned to T=0 by some external parameter δ, such as pressure or dopant concentration. At the QCP ($\delta=\delta_c$), the low-temperature thermodynamics is determined by collective modes corresponding to fluctuations of the order parameter, rather than by single-fermion excitations as in a FL. Therefore, NFL properties arise. NFL behaviour can also occur near quantum spin-glass [27] or superconducting [28] transitions.

Like its finite-temperature counterpart (thermal or classical phase transition), a quantum phase transition is characterized by a diverging correlation length ξ and a diverging relaxation time ξ_τ. However, the critical fluctuations that lead to these diverging length and time scales are quantum fluctuations rather than thermal ones. Contrary to the situation for a classical critical point, the dynamic and static behaviour of a QCP are coupled together. A system at a QCP will be affected in the same way by either a finite frequency or a finite temperature. The system is characterized by the dynamical scaling exponent z that describes the divergence of ξ_τ. The value of z affects strongly the static critical behaviour [29]. The dynamical exponent z takes the value of 2, 3 and 4 for an antiferromagnet, a clean ferromagnet and a dirty ferromagnet, respectively. A d-dimensional quantum system is related to a classical one with an effective dimension $d_{\text{eff}} = d+z$.

When studying the effect of non-zero temperatures on the QCP in itinerant-fermion systems using renormalization-group theory, the diagram of Figure 2.5 applies [12,30]. Different regions close to the QCP must be considered. Region I is the disordered quantum regime where

the FL picture applies, region II is the perturbative classical regime and region III is the classical Gaussian regime. The different regimes are separated by the lines

$$T_{\mathrm{I}} \sim (\delta - \delta_{\mathrm{c}})^{z/2} \tag{2.18a}$$

$$T_{\mathrm{II}} \sim (\delta - \delta_{\mathrm{c}})^{z/(d+z-2)} \tag{2.18b}$$

$$T_{\mathrm{m}} \sim (\delta_{\mathrm{c}} - \delta)^{z/(d+z-2)} \quad . \tag{2.18c}$$

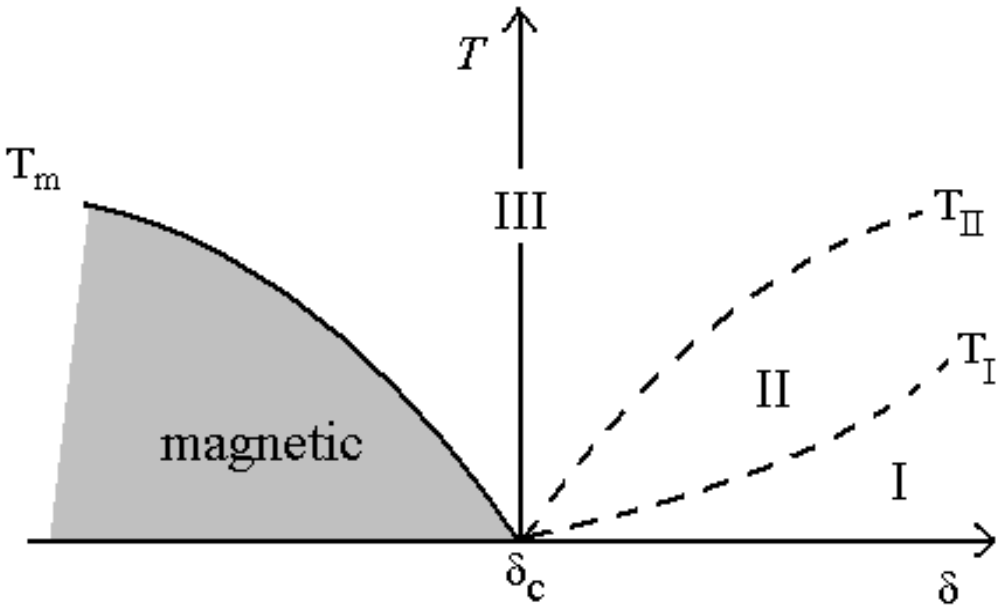

Figure 2.5 - Phase diagram of the temperature versus the control parameter δ. Region I is the disordered quantum regime, region II is the perturbative classical regime and region III is the classical Gaussian regime. The lines T_{I}, T_{II} and T_{m} are defined in the text. After Ref. 12.

Calculations of the specific heat give the same expressions for regions II and III, while the correlation length ξ is the same for regions I and II. For the classical regime, i.e. just above the QCP, and for $d = 3$ the specific heat and resistivity near an antiferromagnetic ($z = 2$) QCP have the temperature dependencies

$$c(T)/T = \gamma_0 - \alpha T^{1/2} \tag{2.19a}$$

$$\rho(T) \sim T^{3/2} \quad , \tag{2.19b}$$

while for a ferromagnetic ($z = 3$) QCP,

$$c(T)/T \sim -\ln(T/T_0) \tag{2.20a}$$

$$\rho(T) \sim T^{5/3} \quad . \tag{2.20b}$$

The same predictions are obtained within the self-consistent renormalization (SCR) theory of spin fluctuations [31]. The SCR theory takes into account the couplings among the different modes of spin fluctuations in a self-consistent way. Although initially developed for itinerant *d*-electrons, the theory can be modified to nearly localized *f*-electron systems [32]. It assumes that around the magnetic phase boundary there are weakly and nearly ferro- and antiferromagnetic regimes with various anomalous properties, which are predominantly due to exchange-enhanced spin fluctuations. Within this theory, the d=3 predictions for $c(T)$ and $\rho(T)$ are the same as in equations 2.19 and 2.20. The pressure dependence of T_N or T_C is also the same as in equation 2.18c. However, at very low temperatures, $c(T)$ and $\rho(T)$ should attain temperature dependencies as in the FL theory.

A phenomenological description of NFL systems at a QCP [27] gives the following scaling relations of the magnetization and specific heat:

$$M = \frac{B}{T^{\gamma}} \mathrm{f}\left(\frac{B}{T^{\beta+\gamma}}\right) \tag{2.21a}$$

$$\frac{c(B,T)}{T} - \frac{c(0,T)}{T} = \mathrm{g}\left(\frac{B}{T^{\beta+\gamma}}\right) , \tag{2.21b}$$

where f(x) and g(x) are non-singular functions. These scaling relations can also be applied to a field-induced QCP by replacing B and $c(0,T)$ by $\Delta B = B\text{-}B_c$ and $c(B_c,T)$, respectively [33].

Another type of QCP, that has been considered theoretically, is the quantum Lifshitz point [34]. A "classical" Lifshitz point is a critical point that, in addition to the onset of magnetic ordering, is characterized by the disappearance of stiffness in one or several directions, i.e., a tricritical point where a disordered phase, a spatial uniformly ordered phase and a spatially modulated ordered phase meet [35]. In the quantum Lifshitz point model, NFL behaviour occurs in the classical Gaussian region near a quantum Lifshitz point in a three-dimensional itinerant antiferromagnet. The Néel temperature is predicted to follow the pressure dependence

$$T_N \sim (P_c - P)^{4/5} . \tag{2.22}$$

The specific heat coefficient and resistivity are predicted to vary as

$$c(T)/T \sim T^{1/4} \tag{2.23a}$$

$$\rho(T) \sim T^{5/4} . \tag{2.23b}$$

Although no NFL system has been found to obey these relations, the concept of loss of stiffness near a QCP might have its relevance in systems like $CeCu_{6-x}Au_x$ [36].

Reviews on quantum critical points are given in Refs. 37-40.

2.3.4. Griffiths phase model

Another model, proposed recently, takes into account the effects of disorder near a quantum critical point. In the Griffiths phase model [13], the presence of disorder is considered to lead to the coexistence of a metallic paramagnetic phase and a granular magnetic phase. These coexisting phases are equivalent to the Griffiths phase [41] of a dilute magnetic system.

The "classical" problem of a Griffiths phase occurs in a lattice of magnetic atoms diluted with non-magnetic atoms. Long-range order is lost at the percolation threshold when the last infinite cluster of magnetic moments ceases to exist. Above the threshold, the system is composed of finite clusters of magnetic atoms. When a magnetic field is applied to the percolation lattice, there is a non-analytic contribution from rare large clusters to the free energy [41].

For the Griffiths phase model for NFL compounds, a similar picture can be drawn. Two electronic liquids coexist: in one of them, the magnetic moments are quenched by the Kondo interaction, giving rise to a FL, while the other is dominated by the RKKY interaction giving rise to ordered regions. This inhomogeneous situation is energetically favoured by disorder, due to the entropy contribution to the free energy.

For a generic magnetic HF compound, which exhibits a QCP upon alloying, a phase diagram can be constructed within this model. For small amounts of doping, the RKKY interaction dominates and the system orders magnetically. With increasing doping, the quantum fluctuations grow due to the Kondo effect and the critical temperature decreases until it vanishes for the critical value of doping. At this QCP, the system percolates. For larger values of doping, i.e. in the paramagnetic phase, only finite clusters of magnetic atoms can be found. Among these clusters, there are some rare ones that are large and strongly coupled, in which the spins behave coherently as a giant spin or a magnetic grain. In this phase, the thermodynamic functions show essential singularities with strong effects at low temperatures. The specific heat coefficient and the static susceptibility diverge as

$$c(T)/T \sim T^{-1+\lambda} \tag{2.24a}$$

$$\chi(T) \sim T^{-1+\lambda} \tag{2.24b}$$

with $\lambda < 1$. Notice that $\lambda = 1$ corresponds to the FL expressions. The parameter λ also characterizes the temperature dependence of the mean square deviation of the susceptibility due to the distribution of susceptibilities in the system and of the non-linear static susceptibility, as well as the frequency dependencies of the local susceptibility and the NMR relaxation rate [13].

In general terms, within the Griffiths phase model, the NFL behaviour can be observed over an extended region in the paramagnetic phase next to a QCP (Figure 2.6).

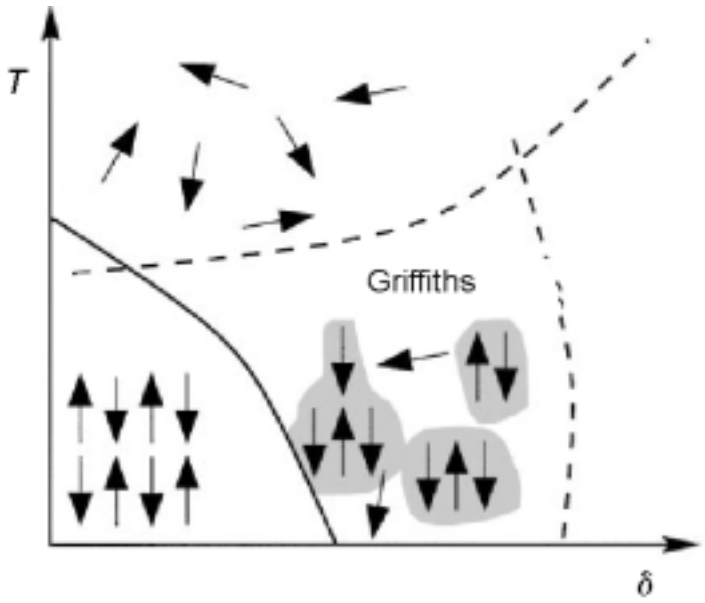

Figure 2.6 - Phase diagram for the Griffiths phase model. δ denotes a control parameter like doping concentration or pressure. Taken from Ref. 42.

2.4. Magnetotransport in nearly antiferromagnetic metals

A magnetotransport theory has recently been developed to explain the transport properties of NFL compounds near an antiferromagnetic QCP [42,43]. Under such conditions, the low-energy excitations of a HF system below a characteristic temperature T_K (see Figure 2.7a) can be assumed to be due to heavy quasiparticles and their collective excitations. The resistivity near the QCP is then determined by scattering of quasiparticles by spin fluctuations. These scattering processes are most important near hot lines, i.e. points on the Fermi surface connected by the

magnetic ordering vector *Q*. In the remaining cold regions, inelastic scattering is weak (Figure 2.7b).

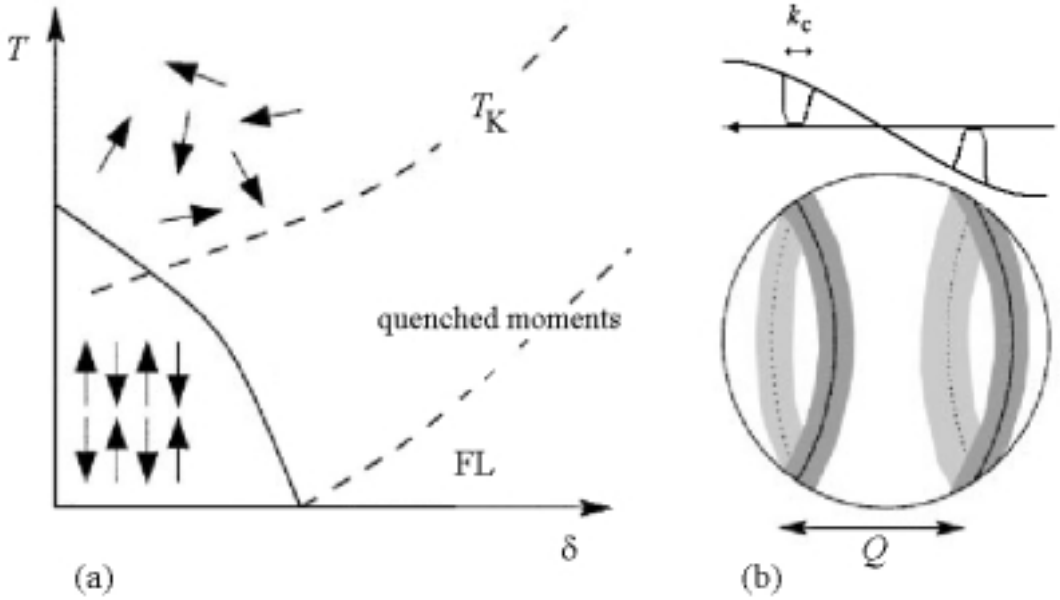

Figure 2.7 - (a) Phase diagram for an antiferromagnetic QCP. (b) Fermi surface with hot lines where scattering is enhanced - *Q* is the ordering vector of the AF phase. Taken from Ref. 42.

The theory presented in Ref. 42 predicts the behaviour of the resistivity and magnetoresistance of compounds in the paramagnetic phase near an antiferromagnetic QCP. Considering that spin fluctuations are destroyed at the temperature scale Γ, where Γ is typically of the order of T_{coh} or T_K, the resistivity is universal for $t < x^{1/2}$ and $r < 1$ in the scaling limit $t,x,r \to 0$ and $t/x, r/x \to$ const, where $t = T/\Gamma$ measures the temperature, $x = \rho_0/\rho_M \approx$ 1/RRR measures the amount of disorder and $r \propto \delta - \delta_c$ measures the distance to the QCP in the paramagnetic phase. Here, ρ_0 is the residual resistivity, ρ_M is a typical high-temperature ($t \sim 1$) resistivity value, δ is a control parameter like pressure and δ_c is its critical value.

Three different regimes are predicted for the resistivity $\Delta\rho = \rho - \rho_0$:

$$\frac{\Delta\rho}{\rho_M} \sim \begin{cases} t^{d/2}, & r < t < x^{2/d-1} \\ t^{2/(5-d)} x^{(4-d)/(5-d)}, & \max\left[x^{2/(d-1)}, x^{1/2} r^{(5-d)/4}\right] < t < x^{1/2} \\ t^2 r^{-2+d/2}, & t < \min\left[r, x^{1/2} r^{(5-d)/4}\right] \end{cases} . \qquad (2.25)$$

For three dimensions ($d = 3$), the diagram of Figure 2.8 results with

$$\Delta\rho \sim \begin{cases} t^{3/2}, & \text{regions I} \\ tx^{1/2}, & \text{regions II} \\ t^2 r^{-1/2}, & \text{region III} \end{cases} . \qquad (2.26)$$

The temperature ranges where the different regimes occur depend on the amount of disorder in the system. In the very dirty limit $x \to 1$, region II is not observed, i.e. no $\rho \sim T$ regime occurs. Regions I ($\rho \sim T^{3/2}$) and III ($\rho \sim T^2$) extend over large ranges in this limit and therefore are called the disorder-dominated regime and the disorder-dominated FL regime, respectively.

The $\rho \sim T^{3/2}$ behaviour predicted by the theories of Millis [12] and Moriya [32] for the AF QCP (see Section 2.3.3) is only observed in a small region close to the QCP. For very clean systems, this behaviour will only be observed at ultra-low temperatures. In the immediate vicinity of the QCP, the scattering process at the hot lines is short-circuited by quasiparticles at the remaining cold regions of the Fermi surface giving way to T^2 behaviour.

In region IIB (see Figure 2.8), the thermodynamic functions show FL characteristics, although the resistivity rises linearly with temperature.

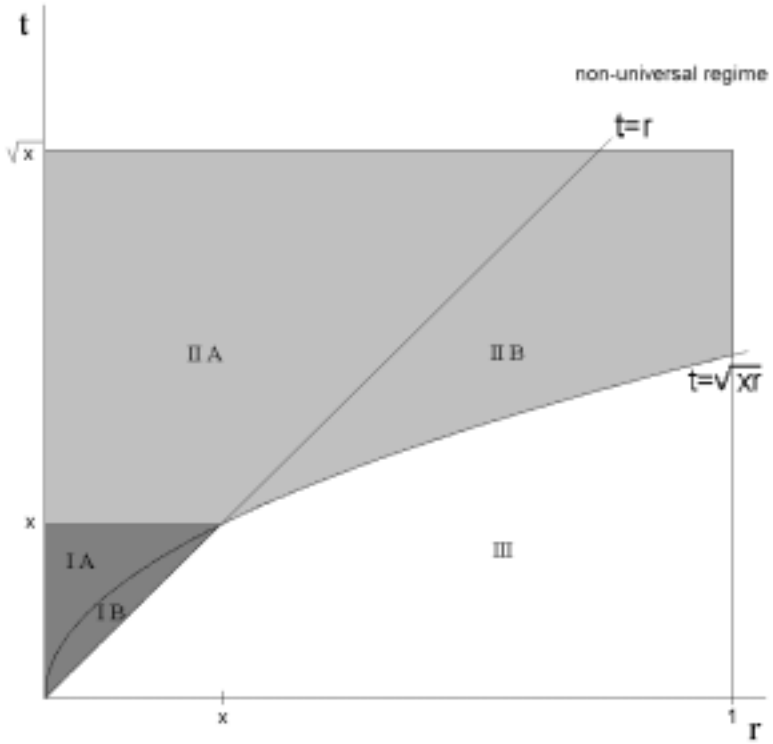

Figure 2.8 - Resistivity scaling regimes for a compound near an antiferromagnetic QCP ($d = 3$). t measures the temperature, x the amount of disorder and r the distance from the QCP in the paramagnetic phase. After Ref. 42.

In the presence of a magnetic field, the resistivity near a QCP is influenced by spin and orbital effects. The spin contribution typically suppresses the antiferromagnetic order. In the paramagnetic phase, AF fluctuations will be suppressed. Within the diagram of Figure 2.8, this corresponds to an increase of r (the distance to the QCP). The suppression of the fluctuations reduces the amount of scattering and the resistivity drops. Therefore, a negative magnetoresistance is expected. Due to the orbital effects, the resistivity increases in field. This positive magnetoresistance originates because B smears out the quasiparticle distribution, minimizing the effect that cold regions short-circuit the hot lines.

The field dependence of the resistance due to the orbital effects is different for the different regions in Figure 2.8. Defining $b = B/B_0$, where B_0 is the typical magnetic field necessary to observe Shubnikov-de Haas oscillations at $t = 1$, the following dependencies have been predicted [43]:

– region I (disorder-dominated regime)

$$\frac{\Delta\rho}{\rho_M} \sim t^{3/2} - \frac{t^{5/2}}{x} + \begin{cases} \dfrac{b^2 t^2}{x^2 g_{t,x,r}}, & b < g_{t,x,r} \\ \dfrac{bt^2}{x^2}, & g_{t,x,r} < b < t^{1/2} x \\ \dfrac{t^{5/2}}{x}, & t^{1/2} x < b < t^{1/2} x^{1/2} \end{cases} \qquad (2.27a)$$

with $g_{t,x,r} = \max[xr^{1/2}, t^{1/2} x e^{-x/4t}]$;

– region II (clean systems)

$$\frac{\Delta\rho}{\rho_M} \sim \begin{cases} tx^{1/2} + \dfrac{b^2}{tx^{1/2}}, & b < tx^{1/2} \\ b, & tx^{1/2} < b < h_{t,r} \\ h_{t,r}, & h_{t,r} < b < x^{3/4} \min\left[t^{1/4}, t^{1/2} r^{-1/4}\right] \end{cases} \qquad (2.27b)$$

with $h_{t,r} = \min[t^{3/2}, t^2 r^{-1/2}]$;

– region III (disorder-dominated FL regime)

$$\frac{\Delta\rho}{\rho_M} \sim \frac{t^2}{r^{1/2}} - \frac{t^4}{xr^{3/2}} + \begin{cases} \dfrac{b^2 t^4}{x^3 r^{5/2}}, & b < xr^{1/2} \quad (t > x^{1/2} r) \\ \dfrac{t^4}{xr^{3/2}}, & xr^{1/2} < b < tx^{1/2} r^{-1/2} \end{cases} . \qquad (2.27c)$$

Therefore, this theory predicts a magnetoresistance with an initial B^2 behaviour and a crossover towards a linear dependence in B before saturation. In the disorder-dominated FL regime (region III), $\Delta\rho \sim B$ is not observed. Besides this positive orbital contribution to the magnetoresistance, spin effects give a negative magnetoresistance in all regions.

2.5. Examples of non-Fermi liquid compounds

A characteristic of most (but not all) HF compounds exhibiting NFL behaviour is the presence of a QCP in the phase diagram. For the majority of the known NFL compounds, the QCP is reached by changing the composition. This introduces disorder in the system and its effect on the critical behaviour may be crucial. A distinction can be made between systems where the 4*f*- or 5*f*-atom is partially substituted and systems where the ligand configuration is changed. In the first case, a "Kondo hole" introduced by dilution may lead to substantial scattering and loss of coherence, while in the second case the *f*-atoms may experience different local environments and possibly different local Kondo temperatures. Therefore, even though a QCP is present in the phase diagram, the mechanism responsible for the NFL behaviour might be of the single-ion type like Kondo disorder or a multichannel Kondo effect.

NFL properties are also found in a few *stoichiometric* compounds. The advantage of stoichiometric compounds is that the role of disorder may not be dominant. Usually, hydrostatic pressure can be applied in weakly magnetic HF compounds in order to reach the QCP. Examples of stoichiometric compounds with NFL properties *at ambient pressure* are U_2Pt_2In [44], $CeNi_2Ge_2$ [45] and $YbRh_2Si_2$ [46]. Evidence for NFL has also been found in the normal state of $CeCu_2Si_2$ [47], which has a complex phase diagram with competition between magnetism and superconductivity, which relates to an intricate metallurgy.

One of the best studied NFL systems is $CeCu_{6-x}Au_x$ [48]. $CeCu_6$ is a non-magnetic HF compound with intersite antiferromagnetic fluctuations, as was shown by inelastic neutron-scattering experiments. The low-temperature properties are characteristic of a FL. Upon alloying with Au, the lattice expands. This leads to a decrease of the hybridization between the 4*f*-orbitals and Cu 3*d*-orbitals and, therefore, to a decrease of the exchange interaction J. For $x > 0.1$, RKKY

interaction between the localized moments leads to antiferromagnetic order. At the critical concentration, $x_c = 0.1$, NFL behaviour is observed (Figure 2.9). Applying pressure has an effect opposite to Au substitution. The antiferromagnetic phase ($x > 0.1$) can be tuned to T_N=0 by pressure: e.g. $p_c = 0.41$ GPa (= 4.1 kbar) for $x = 0.2$ and $p_c = 0.82$ GPa for $x = 0.3$. At these pressure values NFL behaviour is observed, as demonstrated by the logarithmic divergence of the specific heat shown in Figure 2.9. Above the critical-pressure value, FL behaviour is recovered.

Inelastic neutron-scattering studies on $CeCu_{6-x}Au_x$ have revealed the presence of quasi 2-dimensional (2D) magnetic critical fluctuations coupled to quasiparticles with 3D dynamics for $x = 0.1$ [36]. These 2D fluctuations can be viewed as precursors to the 3D ordering for $x > 0.1$. Further support for a 2D character of the critical fluctuations is provided by the fact that the temperature dependencies of the specific heat and the resistivity of $CeCu_{5.9}Au_{0.1}$ are in agreement with the predictions for a 2D antiferromagnetic QCP: $c/T \sim -\ln(T/T_0)$ and $\rho \sim T$ [12]. Also the dependencies of T_N on the pressure and the Au content are consistent with a 2D AF QCP: $T_N \sim |\delta-\delta_c|$.

Recent inelastic neutron-scattering experiments on single crystals of $CeNi_2Ge_2$ also provide evidence for anisotropic magnetic correlations with a quasi-2D character [49].

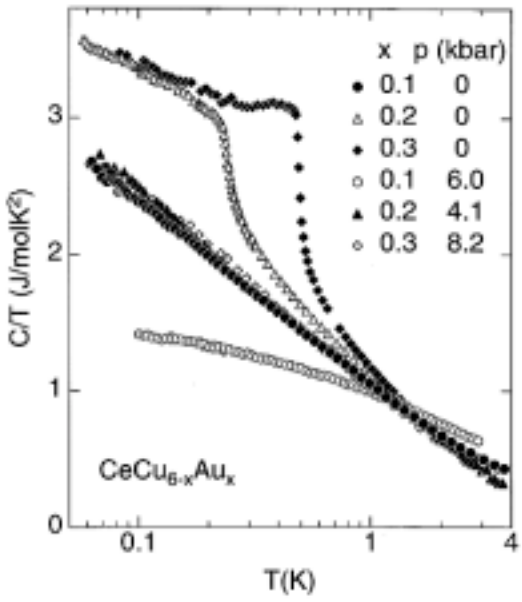

Figure 2.9 - Specific heat of $CeCu_{6-x}Au_x$ ($x = 0.1, 0.2, 0.3$) plotted as c/T versus log$T$ for different pressure values. The sharp kinks indicate T_N, while the log$T$ behaviour is characteristic of a NFL. For $x = 0.1$ and $p = 6$ GPa, the FL is restored. Taken from Ref. 48.

Besides pressure and doping, an external magnetic field can also act as a control parameter. In many NFL compounds, the specific heat and the resistivity display a tendency towards FL

behaviour under the influence of a magnetic field. In magnetic systems like $CeCu_{5.2}Ag_{0.8}$, where $T_N = 0.7$ K, a magnetic field decreases the Néel temperature and NFL properties are observed at a critical field value of 2.3 T where $T_N \rightarrow 0$ [33].

A very interesting aspect of the tuning of T_N by pressure is that superconductivity might occur near p_c. Strong evidence for magnetically mediated superconductivity has been found in systems like $CePd_2Si_2$ and $CeIn_3$ with an unconventional normal state of the NFL type. $CePd_2Si_2$ is an antiferromagnet with $T_N = 10.5$ K. Upon applying pressure, T_N drops to below 1.6 K around 2.5 GPa (Figure 2.10). T_N extrapolates to zero at $p_c = 2.7$ GPa (= 27 kbar) if the linear $T_N(p)$ dependence is assumed to continue. Around this critical pressure, superconductivity appears with a maximum transition temperature, $T_c = 0.6$ K, for $p=p_c$. The superconducting phase extends almost symmetrically to ±0.5 GPa around p_c [50]. The normal state, above the superconducting phase, exhibits NFL behaviour. The superconductivity observed at the edge of magnetic order in NFL compounds like $CePd_2Si_2$ is restricted to high-quality samples. A possible explanation for this is that the attractive magnetic interactions are strong enough to overcome competing interactions and create Cooper pairs. In other words, the superconducting state appears to be magnetically mediated, with the charge carriers held together in pairs by a "magnetic glue" [50]. Traces of superconductivity have also been found in high-purity single crystals of $CeNi_2Ge_2$ at ambient pressure [45].

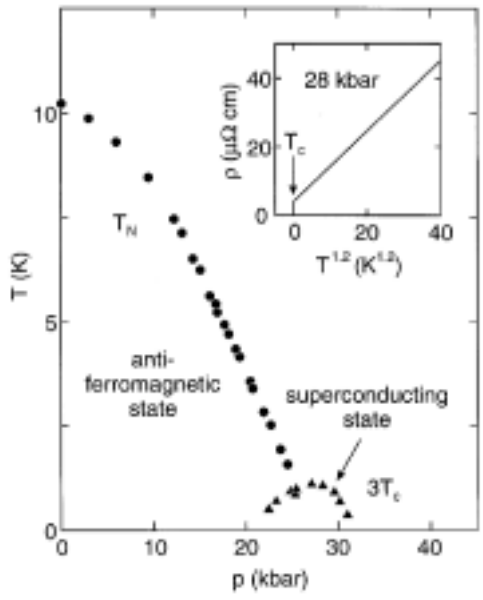

Figure 2.10 - *T*-*p* phase diagram of $CePd_2Si_2$. For clarity, the values of T_c have been scaled by a factor 3. Inset: ρ versus $T^{1.2}$ for $p = 2.8$ GPa. Taken from Ref. 50.

Recently, much attention has been devoted to Yb compounds. The physics of Yb and Ce systems are comparable due to an electron-hole analogy: the missing 4*f*-electron in the $4f^{13}$ configuration of Yb^{3+} can be interpreted as the presence of a 4*f*-hole, in analogy to the $4f^{1}$ electron in Ce^{3+}. Accordingly, Yb systems respond to doping and pressure in reverse with respect to Ce systems. For instance, pressure may drive Yb compounds towards the magnetic regime, crossing the QCP from the non-magnetic side, while in Ce compounds the opposite effect is observed. Another important property is the valence of the Yb ion: divalent Yb ($4f^{14}$ configuration) is non-magnetic, while trivalent Yb ($4f^{13}$) is magnetic. Proper substitutions of the ligand atoms in an Yb system may induce a crossover from the divalent to the trivalent state, hence inducing a crossover from a non-magnetic to a magnetic compound. This occurs e.g. in the system $YbCu_{5-x}Al_x$, where a gradual change of the valence of Yb is observed with increasing Al content x: non-magnetic Yb($4f^{14}$) for x=0 and magnetic Yb($4f^{13}$) for x = 2. A quantum critical point occurs for x = 1.5, where NFL properties are observed [51].

Many attempts have been made to group all NFL heavy-fermion compounds in one universal class. However, there does not seem to be a single and uniform picture of the mechanism responsible for NFL behaviour. One striking example of this diversity is the system $U_{1-x}M_xPd_2Al_3$ with M = Th or Y. UPd_2Al_3 is a well known HF compound with coexistence of antiferromagnetism and superconductivity. Upon Th doping ($x < 0.2$), T_N decreases only slightly and $T_c \to 0$ at $x \sim 0.1$. This small decrease suggests that U is tetravalent, just like Th, in $U_{1-x}Th_xPd_2Al_3$ for $0 \leq x < 0.2$ [52]. As the Th content increases further, a crossover region ($0.2 < x < 0.4$) occurs where neither antiferromagnetism nor superconductivity has been observed. For $x > 0.6$, NFL behaviour is observed. The NFL characteristics of ρ, c and χ scale with x and T_K, indicating that a single-ion mechanism could be responsible for the NFL. No QCP seems to be present in the *T*-x diagram. On the other hand, the *T*-x diagram of the $U_{1-x}Y_xPd_2Al_3$ system is remarkably different. Upon Y doping, T_N decreases rapidly and $T_c=0$ for $x \sim 0.03$. NFL behaviour occurs around the QCP at $x_c = 0.7$, where T_N vanishes. The characteristics of ρ, c and χ are consistent with cooperative phenomena arising from fluctuations related to magnetic order above the QCP [52]. Therefore, substitutions with Y^{3+} or Th^{4+} lead to NFL regimes associated with different mechanisms: single-ion for Th and cooperative for Y.

NFL properties have been observed in many other systems. A list of some representative HF compounds exhibiting NFL behaviour is given in Table 2.1. Recent reviews are given in Refs. 8, 47, 48 and 51.

Table 2.1 - List of some HF compounds exhibiting NFL properties. References to most recent and general papers are given (for the original works see references therein).

compound / system	conditions for NFL	notes	Ref.
$YbRh_2Si_2$	-		46
$CeNi_2Ge_2$	-	traces of superconductivity	45
U_2Pt_2In	-		44
Ce_7Ni_3	p=0.4 GPa	intrinsic crystallographic disorder	53
$CePd_2Si_2$	p=2.7 GPa	superconductivity	50
$CeRu_2Ge_2$	p=6.7 GPa		54
$YbCu_{5-x}Al_x$	x=1.5		51
$CeCu_{6-x}Au_x$	x=0.1	2D antiferromagnetic fluctuations	36,48
$Ce(Ru_{1-x}Rh_x)_2Si_2$	x=0.5	AF phase for x>0.6, SDW phase for x<0.4	55,56
$U_2Cu_{17-x}Al_x$	x=5		57
$UCu_{5-x}Pd_x$	x=1, x=1.5	Kondo disorder	26
$Ce_{1-x}La_xRu_2Si_2$	x=0.075		58
$U_{1-x}Th_xRu_2Si_2$	x=0.93		59
$U_{1-x}Th_xCu_2Si_2$	x=0.9	ferromagnetic QCP	60
$U_{1-x}Th_xBe_{13}$	x=0.1	QKE	61
$U_{1-x}Th_xPd_2Al_3$	x=0.6		52
$U_{1-x}Y_xPd_2Al_3$	x=0.8		52
$U_{1-x}Y_xPd_3$	x=0.8	spin-glass order for x<0.8	62,63

References

1. K. Kadowaki and S.B. Woods, Solid State Commun. 58 (1986) 507.
2. J. Kondo, Prog. Theor. Phys. 32 (1964) 37.
3. S. Doniach, Physica B 91 (1977) 231.
4. G.R. Stewart, Rev. Mod. Phys. 56 (1984) 755.
5. N. Grewe and F. Steglich, in "Handbook on the Physics and Chemistry of the Rare Earths" vol. 14 (K.A. Gschneidner Jr. and L. Eyring, eds.), Elsevier, Amsterdam, 1991, p. 343.
6. D. Pines and P. Nozières, "The Theory of Quantum Liquids", Addison-Wesley, New York, 1989.
7. G. Baym and C.J. Pethick, "Landau Fermi Liquid Theory", John Wiley, New York, 1991.
8. Proc. ITP Conference on Non-Fermi Liquid Behaviour in Metals, Santa Barbara, 1996, in J. Phys.: Condens. Matter 8 (1996) 9675 ff.
9. P. Coleman, Physica B 259-261 (1999) 353.
10. D.L. Cox and M. Jarrel, J. Phys.: Condens. Matter 8 (1996) 9825.
11. E. Miranda, V. Dobrosavljević and G. Kotliar, J. Phys.: Condens. Matter 8 (1996) 9871.
12. A.J. Millis, Phys. Rev. B 48 (1993) 7183.
13. A.H. Castro Neto, G. Castilla and B.A. Jones, Phys. Rev. Lett. 81 (1998) 3531.

14. M. Nicklas, M. Brando, G. Knebel, F. Mayr, W. Trinkl and A. Loidl, Phys. Rev. Lett. 82 (1999) 4268.
15. J.M. Luttinger, J. Math. Phys. 4 (1963) 1154.
16. F.D.M. Haldane, Phys. Rev. Lett. 45 (1980) 1358.
17. X.G. Wen, Phys. Rev. B 41 (1990) 12838.
18. C. Bourbonnais and D. Jérome, Phys. World (sept. 1998) 41.
19. C.M. Varma, P.D. Littlewood, S. Schmitt-Rink, E. Abrahams and A.E. Ruckenstein, Phys. Rev. Lett. 63 (1989) 1996.
20. P. Nozières, J. Low Temp. Phys. 17 (1974) 31.
21. P. Nozières and A. Blandin, J. Physique 41 (1980) 193.
22. T.S. Kim, L.N. Oliveira and D.L. Cox, Phys. Rev. B 55 (1997) 12460.
23. P. Schlottmann and P.D. Sacramento, Adv. Phys. 42 (1993) 641.
24. A.W.W. Ludwig and I. Affleck, Phys. Rev. Lett. 57 (1991) 3160.
25. D.L. Cox, Phys. Rev. Lett. 59 (1987) 1240.
26. O.O. Bernal, D.E. MacLaughlin, H.G. Lukefahr and B. Andraka, Phys. Rev. Lett. 75 (1995) 2023.
27. A.M. Tsvelik and M. Reizer, Phys. Rev. B 48 (1993) 9887.
28. R. Ramazashvili, Phys. Rev. B 56 (1997) 5518.
29. J.A. Hertz, Phys. Rev. B 14 (1976) 1165.
30. U. Zülicke and A.J. Millis, Phys. Rev. B 51 (1995) 8996.
31. T. Moriya, "Spin Fluctuations in Itinerant Electron Magnetism", Springer-Verlag, Berlin, 1985.
32. T. Moriya and T. Takimoto, J. Phys. Soc. Jpn. 64 (1995) 960.
33. K. Heuser, E.W. Scheidt, T. Schreiner and G.R. Stewart, Phys. Rev. B 58 (1998) R15959.
34. R. Ramazashvili, Phys. Rev. B 60 (1999) 7314.
35. P.M. Chaikin and T.C. Lubensky, "Principles of Condensed Matter Physics", Cambridge University Press, Cambridge, 1995, p. 184.
36. A. Rosch, A. Schröder, O. Stockert and H.v. Löhneysen, Phys. Rev. Lett. 79 (1997) 159.
37. T.R. Kirkpatrick and D. Belitz, in "Electron Correlation in the Solid State" (N.H. March, ed.), Imperial College Press, London, 1999.
38. M.A. Continentino, Phys. Rep. 239 (1994) 179.
39. S.L. Sondhi, S.M. Girvin, J.P. Carini and D. Shahar, Rev. Mod. Phys. 69 (1997) 315.
40. S. Sachdev, "Quantum Phase Transitions", Cambridge University Press, Cambridge, 1999.
41. R.B. Griffiths, Phys. Rev. Lett. 23 (1969) 17.
42. A. Rosch, Physica B 280 (2000) 341.
43. A. Rosch, preprint (cond-mat/9910432).
44. P. Estrela, A. de Visser, F.R. de Boer, G.J. Nieuwenhuys, L.C.J. Pereira and M. Almeida, Physica B 259-261 (1999) 409.

45. P. Gegenwart, F. Kromer, M. Lang, G. Sparn, C. Geibel and F. Steglich, Phys. Rev. Lett. 82 (1999) 1293.
46. O. Trovarelli, C. Geibel, C. Langhammer, S. Mederle, P. Gegenwart, F.M. Grosche, M. Lang, G. Sparn and F. Steglich, Physica B 281-282 (2000) 372.
47. F. Steglich, P. Gegenwart, C. Geibel, P. Hinze, M. Lang, C. Langhammer, G. Sparn and O. Trovarelli, Physica B 280 (2000) 349.
48. H.v. Löhneysen, J. Magn. Magn. Mater. 200 (1999) 532.
49. B. Fåk, J. Flouquet, G. Lapertot, T. Fukuhara and H. Kadowaki, J. Phys.: Condens. Matter 12 (2000) 5423.
50. N.D. Mathur, F.M. Grosche, S.R. Julian, I.R. Walker, D.M. Freye, R.K.W. Haselwimmer and G.G. Lonzarich, Nature 394 (1998) 39.
51. E. Bauer, J. Magn. Magn. Mater. 196-197 (1999) 873.
52. M.B. Maple, A. Amann, R.P. Dickey, E.J. Freeman, C. Sirvent, M.C. de Andrade and N.R. Dilley, Physica B 281-282 (2000) 332.
53. K. Umeo, H. Kadomatsu and T. Takabatake, J. Phys.: Condens. Matter 8 (1996) 9743.
54. S. Süllow, M.C. Aronson, B.D. Rainford and P. Haen, Phys. Rev. Lett. 82 (1999) 2963.
55. T. Takeuchi, Y. Yamamoto, M. Sato, Y. Tabata, T. Taniguchi, S. Kawarazaki, M. Ocio, P. Pari, J. Hammann and Y. Miyako, Jpn. J. Appl. Phys. series 11 (1999) 151.
56. C.Y. Liu, D.E. MacLaughlin, A.H. Castro Neto, H.G. Lukefahr, J.D. Thompson, J.L. Sarrao and Z. Fisk, Phys. Rev. B (2000) 432.
57. R. Pietri, B. Andraka, R. Troć and V.H. Tran, Phys. Rev. B 56 (1997) 14505.
58. S. Raymond, L.P. Regnault, S. Kambe, J.M. Mignot, P. Lejay, J. Flouquet, J. Low Temp. Phys. 109 (1997) 205.
59. H. Amitsuka, K. Kuwahara, M. Yokoyama, K. Tenya, T. Sakakibara, M. Mihalik and A.A. Menovský, Physica B 281-282 (2000) 326.
60. M. Lenkewitz, S. Corsépius, G.F.v. Blanckenhagen and G.R. Stewart, Phys. Rev. B 55 (1997) 6409.
61. F.G. Aliev, S. Vieira, R. Villar and V.V. Moshchalkov, J. Phys.: Condens. Matter 8 (1996) 9807.
62. D.A. Gajewski, N.R. Diley, R. Chau and M.B. Maple, J. Phys.: Condens. Matter 8 (1996) 9793.
63. M.A. Lopez de la Torre, J.R. Fernandez and K.A. McEwen, J. Appl. Phys. 79 (1996) 6364.

3. Experimental

A variety of experimental techniques was used to investigate the thermal, magnetic and transport properties of U_2Pt_2In and related compounds. Since most of the techniques and experimental set-ups have been described in detail by others, only a short presentation is given here. General overviews of cryogenic techniques and low-temperature thermometry are given by Pobell [1], White [2] and Betts [3]. Descriptions of the particular ^{3}He system and ^{3}He/^{4}He dilution refrigerator used in this work are given in Refs. 4 and 5 and Refs. 6 and 7, respectively. The pressure cell used for the magnetotransport experiments is described in Section 3.3.1. Section 3.6 is devoted to the μSR technique, which is described in more detail.

3.1. Sample preparation

The preparation methods of the single crystals studied in this work will be described in Chapters 4 (U_2Pt_2In) and 7 (other compounds), where the corresponding experimental results are presented and discussed. Regarding U_2Pt_2In, it should be mentioned that it is a difficult material to prepare under normal arc-melting conditions due to In evaporation. Indium evaporation leads to the formation of a secondary phase, namely UPt. In fact, small single crystals of UPt have been grown recently out of polycrystalline U_2Pt_2In by inducing complete In evaporation through annealing [8].

Traces of superconductivity at about 0.7 K have been detected in the resistivity of certain polycrystalline samples of U_2Pt_2In. A.c.-susceptibility measurements showed however that superconductivity is not a bulk property. Electron probe microanalysis (EPMA) on these samples indicate the presence of a network of UPt as an impurity phase. Upon annealing, the network is partially destroyed and the superconducting transition is suppressed. Other batches of polycrystalline U_2Pt_2In, containing UPtIn as an impurity phase, show a full superconducting resistive transition at 0.85 K. The superconducting phase has a critical field of about 1.4 T. Neither UPt nor UPtIn present a sign of superconductivity at low temperatures. The superconducting phase might be an In-rich phase precipitated at the U_2Pt_2In grain boundaries.

The single-crystalline batches of U_2Pt_2In, from which the specimens used in this work were taken, are, as far as it has been reported, the only ones prepared so far.

For general references on crystal growth of U and Ce intermetallic compounds, see e.g. Refs. 9 and 10.

The structural properties of most of the samples used were checked by means of X-ray and neutron diffraction, optical microscopy and secondary electron microscopy. The quality of the single crystals of U_2Pt_2In was also checked by means of EPMA at the FOM-ALMOS facility.

The single crystals were oriented by means of the X-ray back-reflection Laue method. Next, they were cut by spark-erosion. For the thermal-expansion measurements, the relevant surfaces of the samples were shaped plane-parallel within 5 μm by means of spark-erosion.

3.2. Magnetization

Magnetization measurements were performed by means of a commercial Quantum Design SQUID magnetometer (2 K $\leq T <$ 400 K, -5.5 T $\leq B \leq$ 5.5 T) at the University of Lisbon.

High-field magnetization measurements up to 35 T were performed at the High-Field Facility of the University of Amsterdam [11]. Field pulses of 7, 14, 21 and 35 T were used with the magnetization measured during a 7-step field decay. After each pulse, the empty pick-up coil was measured. The magnetization of the sample plus teflon holder is then given by

$M = M_{\text{sample-in}} - M_{\text{sample-out}}$. The contribution of the teflon sample holder was measured in the same way, in order to correct the data for the diamagnetic signal of teflon.

3.3. Resistivity and magnetoresistance

Resistivity measurements were performed using a standard a.c. 4-probe method with a Linear Research resistance bridge (model LR-400 or LR-700). Since most of the materials used in this work are very brittle, the voltage and current leads (copper wires with thickness of 50 μm) were attached to the bar-shaped samples with silver paste. Excitation currents of 300 μA or lower were applied in order to prevent Joule heating.

High-field magnetoresistance measurements were carried out using the step-wise field decay of 7, 14 and 21 T pulses. In addition, free (exponential-like) decays of 5, 20 and 38 T pulses were used.

3.3.1. Resistivity under pressure

Resistivity measurements were performed under hydrostatic pressures up to 2 GPa (=20 kbar) in a ^{3}He system. An overview of pressure techniques and pressure cells is given in Ref. 12.

A schematic view of the pressure cell used in this work is given in Figure 3.1 (after T. Naka - National Research Institute for Metals in Tsukuba, Japan). Besides a standard 4.7 kΩ RuO_2 thermometer, a cernox thermometer was mounted in order to monitor the cell and sample temperature in the temperature range 10-300 K.

The pressure cell, which can sustain pressures up to at least 2 GPa, is made primarily of CuBe. The outer and inner diameters amount to 25 and 6 mm, respectively. A short tungsten carbide piston is used to transfer the pressure to the teflon holder containing the sample. The sample is mounted on a specially designed plug and put inside the teflon holder together with the pressure-transmitting medium.

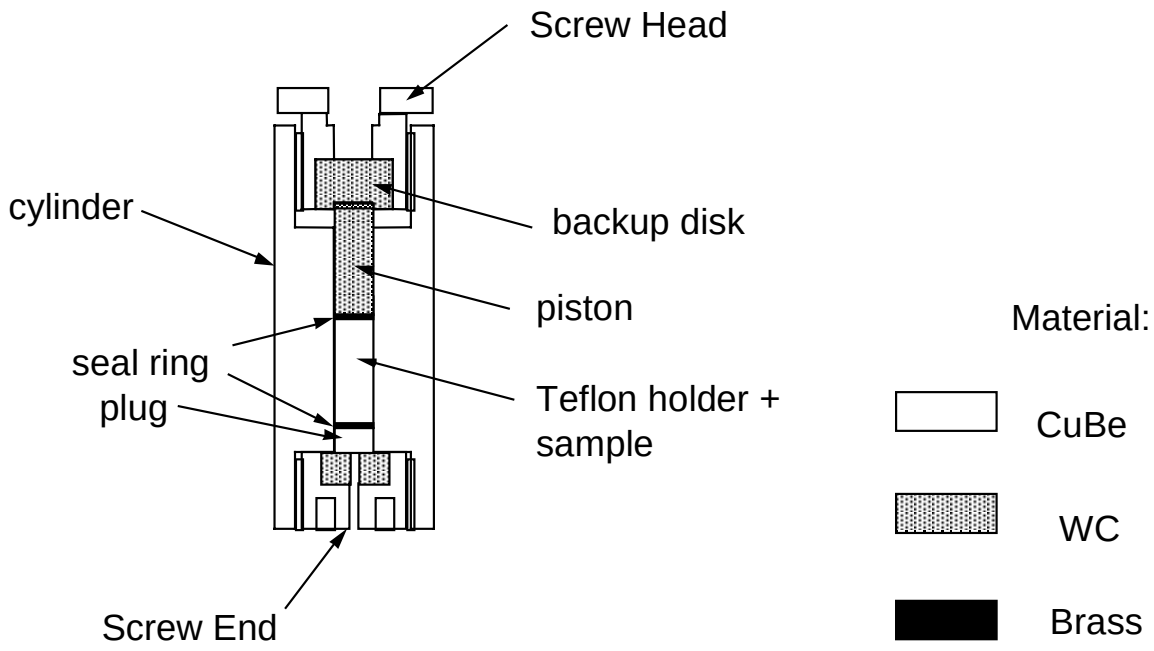

Figure 3.1 - Pressure cell for resistivity measurements.

The cell is placed in a press, in order to apply a load. The load necessary to obtain a pressure p is simply given by $(\pi\phi_{cell}^2/4)p$, where ϕ_{cell} is the inner diameter of the cell (ϕ_{cell} = 6 mm). For p = 2 GPa, the load is 5.8×10^3 kgf. After the load is applied, the screw head is adjusted in order to clamp the piston. In this way, the pressure is maintained when the cell is removed from the press. To change the applied pressure after the experiment, the cell has to be warmed up to room temperature. A load equivalent to the previous pressure is applied, such that the cell can be unclamped, after which a new load is applied.

The pressure medium used is liquid 3M Fluorinert. Fluorinert remains hydrostatic in the applied pressure range due to its low viscosity. Moreover, it has a low compressibility and good thermal conductivity. During solidification, hydrostaticity is conserved. In fact, the pressure medium used is a 1:1 mixture of two Fluorinerts, FC-70 and FC-77, which have glass solidifications at 248 and 163 K, respectively. This difference in solidification temperatures ensures that there are no sudden changes on the thermodynamic properties during the solidification of the pressure medium. The Fluorinerts used are chemically inactive and do not react with the components of the cell, nor with the samples, the wires or the silver paste used for placing the electrical contacts on the samples. Additionally, they have extremely small solubilities (less than 1%) for H_2O, oil, ethanol, methanol, etc.

Due to the different thermal-expansion coefficients of the pressure medium and the cell components, the pressure reduces during cooling. The pressure values presented in this work were corrected for an empirical low-temperature efficiency value of 80% obtained by T. Naka on the same cell.

3.4. Specific heat

Specific-heat measurements were performed using a relaxation method at low temperatures (dilution refrigerator and ^{3}He system) and a semi-adiabatic method at high temperatures (^{4}He bath cryostat).

In the relaxation method, sample and addenda are connected by a weak thermal link to a heat reservoir at constant temperature T_0. A constant power $\dot{Q}$ is applied to a heater on the sample holder (sapphire plate) until thermal equilibrium is achieved at a temperature $T+\Delta T$. When the power is switched off, the sample and addenda will have an exponential relaxation towards the reservoir temperature T_0: $T(t) = T_0 + \Delta T\, e^{-t/\tau}$. The relaxation time τ is related to the heat capacity C by $C = \tau k = \tau \dot{Q}/\Delta T$ where k is the thermal conductivity.

For heavy-fermion compounds, which present large specific heats, the addenda contribution at low temperatures to the total heat capacity is small and can be neglected. Special care was taken to stabilize the temperature of the sample since bad thermalization induces errors in the measured values of ΔT and the calculated values of τ. The power supplied by the heater is calculated after measuring the voltage V_{ref} across a reference resistance R_{ref}, in series with the heater, and the voltage drop over the heater: $\dot{Q} = V_{heater} I_{heater} = V_{heater} V_{ref}/R_{ref}$.

In the semi-adiabatic method, there is no deliberate thermal link between the sample and the heat reservoir. A heat pulse of energy ΔQ gives a sample temperature rise ΔT and the heat capacity is simply given by $C = \Delta Q/\Delta T$. The high-temperature specific-heat data presented in this work have been corrected for the contribution of the addenda.

A description of the used experimental set-ups is given in Refs. 6 and 13.

3.5. Thermal expansion

Thermal-expansion measurements were carried out with a parallel-plate capacitance method. The capacitance of a parallel-plate capacitor is $C = \varepsilon A/d$ where ε is the dielectric constant of the medium between the plates, A the area of the plates and d the distance between the plates. Typical gap distances used are $d = 100$ μm. The length change of the sample as function of temperature is proportional to the change in capacitance. The uncertainty in the determination of the effective area of the capacitor plates, $\varepsilon A = 9.73 \times 10^{-16}$ Fm, gives an accuracy limit of about 3% on the absolute value of the experimental data. The capacitance was measured using a sensitive three-terminal technique with an Andeen-Hagerling capacitance bridge. The maximum sensitivity of the set-up used is about 0.01 Å for a sample of 5 mm. A schematic drawing of the capacitance cell is given in Ref. 14.

The coefficient of linear thermal expansion is given by $\alpha = 1/L\ (\mathrm{d}L/\mathrm{d}T)$ where L is the length of the sample. A heating in steps of ΔT is used. The linear thermal expansion of the sample is calculated from

$$\alpha = -\frac{1}{L}\left(\frac{\Delta d}{\Delta T}\right)_{\text{cell+sample}} + \frac{1}{L}\left(\frac{\Delta d}{\Delta T}\right)_{\text{cell+Cu}} + \alpha_{\text{Cu}} \quad . \tag{3.1}$$

Here, the first term corresponds to the change in gap distance with the sample mounted in the cell, the second term is the corresponding change with a oxygen-free high-conductivity (OFHC) copper sample mounted in the cell (cell effect) and the third term is the correction for the linear thermal expansion of the OFHC copper of the cell. The cell effect is small at low temperatures ($\Delta d/\Delta T$ = -2.5 Å/K at T = 4.2 K). However, a progressive increase is observed when the temperature is further decreased ($\Delta d/\Delta T$ = -9.0 Å/K at T = 0.3 K).

The volume expansion coefficient α_V, where $V = abc$ is the volume, is given by

$$\alpha_{\text{V}} = \frac{1}{V}\frac{\mathrm{d}V}{\mathrm{d}T} = \frac{1}{abc}\left(\frac{\mathrm{d}a}{\mathrm{d}T}bc + a\frac{\mathrm{d}b}{\mathrm{d}T}c + ab\frac{\mathrm{d}c}{\mathrm{d}T}\right) = \alpha_{\text{a}} + \alpha_{\text{b}} + \alpha_{\text{c}} \quad . \tag{3.2}$$

For general references on thermal-expansion measurements see Refs. 15-17.

3.6. Muon Spin Relaxation and Rotation

μSR is an acronym for Muon Spin Relaxation, Rotation, Resonance or even Research. μSR is a technique increasingly used in solid state physics, chemistry and materials science because of its sensitivity to static and dynamic microscopic magnetic fields, which enables a study of relevant aspects of structural, magnetic and electronic phenomena in magnets, superconductors, semiconductors and insulators. In the μSR technique, the positive muon, μ^+, is used as a probe. Intense μ^+ beams with a high spin polarization can be produced. Some properties of μ^+ are given in Table 3.1. A general description of the μSR technique can be found in Refs. 18-20, while experimental results on some exemplary materials are given in Refs. 21-23. The μSR experiments presented in this work were carried out at the Paul Scherrer Institute (PSI) in Villigen (Switzerland), in the General Purpose Spectrometer (GPS), equipped with a gas flow ^{4}He cryostat for 1.5 K $\leq T \leq$ 300 K, and in the Low Temperature Facility (LTF), equipped with a top-loading dilution refrigerator with a base temperature of about 0.025 K.

Table 3.1 - Some properties of the μ^+ particle.

mass	$m_\mu = 206.76826(11)\ m_e$
charge	+e
spin	1/2
magnetic moment	$\mu_\mu = 8.8905981(13)\ \mu_N$
gyromagnetic ratio	$\gamma_\mu / 2\pi = 135.53879(1)$ MHz/T
average lifetime	$\tau_\mu = 2.19703(4)$ μs

Because of its positive charge, the muon localizes at an interstitial site, where it probes the local magnetic environment. Since the muon has no quadrupolar electric moment ($S_\mu = 1/2$) it does not couple to electric-field gradients. The muons produced by the decay of pions have a kinetic energy of 4.119 MeV. At this energy, muons rapidly thermalize within a sample without loosing their polarization.

Once the muon is implanted in a sample, the local magnetic environment dictates the subsequent evolution of its spin vector. If the muon experiences a unique off-axis magnetic field $\boldsymbol{B}_\mu$ (i.e. a magnetic field not in the direction of the muon spin), the spin precesses around the magnetic field at the Larmor frequency: $\omega_\mu = \gamma_\mu B_\mu$. However, any spatial or temporal, site to

site, variation of the magnetic field results in a dephasing or depolarization of the muon spin. This motion of precession and/or spin depolarization can be monitored due to the spatial anisotropy of the direction of positron emission when the muon decays. The decay positrons are distributed around the muon spin direction according to the probability function

$$W(\theta) = 1 + A\cos\theta \quad , \tag{3.3}$$

where θ is the angle between the muon spin and the direction of positron emission. The factor *A*, called the asymmetry factor, increases monotonically with the positron energy up to a value of $A = 1$ for the maximum energy of 52.83 MeV. A value of 1/3 is obtained if all emitted positrons are detected with the same efficiency, irrespective of their energy. The variation of the angular probability function $W(\theta)$ is shown in Figure 3.2 for a number of decay positron energies. The experimentally observed maximum asymmetry depends on the appropriate integration over the energy-dependent probabilities of positron emission and detection, the energy-dependent asymmetry and the solid angle of the detector. A typical experimental value for the asymmetry factor in an actual μSR experiment is about 0.25.

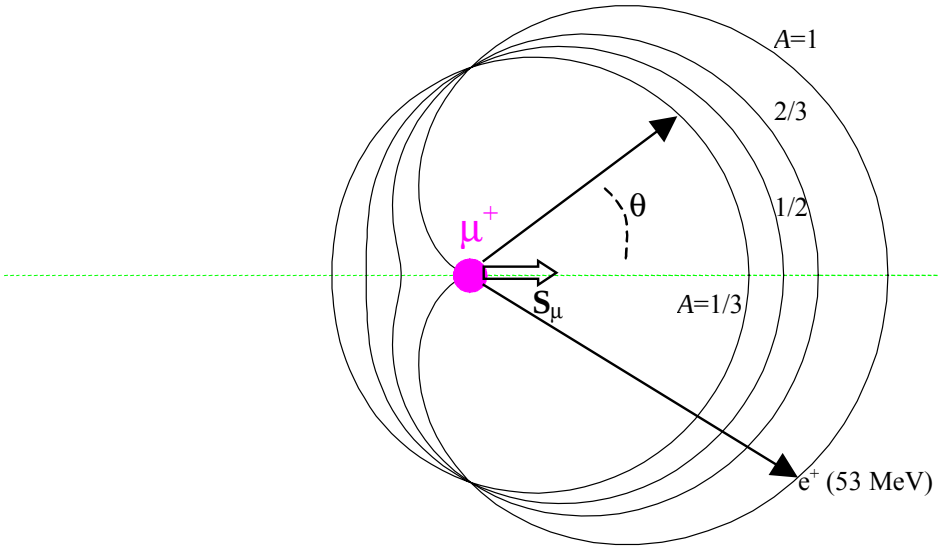

Figure 3.2 - Angular decay positron distribution for various positron energies. After Ref. 19.

The decay positrons, e^+, are monitored by means of a detector array consisting of counters placed perpendicularly to the positive and negative coordinate axes centered on the sample. The time histogram of the collected events in each counter has the form

$$N_{e^+}(t) = N_0\, e^{-t/\tau_\mu}[1 + AP(t)] + b_0 \quad , \tag{3.4}$$

where N_0 is a normalization constant, $\exp(-t/\tau_\mu)$ accounts for the muon decay, A is the asymmetry, $P(t)$ is the muon depolarization function which describes the time dependence of the polarization (with $P(0) = 1$) and b_0 is the background contribution. The depolarization function $P(t)$ reflects the spatial and temporal distribution of the magnetic fields at the muon sites. In the case of a static magnetic field $\boldsymbol{B}_\mu$ at the μ^+ site, $P(t)$ is given by

$$P(t) = \int f(\boldsymbol{B}_\mu)[\cos^2\theta + \sin^2\theta\cos(\omega_\mu t)]\mathrm{d}\boldsymbol{B}_\mu \quad , \tag{3.5}$$

where $f(\boldsymbol{B}_\mu)$ is the magnetic-field distribution function and θ the angle between $\boldsymbol{B}_\mu$ and the initial muon polarization $\boldsymbol{P}_\mu(0)$.

For a particular crystal structure, the possible presence of different muon stopping sites, with different magnetic environments, will be reflected in a μSR signal with different components, i.e. with different depolarization functions. Moreover, since the muons are uniformly implanted in a sample, the coexistence of different domains, characterized by different types of ground states, can also be detected by the presence of different components with distinctive functions $P(t)$, even if only one stopping site is present.

Different experimental geometries can be used with respect to the direction of an external magnetic field $\boldsymbol{B}_{\mathrm{ext}}$. In fact, each geometry corresponds to a different meaning of the acronym μSR: muon spin relaxation for zero or longitudinal field ($\boldsymbol{B}_{\mathrm{ext}} \parallel \boldsymbol{P}_\mu(0)$) and muon spin rotation for transverse field ($\boldsymbol{B}_{\mathrm{ext}} \perp \boldsymbol{P}_\mu(0)$).

The muon beam at the PSI is of the continuous type (compared to beams of the pulsed type). Because each event is treated separately, the continuous beam has a good time resolution but a large background b_0 which limits the time window to about 10 μs. Recently, a new facility, called MORE (Muons On REquest), has been installed at the PSI, which reduces drastically the background, increasing the time window to 16 μs. In this arrangement, a "kicker" sends a muon to the instrument only when it is required, deflecting all the other muons away from the experimental set-up. A disadvantage of MORE is however the initial dead-time (about 0.15 μs) in the histograms, which limits its usefulness to the case where there is no fast depolarization rate.

3.6.1. Zero-field μSR

The μSR technique yields the possibility to probe magnetic signals in zero external field. Its large magnetic moment makes the muon sensitive to internal fields as small as 10^{-5} T (which corresponds to the magnitude of fields originating from nuclear dipoles).

The zero-field (ZF) μSR technique can be used to measure the spontaneous μ^+ Larmor frequencies in magnetically ordered phases and provides information about the magnetic structure and the value of the static moment. In the simplest case of a magnetic structure producing a field of well defined magnitude and direction at the μ^+ sites, $f(\boldsymbol{B}_\mu)$ is represented by a δ function and the muon-depolarization function is

$$P(t) = \cos^2\theta + \sin^2\theta\cos(\omega_\mu t) \quad . \tag{3.6}$$

For a polycrystalline sample, averaging over the angular dependence results in

$$P(t) = \tfrac{1}{3} + \tfrac{2}{3}\cos(\omega_\mu t) \quad . \tag{3.7}$$

A static distribution of internal fields, as the one arising from static nuclear or electronic dipole fields, will produce a depolarization. Assuming that the internal fields are Gaussian distributed in their values and randomly oriented, the field distribution has zero average and no spontaneous precession frequency is observed. $P(t)$ assumes the form of a Kubo-Toyabe function [24]

$$P_{\mathrm{KG}}(t) = \tfrac{1}{3} + \tfrac{2}{3}\left(1-\Delta^2 t^2\right)\mathrm{e}^{-\Delta^2 t^2/2} \quad , \tag{3.8a}$$

where $\Delta^2/\gamma_\mu^2 = \langle B^2 \rangle$ is the second moment of the field distribution. If the field distribution is Lorentzian then

$$P_{\mathrm{KL}}(t) = \tfrac{1}{3} + \tfrac{2}{3}\left(1-\lambda t\right)\mathrm{e}^{-\lambda t} \quad , \tag{3.8b}$$

where λ/γ_μ represents the half width at half maximum of the distributions. For early times ($t << \Delta^{-1}$ or $t << \lambda^{-1}$), these functions approach a Gaussian and an exponential function, respectively:

$$P_{\mathrm{KG}}(t) \approx P_{\mathrm{G}}(t) = \mathrm{e}^{-\Delta^2 t^2/2} \tag{3.9a}$$

$$P_{\mathrm{KL}}(t) \approx P_{\mathrm{E}}(t) = \mathrm{e}^{-\lambda t} \quad . \tag{3.9b}$$

In the case of a time-dependent Gaussian distribution of the internal fields, the Kubo-Toyabe function is modified to a dynamical Kubo-Toyabe function which cannot be expressed

analytically, except in the limiting case of slow and fast fluctuations. If ν is the fluctuation rate of the magnetic moments, the dynamical Kubo-Toyabe function becomes

$$P(t) \approx \tfrac{1}{3}\mathrm{e}^{-2\nu t/3} + \tfrac{2}{3}\left(1-\Delta^2 t^2\right)\mathrm{e}^{-\Delta^2 t^2/2} \qquad (3.10)$$

for slow fluctuations ($\nu << \Delta$). For fast fluctuations, $P(t) \approx P_{\mathrm{E}}(t) = \mathrm{e}^{-\lambda t}$ with $\lambda = 2\Delta^2/\nu$. In the latter case, the depolarization rate λ describes the spin-relaxation rate and involves spin-flip transitions induced by the fluctuating magnetic field with a component perpendicular to the initial muon-polarization direction. The dynamical Kubo-Toyabe function is plotted in Figure 3.3 for several fluctuation rates (notice that the static Kubo-Toyabe function corresponds to the case ν=0).

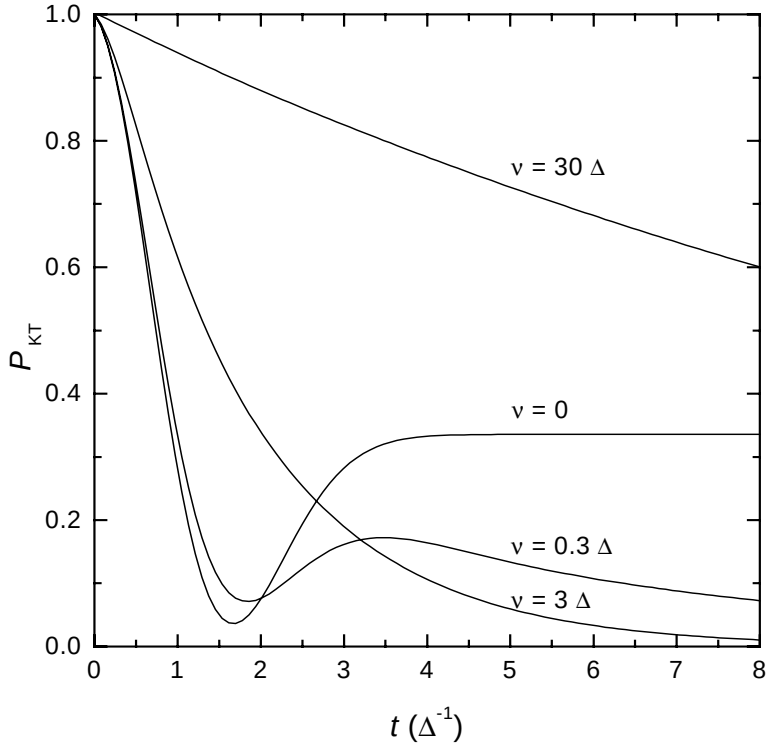

Figure 3.3 - Dynamical Kubo-Toyabe function for several fluctuation rates ν.

3.6.2. Longitudinal-field μSR

In the longitudinal-field (LF) configuration, an external field is applied in the direction of the initial muon polarization. In the case of a random distribution of static internal fields, the

effect of B_{ext} is to gradually remove the time dependence of the polarization. Eventually, by choosing B_{ext} to be stronger than the internal fields ($\gamma_\mu B_{ext} >> \Delta$), the muon's "up" and "down" states are eigenstates of the Zeeman Hamiltonian and any inhomogeneous static distribution of the internal fields will not affect the time evolution of the muon polarization, which will therefore remain constant. This behaviour reflects the decoupling of the muon spin from the static internal fields. This situation is depicted in Figure 3.4 for a random distribution of static moments, where a strong longitudinal field results in local fields parallel to the muon spin, which maintains its initial polarization in the field direction.

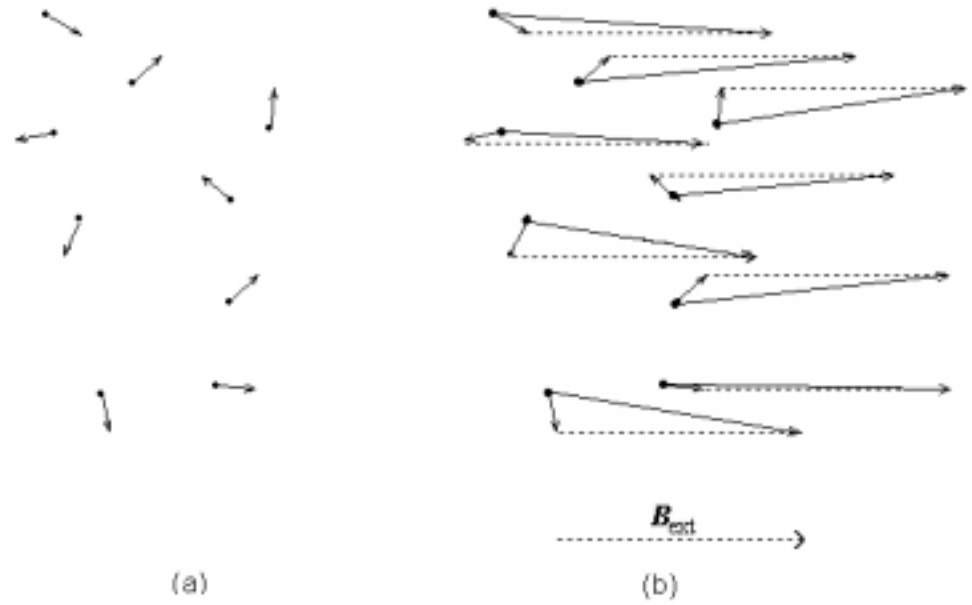

Figure 3.4 - Effect of a longitudinal external field on a random distribution of local fields. a) B_{ext}=0; b) when B_{ext} is significantly larger than the local field at B_{ext}=0, the resulting field is almost parallel to $\boldsymbol{P}_\mu(0)$. After Ref. 25.

The polarization function for a Gaussian distribution as function of applied field is shown in Figure 3.5. It assumes the analytical form [26]

$$P_{KT}(t, B_{ext}) = 1 - \frac{2\Delta^2}{\gamma_\mu^2 B_{ext}^2}\left[1 - e^{-\Delta^2 t^2/2}\cos(\gamma_\mu B_{ext} t)\right] + \frac{2\Delta^3}{\gamma_\mu^3 B_{ext}^3}\int_0^{\Delta t} dy\; e^{-y^2/2}\cos\left(\frac{\gamma_\mu B_{ext}}{\Delta} y\right) \quad (3.11)$$

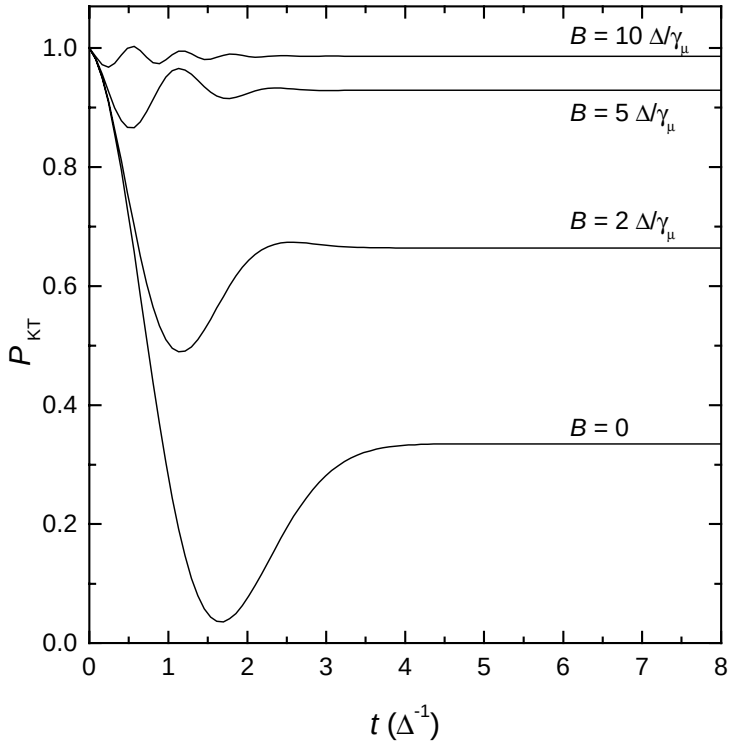

Figure 3.5 - Kubo-Toyabe depolarization function for a decoupling of the muon spin from a Gaussian distribution of static fields due to a longitudinal external field.

However, for fast fluctuations of the internal fields, the spin-lattice relaxation regime is recovered and induced spin-flip transitions will lead to a depolarization in longitudinal fields similar to the one observed in zero field.

Due to these differences, longitudinal-field μSR provides a powerful tool to distinguish static from dynamic distributions of internal fields (if there are no spontaneous Larmor frequencies in the static case, zero-field μSR cannot distinguish the two situations). In the static case, there is no depolarization in an external field, while in the dynamic case the depolarization function will have the same form as in the zero-field case, with a slightly reduced depolarization rate

$$\lambda = \frac{2\Delta^2/\nu}{1+\left(\gamma_\mu B_{ext}/\nu\right)^2} \quad . \tag{3.12}$$

3.6.3. Transverse-field μSR

In the transverse-field (TF) configuration, the external magnetic field $\boldsymbol{B}_{\text{ext}}$ is applied perpendicular to the initial muon polarization $\boldsymbol{P}_{\mu}(0)$. The local magnetic field at the interstitial site where the muon is implanted can be determined from the Larmor precession frequency. The measured frequency or frequencies are expressed in the form of a Knight shift:

$$K_{\mu} = \frac{\left|\boldsymbol{B}_{\mu}\right| - \left|\boldsymbol{B}_{\text{ext}}\right|}{\left|\boldsymbol{B}_{\text{ext}}\right|} = \frac{\omega_{\mu}}{\omega_0} - 1 \quad , \tag{3.13}$$

where $\omega_0 = \gamma_{\mu} B_{\text{ext}}$. Here, we consider only metals in the paramagnetic state that are exposed to a magnetic field. The local magnetic field $\boldsymbol{B}_{\mu}$ at the interstitial site where the muon comes to rest can be written as

$$\boldsymbol{B}_{\mu} = \boldsymbol{B}_{\text{ext}} + \boldsymbol{B}_{\text{dip}} + \boldsymbol{B}_{\text{con}} + A_{\text{con}}\tilde{\chi}\boldsymbol{B}_{\text{ext}} + \boldsymbol{B}_{\text{dia}} \quad . \tag{3.14}$$

$\boldsymbol{B}_{\text{dip}}$ represents the dipolar fields of the localized lattice spins. The third and the fourth term are called the direct and indirect hyperfine contact field, respectively, and are connected with the presence of the muon itself. The direct hyperfine contact field, $\boldsymbol{B}_{\text{con}}$, results from the spin density at the muon site, which is induced by the polarization of the conduction electrons. In the paramagnetic state, this polarization is induced by an external field. $\boldsymbol{B}_{\text{con}}$ is proportional to the Pauli susceptibility of the conduction electrons and is usually assumed to be temperature independent and isotropic, in contrast to the other contributions. The indirect contact field is due to the RKKY interaction between localized moments and the muon. The effective contact coupling constant, A_{con}, is temperature independent, so that the indirect contact field is proportional to the susceptibility tensor $\tilde{\chi}$ and the applied magnetic field. The last contribution, $\boldsymbol{B}_{\text{dia}}$, is due to the diamagnetic response of the electron-cloud screening of the muon charge. The diamagnetic screening produces only a very small contribution to the local magnetic field. For materials with an enhanced effective electron mass m^*, the small diamagnetic contribution is reduced by a factor m_e/m^*, becoming negligible for heavy-fermion compounds.

In order to separate the different contributions to the local magnetic field, the experimental Knight shift in heavy-fermion compounds is usually compared to the calculated one. If the principal axes of the crystalline structure are chosen as the coordinate frame, the dipolar field contribution can be written as

$$\boldsymbol{B}_{\mathrm{dip}} = \vec{\vec{A}}_{\mathrm{dip}} \vec{\vec{\chi}} \boldsymbol{B}_{\mathrm{ext}} \quad . \tag{3.15}$$

The dipolar tensor $\vec{\vec{A}}_{\mathrm{dip}}$ is given by

$$A_{\mathrm{dip}}^{ij} = \sum_{r_f} \frac{1}{r^3} \left(\frac{3 x_i x_j}{r^2} - \delta_{ij} \right) , \tag{3.16}$$

where the sum is over all *f*-moments at positions r_f and $\boldsymbol{r} = \boldsymbol{r}_f - \boldsymbol{r}_\mu$.

In order to calculate this finite sum, one can define a "Lorentz sphere" with radius r_{L}, and separate the sum into a part inside the sphere and a part outside the sphere. If one chooses the radius large enough, the summation over the outer region can be approximated with an integral. The magnetic field resulting from this integral yields the Lorentz field $\boldsymbol{B}_{\mathrm{L}} = \mu_0 \boldsymbol{M}/3$ and the demagnetizing field $\boldsymbol{B}_{\mathrm{D}} = - \vec{\vec{N}} \mu_0 \boldsymbol{M}$, where $\boldsymbol{M}$ is the magnetization and $\vec{\vec{N}}$ the demagnetization tensor related to the shape of the sample (notice that for a sphere $N = 1/3$ and $B_{\mathrm{L}} + B_{\mathrm{D}} = 0$).

After correcting for the demagnetizing and Lorentz fields, the Knight shift is related to the diagonal susceptibility tensor according to

$$K_\mu = K_{\mathrm{con}} + \boldsymbol{b} \cdot (\vec{\vec{A}}_{\mathrm{tot}} \vec{\vec{\chi}} \boldsymbol{b}) \quad , \tag{3.17}$$

where $\boldsymbol{b} = \boldsymbol{B}_{\mathrm{ext}}/|\boldsymbol{B}_{\mathrm{ext}}|$ is the unit vector parallel to the applied magnetic field, K_{con} the Knight shift due to the direct contact field and $\vec{\vec{A}}_{\mathrm{tot}} = \vec{\vec{A}}_{\mathrm{dip}} + \vec{\vec{A}}_{\mathrm{con}}$ the total hyperfine coupling tensor. In contrast to K_{con} and χ_{Pauli}, the contribution from the localized *f*-moments will exhibit a strong temperature dependence. K_{con} can therefore be determined from the experimental data: $K_{\mathrm{con}} = K_\mu(\chi \rightarrow 0)$. The elements of $\vec{\vec{A}}_{\mathrm{tot}} \vec{\vec{\chi}}$ can be determined experimentally from the Knight shift anisotropy for the principal axes. The Knight shift is simply given by

$$K_i = A^{ii} \chi_i \quad . \tag{3.18}$$

With the knowledge of χ_i, the tensor elements A^{ii} can be determined from the observed Knight shift K_i. Because $\vec{\vec{A}}_{\mathrm{tot}}$ is the sum of a traceless dipolar tensor and a scalar contact part, $\vec{\vec{A}}_{\mathrm{tot}}$ can be decomposed using $A_{\mathrm{con}} = \mathrm{Tr}(\vec{\vec{A}}_{\mathrm{tot}})/3$. By comparison of the experimentally determined $\vec{\vec{A}}_{\mathrm{dip}}$ with the calculated values, it is often possible to determine the actual muon stopping site. If a sample orders magnetically and the muon stopping site is known, then it is easy to calculate from the local field in the ordered state (measured by zero-field μSR) the size of the ordered moment.

References

1. F. Pobell, "Matter and Methods at Low Temperatures", Springer, Berlin, 1992.
2. G.K. White, "Experimental Techniques in Low-Temperature Physics", Oxford University Press, Oxford, 1959.
3. D.S. Betts, "An Introduction to Millikelvin Technology", Cambridge University Press, Cambridge, 1989.
4. M. van Sprang, Ph.D. Thesis, University of Amsterdam, 1988 (unpublished).
5. K. Bakker, Ph.D. Thesis, University of Amsterdam, 1993 (unpublished).
6. T. Vorenkamp, Ph.D. Thesis, University of Amsterdam, 1992 (unpublished).
7. N.H. van Dijk, Ph.D. Thesis, University of Amsterdam, 1994 (unpublished).
8. K. Prokeš, T. Fujita, E.H. Brück, F.R. de Boer and A.A. Menovsky, Phys. Rev. B 60 (1999) R730.
9. A.A. Menovsky and J.J.M. Franse, J. Crystal Growth 65 (1983) 286.
10. J.C. Spirlet and O. Vogt, in "Handbook on the Physics and Chemistry of the Actinides" vol. 1 (A.J. Freeman and G.H. Lander, eds.), Elsevier, Amsterdam, 1984, p. 79.
11. R. Gersdorf, F.R. de Boer, J.C. Wolfrat, F.A. Muller and L.W. Roeland, in "High Field Magnetism" (M. Date, ed.), North-Holland, Amsterdam, 1983, p. 277.
12. M. Eremets, "High Pressure Experimental Methods", Oxford University Press, Oxford, 1996.
13. N.H. Kim-Ngan, Ph.D. Thesis, University of Amsterdam, 1993 (unpublished).
14. A. de Visser, Ph.D. Thesis, University of Amsterdam, 1986 (unpublished).
15. E. Grüneisen, Handbook Phys. 10 (1926) 1.
16. R.S. Krishnan, R. Srinivasan and S. Devanarayanan, "Thermal Expansion of Crystals", Pergamon Press, Oxford, 1979.
17. T.H.K. Barron, J.G. Collins and G.K. White, Adv. Phys. 29 (1980) 609.
18. A. Schenck, "Muon Spin Spectroscopy", Adam Hilger, Bristol, 1985.
19. S.L. Lee, S.H. Kilcoyne and R. Cywinski (eds.), "Muon Science", Institute of Physics Publishing, Bristol, 1999.
20. R.J. Keizer, Ph.D. Thesis, University of Amsterdam, 1999.
21. A. Schenck and F.N. Gygax, in "Handbook of Magnetic Materials" vol. 9 (K.H.J. Buschow, ed.), Elsevier, Amsterdam, 1995, p. 57.
22. P. Dalmas de Réotier and A. Yaouanc, J. Phys.: Condens. Matter 9 (1997) 9113.
23. A. Amato, Rev. Mod. Phys. 69 (1997) 1119.
24. R. Kubo and T. Toyabe, in "Magnetic Resonance and Relaxation" (R. Blinc, ed.), North-Holland, Amsterdam, 1967, p. 810.
25. J. Chappert, in "Muons and Pions in Materials Research" (J. Chappert and R.I. Grynszpan, eds.), Elsevier, Amsterdam, 1984, p. 35.
26. R.S. Hayano, Y.J. Uemura, J. Imazato, N. Nishida, T. Yamazaki and R. Kubo, Phys. Rev. B 20 (1979) 850.

4. Non-Fermi liquid behaviour in U_2Pt_2In

4.1. The U_2T_2X family of compounds

The family of U_2T_2X (where T is a transition metal and X is In or Sn) intermetallic compounds has attracted much interest in the past years [1-4], because it may serve as an exemplary system to study hybridization phenomena in 5*f*-electron compounds. The hybridization strength can be tuned by varying the T and X elements and as a result various magnetic ground states are observed, notably Pauli paramagnetism, spin-fluctuation phenomena and antiferromagnetism. The shortest U-U distance in these tetragonal 2:2:1 compounds is close to the Hill limit (~ 3.5 Å) and is found either along the c-axis or within the ab-plane, depending on the T and X elements. Therefore, this family of compounds may be used to study the influence of the direct *f*-*f* coupling on the magnetic *f*-moment direction. On the other hand, it is the strength of the 5*f* - *d*-ligand hybridization that controls the evolution of magnetism across the 2:2:1 series.

4.1.1. Crystallographic structure and overview

In order to carry out a systematic study of the structural and physical properties of the An_2T_2X series (where An is an actinide), single crystals of several uranium 2:2:1 compounds were grown by L.C.J. Pereira at the Institute for Transuranium Elements (Karlsruhe, Germany) [4].

The compounds were prepared in a polycrystalline form by arc melting together the stoichiometric amounts of the elements (U with a purity better than 99.9% and T and X with a purity 99.999%) in a water-cooled copper crucible under a purified argon atmosphere. Small excess amounts of the X element were added in order to compensate for evaporation losses. The mass losses after arc melting were less than 0.5% of the total mass. The single-phase character of the ingots was checked by means of X-ray analysis, optical microscopy and secondary electron microscopy (SEM).

The polycrystalline batches (mass about 20 g) were then encapsulated in tungsten crucibles and sealed by electron-beam welding under vacuum. Single crystals were grown by a modified mineralization technique [4] using radiofrequency heating with an *in situ* temperature reading in order to control the melting temperature plateau. The *in situ* temperature reading made it possible to reduce the mineralization time significantly, from typically 1 week to 5 hours only. The single-phase character of the grown materials was checked by means of X-ray diffraction, optical microscopy and SEM. The single-crystallinity was checked by the X-ray back-reflection Laue method (or by neutron diffraction in the case of some of the compounds).

On several pieces of the single-crystalline materials, a complete structural analysis was carried out on a four-circle diffractometer. The U_2T_2X compounds crystallize in the ordered tetragonal U_3Si_2-type of structure (space group *P*4/*mbm*) [1], except for U_2Ir_2Sn, U_2Pt_2Sn and U_2Pt_2In, which crystallize in the Zr_3Al_2-type of structure (space group $P4_2/mnm$) [5,6]. The Zr_3Al_2-type of structure is a superstructure (doubling of the c-axis) of the U_3Si_2-type. The U_3Si_2-type of structure was also reported for the Np [1,4], Pu and Am [7] 2:2:1 compounds and for the rare-earth based ones [8,9].

In the U_3Si_2-type of structure (Figure 4.1), the U atoms occupy the 4h (x_U,x_U+1/2,1/2) positions, while the T and X atoms occupy the 4g (y_T,y_T+1/2,0) and 2a (0,0,0) positions, respectively, where $x_U \approx 0.17$ and $y_T \approx 0.37$. The point symmetries of the 4h, 4g and 2a positions are *m*2*m*, *m*2*m* and 4/*m*, respectively. On the other hand, the U atoms in the Zr_3Al_2-type

of structure (Figure 4.2) occupy two different crystallographic positions: 4f (x_1,x_1,0) and 4g (x_2,-x_2,0). The X atoms are on the 4d (0,1/2,1/4) positions and the T atoms on the 8j (x_T,x_T,z_T) positions ($x_1 \approx$ 0.31, $x_2 \approx$ 0.16, $x_T \approx$ 0.13 and $z_T \approx$ 0.28). The point symmetries of the 4f, 4g, 8j and 4d positions are *m*2*m*, *m*2*m*, *m* and -4, respectively.

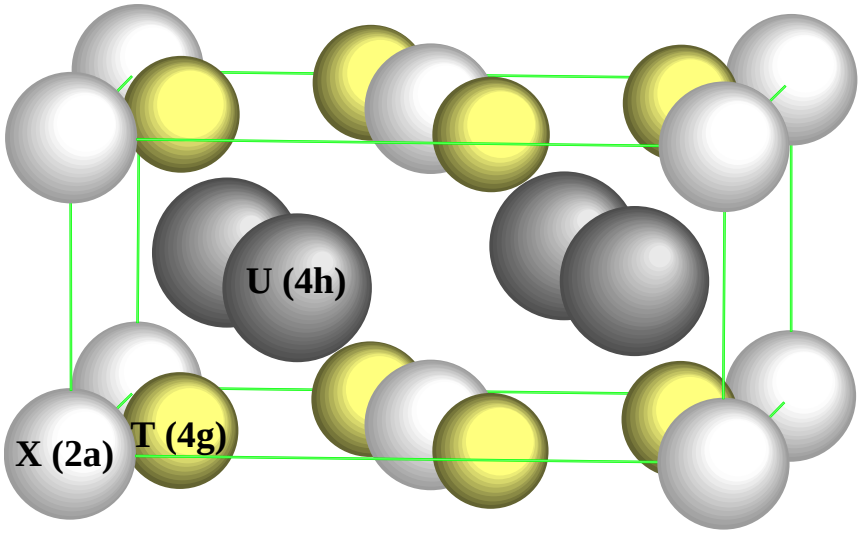

Figure 4.1 - Unit cell of the U_3Si_2-type of structure. Each unit cell contains 2 formula units.

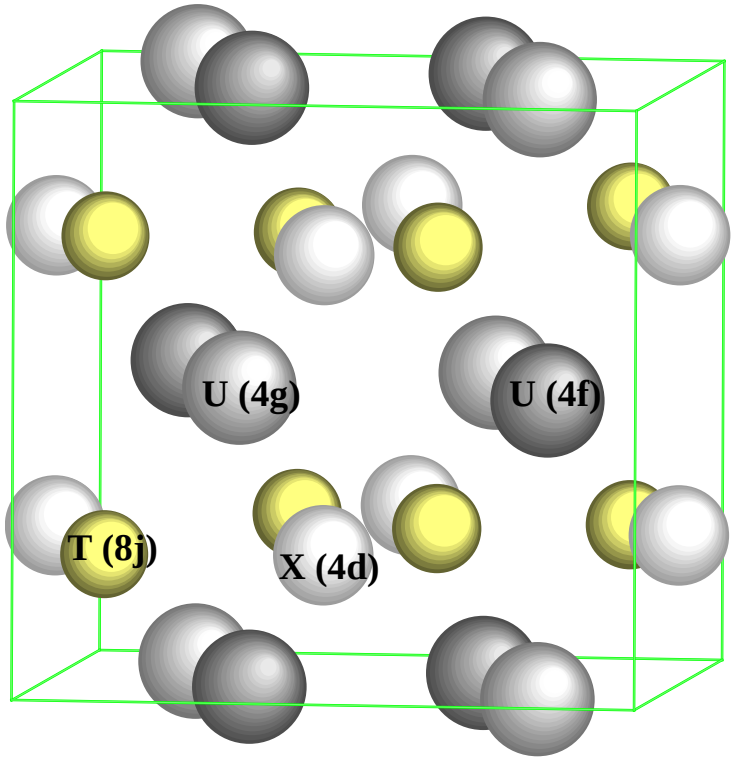

Figure 4.2 - Unit cell of the Zr_3Al_2-type of structure. Each unit cell contains 4 formula units.

In the Zr_3Al_2-type of structure, the U atoms do not form linear chains as is the case for the U_3Si_2-type of structure, but form zig-zag chains along the c-axis. This leads to a reduction of the shortest U-U spacing within the basal plane. Close scrutiny of Figure 4.1 and Figure 4.2 reveals that a transition between the two structures involves only minor shifts in the positions of the atoms.

From the structural point of view, U_2Pt_2In is a special case within the 2:2:1 family of compounds, as poly- and single-crystalline materials form in different structures [10]. The X-ray powder diffraction data taken on polycrystalline U_2Pt_2In confirm the U_3Si_2-type of structure with lattice parameters a = 7.654 Å and c = 3.725 Å. However, U_2Pt_2In single crystals form in the superstructure of the Zr_3Al_2-type with lattice parameters a = 7.695 Å and c = 7.368 Å.

This polymorphism of U_2Pt_2In shows that the stability of the crystallographic structure depends on the experimental conditions, like pressure and temperature, during the sample preparation process. While preparing the arc-melted polycrystalline sample, the temperatures attained are well above the melting point of U_2Pt_2In and the cooling process is rather fast. This leads to the formation of the U_3Si_2-type of structure. During the single crystal growth, i.e. the mineralization process, the temperature range is much reduced (up to 20°C above the melting point) and the cooling takes place very slowly. Under these conditions, which are closer to equilibrium, the preferred structure is the tetragonal Zr_3Al_2-type of structure.

The interatomic distances and near-neighbour ($d < 4.2$ Å) positions, calculated for the U_2Pt_2In single- and polycrystals, are listed in Table 4.1. The number of nearest neighbours for each atom is the same in both structures (since the main effect is the doubling of the c-axis). The average interatomic distances do not change significantly. For the U atoms, the in-plane U(4f)-U(4f) distance decreases, while the in-plane U(4g)-U(4g) increases when moving from polycrystals to single crystals.

As mentioned before, several magnetic ground states are found in the 2:2:1 family of compounds. A review of the properties of the U_2T_2X compounds has been given in Ref. 11 and some of the results are summarized in Table 4.2. Among these compounds, U_2Pt_2In and U_2Pd_2In present heavy-fermion behaviour, as can be concluded from the large value of the linear coefficient of the low-temperature specific heat, which is indicative of an enhanced effective mass.

Table 4.1 - Interatomic distances and near-neighbours numbers (NN) in poly- and single-crystalline U_2Pt_2In.

U_3Si_2-type (polycrystal)			Zr_3Al_2-type (single crystal)		
bond	NN	*d* (Å)	bond	NN	*d* (Å)
U-U	2	3.725	U_1-U_1 | U_2-U_2	1	3.583 | 3.925
U-U	1	3.738	U_1-U_2	2	3.687
U-U	4	4.006	U_1-U_2	2	3.913
			U_1-U_2	2	4.144
U-Pt	2	2.835	U_1-Pt | U_2-Pt	2	2.828 | 2.838
U-Pt	4	2.990	U_1-Pt | U_2-Pt	4	3.013 | 2.975
U-X	4	3.390	U_1-X | U_2-X	4	3.414 | 3.372

U_1=U(4f), U_2=U(4g)

The electronic structure and related properties of the U_2T_2X compounds mainly originate from the band filling of the transition-metal *d*-states and from the 5*f*-moments of the U atoms. A decrease of the *f-d* hybridization strength occurs when the *d*-band is gradually filled, as evidenced by theoretical calculations based on the local density approximation (LDA) [12,13]. Also the evolution of magnetism across the 2:2:1 series (for In and Sn compounds) is shown to be related to the strength of the 5*f* - *d*-ligand hybridization [14]. As shown in Table 4.2, in the U_2T_2In series, U_2Pd_2In and U_2Ni_2In order antiferromagnetically with Néel temperatures of 37 and 14 K, respectively, while in the U_2T_2Sn series, the compounds with Pd, Rh, Ni and Pt have antiferromagnetic transitions at T_N = 41, 28, 26 and 15 K, respectively.

In all other U 2:2:1 compounds, no anomalies have been found in the temperature dependence of the magnetic susceptibility, resistivity and specific heat down to 1.2 K, suggesting paramagnetic ground states. The strong hybridization effects are reflected in reduced effective-moment values with respect to the U^{3+} and U^{4+} free-ion values, as calculated from the Curie-Weiss behaviour of the magnetic susceptibility.

The transition elements in the U_2T_2X compounds do not carry magnetic moments, except for the cases T = Co and Fe. Detailed LDA band-structure calculations on U_2T_2Sn (T = Fe, Co, Ni) compounds [15] show an hybridization-induced magnetic polarization on the transition-metal atoms in both U_2Fe_2Sn and U_2Co_2Sn (with a magnitude that is almost twice as large for the former). This is considered as indicative of a strong covalent interaction between Fe and U and, to a lesser extent, between Co and U. The polarization of Ni in U_2Ni_2Sn is found to be very small. A negligible polarization characterizes the Sn atoms.

Table 4.2 - Magnetic ground states in the U_2T_2X family of compounds.

	ground state	T_N (K)	μ_{ord} (μ_B/U)	γ (mJ/mol$_U$K^2)
U_2Fe_2Sn	PP	-	-	n.d.
U_2Co_2Sn	SF	-	-	130
U_2Ni_2Sn	AF	26	1.05	85
U_2Ru_2Sn	PP	-	-	10
U_2Rh_2Sn	AF	28	0.53	65
U_2Pd_2Sn	AF	41	1.89	100
U_2Ir_2Sn	SF	-	-	65
U_2Pt_2Sn	AF	15	n.d.	185
U_2Co_2In	PP	-	-	30
U_2Ni_2In	AF	15	0.92	105
U_2Ru_2In	PP	-	-	n.d.
U_2Rh_2In	SF	-	-	140
U_2Pd_2In	AF	37	1.40	205
U_2Ir_2In	PP	-	-	n.d.
U_2Pt_2In	NFL	-	-	410 *

AF=antiferromagnet, PP=Pauli paramagnet, SF=spin fluctuator, NFL=non-Fermi liquid
n.d.=not determined, * value of c/T at $T = 1$ K

Table 4.3 - Lattice parameters of the U_2T_2X family of compounds.

U_3Si_2-type	a (Å)	c (Å)	c/a	V (Å^3)
U_2Fe_2Sn	7.296	3.446	0.472	183.436
U_2Co_2Sn	7.208	3.606	0.500	187.351
U_2Ni_2Sn	7.263	3.691	0.508	194.705
U_2Ru_2Sn	7.482	3.558	0.476	199.178
U_2Rh_2Sn	7.534	3.625	0.481	205.759
U_2Pd_2Sn	7.603	3.785	0.498	218.794
U_2Co_2In	7.361	3.431	0.466	185.906
U_2Ni_2In	7.374	3.572	0.484	194.231
U_2Ru_2In	7.505	3.545	0.472	199.672
U_2Rh_2In	7.553	3.605	0.477	205.657
U_2Pd_2In	7.637	3.752	0.491	218.831
U_2Ir_2In	7.596	3.582	0.472	206.679
U_2Pt_2In	7.654	3.725	0.487	218.224
Zr_3Al_2-type	a (Å)	c (Å)	c/a	V (Å^3)
U_2Ir_2Sn	7.557	7.195	0.952	410.894
U_2Pt_2Sn	7.668	7.389	0.964	434.460
U_2Pt_2In	7.695	7.368	0.958	436.282

When comparing the magnetic properties of the 2:2:1 compounds (Table 4.2) with their lattice parameters (Table 4.3), the following trends are noticeable: i) the ordering temperature increases within each T series (from Fe to Ni, Ru to Pd and Ir to Pt), together with the volume

and the c/a ratio; ii) the In compounds have less tendency to magnetic order than the Sn compounds, which may be related to the corresponding decrease of the c/a ratio since the volume remains the same in both series.

High-field magnetization studies have been carried out on several polycrystalline samples [16] in order to study the evolution of the magnetocrystalline anisotropy in the U_2T_2X series. In all cases, the magnetization at 4.2 K does not saturate, not even at the highest fields (quasi-static fields up to 38 T [17] and/or pulse fields up to 57 T [18]), which makes it difficult to determine the type of magnetic anisotropy by comparing values of the saturation magnetization for free- and fixed-powder samples. This lack of saturation and the large high-field magnetization values observed in the paramagnetic U_2T_2X compounds may be an indication of field-induced moments on the U or transition-metal sites. At relatively high magnetic fields, the antiferromagnetically ordered compounds undergo metamagnetic transitions. However, the magnetization steps corresponding to these transitions are small and therefore other metamagnetic transitions at even higher fields can not be excluded (e.g. U_2Ni_2Sn has 3 metamagnetic transitions at 30, 39 and 51 T).

4.1.2. Doniach diagram

A quantitative estimate of the importance of *f*-ligand hybridization in complicated structures can be obtained by means of a tight-binding approximation. The tight-binding approximation has been frequently used to calculate e.g. structural properties, structural stability and the electronic structure of ionic, covalent and metallic systems.

A generalized method based on a muffin-tin orbital model with transition metal pseudopotential model can be applied to calculate the coupling between atomic orbitals of *s*, *p*, *d* or *f* symmetry, mediated by the free-electron states [19,20]. The parameters are the atomic radii of the respective atoms r_l, the interatomic distance *d*, the angular momentum *l* (l = 0, 1, 2 and 3 for *s*, *p*, *d* and *f* orbitals, respectively) and the symmetry of the bond *m* (*m* = 0, 1, 2 and 3 for σ, π, δ and φ bonds, respectively). The general hybridization-matrix element $V_{ll'm}$ is written as [21]

$$V_{ll'm} = \frac{\eta_{ll'm}\hbar^2}{m_e}\frac{\sqrt{r_l^{2l-1}r_{l'}^{2l'-1}}}{d^{l+l'+1}} \quad , \tag{4.1}$$

where the coefficients $\eta_{l'm}$ [22] are given by the expression (see Table 4.4)

$$\eta_{ll'm} = \frac{(-1)^{l'+m+1}(l+l')!(2l)!(2l')!}{6\pi 2^{l+l'} l!l'!}\sqrt{\frac{(2l+1)(2l'+1)}{(l+m)!(l-m)!(l'+m)!(l'-m)!}} \quad . \qquad (4.2)$$

Table 4.4 - Bond coefficients $\eta_{ll'm}$ defined in Equation 4.2.

	ll'		
m	*pf*	*df*	*ff*
σ	$10\sqrt{21}/\pi$	$75\sqrt{35}/\pi$	$20(525/2\pi)$
π	$-15\sqrt{7/2}/\pi$	$-75\sqrt{35/2}/\pi$	$-15(525/2\pi)$
δ	-	$75\sqrt{7}/2\pi$	$6(525/2\pi)$
φ	-	-	$-(525/2\pi)$

The covalent energy of the coupling between the *l* and *l'* states is related to the trace of the hybridization matrices [23]

$$V_{ll'} = \left[\frac{N_{ll'}}{2l+1}\sum_{m=-l}^{l} V_{ll'm}^2\right]^{1/2} = \left[\frac{N_{ll'}}{2l+1}\left(V_{ll'\sigma}^2 + 2V_{ll'\pi}^2 + 2V_{ll'\delta}^2 + 2V_{ll'\varphi}^2\right)\right]^{1/2} , \qquad (4.3)$$

where $N_{ll'}$ is the number of nearest neighbours between the atoms with angular momenta *l* and *l'*.

An estimate of the total conduction electron hybridization on the *f*-atom, V_{cf}, is then given by

$$V_{cf} = \left[V_{df}^2 + V_{pf}^2 + V_{ff}^2\right]^{1/2} \quad . \qquad (4.4)$$

In Table 4.5, average interatomic distances are given for several compounds of the U_2T_2X family. The averages were calculated by considering the number of nearest neighbours for each bond (each U atom has 4 X, 6 T and 7 U nearest neighbours). In the case of the compounds with the Zr_3Al_2-type of structure, the mean value was taken as the average distances to the U(4f) and U(4g) atoms. In order to calculate the hybridization for each compound of the 2:2:1 family, a consistent set of atomic radii was taken from bandwidth calculations in an atomic-surface method [24], based on free-atom wave functions evaluated at the Wigner-Seitz atomic-sphere radius (Table 4.6).

Table 4.5 - Average distances ($d_{ll'}$), hybridization traces ($V_{ll'}$) and total hybridization (V_{cf}) for the U_2T_2X (X=In or Sn) family of compounds.

	d_{pf} (Å)	d_{df} (Å)	d_{ff} (Å)	V_{pf} (eV)	V_{df} (eV)	V_{ff} (eV)	V_{cf} (eV)
U_2Fe_2Sn	3.211	2.764	3.674	0.178	0.657	0.235	0.720
U_2Co_2Sn	3.220	2.782	3.689	0.176	0.572	0.228	0.640
U_2Ni_2Sn	3.256	2.838	3.734	0.166	0.460	0.210	0.532
U_2Ru_2Sn	3.303	2.842	3.775	0.155	0.977	0.194	1.008
U_2Rh_2Sn	3.320	2.880	3.813	0.151	0.825	0.181	0.858
U_2Pd_2Sn	3.383	2.949	3.887	0.137	0.703	0.158	0.733
U_2Ir_2Sn *	3.323	2.816	3.818	0.150	1.036	0.180	1.062
U_2Pt_2Sn *	3.391	2.894	3.887	0.136	0.860	0.159	0.885
U_2Co_2In	3.228	2.773	3.694	0.180	0.583	0.226	0.651
U_2Ni_2In	3.361	2.822	3.740	0.147	0.476	0.207	0.539
U_2Rh_2In	3.331	2.876	3.815	0.154	0.832	0.181	0.865
U_2Pd_2In	3.388	2.945	3.889	0.141	0.709	0.158	0.740
U_2Ir_2In		2.881			0.903		
U_2Pt_2In	3.390	2.938	3.887	0.141	0.785	0.158	0.813
U_2Pt_2In *	3.393	2.940	3.892	0.140	0.781	0.157	0.809

* Zr_3Al_2-type structure

Table 4.6 - Atomic radii *r* (in Å) of the various constituting elements of the compounds in Table 4.5. Taken after Ref. 24.

Fe	0.744	Ru	1.083	Ir	1.085	In	1.930	U 0.590
Co	0.696	Rh	1.020	Pt	1.069	Sn	1.800	
Ni	0.652	Pd	1.008					

The Doniach phase diagram (see Section 2.1) can be constructed by comparing the binding energy of a Kondo singlet

$$k_B T_K \propto \frac{1}{N(0)} e^{-1/N(0)J} \qquad (4.5a)$$

with that of a RKKY antiferromagnetic state

$$k_B T_{RKKY} \propto J^2 N(0) \quad , \qquad (4.5b)$$

where $N(0)$ is the conduction-electron density of states at the Fermi level and J the exchange-coupling constant. One can estimate a conduction-electron - *f*-electron exchange-interaction parameter J_{cf} by assuming a hybridization-mediated mechanism, as treated in the Schrieffer-Wolff [25] and Coqblin-Schrieffer [26] models, according to the proportionality

$$J_{cf} \propto \frac{V_{cf}^2}{E_F - E_f} \quad , \qquad (4.6)$$

where V_{cf} is the hybridization-matrix element for conduction-electron - *f*-electron hybridization and the denominator gives the position of the *f*-level energy E_f relative to the Fermi energy E_F. Within a transition-metal series, the distance E_F - E_f can be taken constant since the *f*-level is stable with respect to the Fermi energy [20]. The evolution of J_{cf} can then be traced by calculation of the conduction-electron - *f*-electron hybridization of the compounds. Using the hybridization values calculated for the U_2T_2In and U_2T_2Sn series (Table 4.5), the Doniach-type phase diagram depicted in Figure 4.3 emerges by plotting T_N versus V_{cf}^2.

It should be noted that a comparison between the d_{lf} distances in polycrystalline U_2Pt_2In (U_3Si_2-type of structure) and single-crystalline U_2Pt_2In (Zr_3Al_2-type of structure) clearly shows that there is no significant difference between the hybridization effects in the two structures (Table 4.5). Therefore the compounds forming in the Zr_3Al_2-type of structure can be included in the overall Doniach diagram.

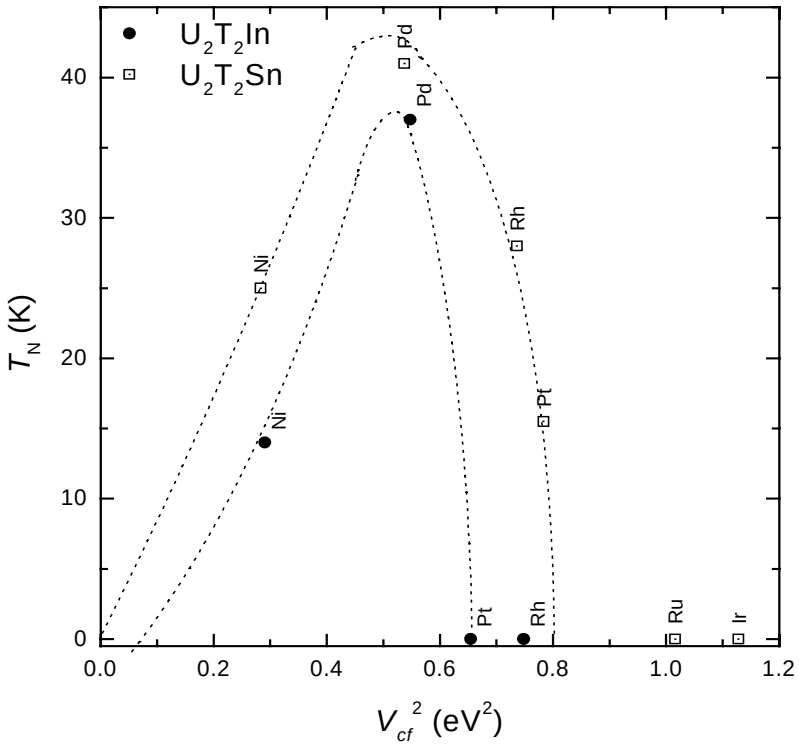

Figure 4.3 - Doniach-type of diagram for the U_2T_2X (X = In, Sn) family of compounds. The dotted lines are guides to the eye.

The compounds with Fe and Co do not fit in the general trend of the diagram (not shown in Figure 4.3). However, as discussed in the previous section, these compounds may present hybridization-induced magnetic polarization of the transition-metal atoms, and therefore should

be treated separately from the other U_2T_2X compounds when discussing the evolution of magnetism within a Doniach-type of diagram.

An important point to extract from this diagram, is the location of U_2Pt_2In at the border line between magnetic and non-magnetic compounds. This strongly suggests that U_2Pt_2In is close to a magnetic instability and explains its heavy-fermion behaviour.

4.2. U_2Pt_2In

U_2Pt_2In has a number of unrivalled properties. The heavy-electron properties of U_2Pt_2In were first reported by Havela et al. [2]. Specific-heat experiments carried out on a polycrystalline sample [2,3] in the temperature range 1.3-40 K revealed the presence of a pronounced upturn of the electronic specific heat divided by temperature (c/T) below about 8 K, insensitive to an applied field of 5 T. The $c(T)$ data could be fitted with a $T^3 \ln T$ term below 5 K, providing evidence for spin-fluctuation phenomena. The resulting linear coefficient of the electronic specific heat γ ($T \to 0$ K) amounted to 415 $mJ/mol_U K^2$, which classifies U_2Pt_2In as a heavy-electron compound. In line with this, the electrical resistivity, $\rho(T)$, of U_2Pt_2In was found to show a weak maximum around 80 K and coherence effects at low temperatures [3], which could be attributed to the Kondo-lattice effect. The magnetic susceptibility, $\chi(T)$, shows deviations from the Curie-Weiss behaviour below about 150 K [2]. In the limit $T \to 1.2$ K, χ is enhanced and continues to rise. No sign of magnetic ordering has been observed.

More recently, data taken on a polycrystalline sample [27] showed that $\rho(T) = \rho_o + aT$ in the temperature range 1.4-6 K. This led to the suggestion that U_2Pt_2In might be a good candidate to study non-Fermi liquid (NFL) phenomena.

In order to probe and investigate the NFL behaviour in U_2Pt_2In, it is of interest to study the thermal, transport and magnetic properties of single crystals at lower temperatures ($T < 1.2$ K). As discussed in Section 2.5, only a few stoichiometric compounds (like e.g. $CeNi_2Ge_2$) show NFL properties at ambient pressure. U_2Pt_2In is the first U compound exhibiting NFL behaviour without chemical substitution, pressure or magnetic field as a control parameter. In this section, results of magnetization ($2\text{ K} \leq T \leq 350$ K, $B \leq 35$ T), resistivity ($0.3\text{ K} \leq T \leq 300$ K),

magnetoresistance ($B \leq 38$ T), specific-heat (0.1 K $\leq T \leq$ 180 K), specific-heat in field ($B \leq 8$ T) and thermal-expansion (0.35 K $\leq T \leq$ 200 K) experiments carried out on U_2Pt_2In single crystals are presented (for details on the preparation and characterization of the single crystals see Section 4.1.1 and Ref. 10).

4.2.1. Magnetization

Magnetization measurements were performed on several single crystals (with a mass of 10-50 mg) using a SQUID magnetometer (Quantum Design) in the temperature range 2-350 K and in applied fields up to 5.5 T. In addition, magnetization measurements were carried out in high magnetic fields up to 35 T at 4.2 K in the Amsterdam High-Field Facility.

The magnetizations $M_a(B)$ and $M_c(B)$ at some selected temperatures are shown in Figure 4.4a, where a and c refer to the crystallographic direction along which the magnetic field is applied. In both cases, the magnetization is linear in fields up to 5.5 T. The slope dM/dB is always higher for $\boldsymbol{B} \parallel \mathbf{c}$ than for $\boldsymbol{B} \parallel \mathbf{a}$, though the anisotropy is not substantial. M (T = 2 K) reaches the value of 0.25 (0.21) μ_B/f.u. in a field of 5.5 T applied along the c- (a-) axis. No hysteresis in M_a and M_c was observed. Magnetization measurements for $\boldsymbol{B} \parallel \mathbf{c}$ at 4.2 K were carried out up to 35 T (Figure 4.4b). No significant deviation from a linear behaviour was observed. In the maximum field, M_c (35 T) = 1.48 μ_B/f.u. These results are similar to the ones obtained on polycrystalline samples up to 35 T [17] and 57 T [18]. In the polycrystalline data, a weak non-linearity was observed, which was not found in the single-crystal data. This non-linearity is due to the saturation of magnetic impurities in the polycrystalline sample (about 2% of ferromagnetic UPt was present as a second phase [3]). The data taken on free and fixed powder are identical, which is another indication that the magnetic anisotropy is rather weak in this compound.

The temperature variation of the d.c. susceptibility (M/H), $\chi_a(T)$ and $\chi_c(T)$, is presented in Figure 4.5 for B = 0.1 T. The susceptibility is anisotropic, with the c-axis as the easy axis of the magnetization. This anisotropy persists in the whole temperature range (up to 350 K).

At low temperatures, a clear difference between χ_a and χ_c is observed. χ_a continues to increase as the temperature is lowered down to 2 K, while χ_c displays a broad maximum (Figure 4.5). Tracing the derivatives, dχ/dT, shows that the maximum occurs at T_{max} = 7.9(3) K. The

relative height and width of the maximum do not change significantly with the applied field strength (from 0.005 to 5.5 T). This type of behaviour is frequently observed in systems which exhibit exchange-enhanced Pauli paramagnetism. The maximum in χ_c is indicative of the stabilization of short-range antiferromagnetic correlations along the c-axis [28,29].

Above 10 K, the susceptibility follows a modified Curie-Weiss law, $\chi = \chi_0 + C/(T-\theta)$. For $\boldsymbol{B} \parallel \mathbf{c}$, the parameters obtained are $\chi_0 = 1.1\times10^{-8}$ m^3/mol$_U$, θ = -62 K and $\mu_{eff} = 2.6\ \mu_B$/U, while for $\boldsymbol{B} \parallel \mathbf{a}$, $\chi_0 = 1.1\times10^{-8}$ m^3/mol$_U$, θ = -63 K and $\mu_{eff} = 2.2\ \mu_B$/U. The fitted Curie-Weiss behaviour is represented by the lines in Figure 4.5. The near-equality of the paramagnetic Pauli temperatures θ reflects the weak magnetic anisotropy in this system. The μ_{eff} values are considerably reduced with respect to the free-ion values for U^{3+} and U^{4+} of 3.62 μ_B and 3.58 μ_B, respectively, which points to a strong V_{cf} hybridization.

The magnetization data do not show any sign of long-range magnetic order down to 2 K. In order to investigate the presence of possible spin-glass effects, magnetization measurements were performed after zero-field cooling and field cooling to 2 K. However, no difference was observed for 0.01 T $\leq B \leq$ 5.5 T, indicating the absence of a spin-glass ground state.

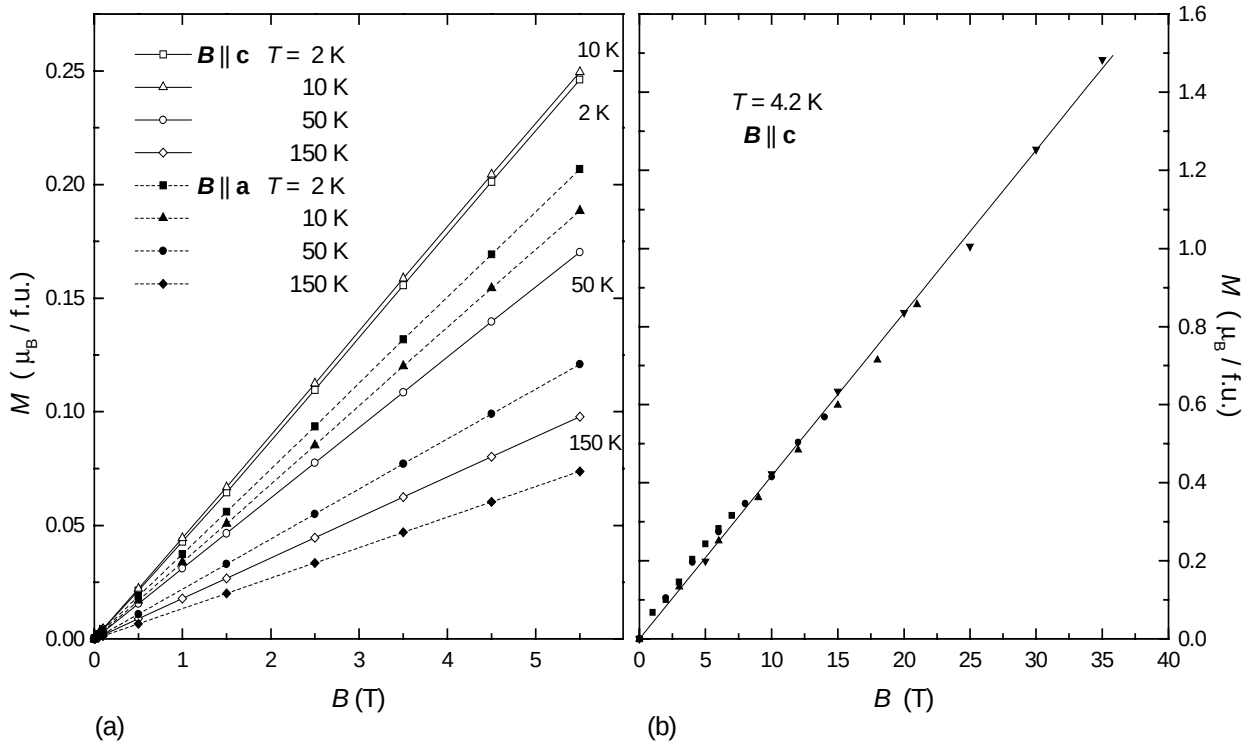

Figure 4.4 - a) Field dependence of the magnetizations M_a and M_c of U_2Pt_2In for several temperatures and b) high-field magnetization at 4.2 K for $\boldsymbol{B} \parallel \mathbf{c}$ (different symbols represent different field pulses). The lines are linear fits through the data points.

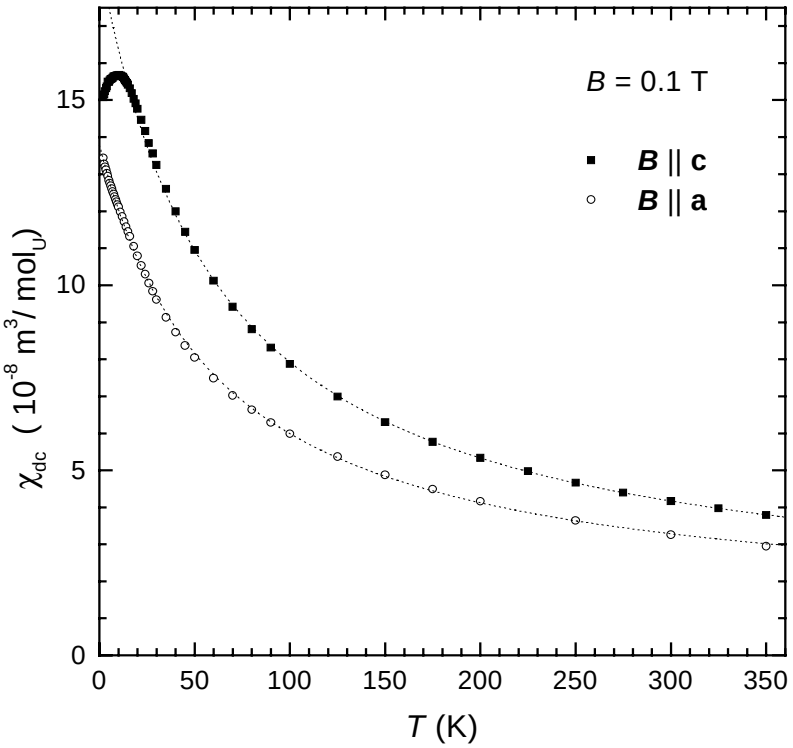

Figure 4.5 - Temperature dependence of the d.c. susceptibility of U_2Pt_2In in a magnetic field of 0.1 T applied along the a- or c-axis. The dotted lines represent modified Curie-Weiss fits.

4.2.2. Resistivity

Resistivity measurements were carried out on bar-shaped crystals with typical dimensions $3\times1\times1$ mm^3, for electrical currents along the a- and c-axis, in the temperature range 0.3-300 K using a ^{3}He system. A standard a.c. four-point method was used with an excitation current of the order of 300 μA. The excitation current was varied in order to check for Joule-heating effects.

The resistance curves for $\boldsymbol{I} \parallel \mathbf{a}$ and $\boldsymbol{I} \parallel \mathbf{c}$ are shown in Figure 4.6a for temperatures below 10 K and in Figure 4.6b for temperatures below 300 K. The $R(T)$ values are normalized to the room temperature values R_{RT}. For both $\boldsymbol{I} \parallel \mathbf{a}$ and $\boldsymbol{I} \parallel \mathbf{c}$, the resistivity ρ_{RT} amounts to 220 ± 20 μΩcm. The experimental error in ρ_{RT} is mainly due to the uncertainty in the determination of the distance between the voltage contacts. Upon cooling, $\rho_{a,c}(T)$ starts to rise and a weak broad maximum is observed at about 80 K followed by a relatively sharp decrease at

lower temperatures, typical of coherence effects in heavy-fermion compounds. As shown in Figure 4.6, the resistivity is anisotropic: $\rho_c > \rho_a$ for $T < 150$ K.

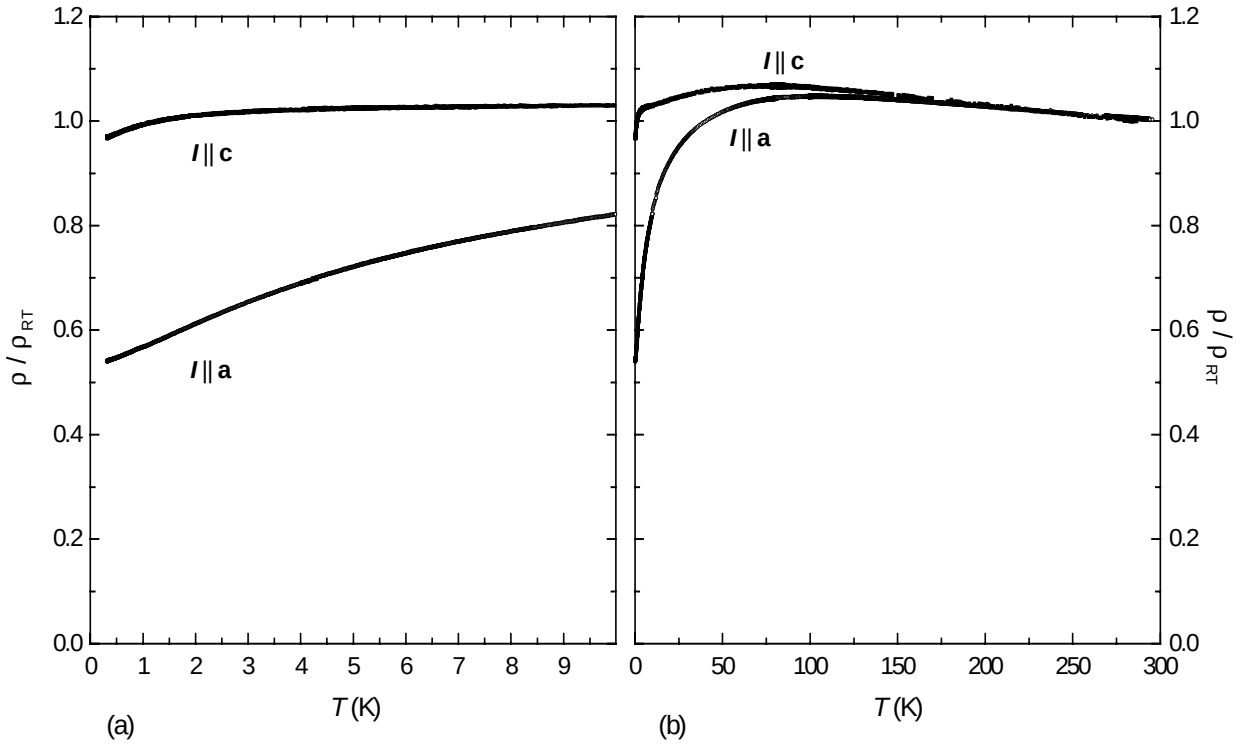

Figure 4.6 - Resistivity (normalized to the room temperature values) of U_2Pt_2In for ***I*** || **a** and ***I*** || **c** for $T < 10$ K (a) and $T < 300$ K (b).

Clearly, the resistivity curves do not obey the Fermi-liquid expression $\rho \sim T^2$ at low temperatures. Instead, as shown below, $\rho \sim T^{\alpha}$ with $\alpha < 2$.

If the resistivity below a certain temperature T' can be expressed by

$$\rho = \rho_0 + aT^{\alpha} \quad , \tag{4.7}$$

then the exponent α can be calculated by

$$\alpha = \frac{d\ln(\rho - \rho_0)}{d\ln T} \quad . \tag{4.8a}$$

However, using Equation 4.8a may result in significant errors in α due to the uncertainty in evaluating the residual resistivity ρ_0, especially when α is small. Alternatively, the following expression can be used:

$$\alpha = 1 + \frac{d\ln\frac{d\rho}{dT}}{d\ln T} \quad . \tag{4.8b}$$

One can define an effective temperature-dependent exponent $\alpha_{eff}(T)$ by applying equation 4.8b at all temperatures. The effective exponent can be identified with α if $\alpha_{eff}(T) \approx$ constant in a certain temperature range.

Figure 4.7 shows $\alpha_{eff}(T)$ computed from the derivative of the smoothed low-temperature resistivity curves. For $\boldsymbol{I} \parallel \mathbf{a}$, one obtains $\alpha_a = 1.25(5)$ below about 1 K. For $\boldsymbol{I} \parallel \mathbf{c}$, $\alpha_{eff}(T)$ does not attain a constant value and thus ρ_c does not follow a clear T^{α} law down to 0.3 K. Assuming that $\alpha_{eff,c}(T)$ levels off below 0.3 K in a way similar to $\alpha_{eff,a}(T)$, the rough estimate $\alpha_c \sim 0.9(1)$ can be made.

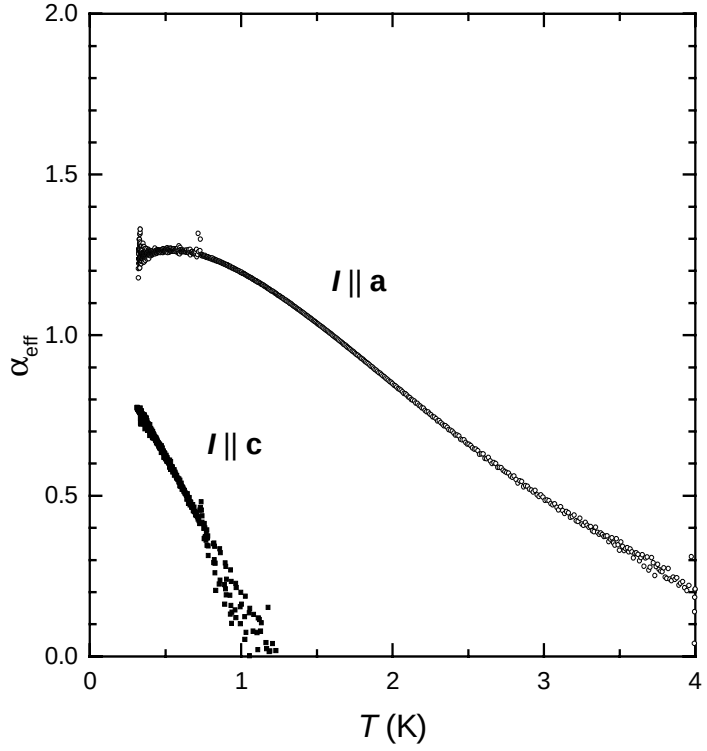

Figure 4.7 - Effective exponent α_{eff} of the resistivity of U_2Pt_2In for $\boldsymbol{I} \parallel \mathbf{a}$ and $\boldsymbol{I} \parallel \mathbf{c}$.

With these α-values the following residual resistivities result: $\rho_{0,a} = 0.53\ \rho_{RT}$ and $\rho_{0,c} = 0.95\ \rho_{RT}$, i.e. $\rho_0 \approx 115\ \mu\Omega$cm for $\boldsymbol{I} \parallel \mathbf{a}$ and $\rho_0 \approx 210\ \mu\Omega$cm for $\boldsymbol{I} \parallel \mathbf{c}$. The residual resistivity values are large, which is normally taken as evidence that some disorder is present in the crystals. However, this has not been confirmed by single-crystal X-ray [10] and neutron-diffraction [30] experiments. The structure refinement confirms the high crystalline quality. The possibility of site inversion (e.g. Pt and In inversion) is also excluded by the neutron-diffraction refinement. Moreover, because the residual resistivity depends strongly on the direction of the

applied current, it is clear that besides impurities other scattering mechanisms contribute to ρ_0. It should be noted that the low-temperature resistivity data were taken on several single crystals, all showing the same behaviour.

4.2.2.1. Magnetoresistance

Transport properties in a magnetic field provide an important tool to investigate the non-Fermi liquid state. In general, a magnetic field is expected to restore the Fermi liquid state, as for the case of a proximity to a quantum critical point. If a compound is driven away from the magnetic instability, the suppression of magnetic correlations should be observable in the resistivity.

In Figure 4.8, the temperature dependence of the resistivity is shown in a field of 8 T applied along the different crystallographic directions. Below 4.2 K the magnetoresistance (MR) for $\boldsymbol{I} \parallel \mathbf{c}$ is negative for both $\boldsymbol{B} \parallel \mathbf{c}$ (longitudinal configuration) and $\boldsymbol{B} \parallel \mathbf{a}$ (transverse configuration). At the lowest temperatures, the $\rho(T)$ curves show a tendency to level off. For $\boldsymbol{I} \parallel \mathbf{a}$, the curves obtained in the two transverse configurations ($\boldsymbol{B} \parallel \mathbf{b}$ and $\boldsymbol{B} \parallel \mathbf{c}$) are essentially the same, i.e. a negative MR at high temperatures and a positive MR below 0.8 K. At the lowest temperatures, an approximate $\rho \sim T^2$ behaviour is observed in 8 T. In the longitudinal configuration, the magnetoresistance is always positive and shows no tendency to level off at low temperatures.

Assuming that the $\rho(T)$ curves follow power laws of the type $\rho \sim T^{\alpha}$, the exponent α can be estimated using equation 4.8b. The effective exponent obtained for different magnetic fields is plotted in Figure 4.9 for the transverse configurations (since for $\boldsymbol{I} \parallel \mathbf{a}$ the data for $\boldsymbol{B} \parallel \mathbf{b}$ and $\boldsymbol{B} \parallel \mathbf{c}$ are almost identical, only $\boldsymbol{B} \parallel \mathbf{c}$ is shown). The low-temperature value of α increases with increasing magnetic-field strength, reaching values close to 2 for 8 T, as expected for a Fermi liquid. The field evolution of the exponent α is shown in Figure 4.10, which clearly illustrates that there is a tendency towards a Fermi-liquid $\rho \sim T^2$ law near 8 T.

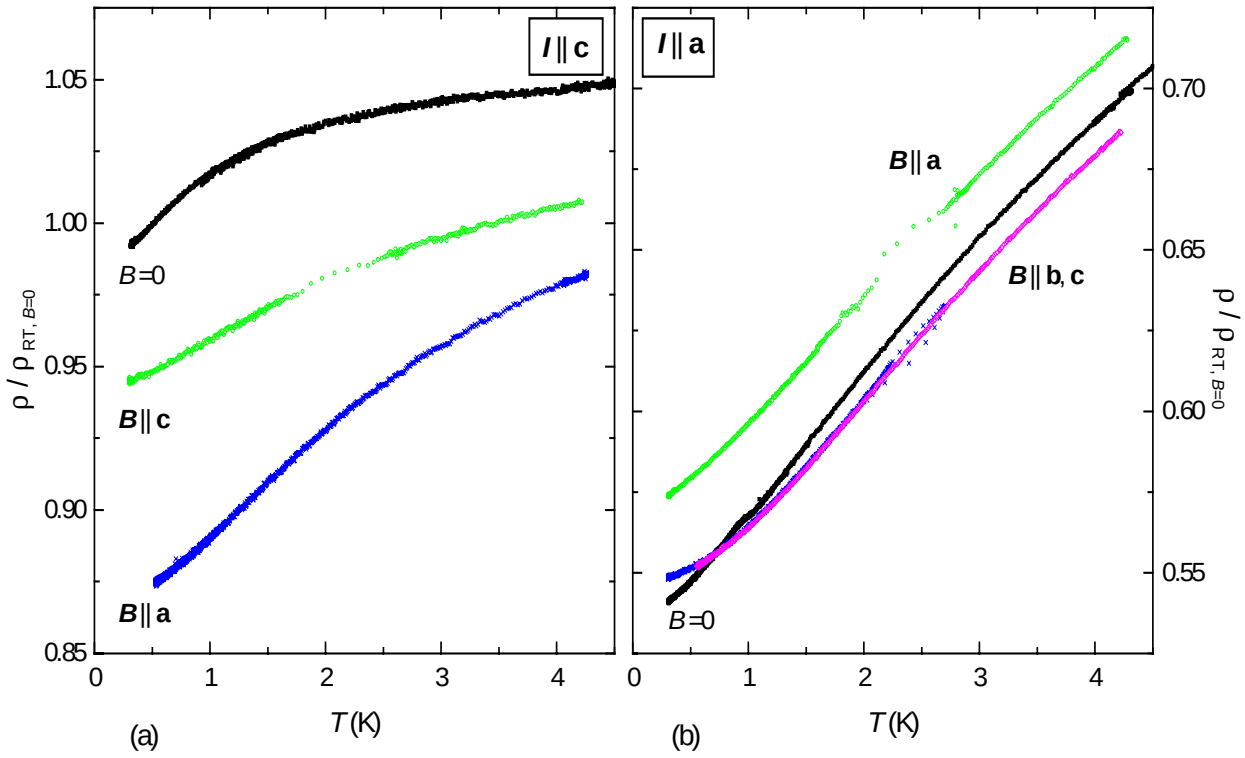

Figure 4.8 - Temperature dependence of the resistivity of U_2Pt_2In in a field of 8 T applied along the main crystallographic directions.

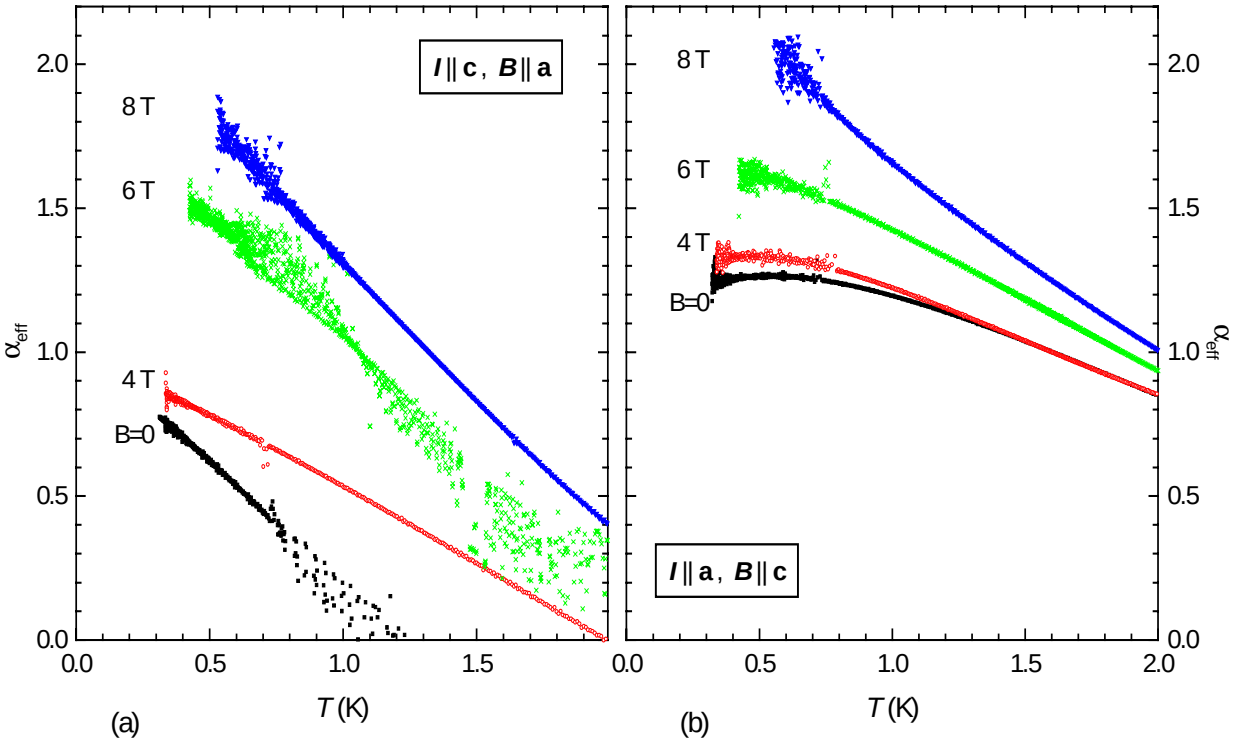

Figure 4.9 - Effective exponent α of the resistivity of U_2Pt_2In in magnetic fields in the transverse configuration ($\boldsymbol{B} \perp \boldsymbol{I}$).

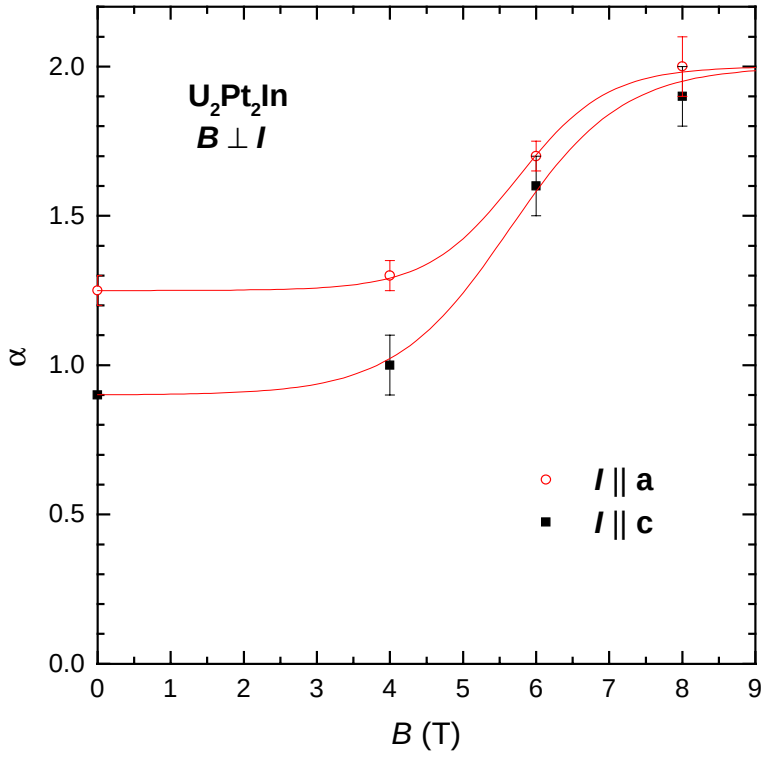

Figure 4.10 - Field dependence of the resistivity exponent α in the transverse configuration. The lines are guides to the eye.

In Figure 4.11 and Figure 4.12, the magnetoresistance in the longitudinal and transverse configurations is shown at 0.48, 1.3, 4.2 and 10 K. The magnetoresistance curves show several unusual features.

In the longitudinal configuration, a negative MR is obtained when current and field are applied along the c-axis. A weak upward curvature is observed at the lowest temperatures at high fields. On the other hand, when current and field are applied along the a-axis the magnetoresistance is positive and approximately follows a $\Delta\rho/\rho \sim B^2$ law.

In the transverse configuration, the MR obtained for $\boldsymbol{I} \parallel \mathbf{c}$ is also negative with $\Delta\rho/\rho$ values higher (in absolute value) than for $\boldsymbol{B} \parallel \boldsymbol{I} \parallel \mathbf{c}$. No tendency to upward curvature is visible at the lowest temperatures. In the $\boldsymbol{B} \perp \boldsymbol{I} \parallel \mathbf{a}$ case, the MR values are negative at low fields, pass through a minimum and then become positive. The position of the minimum increases with temperature: $B_{min} \sim 3.5$, 5 and 14 T at $T = 0.48$, 1.3 and 4.2 K, respectively (see Figure 4.13 for the high-field MR at 4.2 K).

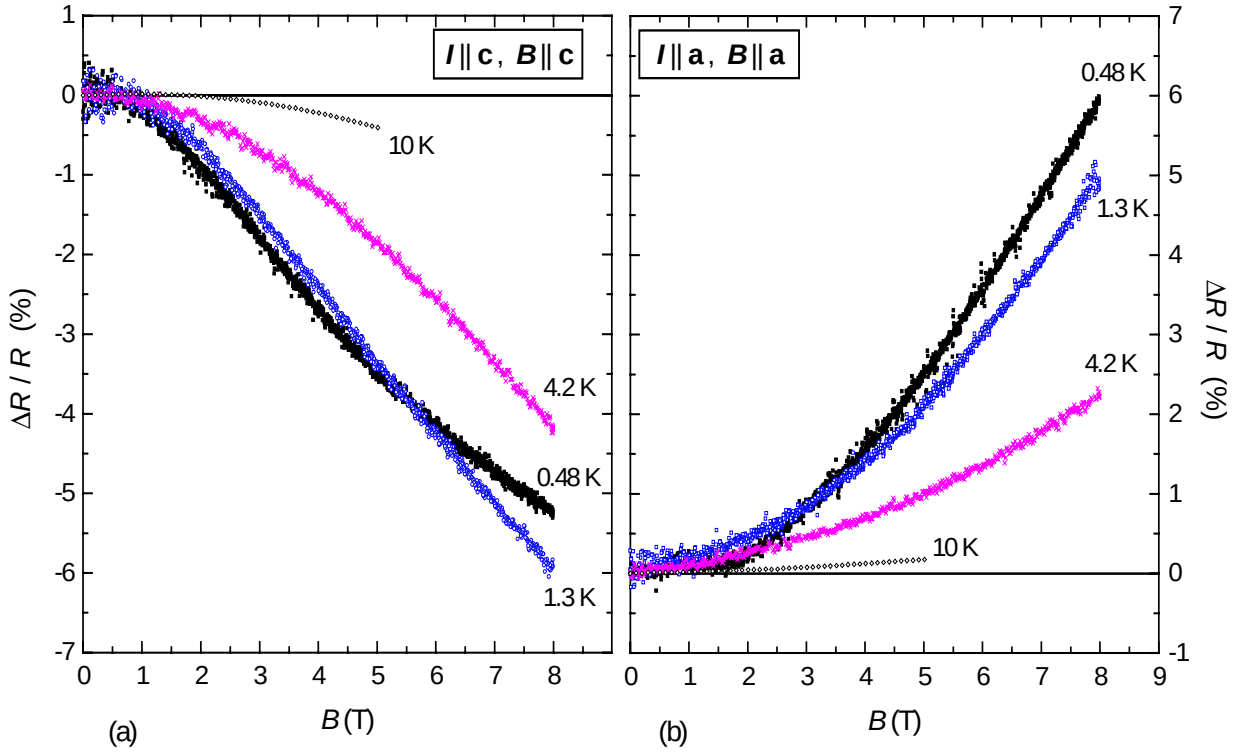

Figure 4.11 - Magnetoresistance of U_2Pt_2In in the longitudinal configuration (***B*** ∥ ***I***) at temperatures as indicated.

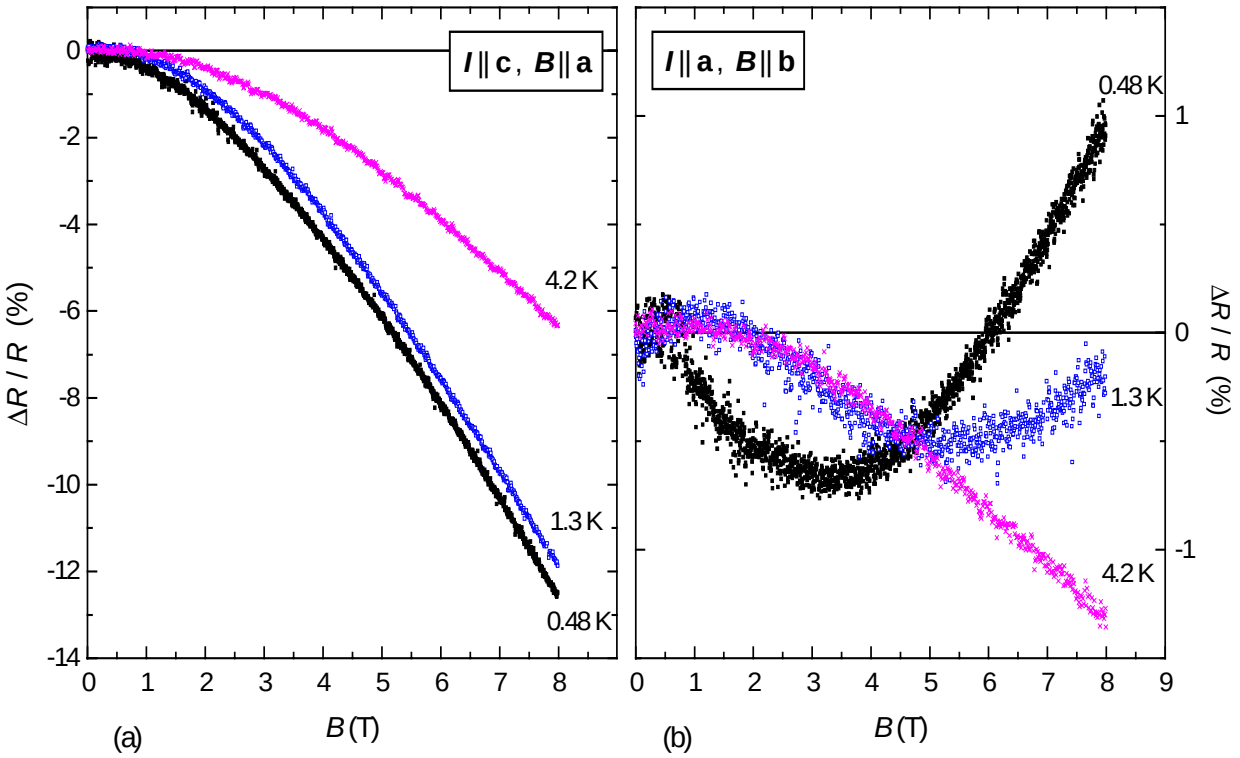

Figure 4.12 - Magnetoresistance of U_2Pt_2In in the transverse configuration (***B*** ⊥***I***) at temperatures as indicated.

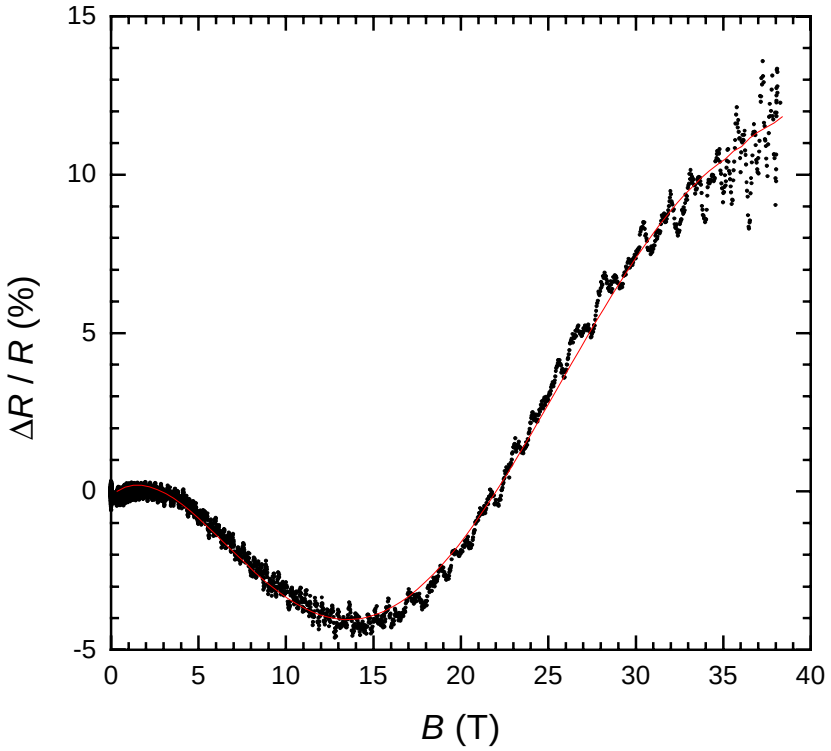

Figure 4.13 - High-field magnetoresistance of U_2Pt_2In at 4.2 K for $\boldsymbol{I} \parallel \mathbf{a}$ and $\boldsymbol{B} \parallel \mathbf{c}$. The line is a polynomial fit through the data points. Note: the oscillations observed are an artefact of the averaging procedure.

According to Ref. 31, the magnetoresistance of weakly- or non-disordered metals in the NFL regime close to an antiferromagnetic quantum critical point (see Section 2.3) can be separated into spin and orbital effects. For the spin effects, small magnetic fields will suppress the antiferromagnetic fluctuations as the compound is driven away from the QCP. This suppression of the fluctuations will reduce the amount of scattering and the MR will be negative. For localized-moment paramagnets, applying a magnetic field results in a net polarization of the disordered magnetic moments and thus to a reduction of their scattering contribution to the resistivity. The magnetoresistance is related to the correlation function $\langle S_i S_j \rangle$ between the ion spins and therefore to the low-field magnetization M [32]:

$$\frac{\Delta\rho}{\rho} = -a\left(\frac{M}{M_{sat}}\right)^2 , \qquad (4.9)$$

where $\Delta\rho/\rho \equiv [\rho(B,T)-\rho(0,T)]/\rho(0,T)$, $a > 0$ and M_{sat} is the saturation magnetization obtained at extremely high fields. Since the magnetization of U_2Pt_2In is proportional to the field, it follows that $\Delta\rho/\rho \sim -B^2$.

On the other hand, for the orbital effects a positive MR is expected, which varies initially as B^2, then crosses over to a linear behaviour in B and finally saturates at high fields [31].

In addition, if the Lorentz force would be responsible for the B^2 behaviour observed, then one would expect a weak positive B^2 contribution to the transverse MR and, to a lesser extent, to the longitudinal magnetoresistance. A comparison of the MR values obtained for the different configurations (Figure 4.14) shows that this contribution is very weak and not significant. In fact, the opposite effect is observed: for $\boldsymbol{I} \parallel \mathbf{c}$, $\Delta\rho/\rho$ is less negative for $\boldsymbol{B} \parallel \boldsymbol{I}$ than for $\boldsymbol{B} \perp \boldsymbol{I}$, while for $\boldsymbol{I} \parallel \mathbf{a}$ the positive contribution is clearly stronger in the longitudinal configuration than in the transverse one.

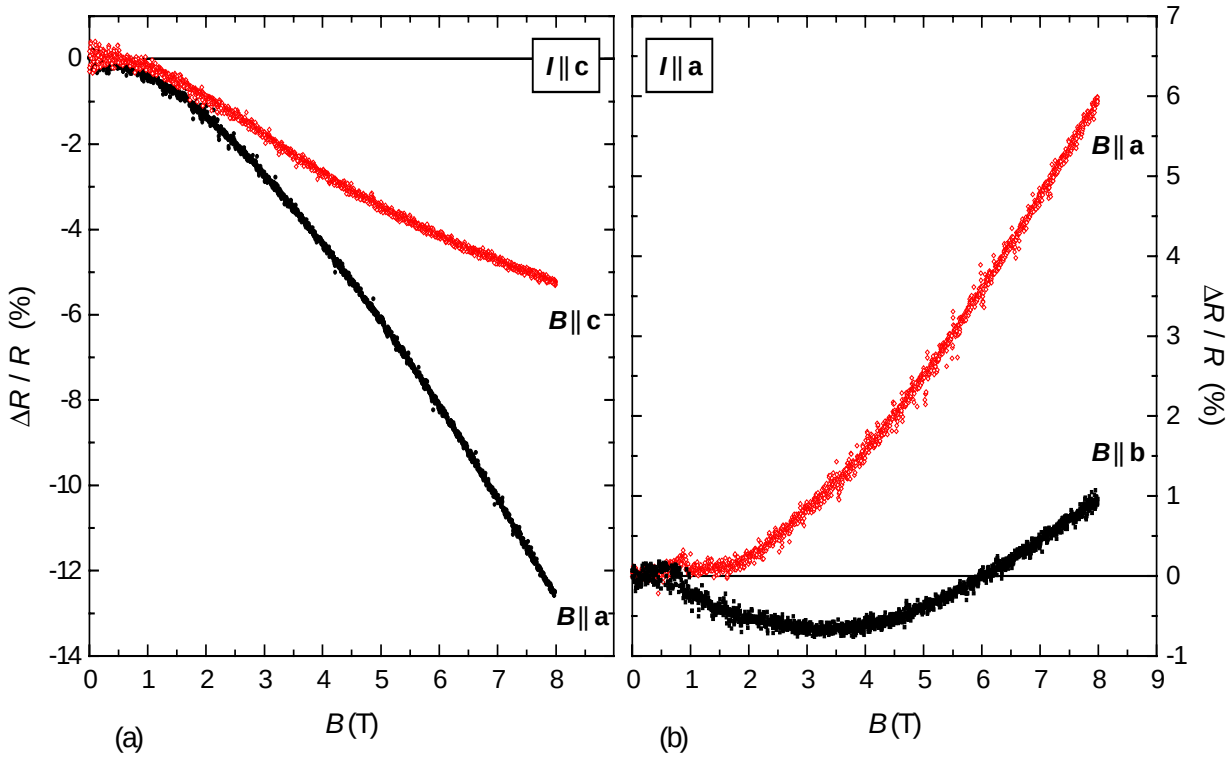

Figure 4.14 - Magnetoresistance of U_2Pt_2In at $T = 0.48$ K for $\boldsymbol{B} \parallel \boldsymbol{I}$ and $\boldsymbol{B} \perp \boldsymbol{I}$.

When summarizing the magnetoresistance data, a competition of a positive and a negative contribution is clearly found. At low fields, the negative contribution is always dominant, except when $\boldsymbol{B} \parallel \boldsymbol{I} \parallel \mathbf{a}$. As the field increases, the positive contribution becomes dominant. The high field experiments show that the MR has a tendency to saturate at extremely high fields (about 100 T). This is also predicted by the theory of magnetotransport in nearly antiferromagnetic metals [31].

A proper analysis of the relative weight of the different contributions is difficult due to their competition, although it is evident that the negative contribution, associated with a polarization of the moments, is stronger when the current is applied along the c-axis.

A closer inspection of the zero-field resistivity curves for $\boldsymbol{I} \parallel \mathbf{c}$ reveals the presence of a shoulder in $\rho(T)$ centered at about 7 K. The shoulder becomes more clear in a ρ versus log$T$ plot (Figure 4.15). This anomaly is not observed for $\boldsymbol{I} \parallel \mathbf{a}$. It should be noted that $\boldsymbol{B} \parallel \mathbf{c}$ is the direction for which a maximum at $T_{max} = 7.9$ K is observed in the magnetic susceptibility. This suggests that the resistivity shoulder may be related to short-range antiferromagnetic correlations along the c-axis. The field effect ($\boldsymbol{B} \parallel \boldsymbol{I}$, $B \leq 5$ T) on the shoulder is shown in Figure 4.15. The shoulder is suppressed under the influence of the magnetic field and becomes very faint at 5 T. As antiferromagnetic fluctuations tend to be suppressed by a magnetic field, also the shoulder should be gradually suppressed with field. However, suppression of the magnetic fluctuations was not observed in the susceptibility in fields up to 5.5 T. Since the shoulder in $\rho(T)$ is very faint, it may possibly be more sensitive to this effect than the maximum in $\chi(T)$.

Another important point is that ρ_0 varies significantly with the applied magnetic field, which clearly shows that the residual resistivity is not uniquely due to impurity or defect scattering.

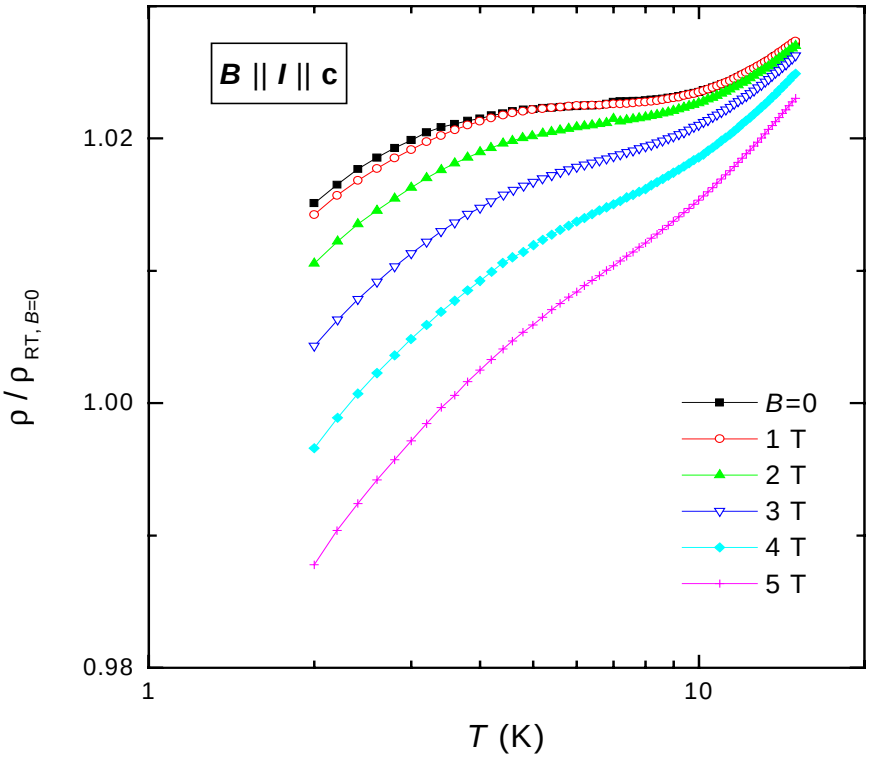

Figure 4.15 - Temperature dependence ($T \leq 15$ K) of the resistivity of U_2Pt_2In for $\boldsymbol{B} \parallel \boldsymbol{I} \parallel \mathbf{c}$.

4.2.3. Specific heat

The specific heat of U_2Pt_2In was measured on several single-crystalline samples, using a semi-adiabatic technique in a bath cryostat above 1.5 K, while data below 5 K were taken in a ^{3}He system (0.3 K < T < 5 K) and a dilution refrigerator (0.1 K < T < 0.7 K) employing the relaxation method. The results are shown in Figure 4.16 in a plot of c/T versus log$T$. Below 10 K, c/T shows an upturn and instead of attaining a constant value in the limit $T \to 0$ K, as expected for a Fermi liquid, c/T diverges logarithmically, which is one of the hallmarks of a non-Fermi-liquid ground state.

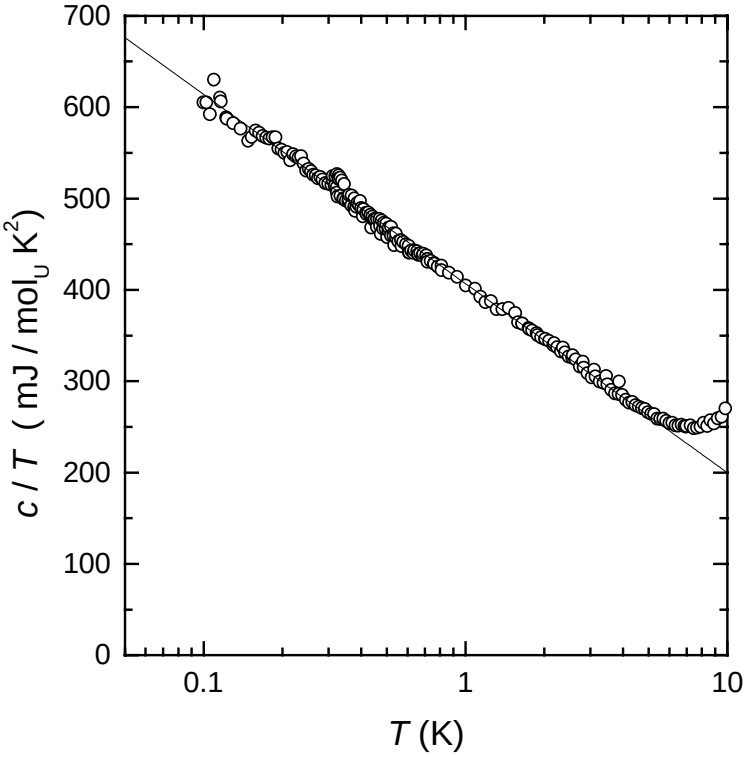

Figure 4.16 - Low-temperature specific heat of U_2Pt_2In divided by temperature as a function of log$T$. The line is a $c/T \sim -\ln(T/T_0)$ fit.

The data below 6 K are well described by

$$\frac{c}{T} = \gamma_1 - \delta \ln\left(\frac{T}{T_1}\right) = -\delta \ln\left(\frac{T}{T_0}\right) \qquad (4.10)$$

with $\gamma_1 = 406.8(5)$ mJ/mol$_U$K^2 and $\delta = 89.9(5)$ mJ/mol$_U$K^2. Here, $T_1 \equiv 1$ K and $T_0 = \exp(\gamma_1/\delta) = 92(1)$ K. In this case, γ_1 is the value of c/T at 1 K and not the enhanced-Sommerfeld coefficient, as usually observed for heavy-fermion compounds.

Of main importance is that U_2Pt_2In is one of the few stoichiometric systems exhibiting non-Fermi liquid behaviour with a strong logarithmic divergency of the specific heat. Moreover, this logarithmic divergency has been found in the data over almost 2 decades of temperature.

At higher temperatures, the dominant contribution to the specific heat is the lattice contribution. Since no samples of the non-magnetic compound Th_2Pt_2In were available, the phonon contribution to the specific heat could not be estimated. However, an approximation can be given by the Debye function

$$c_V = 3\mathrm{R}\left[12\left(\theta_\mathrm{D}/T\right)^{-3}\int_0^{\theta_\mathrm{D}/T}\frac{x^3}{\mathrm{e}^x-1}\mathrm{d}x-\frac{3\theta_\mathrm{D}/T}{\mathrm{e}^{\theta_\mathrm{D}/T}-1}\right] \quad . \tag{4.11}$$

This expression is valid for the specific heat at constant volume (c_V) but, experimentally, the specific heat at constant pressure (c_p) is obtained. The difference between c_V and c_p can usually be neglected as it will be shown in Section 4.2.4.

The Debye function has been tabulated in Refs. 33 and 34 and can therefore easily be compared to the experimental data. The high-temperature slope of the specific heat of U_2Pt_2In can be approximated by a linear electronic term $c_{\mathrm{el}} = \gamma T$ with γ = 88 mJ/mol$_\mathrm{U}$K^2. Using this value, $c_{\mathrm{ph}} = c - c_{\mathrm{el}}$ is in good agreement with the Debye function calculated with θ_D = 175 K (see the line in Figure 4.17a). However, the subtracted linear term has an unusually large coefficient, about 10 times higher than expected, which possibly indicates that the Debye function underestimates the lattice contribution to the specific heat of U_2Pt_2In.

The electronic contribution obtained after subtracting the Debye function from the total specific heat is plotted in Figure 4.17b. In this contribution, the logarithmic divergency is observed up to about 35 K. However, the high-temperature linear term above 50 K is extremely large. The entropy associated with it is also too large to account for a possible crystalline electric-field effect.

Assuming that the low-temperature phonon contribution to the specific heat is $c_{\mathrm{ph}} = \beta T^3$, with β obtained from θ_D = 175 K, the low-temperature entropy associated with the electronic specific heat can be determined by the integral of $(c\text{-}c_{\mathrm{ph}})/T$,

$$S_{\mathrm{el}}(T) - S_{\mathrm{el}}(T = 0.1\mathrm{K}) = \int_{0.1\mathrm{K}}^{T}\frac{c_{\mathrm{el}}(T)}{T}\mathrm{d}T \quad . \tag{4.12}$$

The entropy is shown in Figure 4.18. In the S=½ two-channel Kondo effect, the entropy is predicted to saturate at ½ Rln2 (≈ 2.88 J/mol$_\mathrm{U}$K) before continuing to increase at higher

temperatures (see Section 2.3). For U_2Pt_2In, there is no clear evidence for this effect.

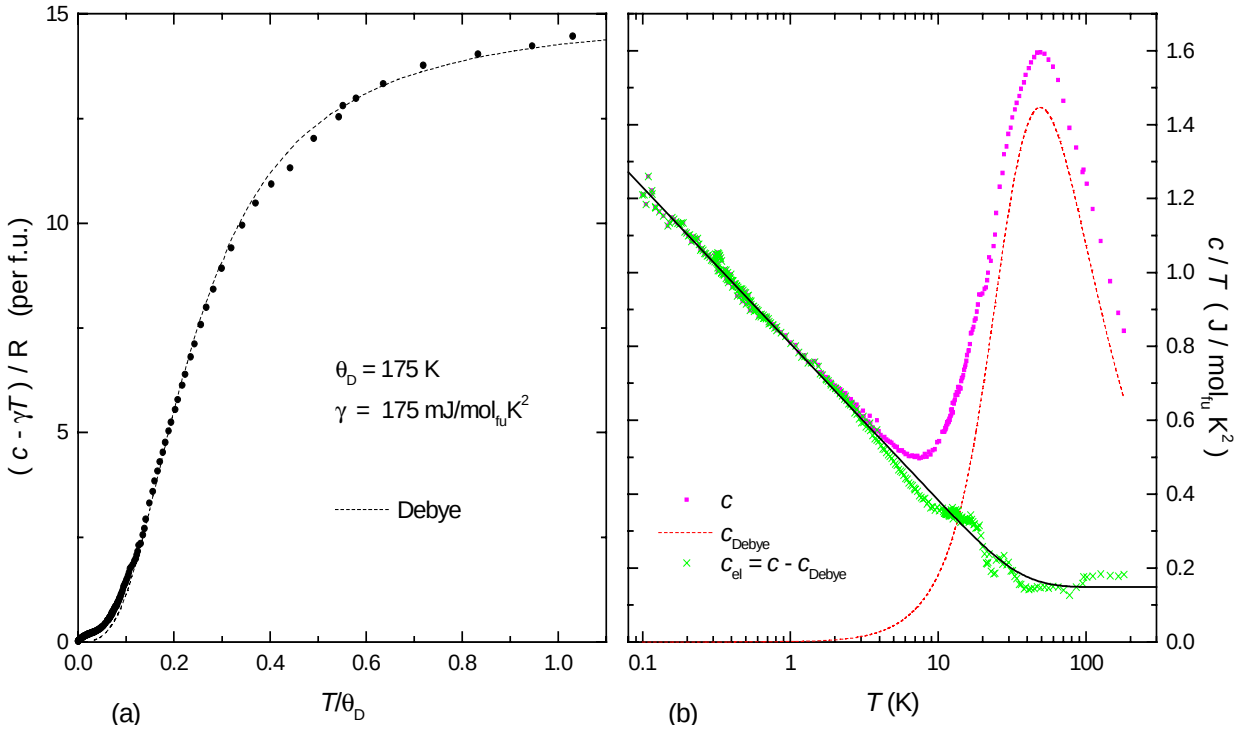

Figure 4.17 - (a) Lattice specific heat (per mole formula unit) of U_2Pt_2In. The dashed line is the Debye function with θ_D = 175 K. (b) Lattice (c_{Debye}/T) and electronic (c_{el}/T) contributions to the total specific heat c/T. Notice the logarithmic T scale. The full line is a guide to the eye.

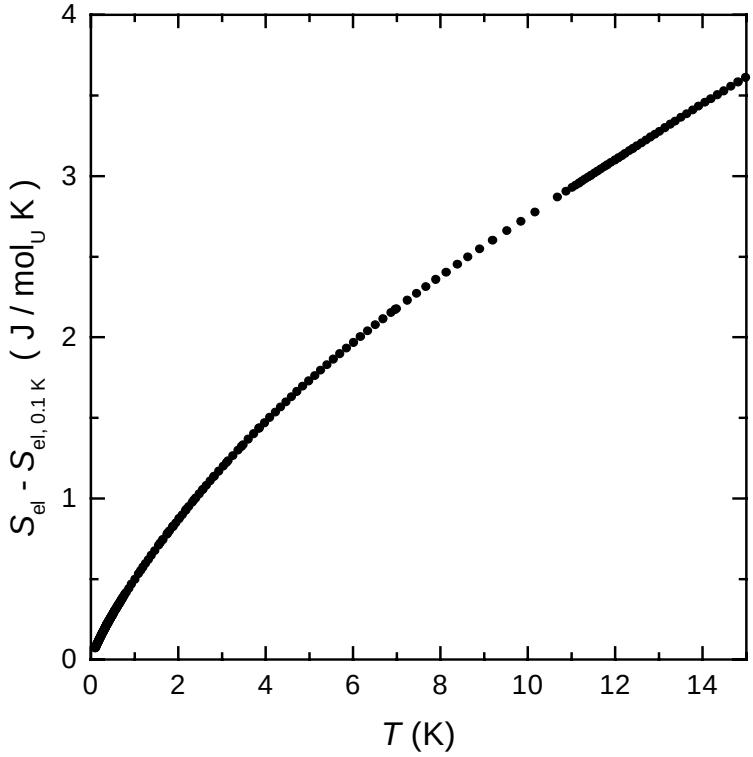

Figure 4.18 - Entropy (per mole U) derived from the electronic specific heat of U_2Pt_2In.

4.2.3.1. Specific heat in field

In order to investigate the robustness of the non-Fermi-liquid state in U_2Pt_2In in an external magnetic field, specific-heat measurements were performed in the temperature range 0.1-1 K with $\boldsymbol{B} \parallel \mathbf{c}$ up to field values of 8 T. In Figure 4.19, the results obtained in the dilution refrigerator ($T < 0.7$ K) are shown. The straight line represents the zero-field $c/T = -\delta\ln(T/T_0)$ behaviour taken from Figure 4.16.

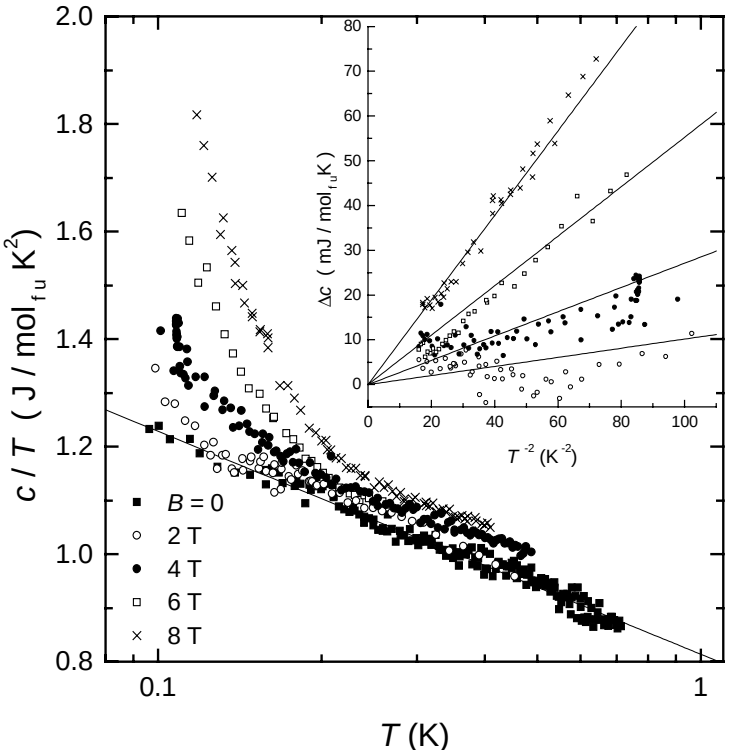

Figure 4.19 - Specific heat divided by temperature versus log$T$ for U_2Pt_2In under magnetic fields applied along the c-axis. Insert: nuclear specific heat $c_N \equiv c - c|_{B=0}$ versus T^{-2} for $T < 0.25$ K; the lines are functions $c_N = D_2T^{-2}$ (see text below).

A strong enhancement of the specific heat is observed at low temperatures as the field strength increases. As will be shown below, this enhancement is predominantly due to the specific heat of the In nuclei.

A nuclear contribution to the specific heat arises when an interaction lifts the degeneracy of the states, which are characterized by different orientations of the nuclear moments. This interaction may be provided by an external magnetic field, an effective hyperfine field or an electric field gradient. The energy levels, ε_m, of a nucleus with spin quantum number I in a magnetic field and in an electrical field gradient with axial symmetry are given by [35,36]

$$\frac{\varepsilon_m}{k_B} = -a'm + P\left[m^2 - \frac{I(I+1)}{3}\right] \qquad (m = -I,-I+1,\ldots,I) \tag{4.13}$$

with

$$a' = \frac{\mu B_{\text{eff}}}{k_B I} \qquad \text{(magnetic-interaction parameter)} \tag{4.14a}$$

$$P = \frac{3e^2qQ}{4k_B I(2I-1)} \qquad \text{(quadrupole-coupling constant)} \tag{4.14b}$$

where $\mu = g_N I \mu_N$ is the magnetic moment of the nucleus (μ_N is the nuclear magneton and g_N the nuclear g-factor) and B_{eff} is the effective field at the nucleus arising from the hyperfine field B_{hf} and/or an external field B. eq is the component of the electric-field gradient tensor along the high-symmetry axis and Q is the nuclear quadrupole moment. One has $Q = 0$ for $I = 1/2$, while $q = 0$ for nuclei in a cubic environment.

The exact expression for the nuclear specific heat (of the Schottky-anomaly type) is

$$\frac{c_N}{R} = \frac{\sum_{m=-I}^{I}\sum_{n=-I}^{I}\left(\varepsilon_m^2 - \varepsilon_m\varepsilon_n\right)\exp\left(-\frac{\varepsilon_m+\varepsilon_n}{k_B T}\right)}{(k_B T)^2 \sum_{m=-I}^{I}\sum_{n=-I}^{I}\exp\left(-\frac{\varepsilon_m+\varepsilon_n}{k_B T}\right)} \quad . \tag{4.15}$$

From this expression it follows that at low temperatures $c_N \sim \exp(-1/T)$, while at high temperatures $c_N \sim T^{-2}$. A maximum occurs at $T_{\max} = (\varepsilon_{m+1}-\varepsilon_m)/k_B I$ and the entropy associated with c_N equals $R\ln(2I+1)$.

Since the measurements are usually made at temperatures well above $T_{\max}$ of c_N (for most metals the maximum is found at $T << 0.1$ K), one can use a high-temperature expansion of c_N in a power series of $1/T$:

$$c_N = \sum_{i\geq 2} D_i T^{-i} \quad . \tag{4.16}$$

The coefficients D_i are determined by the various moments of the energy levels. If the magnetic field is parallel to the symmetry axis of an axially symmetric electric-field gradient, the first two coefficients are given by [37]

$$\frac{D_2}{R} = \tfrac{1}{3} I(I+1)\, a'^2 + \tfrac{1}{45} I(I+1)(2I-1)(2I+3) P^2 \tag{4.17a}$$

$$\frac{D_3}{R} = -\tfrac{1}{45} I(I+1)(2I-1)(2I+3)\, a'^2 P - \tfrac{1}{1890} I(2I-3)(2I-1)(2I+2)(2I+3)(2I+5)\, P^3 \tag{4.17b}$$

If the quadrupole interaction is zero (P=0), all odd coefficients in Equation 4.16 vanish. In most cases, the first term is sufficient for fitting the experimental data: $c_N = D_2 T^{-2}$.

In Table 4.7, the nuclear spin quantum number, magnetic moment and quadrupole moment of the isotopes that may contribute to the nuclear specific heat of U_2Pt_2In (i.e. the isotopes with $I \neq 0$) are shown. Considering the abundancies and the nuclear moments of these isotopes, one can assume that the origin of the nuclear specific heat shown in Figure 4.19 is mainly due to the nuclei of In (^{113}In and ^{115}In have a nuclear magnetic moment that is one order of magnitude higher than ^{195}Pt and ^{235}U). The In nuclei have a spin of 9/2 and the average (taking into account the relative abundancies) magnetic and quadrupole moments are equal to $\mu = 5.5403\ \mu_N$ and $Q = 0.81 \times 10^{-24}$ cm^2, respectively.

Table 4.7 - Some nuclear data for the isotopes with $I \neq 0$ present in U_2Pt_2In. Source: WebElements [http://www.shef.ac.uk/chemistry/web-elements].

isotope	abundancy (%)	I	μ (μ_N)	Q (10^{-24} cm^2)
^{113}In	4.29	9/2	5.5289	0.799
^{115}In	95.71	9/2	5.5408	0.81
^{195}Pt	33.83	1/2	0.60950	0
^{235}U	0.72	7/2	-0.35	4.936

The insert in Figure 4.19 shows the field effect on the specific heat, obtained by subtracting the zero-field function, $\Delta c = c - c_{B=0} = c - (\gamma_1 - \delta \ln T)$. This figure shows that Δc varies approximately linearly with T^{-2}. Extracting values of D_2 from the B = 6 T and 8 T curves (for the lower fields the scatter is rather large after subtracting the zero-field curve), one obtains B_{hf} = 51.5 mT and a quadrupole-coupling constant $P \approx$ 0.9 mK. With these parameters, values of D_2 can then be calculated for B = 2 and 4 T (insert of Figure 4.19).

Although above 0.3 K the nuclear contribution to c/T is small, the data in Figure 4.19 show c/T values a few percent higher than for the zero-field data in this temperature range. There are two possible explanations for this behaviour: i) it can be attributed to small errors in the calibration of the thermometer on the sapphire plate in field. In fact, data taken above 0.4 K in a ^{3}He system with another calibrated thermometer did not show this effect. Notice that a small calibration error does not affect significantly the overall $c(T)$ curve; ii) the nuclear contribution might overshadow a decrease of the electronic term at low temperatures. As under influence of a magnetic field, a compound is pushed away from a magnetic instability, the low-temperature c/T will level off in order to recover the Fermi liquid behaviour. A decrease of c/T at low

temperatures has to be accompanied by an increase at higher temperatures because of the conservation of entropy [38].

In zero field, the calculated value of D_2 amounts to 4.303×10^{-5} JK/mol$_{In}$, which indicates that the nuclear contribution can be neglected with respect to the U electronic specific heat ($T \geq 0.1$ K). This value of D_2 is about 40 times larger than the one calculated for pure In in its tetragonal structure [39]. This is possibly explained by a substantial enhancement of the hyperfine interactions, which is not an unusual phenomenon in intermetallic compounds [40].

This large nuclear contribution hampers the study of the field effect on the non-Fermi liquid contribution. As a result, the proposed scaling properties of the specific heat (see Section 2.3) cannot be investigated. Magnetoresistance measurements showed a recovery of the Fermi liquid behaviour at the lowest temperatures. This seems, however, not to be confirmed by the specific-heat data.

4.2.4. Thermal expansion

Thermal-expansion measurements were performed on a single crystal of U_2Pt_2In in the temperature intervals 0.3-10 K (using a ^{3}He system) and 1.7-200 K (using a ^{4}He bath cryostat). Data were taken along the a-axis (L = 4.478 mm) and the c-axis (L = 1.570 mm). The linear thermal-expansion coefficients, α_a and α_c, obtained along the a- and c-axis, respectively, are shown in Figure 4.20, together with the temperature dependence of the volume expansion coefficient $\alpha_V = 2\alpha_a + \alpha_c$ (tetragonal structure).

The coefficients α_a and α_c are both positive and show a rapid increase with increasing temperature below 3 K. α_a varies approximately linearly with temperature for 3 K < T < 60 K and levels off at higher temperatures. α_c is much larger than α_a below 12 K, but $\alpha_c \approx \alpha_a$ above this temperature. The observed anisotropy in the thermal-expansion coefficients shows that when lowering the temperature below the coherence temperature, the c-axis shrinks more rapidly than the a-axis. The coefficient of the volume expansion shows, besides the heavy-fermion contribution, an unusual quasi-linear temperature dependence between 12 K and 60 K.

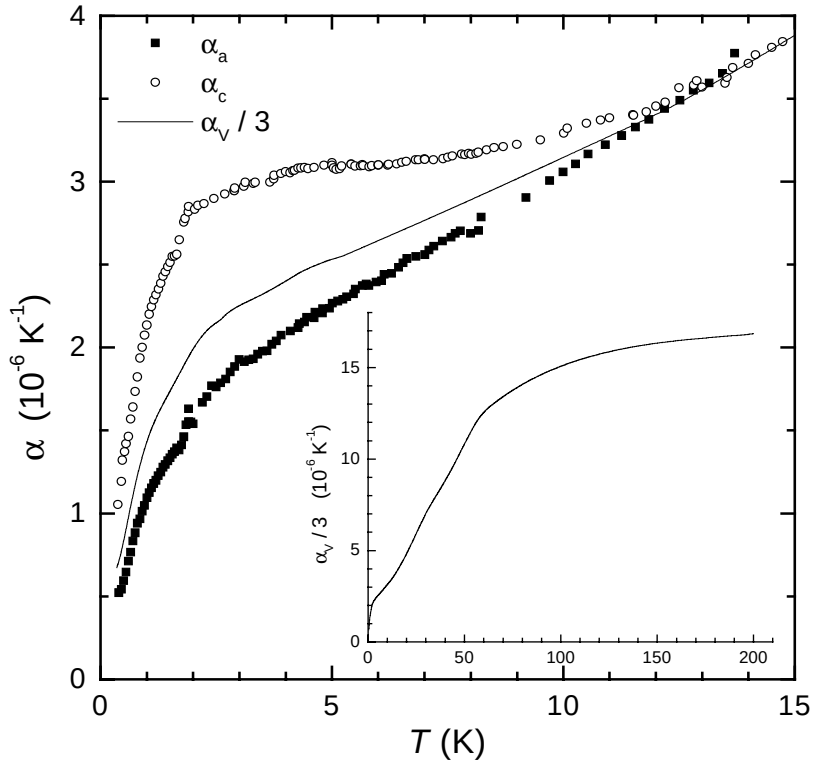

Figure 4.20 - Low-temperature ($T \leq 15$ K) linear thermal-expansion coefficient of U_2Pt_2In along the a- and c-axis. The line corresponds to 1/3 of the derived coefficient of the volume expansion. Insert: $\alpha_V/3$ ($T \leq 200$ K).

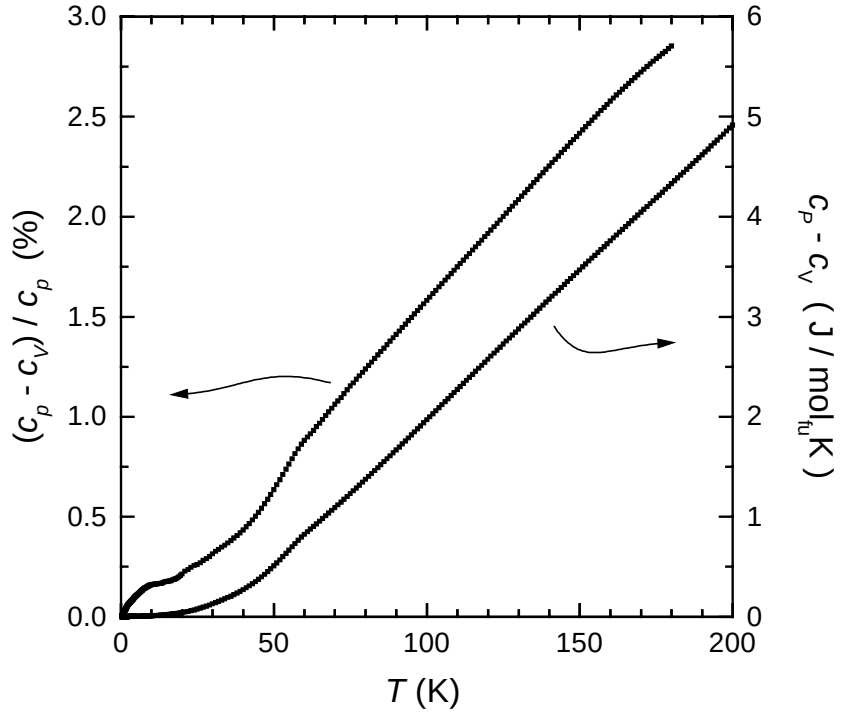

Figure 4.21 - Difference between the specific heats of U_2Pt_2In at constant pressure and volume.

The thermal-expansion data can be used to estimate the specific heat at constant volume. The difference between c_V and c_p can be expressed as

$$c_V - c_P = -\frac{9\alpha^2 V_m T}{\kappa} \quad . \tag{4.18}$$

Using the compressibility value of $\kappa = 0.68$ Mbar^{-1} (see Section 6.1), the difference c_p-c_V shown in Figure 4.21 is obtained. The relative value $(c_p\text{-}c_V)/c_p$ is limited to 3% up to 200 K. Therefore, the specific-heat data presented in the previous section do not need to be corrected for the difference between c_p and c_V.

The thermal expansion can be related to the specific heat by means of a Grüneisen parameter. A physically meaningful Grüneisen parameter emerges when part of the entropy can be written as $S_i(T/T_i)$ where T_i is a (volume dependent) characteristic temperature of the entropy term. The Grüneisen parameter is defined as [41]

$$\Gamma_i = \frac{V\left(\frac{\partial S_i}{\partial V}\right)_T}{T\left(\frac{\partial S_i}{\partial T}\right)_V} = -\frac{\partial \ln T_i(V)}{\partial \ln V} \quad . \tag{4.19}$$

Taking into account the relations

$$\alpha_V = \frac{1}{V}\left(\frac{\partial V}{\partial T}\right)_P = \kappa\left(\frac{\partial S_i}{\partial V}\right)_T \tag{4.20a}$$

and

$$c_V = T\left(\frac{\partial S_i}{\partial T}\right)_V \quad , \tag{4.20b}$$

where κ is the isothermal compressibility

$$\kappa = -\frac{1}{V}\left(\frac{\partial V}{\partial P}\right)_T \quad , \tag{4.20c}$$

one obtains

$$\Gamma = \frac{\alpha_V V}{\kappa c_V} \quad . \tag{4.21}$$

It is useful to define an effective temperature-dependent Grüneisen parameter

$$\Gamma_{eff}(T) = \frac{\alpha_V(T) V_m}{\kappa c(T)} \quad , \tag{4.22}$$

where V_m is the molar volume ($V_m = 6.568\times 10^{-5}$ m^3/mol$_{fu}$ for U_2Pt_2In). The temperature dependencies of V_m and κ are usually small and can be neglected.

In general, if the effective Grüneisen parameter is constant in a certain temperature interval, one can identify Γ_{eff} with the Grüneisen parameter for the particular mechanism that governs the thermal properties in that temperature range [41,42].

The temperature dependence of the effective Grüneisen parameter of U_2Pt_2In is shown in Figure 4.22. At high temperatures, the Grüneisen parameter amounts to $\Gamma_{ph} = 3.1$. This value can be compared to the value of 2 normally found for the phonon contribution in metals. Γ_{eff} increases smoothly as the temperature is decreased down to about 40 K, below which a fast increase occurs, reflecting the heavy-fermion character of U_2Pt_2In. At the lowest temperature of 0.35 K, $\Gamma_{eff} = 56$. Similar values have been observed in other heavy-fermion compounds [43]. The small anomaly near 0.5 K is not significant, as it is an artefact of the experiment. The continuous increase of $\Gamma_{eff}(T)$ at low temperatures hampers the extraction of the bare NFL form from the thermal-expansion data.

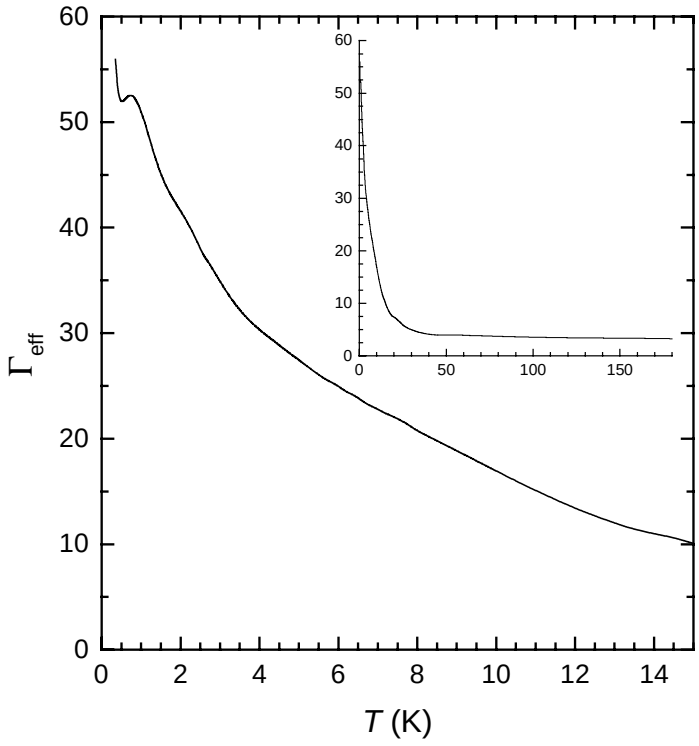

Figure 4.22 - Low-temperature ($T \leq 15$ K) dependence of the effective Grüneisen parameter of U_2Pt_2In. Insert: Γ_{eff} at temperatures up to 180 K.

4.3. Discussion

4.3.1. Hybridization phenomena and evidence for NFL behaviour

The inter-uranium distances in U_2Pt_2In, shown in Table 4.1, are slightly above the Hill limit (~ 3.5 Å) for uranium [44]. From this, one may conjecture that U_2Pt_2In would order magnetically, as it is located on the magnetic side in the Hill plot. However, in the past decade it has become clear that the electronic structure in many U compounds is governed by the 5*f* - *d*-ligand overlap and that the Hill-limit picture is too simple.

If the magnetic ordering temperatures of the In and Sn 2:2:1 compounds are plotted versus the square of the calculated hybridization matrix elements, a Doniach-like phase diagram results (Section 4.1.2 and Ref. [45]). Interestingly, U_2Pt_2In is close to the border line between magnetic and non-magnetic compounds.

The participation of 5*f*-electrons in the bonding in light-actinide intermetallics, leads to a compression of the 5*f* charge densities towards the bonding directions, which are given primarily by the shortest inter-actinide directions [46]. In the UTX (1:1:1) family, it was found as an empirical rule that the magnetic moment is always directed perpendicular to the shortest U-U direction. However, exceptions for this rule have been found in the 2:2:1 family. In U_2Rh_2Sn [47] the shortest U-U distance is located along the c-axis and yet the U moments are aligned along the c-axis. In the case of U_2Pt_2In, the shortest U-U distance is located in the tetragonal plane. The susceptibility data show that antiferromagnetic correlations (of the Ising type) are found along the c-axis. This complies with the shortest U-U distance rule, as reported for the 1:1:1 compounds.

The analysis of the resistivity leads to a description with a low-temperature term T^{α} (T–0 K), with $\alpha = 1.2$ and 0.9 for the a- and c-axis, respectively. The absence of the usual Fermi-liquid T^2 term gives strong support for non-Fermi liquid behaviour in U_2Pt_2In. The specific-heat measurements on a single crystal down to 0.1 K show a clear logarithmic divergency of c/T below 6 K, i.e. over almost two decades of temperature. This puts the NFL behaviour in U_2Pt_2In on firm footing.

Neutron-diffraction studies carried out on single-crystalline U_2Pt_2In [30] confirmed that the crystallographic structure is of the Zr_3Al_2-type. The structure refinement showed a perfect stoichiometry in the sense that no significant improvements in the final refinement factor could be achieved by allowing the occupational parameters to vary (including possibilities of atomic disorder like, e.g., Pt-In site inversion). At 1.5 K, exhaustive scans along different reciprocal lattice lines revealed no evidence of any long- or short-range magnetic ordering.

Polarized neutron-diffraction experiments carried out on the same U_2Pt_2In single crystal [30] probed the local susceptibility at the two U sites: U(4f) and U(4g). The observed magnetization density in the unit cell, constructed using the maximum entropy method, is reproduced in Figure 4.23 for $T = 10$ K and $B = 4.6$ T applied along the [101] direction. The site susceptibility of the U atoms at the 4f positions is almost twice that of U(4g).

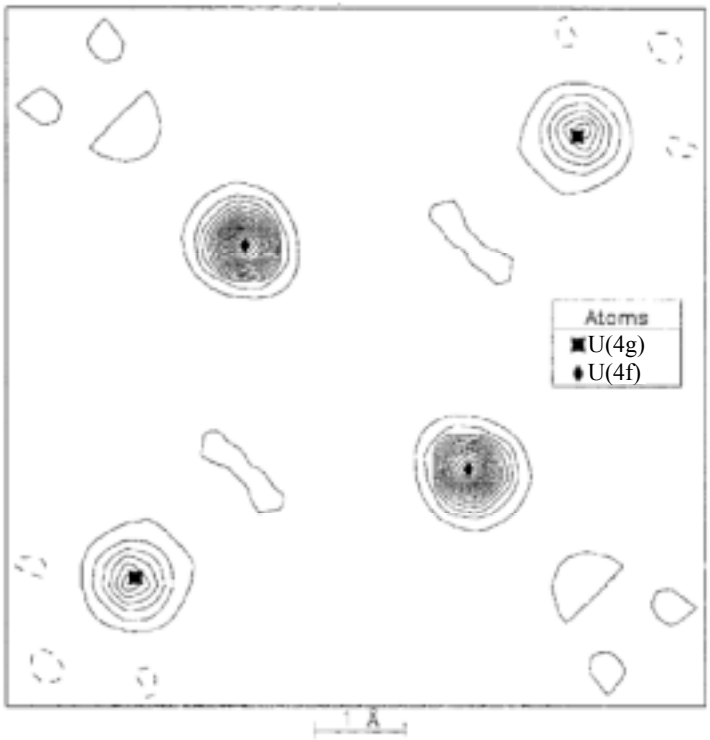

Figure 4.23 - Magnetization density ((001) projection) induced at 10 K by a field of 4.6 T in the [101] direction of U_2Pt_2In. Contour levels are from -0.01 (dashed) to 0.41 in steps of 0.02 $\mu_B/Å^3$. Taken from Ref. 30.

Considering the average (room temperature) interatomic distances for the two U sites (Table 4.1), the hybridization on the U(4f) and U(4g) atoms can be calculated separately in the same way as described in Section 4.1.2. The *p*-, *d*- and *f*- hybridizations at the two sites and the total conduction-electron - *f*-electron hybridization are shown in Table 4.8. As can be seen, the

hybridization is smaller for the U(4f) atoms than for the U(4g). Within the Doniach phase diagram (T_N versus V_{cf}^2) presented before, one may conjecture that the hybridization on the 4f sites "pushes" U_2Pt_2In towards magnetic order in a stronger way than the hybridization at the 4g sites. Therefore, a stronger site susceptibility may be found at the 4f sites.

Table 4.8 - *p*-, *d*-, *f*- and total hybridization at the two U sites in U_2Pt_2In.

	$V_{In\text{-}U}$ (eV)	$V_{Pt\text{-}U}$ (eV)	$V_{U\text{-}U}$ (eV)	$V_{c\text{-}U}$ (eV)
U(4f)	0.136	0.764	0.164	0.793
U(4g)	0.144	0.781	0.151	0.825

The ratio of the orbital and spin magnetic moments was also estimated and found to be approximately the same for the two sites, $|\mu_L/\mu_S| \approx 1.8$. This value corresponds to values frequently found for U ions in intermetallic compounds [48] and indicates an appreciable quenching of the orbital moment, when compared to the free-ion U^{3+} and U^{4+} configurations, due to hybridization processes.

The total moment measured at 10 K in a field of 4.6 T applied along the [101] direction was 0.139(9) μ_B/f.u.. This moment is about 24% lower than that found in the magnetization measurements (Section 4.2.1). Although the magnetization was not measured for fields applied along the [101] direction, a value of 0.182 μ_B/f.u. at 4.6 T can be estimated by considering $M_{[101]} \approx M_c\cos^2\phi + M_a\sin^2\phi$, where ϕ is the angle between the [101] and the **c** direction. The neutron experiments are only sensitive to the magnetization associated with the localized 5*f*-states, which is normally larger than that obtained by bulk measurements. The difference is attributed to a negative conduction-electron polarization [49]. Thus, the positive discrepancy in the case of U_2Pt_2In is unusual and at least two possibilities exist for this additional conduction-electron polarization: it can arise from either the Pt 5*d*-electrons or a fraction of the U 5*f*-states that is delocalized [30]. A positive conduction-electron polarization has also been found in the heavy-fermion superconductor UPd_2Al_3 [50].

4.3.2. Single-ion scaling and the two-channel Kondo model

Irrespective of the microscopic mechanism responsible for the NFL behaviour in U_2Pt_2In, it is of interest to investigate single-ion Kondo scaling of the NFL properties. Within the two-

channel Kondo effect (TCKE - see Section 2.3), the specific heat can be expressed as $c/T = B'-(A'/T_K)\ln(T/bT_K)$ [51]. Using the values $A' = 0.251R$ and $b = 0.41$ from the TCKE, one obtains $T_K = 23.2$ K and $B' = 204.3$ mJ/mol$_U$K^2. This value of T_K is close to the Kondo temperature $16 < T_K < 21$ K, which can be deduced from the susceptibility data, assuming that the paramagnetic Curie temperature θ is 3-4 times larger than T_K [52]. The value of B' is however extremely high, since it should account for a temperature independent electronic or crystal-field background in c/T.

This value of T_K in U_2Pt_2In is also consistent with the one extracted from thermoelectric-power data taken on a single crystal [53]. In the temperature range 5-150 K, the thermopower is negative with a minimum at $T_{min} \approx 25$ K. Similar minima were reported for several other heavy-fermion compounds exhibiting spin-fluctuation phenomena, with $T_{min} \sim T_K$ [54].

With the value of T_K, the coefficient a of the power law in the resistivity, $\rho/\rho_0 = 1 + a\,(T/T_K)^{\alpha}$, can be calculated: $a_a = 2.89$ and $a_c = 0.71$ for $\alpha_a = 1.2$ and $\alpha_c = 0.9$, respectively.

The unusual low-temperature susceptibility data yield further support for NFL behaviour. The theoretical expressions for the magnetic susceptibility of a NFL compound are $\chi \sim -\ln(T/T_0)$ or $\chi \sim 1-bT^{\beta}$ ($\beta < 1$), depending on the type of system (see Section 2.3). In U_2Pt_2In, $\chi_c(T)$ is dominated by antiferromagnetic correlations below 10 K, therefore, no low-temperature analysis can be done confidently. However, $\chi_a(T)$ continues to rise, at least down to 2 K. Analysing χ_a ($T < 10$ K) with a term $\chi_a \sim 1 - b'\,(T/T_K)^{\beta}$ one finds $\beta = 0.7$ and $b' = 0.25$, but the limited temperature range where this behaviour occurs does not allow for a reliable estimate of the exponent β.

The results of the scaling analysis within single-ion Kondo models are summarized in Table 4.9. The reduced values of the parameters should be considered as rough estimates since the data were not corrected for the phononic contributions. The high value of B' indicates that the specific heat can not be fully described by the TCKE expression. Furthermore, single-ion models are normally applied in diluted systems where small amounts of an *f*-element are used to partially replace a non-magnetic rare earth or actinide element (e.g. systems like $Y_{1-x}U_xPd_3$ and $Th_{1-x}U_xPd_2Al_3$ [51,55]), while U_2Pt_2In should be considered as a Kondo-lattice system. A clear indication that the TCKE does not apply to U_2Pt_2In is that the entropy does not saturate at the value ½ Rln2 as expected for this model. Nevertheless, the observed scaling of the low temperature properties shows that the Kondo temperature, being a characteristic temperature of

the heavy-fermion character of U_2Pt_2In, can also be taken as a characteristic temperature of its non-Fermi liquid behaviour.

Table 4.9 - Parameters from single-ion scaling of some low-temperature properties of U_2Pt_2In.

	a-axis	c-axis
$c/T = -(A'/T_K)\ln(T/bT_K) + B'$	$T_K = 23$ K $B' = 0.20$ J/mol$_U$K^2	
$\rho = \rho_0 [1 + a (T/T_K)^{\alpha}]$	$\alpha = 1.2$ $\rho_0 \approx 115$ μΩcm $a = 2.89$	$\alpha \approx 0.9$ $\rho_0 \approx 210$ μΩcm $a = 0.71$
$\chi = \chi(T=0) [1 - b' (T/T_K)^{\beta}]$	$\beta = 0.7$ $\chi(0) \approx 14\times10^{-8}$ m^3/mol$_U$ $b' = 0.25$	-

4.3.3. Kondo disorder

An alternative mechanism which can lead to NFL behaviour is the Kondo disorder model [56], where the Kondo effect on each *f*-electron atom sets a different temperature scale, resulting in a broad range of effective Kondo temperatures. One should note that the residual resistivity values of the U_2Pt_2In single-crystals are large. $\rho_{0,a}$ and $\rho_{0,c}$ equal 110 and 200 μΩcm, respectively, which indicates that disorder is present in the crystals. The origin of this disorder remains unclear. The single-crystal X-ray and neutron-diffraction structure refinement with final agreement factors of 4.3% and 2.6% respectively, are considered to indicate a high crystalline quality. A small percentage of site inversion (Pt and In inversion) seems also to be excluded by the neutron-diffraction structure refinement. It is also possible that the disorder is somehow related to the polymorphism of U_2Pt_2In and the presence of two U sites with different magnetic susceptibilities.

Specific-heat measurements performed on a polycrystalline sample in the temperature range 0.3 K < *T* < 5 K yield the same logarithmic divergency as measured on the single crystals. This shows that the NFL behaviour is found for the U_3Si_2-type of structure (polycrystals) as well as for the Zr_3Al_2-type of structure (single crystals). Therefore, the NFL behaviour in U_2Pt_2In is not related to the presence of two different crystallographic U sites and the difference in U site susceptibility is not a main ingredient in the origin of the NFL behaviour.

On the other hand, it is clear that the ρ_0 values found do not reflect bare residual resistivities. This may be concluded from the following: i) there is a strong current-orientation dependence of the values of ρ_0, with $\rho_{0,a} = 0.56\rho_{0,c}$ at zero field, which cannot simply be attributed to impurity or defect scattering; ii) both $\rho_{0,a}$ and $\rho_{0,c}$ vary in field, which indicates that at least part of ρ_0 is caused by scattering mechanisms other than scattering at crystallographic defects.

4.3.4. Magnetic critical point

An appealing scenario for the origin of the non-Fermi liquid behaviour in U_2Pt_2In is the proximity to a quantum critical point [57]. This is reflected in the location of U_2Pt_2In at the border line between magnetic and non-magnetic compounds in a Doniach-type of diagram for the U_2T_2X series (X = In, Sn). Tuning the quantum critical point with an external parameter, e.g. a magnetic field or (chemical) pressure, should elucidate the applicability of this scenario. Magnetoresistance measurements show a tendency towards a $\rho \sim T^2$ law as the field strength increases, suggesting that the magnetic field shifts U_2Pt_2In away from the quantum critical point towards a Fermi-liquid regime. Specific-heat measurements in field were inconclusive in this respect due to the presence of an important contribution from the In nuclear moments.

The proximity of U_2Pt_2In to a quantum critical point is best probed with pressure experiments and chemical substitutions. Usually, compounds located at a magnetic instability are tuned towards the Fermi-liquid regime by applying pressure since a reduction of the interatomic distances results in an increase of the hybridization. On the other hand, chemical substitution of U by a larger non-magnetic element like Th should have the opposite effect. Resistivity measurements under pressure were carried out on U_2Pt_2In up to $p = 1.8$ GPa and will be presented in Section 6.1, while some preliminary results of studies on Th-doped U_2Pt_2In will be presented in Section 6.2.

The absence of static magnetism in U_2Pt_2In has been confirmed by detailed muon spin relaxation and rotation (μSR) experiments, which will be presented in Chapter 5. As discussed in Chapter 3, the μSR technique is a very powerful probe as it enables the detection of tiny ordered moments (which might be overlooked by other techniques). The μSR technique may also be used to investigate whether Kondo disorder is the origin of non-Fermi liquid behaviour.

References

1. M.N. Péron, Y. Kergadallan, J. Rebizant, D. Meyer, J.M. Winand, S. Zwirner, L. Havela, H. Nakotte, J.C. Spirlet, G.M. Kalvius, E. Colineau, J.L. Oddou, C. Jeandey and J.P. Sanchez, J. Alloys Compounds 201 (1993) 203.
2. L. Havela, V. Sechovský, P. Svoboda, M. Diviš, H. Nakotte, K. Prokeš, F.R. de Boer, A. Purwanto, R.A. Robinson, A. Seret, J.M. Winand, J. Rebizant, J.C. Spirlet, M. Richter and H. Eschrig, J. Appl. Phys. 76 (1994) 6214.
3. H. Nakotte, Ph.D. Thesis, University of Amsterdam, 1994 (unpublished).
4. L.C.J. Pereira, Ph.D. Thesis, University of Lisbon, 1998 (unpublished).
5. F. Mirambet, P. Gravereau, B. Chevalier, L. Trut and J. Etourneau, J. Alloys Compounds 203 (1993) 29.
6. P. Gravereau, F. Mirambet, B. Chevalier, F. Weill, L. Fournès, D. Laffargue, F. Bourée and J. Etourneau, J. Mater. Chem. 4 (1994) 1893.
7. L.C.J. Pereira, F. Wastin, J.M. Winand, B. Kanellakopoulos, J. Rebizant, J.C. Spirlet and M. Almeida, J. Solid State Chem. 134 (1997) 138.
8. R.A. Gordon, Y. Ijiri, C.M. Spencer and F.J. DiSalvo, J. Alloys Compounds 224 (1995) 101.
9. B. Chevalier, F. Fourgeot, D. Laffargue, P. Gravereau, L. Fournès and J. Etourneau, J. Alloys Compounds 262-263 (1997) 114.
10. P. Estrela, L.C.J. Pereira, A. de Visser, F.R. de Boer, M. Almeida, M. Godinho, J. Rebizant and J.C. Spirlet, J. Phys.: Condens. Matter 10 (1998) 9465.
11. V. Sechovský and L. Havela, in "Handbook of Magnetic Materials" vol. 11 (K.H.J. Buschow, ed.), Elsevier, Amsterdam, 1998, p. 1.
12. M. Diviš, M. Richter and H. Eschrig, Solid State Commun. 90 (1994) 99.
13. M. Diviš, M. Olšovec, M. Richter and H. Eschrig, J. Magn. Magn. Mater. 140-144 (1995) 1365.
14. K. Prokeš, E. Brück, H. Nakotte, P.F. de Châtel and F.R. de Boer, Physica B 206-207 (1995) 8.
15. S.F. Matar, J. Magn. Magn. Mater. 151 (1995) 263.
16. F.R. de Boer, K. Kindo, H. Nakotte, K. Prokeš and V. Sechovský, Physica B 246-247 (1998) 129.
17. H. Nakotte, K. Prokeš, E. Brück, N. Tang, F.R. de Boer, P. Svoboda, V. Sechovský, L. Havela, J.M. Winand, A. Seret, J. Rebizant and J.C. Spirlet, Physica B 201 (1994) 247.
18. T. Fukushima, S. Matsuyama, T. Kumada, K. Kindo, K. Prokeš, H. Nakotte, F.R. de Boer, L. Havela, V. Sechovský, J.M. Winand, J. Rebizant and J.C. Spirlet, Physica B 211 (1995) 142.
19. E.H. Brück, Ph.D. Thesis, University of Amsterdam, 1991 (unpublished).
20. T. Endstra, G.J. Nieuwenhuys and J.A. Mydosh, Phys. Rev. B 48 (1993) 9595.
21. W.A. Harrison, Phys. Rev. B 28 (1983) 550.
22. J.M. Wills and W.A. Harrison, Phys. Rev. B 28 (1983) 4363.
23. W.A. Harrison and G.K. Straub, Phys. Rev. B 36 (1987) 2695.

24. G.K. Straub and W.A. Harrison, Phys. Rev. B 31 (1985) 7668.
25. J.R. Schrieffer and P.A. Wolff, Phys. Rev. 149 (1966) 491.
26. B. Coqblin and J.R. Schrieffer, Phys. Rev. 185 (1969) 847.
27. A.M. Strydom and P. de V. du Plessis, Physica B 230-232 (1997) 62.
28. M.T. Béal-Monod and J.M. Lawrence, Phys. Rev. B 21 (1980) 5400.
29. J.M. Lawrence, P.S. Riseborough and R.D. Parks, Rep. Prog. Phys. 44 (1981) 1.
30. A. Martin-Martin, L.C.J. Pereira, G.H. Lander, J. Rebizant, F. Wastin, J.C. Spirlet, P. Dervenagas and P.J. Brown, Phys. Rev. B 59 (1999) 11818.
31. A. Rosch, preprint (cond-mat/9910432).
32. P.G. De Gennes and J. Friedel, J. Phys. Chem. Solids 4 (1958) 71.
33. P. Debye, Ann. Physik 39 (1912) 789.
34. J.K. Roberts, "Heat and Thermodynamics", Blackie & Son Ltd, London, 1940, p. 425.
35. O.V. Lounasmaa, in "Hyperfine Interactions" (A.J. Freeman and R.B. Frankel, eds.), Academic Press, New York, 1967, p. 467.
36. N.E. Phillips, Critical Reviews in Solid State Sciences 2 (1971) 467.
37. B. Bleaney and R.W. Hill, Proc. Phys. Soc. 78 (1961) 313.
38. S.G. Mishra and P.A. Sreeram, Eur. Phys. J. B 14 (2000) 287.
39. H.R. O'Neal and N.E. Phillips, Phys. Rev. 137 (1965) A748.
40. G.C. Carter, L.H. Bennett and D.J. Hahon, Progr. Mater. Sci. 20 (1975) 1.
41. P.E. Brommer, Physica B 112 (1982) 343.
42. A. de Visser, A. Lacerda, P. Haen, J. Flouquet, F.E. Kayzel and J.J.M. Franse, Phys. Rev. B 39 (1989) 11301.
43. A. de Visser, J.J.M. Franse, A. Lacerda, P. Haen and J. Flouquet, Physica B 163 (1990) 49.
44. H.H. Hill, in "Plutonium and Other Actinides" (W.N. Miner, ed.), AIME, New York, 1970, p. 2.
45. V.H. Tran, Z. Zolnierek, A.J. Zaleski and H. Noël, Solid State Commun. 101 (1997) 709.
46. V. Sechovský, L. Havela, H. Nakotte, F.R. de Boer and E. Brück, J. Alloys Compounds 207-208 (1994) 221.
47. L.C.J. Pereira, J.A. Paixão, P. Estrela, M. Godinho, F. Boudarot, M. Bonnet, J. Rebizant, J.C. Spirlet and M. Almeida, J. Phys.: Condens. Matter 8 (1996) 11167.
48. G.H. Lander, in "Handbook on the Physics and Chemistry of the Rare Earths" vol. 17 (K.A. Gschneidner Jr., L. Eyring, G.H. Lander and G.R. Choppin, eds.), Elsevier, Amsterdam, 1993, p. 635.
49. F.A. Wedgwood, J. Phys. C 5 (1972) 2427.
50. L. Paolasini, J.A. Paixão, G.H. Lander, A. Delapalme, N. Sato and T. Komatsubura, J. Phys.: Condens. Matter 5 (1993) 8905.
51. M.B. Maple, M.C. de Andrade, J. Herrmann, Y. Dalichaouch, D.A. Gajewski, C.L. Seaman, R. Chau, R. Movshovich, M.C. Aronson and R. Osborn, J. Low Temp. Phys. 99 (1995) 223.
52. N.B. Brandt and V.V. Moshchalkov, Adv. Phys. 33 (1984) 373.

53. L.C.J. Pereira, M. Almeida, P. Estrela, M. Godinho, J. Rebizant, J.C. Spirlet, R.P. Pinto, M.M. Amado, M.E. Braga and J.B. Sousa, J. Magn. Magn. Mater. 196-197 (1999) 885.
54. N. Grewe and F. Steglich, in "Handbook on the Physics and Chemistry of the Rare Earths" vol. 14 (K.A. Gschneidner Jr. and L. Eyring, eds.), Elsevier, Amsterdam, 1991, p. 343.
55. M.B. Maple, R.P. Dickey, J. Herrmann, M.C. de Andrade, E.J. Freeman, D.A. Gajewski and R. Chau, J. Phys.: Condens. Matter 8 (1996) 9773.
56. E. Miranda, V. Dobrosavljević and G. Kotliar, J. Phys.: Condens. Matter 8 (1996) 9871.
57. A.J. Millis, Phys. Rev. B 48 (1993) 7183.

5. Muon spin relaxation and rotation in U_2Pt_2In

The main purpose of using the μSR technique in the study of non-Fermi liquid compounds is to demonstrate the absence of static magnetism with tiny ordered moments. This weak magnetism is commonly observed in heavy-fermion compounds, and might be overlooked by macroscopic magnetic, thermal and transport techniques. Also, because the muon is an extremely sensitive magnetic probe, important information about magnetic fluctuations can easily be extracted from the data. In this chapter, results of zero-, longitudinal- and transverse-field μSR experiments carried out on single-crystalline U_2Pt_2In are presented. The experiments were performed at the GPS and LTF spectrometers of the Paul Scherrer Institute (Switzerland). For a brief description of the μSR technique and the relevant theoretical aspects see Section 3.6.

5.1. Zero field

Zero-field (ZF) μSR experiments were performed in the temperature range 0.05-200 K. The spectra obtained give no evidence of magnetic order down to the lowest temperatures. Best fits to the muon relaxation curves, as measured in the GPS, were obtained using a two-component function, consisting of an exponential and a Gaussian term (Figure 5.1):

$$P(t) = A_E P_E(t) + A_G P_G(t) = A_E \exp(-\lambda_E t) + A_G \exp\left(-(\Delta_G t)^2/2\right) \quad . \qquad (5.1)$$

In this nomenclature, A_i is the amplitude of the component i with the normalization $A_E+A_G = 1$. Notice that in this case the sample was mounted with mylar foil on a fork-like holder, such that the contribution from the sample holder can be neglected. For the measurements in the LTF, the sample was mounted on a silver plate. Since the dimensions of the sample are smaller than the muon-beam window, an extra nuclear contribution of the Kubo-Toyabe type arises from the silver plate. This Kubo-Toyabe term has a temperature-independent amplitude $A_{KG} = 0.76$ (with $A_E+A_G+A_{KG} = 1$) and a depolarization rate $\Delta_{KG} \sim 0.01\ \mu s^{-1}$.

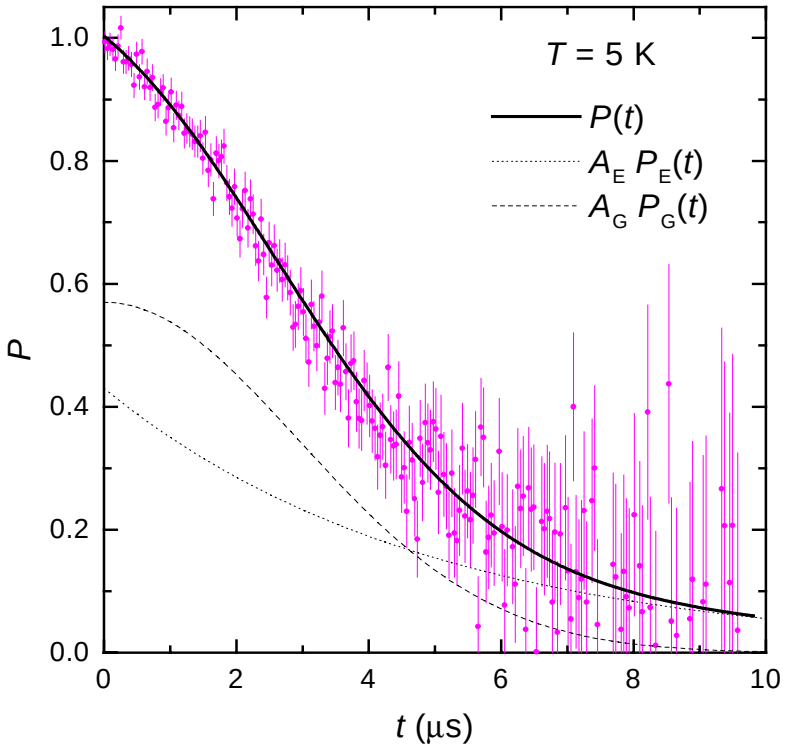

Figure 5.1 - Depolarization spectrum of U_2Pt_2In at 5 K. The solid line is the total depolarization function and the dashed and dotted lines represent the exponential and Gaussian components, respectively.

In Figure 5.2, the depolarization rate of the exponential component is shown. λ_E is almost constant above 7.5 K, while it increases strongly below this temperature. Notice that the susceptibility of U_2Pt_2In goes through a maximum at $T_{max} = 8$ K, which indicates the presence of short-range antiferromagnetic correlations. Therefore, the strong increase of λ_E may very well be related to the stabilization of antiferromagnetic correlations. For the Gaussian component, on the other hand, $\Delta_G \sim 0.34\ \mu s^{-1}$, independent of temperature. This temperature-independent behaviour suggests that the Gaussian component is associated with a random distribution of nuclear

moments. The dominant nuclear contribution comes from the In nuclei, with spin 9/2 and magnetic moment 5.5 μ_N. The contribution of the Pt nuclei (I = 1/2, $\mu \sim 0.6\ \mu_N$, 34% abundancy) is much smaller.

$A_E(T)/[A_E(T)+A_G(T)]$ has approximately the same form as $\lambda_E(T)$ with values ranging from 0.2 at high temperatures to about 0.8 at 0.05 K. If each of the two components is associated with a different muon-stopping site (μ-s.s.), the amplitude ratio should be temperature independent as it depends only on the crystallographic multiplicity of the μ-s.s.. The observed temperature dependence of the amplitude ratio indicates that the two components represent two magnetic contributions to the ZF-μSR signal, originating from *one or more* stopping sites.

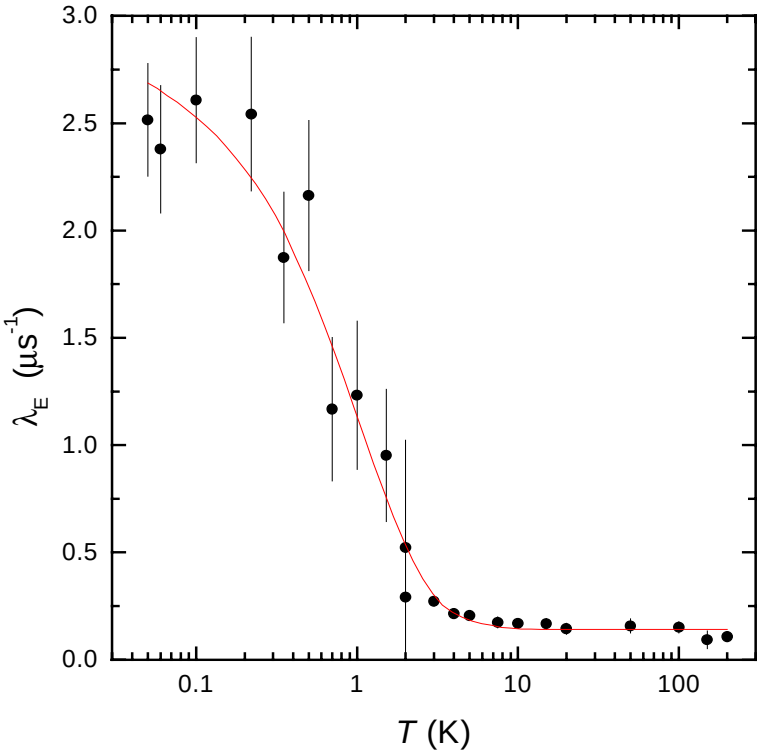

Figure 5.2 - Temperature dependence of the depolarization rate of the exponential contribution to the ZF-μSR signal in U_2Pt_2In. Notice the logarithmic T scale. The line is a guide to the eye.

The observed value of Δ_G can be compared with the calculated one for a random distribution of In nuclear moments. A distribution of randomly oriented nuclear moments will produce a depolarization rate (Kubo-Toyabe depolarization rate) given by [1]

$$\Delta_{KT}^2 = \tfrac{1}{6} I(I+1)\left(\frac{\mu_0}{4\pi}\gamma_\mu \gamma_N\right)^2 \sum_i \frac{5-3\cos^2\theta_i}{r_i^6} \quad , \qquad (5.2)$$

where μ_0 is the vacuum permeability and γ_N the gyromagnetic ratio of the nuclei with spin I. $\boldsymbol{r}_i$ is the vector connecting the muon site and the nucleus *i*, while θ_i is the angle defined by $\boldsymbol{r}_i$ and the initial muon polarization $\boldsymbol{P}_\mu(0)$.

Since the μ-s.s. are not known, Δ_{KT} is calculated for different possible sites. In U_2Pt_2In several interstitial positions with high symmetry are unoccupied. These are the best candidates for stopping sites. The crystallographic sites and their coordinates for the $P4_2/mnm$ space group are listed in Table 5.1. The sites with the highest symmetries are shown in Figure 5.3.

Table 5.1 - Crystallographic positions and coordinates for the $P4_2/mnm$ space group (U_2Pt_2In).

2a (0,0,0)	2b (0,0,½)	4c (0,½,0)	4d (0,½,¼)	4e (0,0,z)	4f (x,x,0)	4g (x,-x,0)	8h (0,½,z)	8i (x,y,0)	8j (x,x,z)	16k (x,y,z)
-	-	-	**In**	-	**U** x=0.335	**U** x=0.180	-	-	**Pt** x=0.130 z=0.234	-

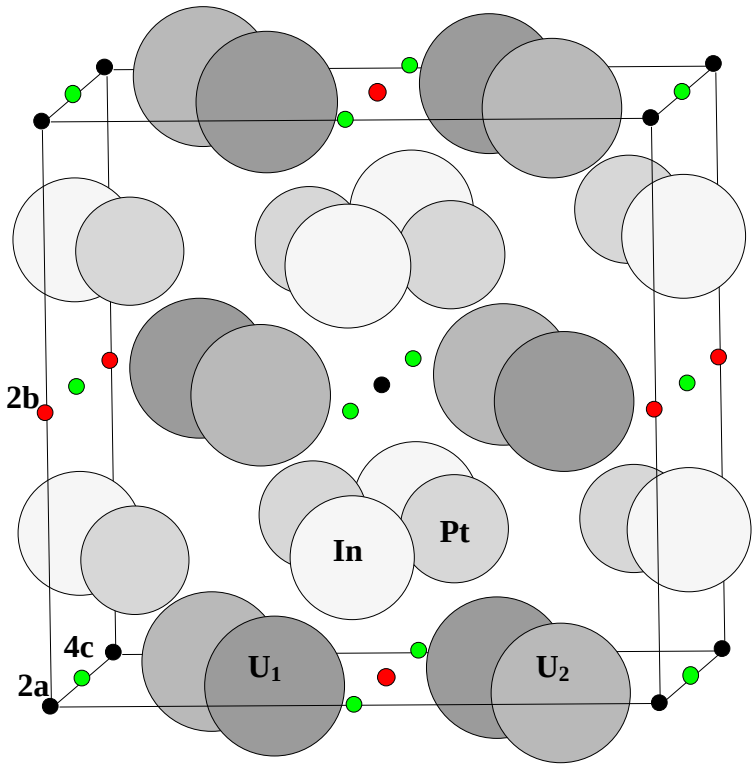

Figure 5.3 - Crystal structure of U_2Pt_2In with some interstitial sites with high symmetry indicated. Note: U_1 = U(4f), U_2 = U(4g).

The Kubo-Toyabe depolarization rate can be calculated by taking into the account the gyromagnetic ratio of the In nuclei (I_{In} =9/2, μ_{In} = 5.5408 μ_N): $\gamma_{In}/2\pi = \mu/hI$ = 9.3855 MHz/T.

Usually, Δ_{KT} is calculated by performing the sum in equation 5.2 inside a Lorentz sphere and approximating the sum outside the sphere by an integral [2]. Considering the symmetry of the In positions, Δ_{KT} can also be calculated by evaluating the sum inside a parallelepiped of dimensions $Na \times Na \times Nc$ centered at the possible muon stopping site. Since the sum is over r_i^{-6}, N does not need to be very large. In fact, the values of Δ_{KT} do not change more than 1×10^{-4} μs^{-1} when going from $N = 20$ to $N = 500$. Values of Δ_{KT} for some of the possible μ-s.s. calculated with $N = 50$ and $\boldsymbol{P}_\mu(0) \parallel \mathbf{c}$ are given in Table 5.2

Table 5.2 - Calculated Kubo-Toyabe depolarization rates at different interstitial positions due to a random distribution of In nuclear moments in U_2Pt_2In.

site		Δ_{KT} (μs^{-1})	
2a	(0,0,0)	0.09408	
2b	(0,0,½)	0.09408	
4c	(0,½,0)	0.35382	
4e	(0,0,z)	0.09408 (z→0)	≡ 2a
		0.13072 (z=¼)	
		0.09408 (z→½)	≡ 2b
4f	(x,x,0)	0.09408 (x→0)	≡ 2a
		0.16806 (x=0.17)	
4g	(x,-x,0)	0.16435 (x=0.34)	
		0.09408 (x→½)	≡ 2b
8h	(0,½,z)	0.35382 (z→0)	≡ 4c
		0.58754 (z=0.04)	

Considering the symmetry of the In positions, $\Delta_{KT}^{4e}(z_{4e}) = \Delta_{KT}^{4e}(½ - z_{4e})$ and only the positions with $z_{4e} \leq ¼$ need to be calculated. Due to the positioning of the In and U atoms, the following conditions can be imposed for the possible muon sites: $z_{8h} < ¼ - r_{In}/c$, $x_{4f} < x_{U(4f)} - r_U/(a\sqrt{2})$ and $x_{4g} > x_{U(4g)} - r_U/(a\sqrt{2})$, where r_{In} and r_U are the radii of the In and U atom, respectively. For $r_{In} = 1.55$ Å and $r_U = 1.75$ Å [3], it follows $z_{8h} < 0.04$, $x_{4f} < 0.17$ and $x_{4g} > 0.34$. The variation of Δ_{KT} with the x and z values of these positions is shown in Figure 5.4.

The value of the depolarization rate observed for the Gaussian component, $\Delta_G = 0.34$ μs^{-1}, indicates that the muon might stop at the 4c sites. However, the temperature dependence of $A_E/(A_E+A_G)$ indicates that the Gaussian component is not attributed to one stopping site but rather to an effective magnetic contribution to several μ-s.s.. This means that, besides at the 4c sites, the muons might also come to rest at a site with a lower Δ_{KT}. For two μ-s.s., the depolarization function can be written as the sum of e.g. two damped Gaussians:

$$P(t) = A_1 P_G(\Delta_1 t)\exp(-\lambda_1 t) + A_2 P_G(\Delta_2 t)\exp(-\lambda_2 t) \quad , \qquad (5.3)$$

where $P_G(\Delta_i t) = \exp(-(\Delta_i t)^2/2)$. Δ_1 and Δ_2 account for the In nuclear contribution from sites 1 and 2, respectively, while the amplitudes reflect the crystallographic multiplicity of the sites. At low temperatures, the two components are damped by magnetic fluctuations characterized by the rates λ_1 and λ_2. Approximating Equation 5.3 by Equation 5.1 implies that the extracted values of Δ_G and λ_E represent effective depolarization rates. This means that at least one μ-s.s. is a site with a high nuclear depolarization rate ($\Delta_{KT} \sim 0.35\ \mu s^{-1}$) but other sites with a lower Δ_{KT} might also be μ-s.s..

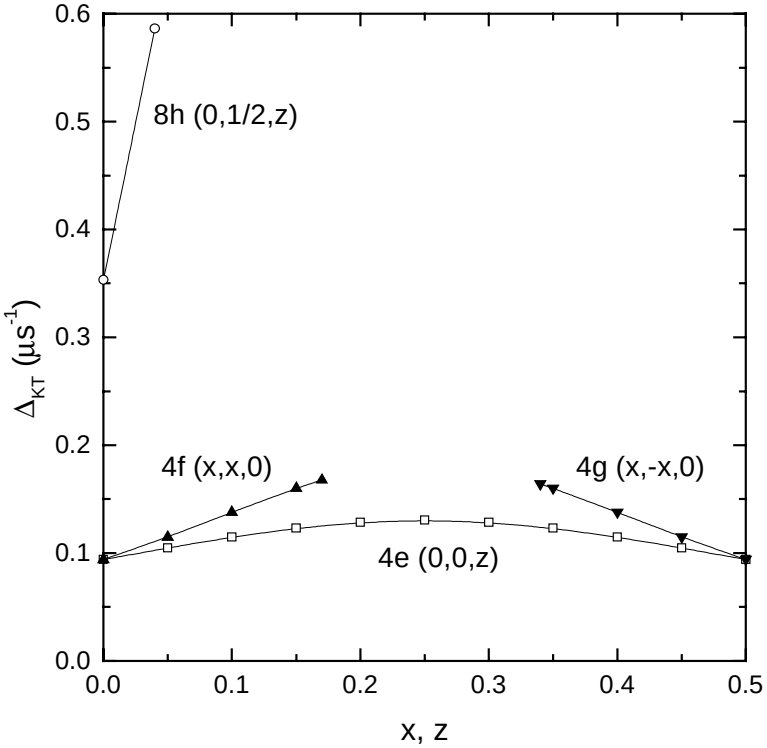

Figure 5.4 - Kubo-Toyabe depolarization rate calculated for the 4e (0,0,z), 4f (x,x,0), 4g (x,-x,0) and 8h (0,1/2,z) positions due to a random distribution of In nuclear moments in U_2Pt_2In.

5.2. Longitudinal field

In order to check the nature of the observed ZF signals, longitudinal-field (LF) experiments were carried out. In this configuration, an external field $\boldsymbol{B}_{ext}$ is applied along the initial muon-polarization direction. If a signal has a static origin, there will be a decoupling of the muon spin

from the static magnetic moments and the muon will be weakly depolarized. On the other hand, a signal with a dynamic origin will not be significantly changed as long as $\nu >> \gamma_\mu B_{ext}$, where ν is the fluctuation rate of the magnetic moments.

The field dependence of the depolarization rates of the observed exponential and Gaussian components is shown in Figure 5.5 for $T = 0.06$ K and $B_{ext} \leq 0.01$ T. λ_E maintains an almost constant value, while Δ_G drops drastically with increasing field. This indicates that the exponential signal has a dynamic origin and that the Gaussian component is static. This is in agreement with the conclusions reached in the previous section, namely that the exponential component is related to the magnetic fluctuations on the U sites, while the Gaussian component is related to the In nuclear moments.

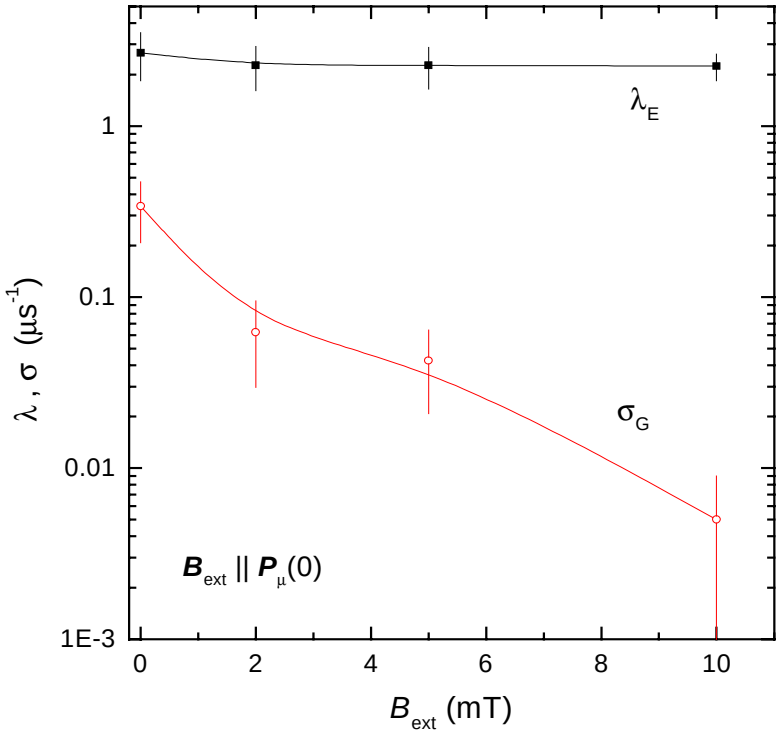

Figure 5.5 - Longitudinal-field dependence of the depolarization rates of the exponential (λ_E) and Gaussian (σ_G) components observed in ZF of U_2Pt_2In at $T = 0.06$ K. Notice the vertical logarithmic scale. The lines are guides to the eye.

5.3. Transverse field

Transverse-field (TF) experiments are useful for the determination of the μ-s.s.. Different stopping sites will have different local magnetic fields and therefore different muon-precession frequencies will be observed. Also the ratio of the amplitudes of the signals corresponds to the ratio of the multiplicity of the sites.

In a tetragonal system, the dipolar tensor is simply

$$\ddot{A}_{\mathrm{dip}} = \begin{pmatrix} A_{\mathrm{dip}}^{\mathrm{aa}} & 0 & 0 \\ 0 & A_{\mathrm{dip}}^{\mathrm{aa}} & 0 \\ 0 & 0 & A_{\mathrm{dip}}^{\mathrm{cc}} \end{pmatrix} . \qquad (5.4)$$

Since $\mathrm{Tr}(\ddot{A}_{\mathrm{dip}}) = 0$, $A_{\mathrm{dip}}^{\mathrm{aa}} = -\frac{1}{2} A_{\mathrm{dip}}^{\mathrm{cc}}$. Therefore, only measurements with $\boldsymbol{B}_{\mathrm{ext}} \parallel \mathbf{c}$ and $\boldsymbol{B}_{\mathrm{ext}} \parallel \mathbf{a}$ are required in order to determine the components of the tensor. The Knight shifts are given by

$$\begin{cases} K_{\mathrm{c}} = (A_{\mathrm{con}} + A_{\mathrm{dip}}^{\mathrm{cc}})\chi_{\mathrm{c}} \\ K_{\mathrm{a}} = (A_{\mathrm{con}} - \frac{1}{2} A_{\mathrm{dip}}^{\mathrm{cc}})\chi_{\mathrm{a}} \end{cases} , \qquad (5.5)$$

i.e. by plotting the Knight shifts versus the bulk susceptibilities, $K_{\mathrm{c}}(\chi_{\mathrm{c}})$ and $K_{\mathrm{a}}(\chi_{\mathrm{a}})$, the dipolar tensors at the μ-s.s. can be evaluated and compared with the ones calculated for the different interstitial crystallographic sites.

TF-μSR spectra were taken in a field of $B_{\mathrm{ext}} = 0.6$ T applied along the a- and c-axis in the temperature range 2-300 K. Typical fast Fourier transforms of the signals are shown in Figure 5.6. The asymmetric shape of the peak at low temperatures indicates that at least two frequencies are present. As the temperature increases the frequencies tend to "collapse".

Best fits to the data were obtained by using a two component depolarization function:

$$P(t) = A_1 \cos(\omega_1 t + \phi)\, \mathrm{e}^{-\lambda_1 t} + A_2 \cos(\omega_2 t + \phi)\, \mathrm{e}^{-\lambda_2 t} , \qquad (5.6)$$

where the phase ϕ is the angle between $\boldsymbol{P}_{\mu}(0)$ and the direction perpendicular to the detector. The best fits are obtained for $A_1 = A_2$, which means that the two stopping sites have the same multiplicity. The observed frequency shifts and line widths are shown in Figure 5.7a and Figure 5.8a, respectively. The Knight shift is calculated by

$$K_{\mathrm{a,c}} = \frac{\omega_{\mathrm{a,c}} - \omega_0}{\omega_0} - \left(\tfrac{1}{3} - N_{\mathrm{a,c}}\right) \frac{4\pi M_{\mathrm{a,c}}}{B_{\mathrm{ext}}} , \qquad (5.7)$$

where the magnetization $4\pi M$ has the same units as B_{ext} and $\omega_0 = \gamma_\mu B_{ext}$. The sample has an irregular shape which hampers an accurate estimate of the demagnetizing factors $N_{a,c}$. In Figure 5.7b, the Knight shift is shown in a plot of $K_{a,c}$ versus $\chi_{a,c}$ (Clogston-Jaccarino plot) where the approximate values $N_a \sim 0.3$ and $N_c \sim 0.6$ were used. Due to the small frequency shifts observed, small differences in $N_{a,c}$ change significantly the slopes of $K_a(\chi_a)$ and $K_c(\chi_c)$. The large error bars in Figure 5.7b result from an assumed uncertainty $\delta N = 0.1$. Since the dipolar tensor elements follow from the relation

$$A_{dip}^{cc} = \frac{2}{3}\left(\frac{dK_c}{d\chi_c} - \frac{dK_a}{d\chi_a}\right), \qquad (5.8)$$

it is obvious that they cannot be extracted reliably from the experimental data. Hence the muon stopping sites cannot be determined in this way.

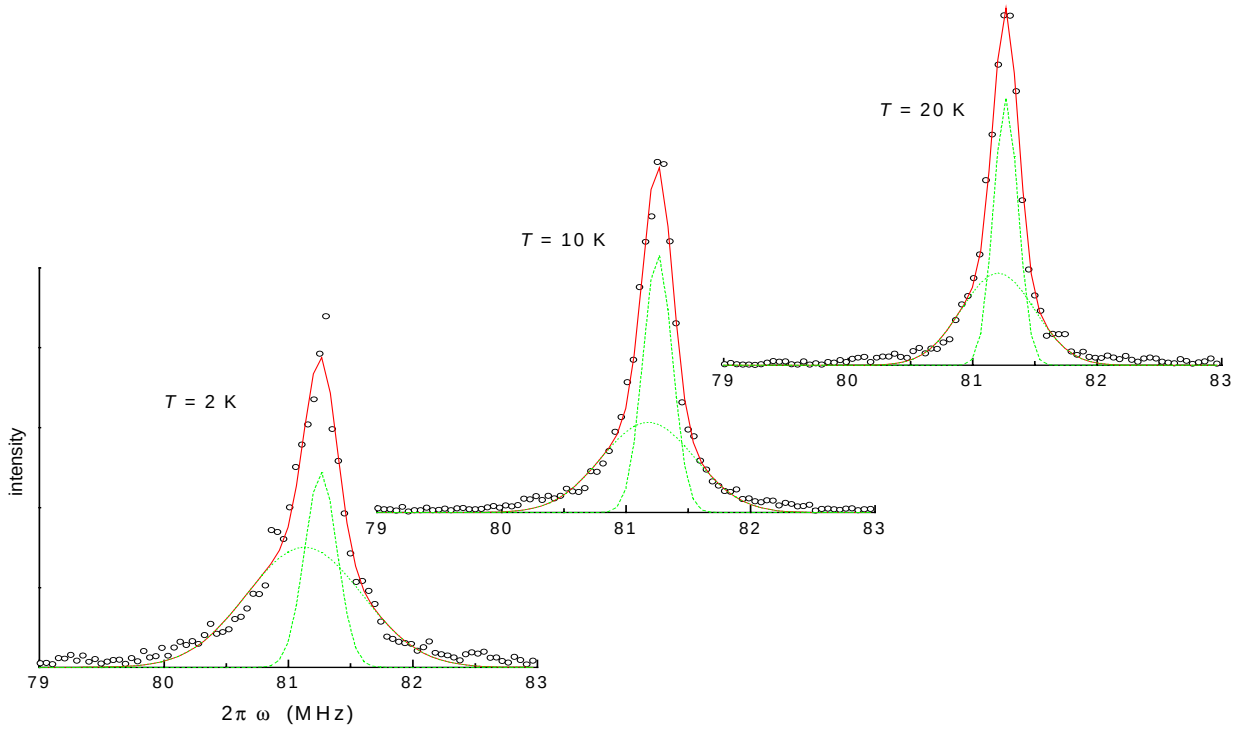

Figure 5.6 - Fast Fourier transforms of the TF-μSR signals at $T = 2$, 10 and 20 K with $B_{ext} = 0.6$ T and $\boldsymbol{B}_{ext} \parallel \mathbf{c}$ in U_2Pt_2In. The full lines are the sum of the two components represented by the dashed lines.

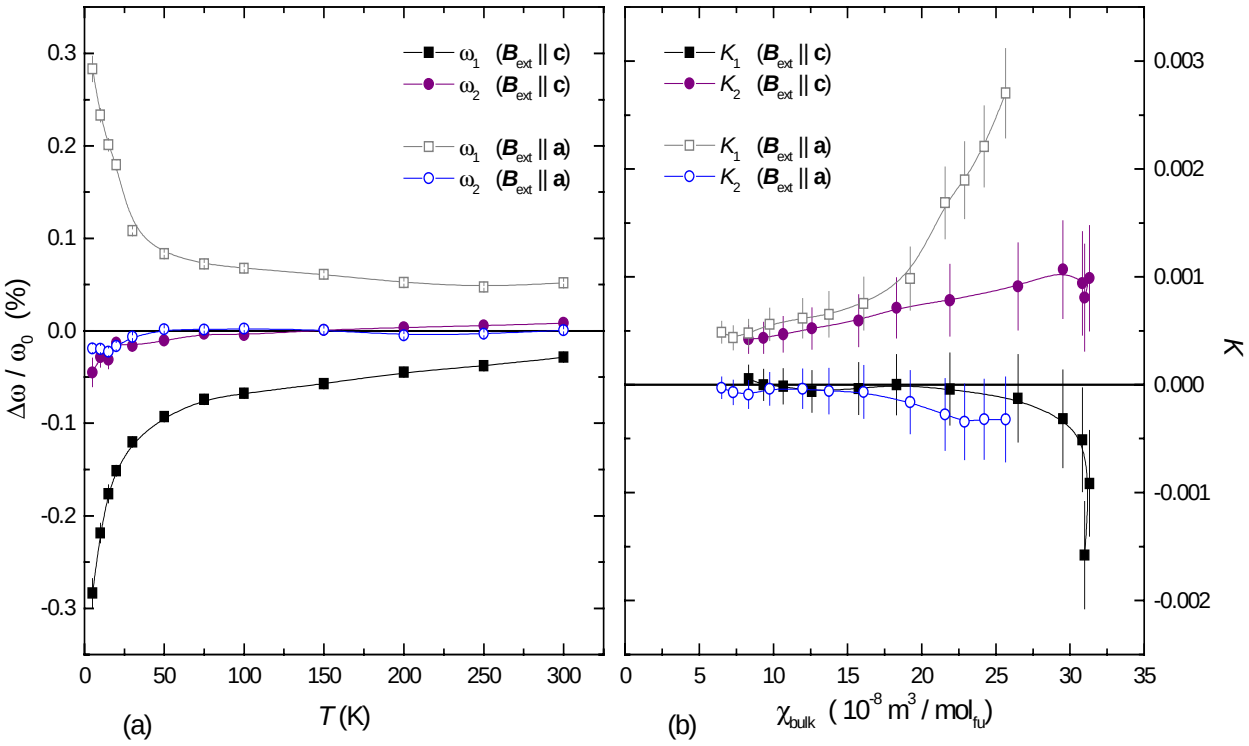

Figure 5.7 - TF (B_{ext} = 0.6 T) frequency shift (a) and Knight shift (b) of U_2Pt_2In. The error bars in K include the uncertainty in the demagnetizing field corrections. The lines are guides to the eye.

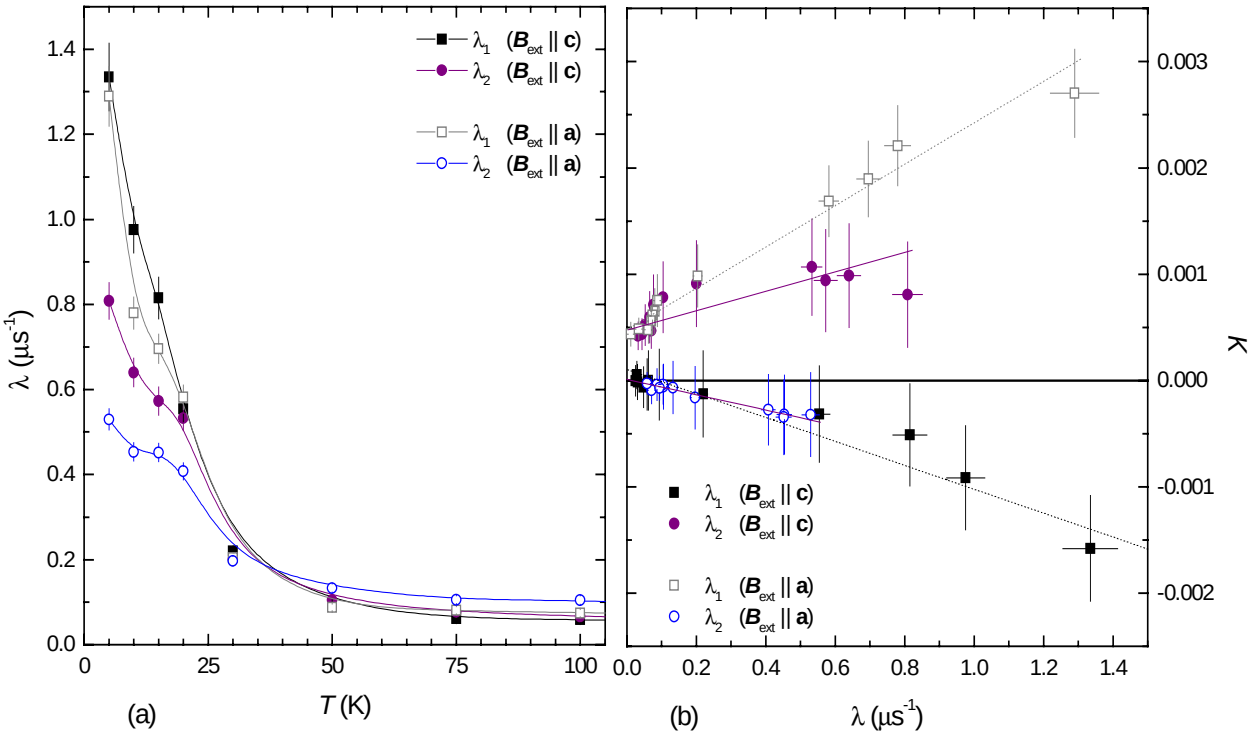

Figure 5.8 - Temperature (a) and Knight shift (b) dependence of the TF (B_{ext} = 0.6 T) line width in U_2Pt_2In. The error bars in K include the uncertainty in the demagnetizing field corrections. The lines are guides to the eye.

In Refs. 4 and 5, the μSR technique has been used to investigate the possibility of Kondo disorder as the main route for non-Fermi liquid behaviour in the system $UCu_{5-x}Pd_x$. Due to the inhomogeneous distribution of Kondo temperatures arising from disorder, there is a broad distribution of the heavy-fermion spin polarization, which is reflected in the μSR line width.

In the case of U_2Pt_2In, the μ-s.s. are not known and the Knight shifts cannot be determined accurately. Therefore, these data cannot be used to test the Kondo disorder model. However, because the Knight shift is proportional to the local susceptibility and the line width is related to the spread of the local susceptibilities, an inhomogeneous line broadening is expected if Kondo disorder is present in the system. This means that the line width will have a stronger dependence on χ than the Knight shift and $\lambda(K)$ will deviate from a straight line. In Figure 5.8b, $K(\lambda)$ is plotted for U_2Pt_2In. Considering the error bars, there is no evidence of an inhomogeneous line broadening due to Kondo disorder.

The ZF-μSR data suggests that one of the μ-s.s. is the 4c site. Since $A_1 = A_2$ in the TF-μSR, the other signal should originate from a site with the same multiplicity as 4c. However, considering the large value of λ_1, it is possible that signal 1 corresponds in fact to a sum of two signals originating from two μ-s.s. with lower multiplicity, which cannot be resolved in the fits due to the small frequency shifts. The only possible sites are 2a and 2b. This means that the total TF-μSR spectra could be fitted with the function

$$P(t) = \frac{1}{2}\left[P_G(\omega_{2a}t,\lambda_{2a}t) + P_G(\omega_{2b}t,\lambda_{2b}t)\right] + \frac{1}{2}P_G(\omega_{4c}t,\lambda_{4c}t) \quad , \tag{5.9}$$

with $P_G(\omega t,\lambda t) = \cos(\omega t+\phi)\, e^{-\lambda t}$. Due to the different low-temperature susceptibilities at the sites 2a and 2b, a sum over the two signals would be reflected by a large value of λ_1, while ω_1 corresponds to an average frequency for the two sites. The different susceptibilities at the 2a and 2b sites are well justified by considering their distances to the nearest U neighbours (Table 5.3). The 2a site is relatively close to U(4g) and the 2b site is close to U(4f). As mentioned in Section 4.3, polarized-neutron experiments show that the field-induced susceptibility of the U atoms is stronger at the 4f site than at the 4g site. Therefore, the susceptibility at the 2b site is expected to be higher than at the 2a site.

Table 5.3 - Distances between different interstitial sites and the U sites in U_2Pt_2In.

site	U-site	*d* (Å)	site	U-site	*d* (Å)	site	U-site	*d* (Å)
2a	4f	3.647	2b	4f	1.790	4c	4f	2.873
	4g	1.961		4g	3.476		4g	2.822

5.4. Summary

The most important conclusion that can be drawn from the ZF-, LF- and TF-μSR experiments on U_2Pt_2In is the absence of weak static magnetic order.

Best fits to the ZF muon relaxation curves are obtained by using a two-component function, consisting of a Gaussian and an exponential term. LF-μSR spectra clearly show that the exponential component is of dynamic origin, while the Gaussian component is static. The Gaussian term is attributed to a random distribution of In nuclear moments. The amplitude and the line width of the exponential term increase strongly below 7.5 K. Since $\chi_c(T)$ goes through a maximum at about the same temperature, this term is most likely associated with the stabilization of antiferromagnetic fluctuations.

The depolarization rate of the Gaussian component strongly suggests that one of the muon stopping sites is the 4c site. The irregular shape of the sample and the small frequency shifts observed hamper a proper analysis of the TF data. The data are however consistent with an occupancy of the 2a, 2b and 4c sites by the muons. No evidence for Kondo disorder was found from the TF line widths.

References

1. A. Schenck, "Muon Spin Spectroscopy", Adam Hilger, Bristol, 1985, p. 43.
2. A. Schenck and F.N. Gygax, in "Handbook of Magnetic Materials" vol. 9 (K.H.J. Buschow, ed.), Elsevier, Amsterdam, 1995, p. 57.
3. Source: WebElements [http://www.shef.ac.uk/chemistry/web-elements].

4. O.O. Bernal, D.E. MacLaughlin, A. Amato, R. Feyerherm, F.N. Gygax, A. Schenck, R.H. Heffner, L.P. Le, G.J. Nieuwenhuys, B. Andraka, H.v. Löhneysen, O. Stockert and H.R. Ott, Phys. Rev. B 54 (1996) 13000.
5. D.E. MacLaughlin, O.O. Bernal and H.G. Lukefahr, J. Phys.: Condens. Matter 8 (1996) 9855.

6. Probing U_2Pt_2In in the Doniach phase diagram

In order to probe the (Doniach) phase diagram of U_2Pt_2In, resistivity experiments under pressure and Th-doping studies were carried out. The main role of replacing small amounts of U by Th is an expansion of the unit cell, while applying hydrostatic pressure gives the opportunity to study the effects of unit-cell volume reduction. This in turn changes the conduction-electron - *f*-electron hybridization and therefore the exchange interaction *J*. Assuming that U_2Pt_2In is close to a quantum critical point, it is of interest to study the eventual emergence of magnetic order with Th doping or the recovery of the Fermi-liquid state under pressure.

Experiments under pressure were also performed on U_2Pd_2In in order to study the suppression of the antiferromagnetic ground state. As mentioned in Section 4.1, U_2Pd_2In is an antiferromagnetic heavy-fermion material. On the magnetic side of the Doniach diagram (see Figure 6.17a in Section 6.5), it is the compound closest to U_2Pt_2In.

The magnetic ground states of some of the 2:2:1 compounds, prepared in single-crystalline form, were investigated, which confirmed their location in the Doniach diagram (Section 4.1.2). The results are presented in Section 6.4.

6.1. Pressure effects on the resistivity of U_2Pt_2In

Resistivity measurements under pressures up to 1.8 GPa and in magnetic fields up to 8 T, were carried out in the temperature range 0.3-300 K. The data were taken on bar-shaped single-crystals of U_2Pt_2In by using a standard four-probe method. Experiments under pressure were carried out by using the CuBe piston cylinder-type clamp cell described in Section 2.3.1. The pressure values presented in this chapter were corrected for an empirically established efficiency of 80%. For each pressure, the resistance curves were normalized to 1 at room temperature. In this way, possible changes in the geometrical factor (mainly in the distance between the voltage contacts) are taken into account.

As shown in Section 4.2.2, the zero-pressure resistivity curve of U_2Pt_2In for $\boldsymbol{I} \parallel \mathbf{c}$ follows a power law of the type $\rho \sim T^{\alpha}$ with $\alpha \sim 0.9$ at the lowest temperatures. Upon increasing the pressure, α gradually increases for $p < 1.0$ GPa (Figure 6.1). However, as the pressure is increased above 1.0 GPa, a minimum in the resistivity develops, which becomes more pronounced at the highest pressures.

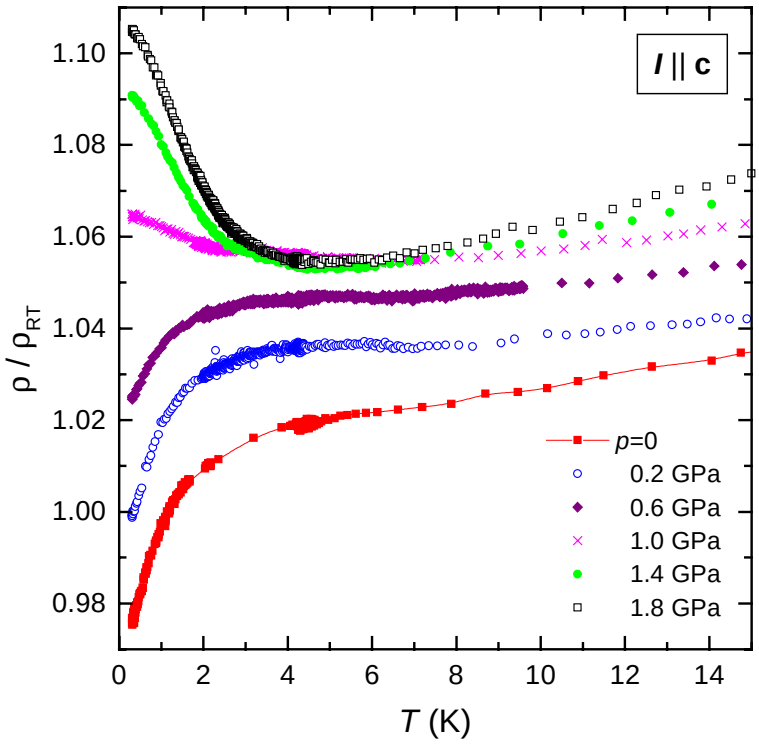

Figure 6.1 - Low-temperature dependence of the resistivity of U_2Pt_2In for $\boldsymbol{I} \parallel \mathbf{c}$ at different pressures.

In order to investigate whether the observed minimum has a magnetic origin, measurements of ρ(T) in magnetic fields ($\boldsymbol{B} \parallel \boldsymbol{I}$) were performed at $p = 1.8$ GPa (Figure 6.2a). T_{min} decreases smoothly with the strength of the applied magnetic field: $T_{min} \sim 4.8$ K for $B = 0$ and $T_{min} \sim 2.2$ K for 8 T. Also, the minimum becomes less pronounced with increasing field. Due to the limited range of temperatures and fields available and the relative uncertainty in determine T_{min}, it is not possible to clearly trace the evolution of T_{min} with B. Figure 6.2b shows that the data can be fitted with a linear dependence, $B = B_0(1 - T_{min}/T_0)$ with $B_0 = 14.2(7)$ T and $T_0 = 4.7(1)$ K. A typical antiferromagnetic-like field dependence of the ordering temperature, $B = B_0[1 - (T_{min}/T_0)^2]^{\beta}$ with $\beta = 0.8$, $B_0 = 9.2(8)$ T and $T_0 = 4.4(2)$ K, cannot be excluded. However, the latter produces a poorer fit. The field effect on the resistivity curves suggests that T_{min} has a magnetic origin. Whether T_{min} is associated with magnetic ordering remains unresolved.

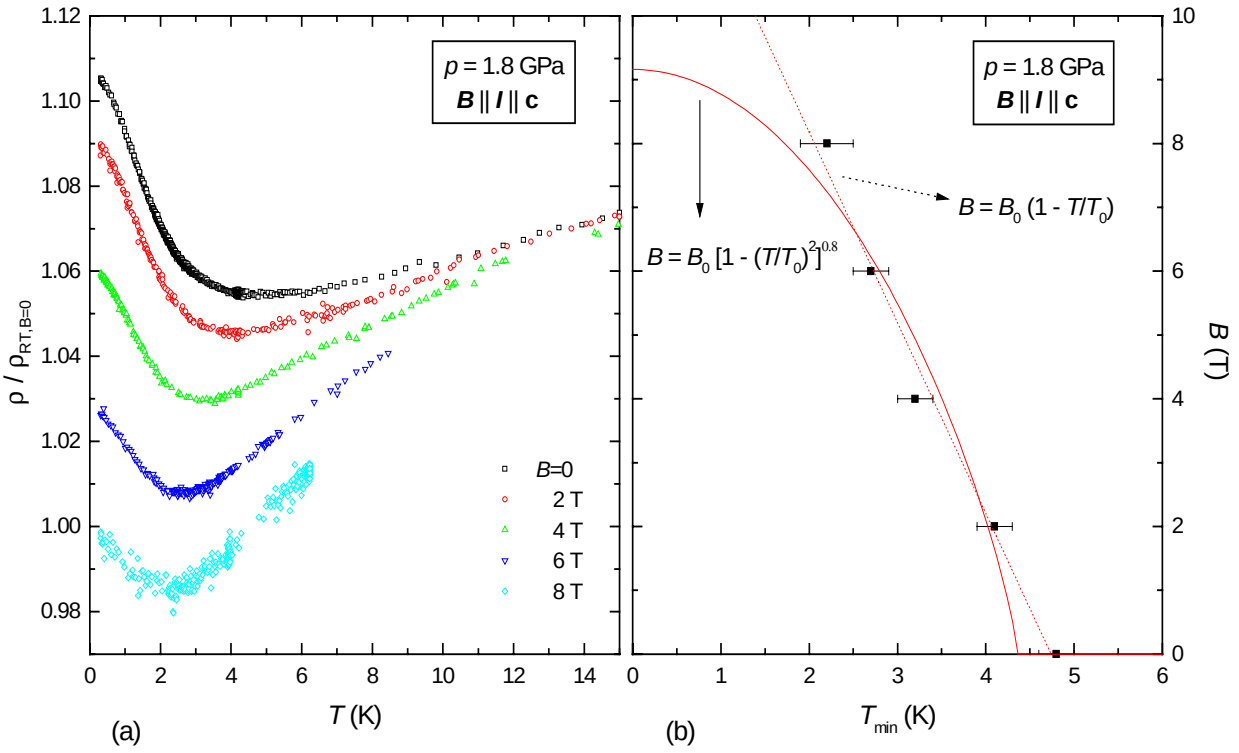

Figure 6.2 - (a) Temperature dependence of the resistivity of U_2Pt_2In for $\boldsymbol{I} \parallel \mathbf{c}$ and $p = 1.8$ GPa at different longitudinal fields. (b) Field dependence of T_{min}.

It is of interest to note, however, that the structure in ρ(T) at $p = 1.8$ GPa resembles, to a certain extent, the one of an antiferromagnetic phase transition of the spin-density wave type, as observed e.g. in the heavy-fermion antiferromagnets URu_2Si_2 ($T_N = 14$ K) [1] and $U(Pt_{0.95}Pd_{0.05})_3$ ($T_N = 5.8$ K) [2]. In these compounds, ρ(T) increases below T_N because of the opening of an

energy gap. At about $0.9T_N$, $\rho(T)$ develops a local maximum, below which the resistivity drops because of the ordered structure. The data in Figure 6.1 for U_2Pt_2In under pressure, show no local maximum at temperatures $T > 0.15T_{min}$. If T_{min} is indeed associated with magnetic ordering, the absence of a local maximum is possibly due to the large value of the residual resistance of the samples.

The emergence of a magnetic component to $\rho(T)$ upon applying pressure is quite surprising. Applying pressure on a compound at the magnetic instability normally leads to an increase of the control parameter J and brings the compound in the non-ordering Fermi-liquid regime. A possible explanation for this unusual behaviour might be offered by assuming that the control parameter J is not governed by the volume, but by the c/a ratio of the tetragonal unit cell. This is suggested by the comparison of the unit-cell volumes and c/a ratios of U_2Pt_2In and the antiferromagnets U_2Pd_2In ($T_N = 37$ K) and U_2Pt_2Sn ($T_N = 15$ K) [3]. Whereas the unit-cell volume of U_2Pt_2In is smaller than that of U_2Pd_2In and larger than that of U_2Pt_2Sn, the c/a ratio is always smaller (for simplicity the doubling of the crystal structure along the c-axis in single-crystalline U_2Pt_2In has not been taken into account) [4]. Thus the appearance of magnetic ordering under pressure could be the result of an increase of the c/a ratio. This in turn requires the compressibility to be anisotropic.

In order to determine the compressibility of U_2Pt_2In, X-ray diffraction experiments were performed under pressure at RT by T. Naka (NRIM-Tsukuba, Japan). The resulting lattice parameters under pressure are presented in Figure 6.3. Both the c and a parameters decrease almost linearly with pressure. The compressibility values are almost identical for both axes: $\kappa_a = 0.220$ Mbar^{-1} and $\kappa_c = 0.242$ Mbar^{-1}, while the volume compressibility amounts to $\kappa = 0.682$ Mbar^{-1}. This means that between p=0 and 1.8 GPa, the c/a ratio does not change significantly (it actually decreases 0.04%). This invalidates the hypothesis that the c/a ratio is the control parameter for U_2Pt_2In in the Doniach diagram.

Resistivity experiments under pressure were also carried out for the current along the a-axis (Figure 6.4). Interestingly, the results differ very much from the results for $\boldsymbol{I} \parallel \mathbf{c}$. In Section 4.2.2 it was shown that the zero-pressure resistivity curve for $\boldsymbol{I} \parallel \mathbf{a}$ follows a power law $\rho \sim T^{\alpha}$ with $\alpha = 1.25$ at the lowest temperatures. Upon increasing the pressure, α gradually increases and no minimum in $\rho(T)$ is observed up to $p = 1.8$ GPa.

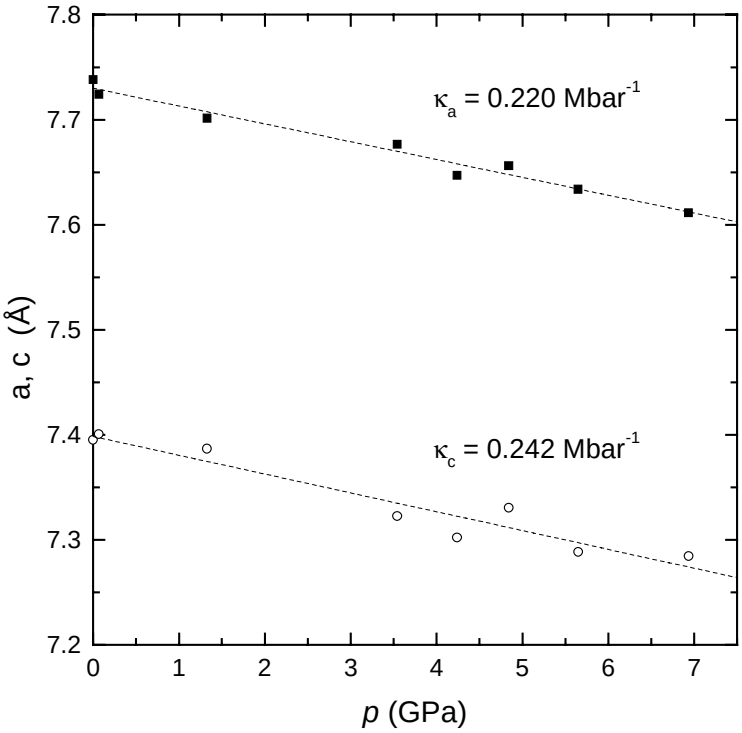

Figure 6.3 - Pressure dependence of the lattice parameters of U_2Pt_2In.

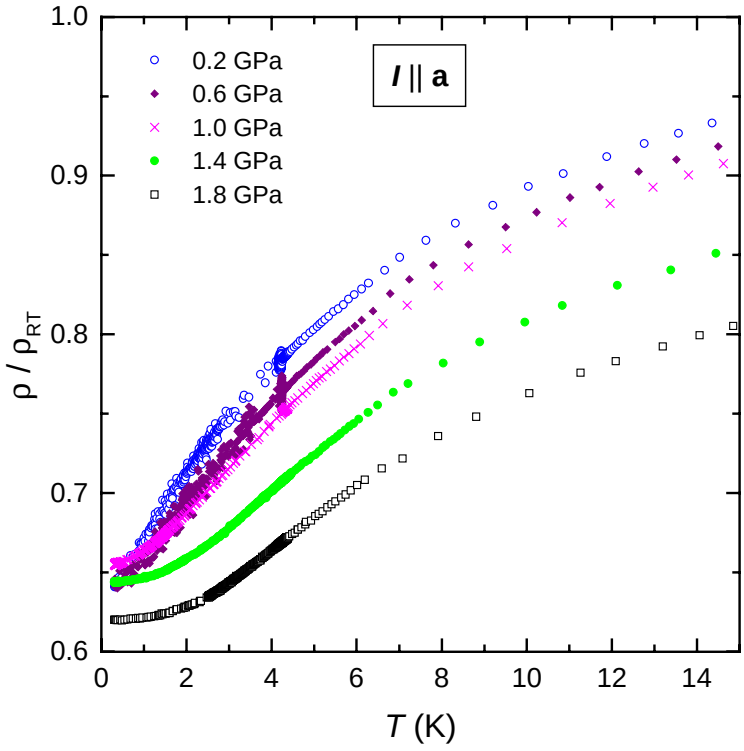

Figure 6.4 - Low-temperature dependence of the resistivity of U_2Pt_2In for ***I*** || **a** at different pressures.

The pressure dependence of the exponent α is shown in Figure 6.5a. The Fermi-liquid value of $\alpha = 2$ is reached at $p \sim 1.0$ GPa. Upon further pressure increase, there is an increase of

the temperature T_{FL} below which a $\rho \sim T^2$ behaviour is observed. The pressure dependence of T_{FL} is shown in Figure 6.6b. According to the theory of Rosch [5] for the resistivity of heavy-fermion materials close to an antiferromagnetic quantum critical point (see Section 2.4), the temperature below which a $\rho \sim T^2$ behaviour is observed should vary initially as $T_{FL} = a_1 (p\text{-}p_c)$ and at higher pressures as $T_{FL} = a_{1/2} (p\text{-}p_c)^{1/2}$, where p_c is the pressure at which the QCP occurs. The region where the linear behaviour is observed depends on the amount of disorder x in the system ($x \approx$ 1/RRR). The $T_{FL}(p)$ behaviour in U_2Pt_2In for $\boldsymbol{I} \parallel \mathbf{a}$ is consistent with a linear dependence with $p_c = 0$. A $\rho \sim T$ region is predicted to occur for $x < T/\Gamma < x^{1/2}$ ($x < 1$), where Γ defines the temperature scale where the spin fluctuations are destroyed ($\Gamma \sim T_K$ or T_{coh}). Defining a region where $\rho \sim T$ for the different pressure values (see Figure 6.6a for $p = 1.8$ GPa), the diagram of Figure 6.6b can be constructed, from which it follows that $x = 0.34$ and $\Gamma = 8.1$ K. The fact that $x <$ 1/RRR indicates that the residual resistivity observed in U_2Pt_2In for $\boldsymbol{I} \parallel \mathbf{a}$ is not uniquely due to impurity or defect scattering. The distance to the QCP is given by $r = \zeta p$ with $\zeta = 0.11$ GPa^{-1}.

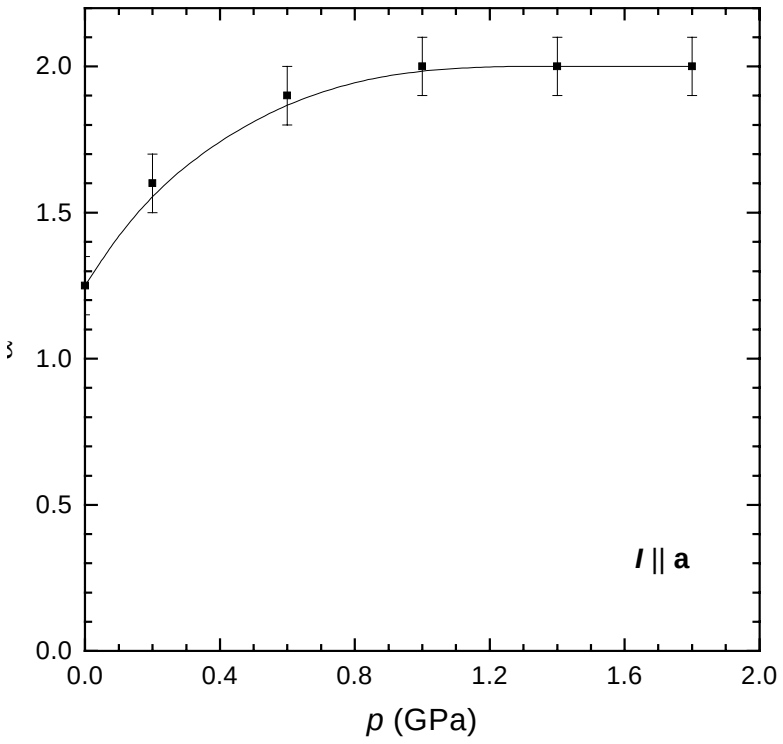

Figure 6.5 - Pressure dependence of the resistivity exponent α for $\boldsymbol{I} \parallel \mathbf{a}$.

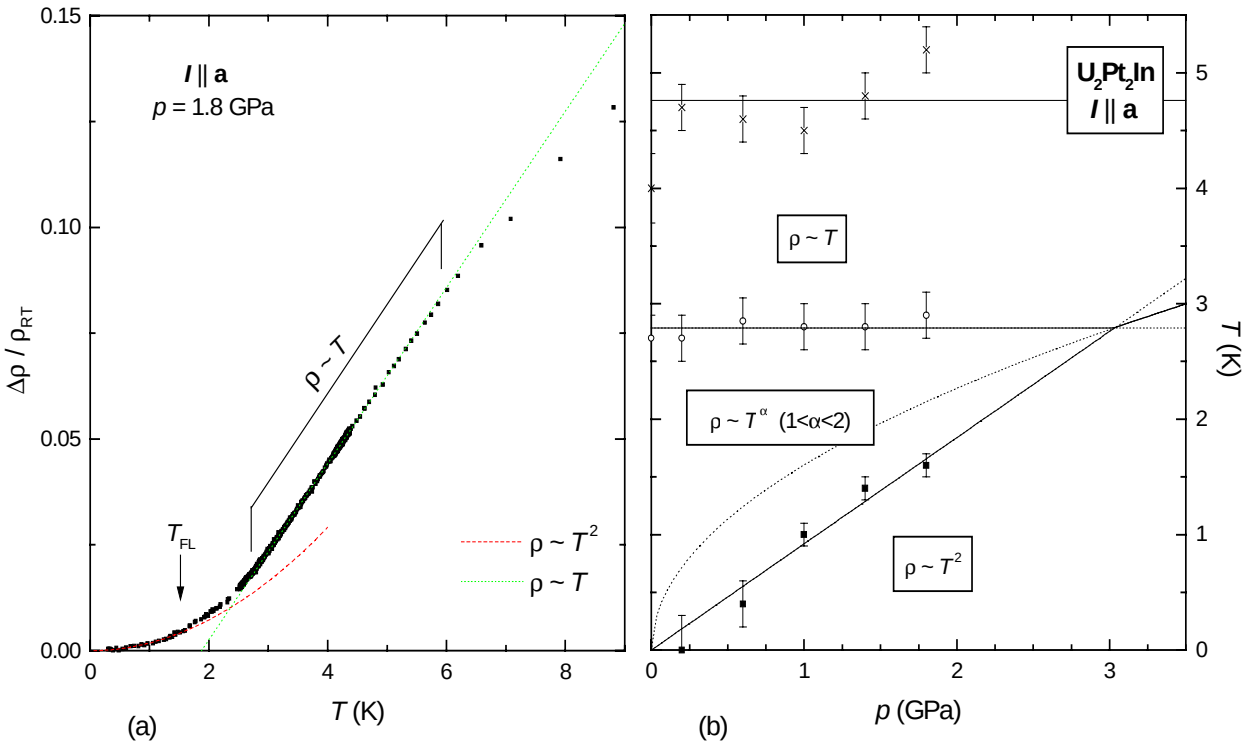

Figure 6.6 - (a) Temperature dependence of $\rho_a - \rho_{0,a}$ for U_2Pt_2In under $p = 1.8$ GPa. (b) Pressure dependence of the temperature below which $\rho \sim T^2$ and the temperature interval where $\rho \sim T$. The lines are defined in the text.

Therefore, the resistivity data under pressure for ***I*** || **a** are consistent with the location of U_2Pt_2In at or close to a QCP. Pressure increases the exchange parameter J, shifting the compound towards the non-ordering Fermi-liquid regime. These results for ***I*** || **a** indicate that the minimum in $\rho_c(T)$ is most probably not related to magnetic order.

At high temperatures, the resistivity curves also have different characteristics for the two crystallographic directions. The anisotropy in the transport properties increases with pressure in the whole temperature range studied, as shown in Figure 6.7. As the pressure is increased, ρ_a tends to decrease, while ρ_c increases, thus the difference $\rho_c - \rho_a$ increases (Figure 6.7b). Assuming that the difference $\rho_c(T) - \rho_a(T)$ is due to an extra resistivity component only present for ***I*** || **c**, the effect of pressure is to enhance this component, without significantly changing its temperature dependence. This implies that the minimum in $\rho_c(T)$ is probably a consequence of the enhancement of a resistivity component for ***I*** || **c**.

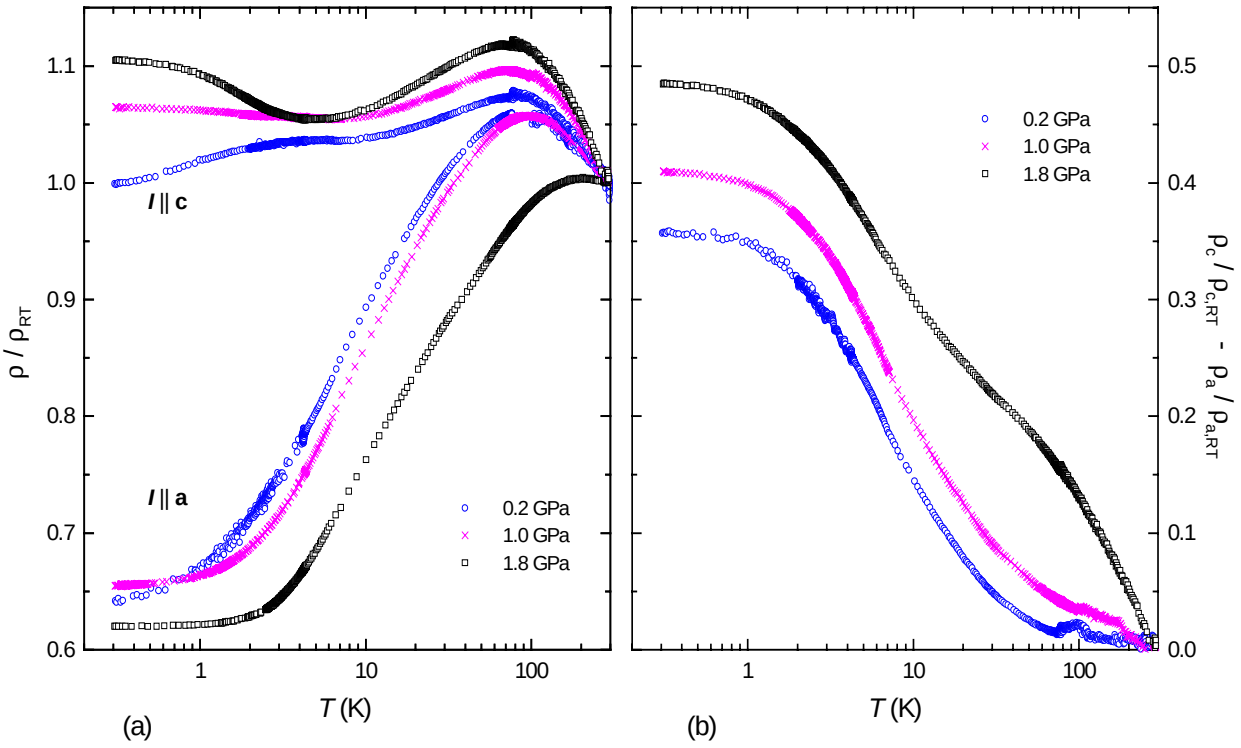

Figure 6.7 - (a) Temperature dependence of the resistivity of U_2Pt_2In for $\boldsymbol{I} \parallel \mathbf{a}$ and $\boldsymbol{I} \parallel \mathbf{c}$ at different pressures; (b) Difference $\rho_c(T)$-$\rho_a(T)$. Notice the log$T$ scale.

The temperature T_m at which a maximum in the resistivity occurs increases strongly for $\boldsymbol{I} \parallel \mathbf{a}$, but decreases slightly for $\boldsymbol{I} \parallel \mathbf{c}$. According to the theory of Yoshimori-Kasai for the dense Kondo system [6], the temperature T_m is approximately proportional to the Kondo temperature T_K. The volume dependence of T_K is given by a Grüneisen parameter defined as

$$\Gamma_K = -\left.\frac{\partial \ln T_K}{\partial \ln V}\right|_{V=V_0}, \qquad (6.1)$$

where $V_0 = V(p=0)$. Since $T_m \propto T_K$, it follows that [7]

$$\Gamma_K = -\left(\frac{V - V_0}{V_0}\right)^{-1} \ln \frac{T_m(P)}{T_m(0)} \quad . \qquad (6.2)$$

The volume change is $\Delta V/V_0 = -\kappa p$. The values of $\ln[T_m(p)/T_m(p=0)]$ are plotted versus $\Delta V/V_0$ in Figure 6.8. The slope of the straight lines through the data points yields the value of Γ_K. Not considering the point for $\boldsymbol{I} \parallel \mathbf{a}$ at $p = 1.8$ GPa, where the maximum is not well defined, a value of $\Gamma_{K,a} = 49.7 \pm 7.1$ can be estimated for $\boldsymbol{I} \parallel \mathbf{a}$. This value is close to the values of 59 and 65 reported for the heavy-fermion compounds $CeInCu_2$ and $CeCu_6$, respectively [7]. This indicates that the strong pressure dependence of T_m observed in U_2Pt_2In ($\boldsymbol{I} \parallel \mathbf{a}$) is not unusual. The increase of T_K reflects the increase of the conduction electron - f-electron hybridization and, therefore, the

increase of the exchange parameter J. This is in agreement with the appearance of a FL $\rho \sim T^2$ behaviour at low temperatures.

The slight decrease of T_m for $\boldsymbol{I} \parallel \mathbf{c}$, on the other hand, is unexpected. A similar analysis of the pressure dependence of T_m as performed for $\boldsymbol{I} \parallel \mathbf{a}$, yields a Grüneisen parameter $\Gamma_{K,c} = -6.8(7)$. Since T_K should not depend on the current direction, this value of $\Gamma_{K,c}$ indicates that the maximum observed in $\rho_c(T)$ is not due uniquely to the Kondo effect. The enhancement of an extra anisotropic resistivity component under pressure (mainly present for $\boldsymbol{I} \parallel \mathbf{c}$) occurs even at high temperatures (Figure 6.7b). Therefore T_m cannot be taken to be proportional to T_K for this current direction.

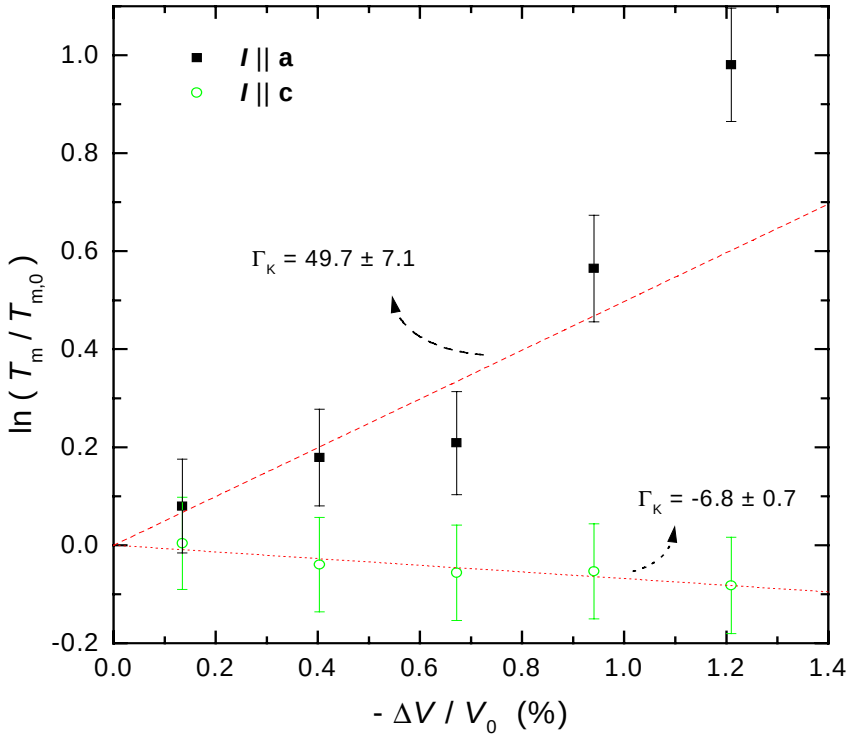

Figure 6.8 - Values of $\ln[T_m(p)/T_m(p=0)]$ as a function of volume change $[V(p=0)-V(p)]/V(p=0)$ for U_2Pt_2In.

Resistivity measurements under pressure were also performed on other single-crystals of U_2Pt_2In. Although all the crystals were cut from the same batch, there is a slight sample dependence of some of the features. The data under pressure presented so far were all measured on one single crystal (sample #1). It had a platelet shape such that the current could be applied along the a- and c-axis. Measurements on a second crystal (sample #2) with $\boldsymbol{I} \parallel \mathbf{c}$ and on a third crystal (sample #3) with $\boldsymbol{I} \parallel \mathbf{a}$, confirm the overall behaviour of the resistivity curves under

pressure: an increase of the transport anisotropy, the development of a minimum in $\rho_c(T)$ at low temperatures and the recovery of a T^2 term in $\rho_a(T)$.

However, the values of T_{min} are different for samples #1 and #2. For sample #2, the minimum shows up for $p > 1.2$ GPa and attains values of $T_{min} \sim 1.2$ K at $p = 1.5$ GPa and $T_{min} \sim 2.1$ K at $p = 1.8$ GPa [8]. The field dependence of T_{min} at $p = 1.8$ GPa has the same form as shown in Figure 6.2b for sample #1. Also, at high temperatures, the absolute values of the maximum T_m are slightly different, but the pressure dependence of T_m remains the same. The Grüneisen parameters obtained are $\Gamma_{K,a} \sim 45$ (sample #3) and $\Gamma_{K,c} \sim -2$ (sample #2). These values do not differ significantly from the values obtained for sample #1.

6.2. Studies of Th doping in U_2Pt_2In

Resistivity studies on polycrystalline $(U_{1-x}Th_x)_2Pt_2In$ samples ($0 \leq x \leq 1$) reported in the literature [9,10], indicate that the low-temperature behaviour of $\rho(T)$ gradually changes, from linear in T as observed for undoped U_2Pt_2In towards a quadratic behaviour as the Th content increases. The resistivity of the sample with x = 0.1 shows a knee at about 19 K, which suggests magnetic ordering. However, it should be noted that a small amount of UPt impurity phase, possibly present in the sample, could also give rise to a similar anomaly, as UPt has two ferromagnetic transitions at 19 K and 27 K [11].

In this section, results are presented on polycrystalline samples of $(U_{1-x}Th_x)_2Pt_2In$ with x = 0, 0.03, 0.08 and 0.1. The samples were prepared by L.C.J. Pereira (Technological and Nuclear Institute, Portugal) by arc-melting the constituents under a purified Ar atmosphere. The crystallographic structure and the lattice parameters were determined by X-ray diffraction [12]. It was found that all polycrystalline samples crystallize in the simple U_3Si_2-type of structure. The lattice parameters and unit-cell volume are given as a function of x in Figure 6.9. The unit-cell expansion is almost isotropic. The volume increases linearly with x. However, the prepared materials were not single phase. All samples have small amounts of UPt and/or UPtIn as impurity phases. UPtIn is an antiferromagnet with $T_N = 15$ K [13]. Due to the non-single phase

character of the Th-doped samples, the results presented here should be considered as preliminary.

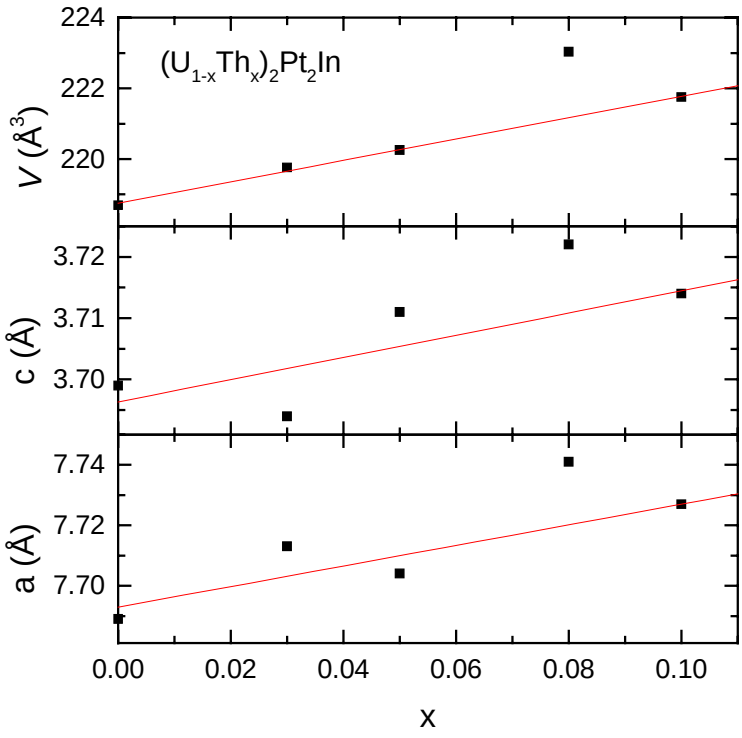

Figure 6.9 - Lattice parameters and unit-cell volume of polycrystalline $(U_{1-x}Th_x)_2Pt_2In$. Data taken from Ref. 12.

As mentioned in Section 4.3.3, specific-heat measurements on polycrystalline U_2Pt_2In show the same logarithmic divergence of c/T as observed on single crystals. However, in the polycrystals small amounts of UPtIn and UPt impurity phases were detected by X-ray diffraction and magnetization measurements. These small amounts of impurity phases (less than 5 w.%) were not detected in the specific heat. Due to the high electronic specific heat of U_2Pt_2In, the low-temperature contribution from the impurity phases is unobservable.

Magnetization measurements were performed on $(U_{0.95}Th_{0.05})_2Pt_2In$ in the temperature range 2-300 K and in fields up to 5 T. Both the temperature and field dependence of the magnetization M reveal the presence of a ferromagnetic component with $T_C \sim 25$ K, consistent with an UPt impurity phase. The $M(B)$ curves are shown in Figure 6.10a. Below 30 K, the saturation of the ferromagnetic contribution of the UPt impurity phase in low fields is clearly visible. At higher fields $M(B)$ is almost linear. Assuming that the high-field linear behaviour ($B > 1$ T) is only due to the main phase, the susceptibility χ_{DC} of $(U_{0.95}Th_{0.05})_2Pt_2In$ can be extracted by taking the slopes of the $M(B)$ curves at high fields. The low temperature values of

the magnetization obtained by extrapolating the linear high-field behaviour to B=0 are consistent with the presence of about 3 w.% of UPt, in agreement with the value estimated from the X-ray structure refinement. The results of $\chi_{dc} = \mu_0 dM/dB$ are shown in Figure 6.10b. A maximum in $\chi_{dc}(T)$ appears at low temperatures. The maximum possibly indicates antiferromagnetic ordering at $T_N \sim 8(2)$ K. However, it is also possible that the maximum is related to the presence of short-range antiferromagnetic correlations, as in the case of U_2Pt_2In with $\boldsymbol{B} \parallel \mathbf{c}$. The high-temperature ($T \geq 25$ K) $\chi_{dc}(T)$ curve follows a modified Curie-Weiss law with $\chi_0 = 1.4(1) \times 10^{-8}$ m^3/mol$_U$, $\mu_{eff} = 1.8(4)\ \mu_B$/U and $\theta = -29(2)$ K. However, it should be stressed that due to the presence of impurity phases, the $\chi_{dc}(T)$ curve should be considered as indicative and its analysis should be taken with care.

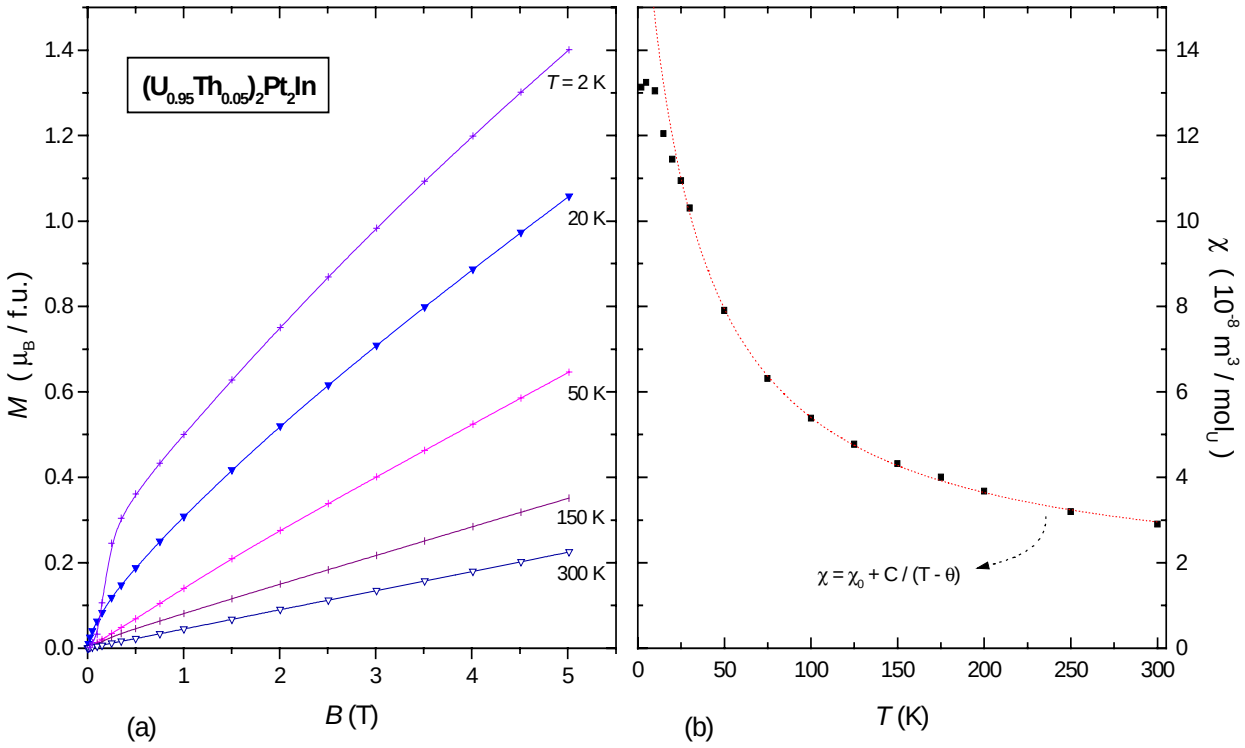

Figure 6.10 - (a) Field dependence of the magnetization of $(U_{0.95}Th_{0.05})_2Pt_2In$. (b) Temperature dependence of the high-field slope of the $M(B)$ curves. The line represents a modified Curie-Weiss law.

Zero- and transverse-field μSR experiments were carried out on the same $(U_{0.95}Th_{0.05})_2Pt_2In$ sample in the temperature range 2-200 K. Reasonable fits to the zero- and 0.01 T transverse-field spectra can be obtained with a Gaussian or exponentially damped depolarization function. An important feature of the data is that part of the asymmetry is missing. In the TF-μSR spectra with $B = 0.01$ T, the full asymmetry $A \sim 0.24$ is observed above 15 K. This

value of the asymmetry is determined by the experimental geometry and sample size. Below about 15 K the asymmetry drops to a value of $A \sim 0.15$, which implies that an additional fast component to the μSR signal appears, which has not been accounted for in the fits. A fast component, i.e., a component with a high depolarization rate, must have its origin in a magnetically ordered phase. The drop in the asymmetry near 15 K ($\Delta A \sim 0.09$), is too high to be attributed to the presence of ~ 3 w.% of UPt impurity phase.

Although no reliable fits to the spectra at low temperature were obtained, a common feature appeared in all fit attempts: as the temperature is decreased below 25 K, the zero-field depolarization rate increases and has a tendency to diverge at about 10 K, below which it regains a low value. A divergency of the depolarization rate is often associated with an antiferromagnetic transition [14], which is in agreement with the antiferromagnetic-like $\chi_{DC}(T)$ curve.

Transverse field μSR experiments in 0.01 T were carried out on $(U_{0.97}Th_{0.03})_2Pt_2In$ for $2.5 \leq T \leq 100$ K. In contrast to the results obtained on the x = 0.05 sample, no significant loss of asymmetry was found at low temperatures. Best fits to the spectra were obtained using a damped-Gaussian depolarization function: $P(t) = P_G(t) \exp(-\lambda_E t)$ with $P_G(t) = \exp(-\Delta_G^2 t^2/2)\cos(\omega t)$. Here, the temperature-independent Gaussian relaxation rate was found to be $\Delta_G = 0.17\ \mu s^{-1}$, which possibly accounts for the In nuclear contribution. This value is much reduced with respect to the one observed on U_2Pt_2In ($\Delta_G = 0.34\ \mu s^{-1}$). It should be noted that the crystallographic structures are different and therefore different muon stopping sites might be involved, leading to a different value of Δ_G from the distribution of In nuclear moments. The damping of the Gaussian term is observed below 10 K with λ_E increasing below this temperature. Whether this increase is associated with a dynamic or a static magnetic component cannot be determined from the available data set.

Recently, polycrystalline $(U_{1-x}Th_x)_2Pt_2In$ samples with x = 0.03, 0.05, 0.08 and 0.1 were prepared with lower amounts of impurity phases [12]. Specific-heat measurements carried out by G. Bonfait (Technological and Nuclear Institute, Portugal) on these samples do not confirm magnetic order above 2 K. It would be of interest to carry out μSR experiments on these samples as well, in order to look for weak magnetism. Clearly, single-phase samples are highly desirable to reliably determine the presence of magnetic order.

6.3. U_2Pd_2In - resistivity under pressure

As mentioned in Section 4.1, U_2Pd_2In is an antiferromagnet with $T_N = 37$ K [15,16]. The U magnetic moments are confined to the basal plane and form a non-collinear magnetic structure. At 10 K, $\mu_U = 1.6\ \mu_B$ [15].

Resistivity measurements under pressure were performed on a single crystal of U_2Pd_2In in the temperature range 0.3-300 K at pressures up to 1.8 GPa. The shape of the sample restricted the current to be applied along the [101] direction. The $\rho(T)$ curves are shown in Figure 6.11a for $p = 0.2$, 1.0 and 1.8 GPa. The shape of the curves does not change significantly with pressure. The value of T_N decreases only slightly from 37.4(5) K at $p = 0.2$ GPa to 35.2(5) K at $p = 1.8$ GPa (Figure 6.11b).

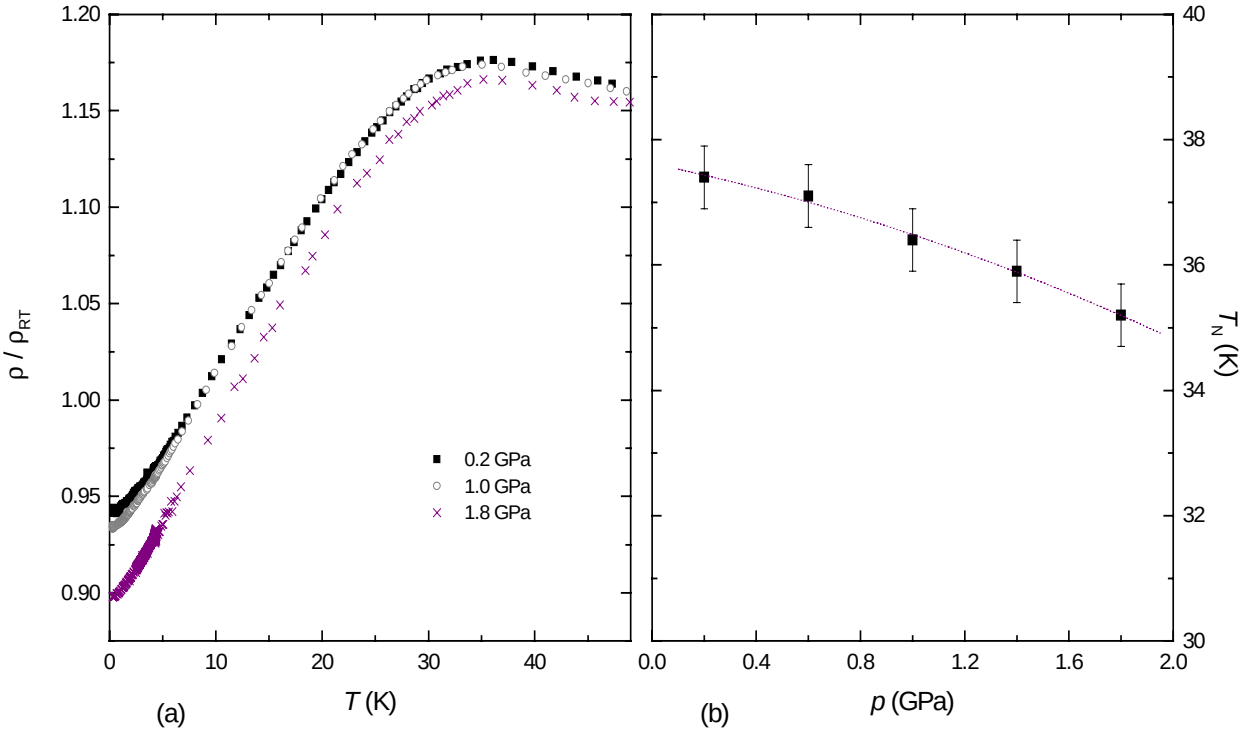

Figure 6.11 - (a) Temperature dependence of the resistivity of U_2Pd_2In for different pressure values. (b) Pressure dependence of T_N. The line is a guide to the eye.

The small decrease of T_N under pressure is consistent with the location of U_2Pd_2In at the maximum in the Doniach phase diagram for the U_2T_2In family of compounds (Section 4.1.2 - see also Figure 6.17). Upon pressure, the hybridization increases and thus also the exchange

interaction J. For $p \leq 1.8$ GPa, the increase of the hybridization strength only shifts the position of the compound in the Doniach phase diagram around the relatively broad maximum of $T_N(J)$.

6.4. Magnetization studies of several U_2T_2X compounds

In order to partially confirm the general Doniach phase diagram for the U_2T_2X family of compounds presented in Section 4.1.2, the magnetization M_a and M_c, where a and c denote the direction of the applied field, of several U_2T_2X single-crystals was measured for $T \geq 2$ K and $B \leq 5.5$ T. The measurements were performed after zero-field cooling (ZFC) and, in some cases, after field cooling (FC), using a SQUID magnetometer at the University of Lisbon.

6.4.1. U_2Co_2Sn

Above 25 K the magnetizations M_a and M_c of U_2Co_2Sn (Figure 6.12a) are linear functions of B, which is typical of a paramagnetic state. At lower temperatures, $M_c(B)$, and to a lesser extent $M_a(B)$, depart significantly from linear behaviour. Over the entire temperature range and for $B \leq 5.5$ T, $M_c > M_a$ which shows an important easy-axis anisotropy.

The $M(T)$ curves do not show any sign of magnetic ordering (see Figure 6.12b for $\boldsymbol{B} \parallel \mathbf{c}$ at 2 T). Above 20 K, the d.c. susceptibility curve, $\chi_c(T) = M(T)/H$, follows a Curie-Weiss law with $\theta = -24.5$ K and a reduced effective moment $\mu_{eff} = 1.65\ \mu_B$/U, indicating the presence of hybridization effects. For all field directions, the low-temperature ($T < 20$ K) M/H values are higher than those given by the Curie-Weiss law extrapolated from the high-temperature range, as shown in Figure 6.12b for the **c** direction. The observed difference could indicate the presence of ferromagnetic spin fluctuations. However, the negative paramagnetic Curie-Weiss temperature θ suggests antiferromagnetic correlations. The two contributions indicate the possibility of different magnetic interactions on the U and Co sublattices. It should be noted however, that the $M(B)$ curves are not linear below 25 K. This means that the comparison of the M/H values with the Curie-Weiss behaviour should be taken with care.

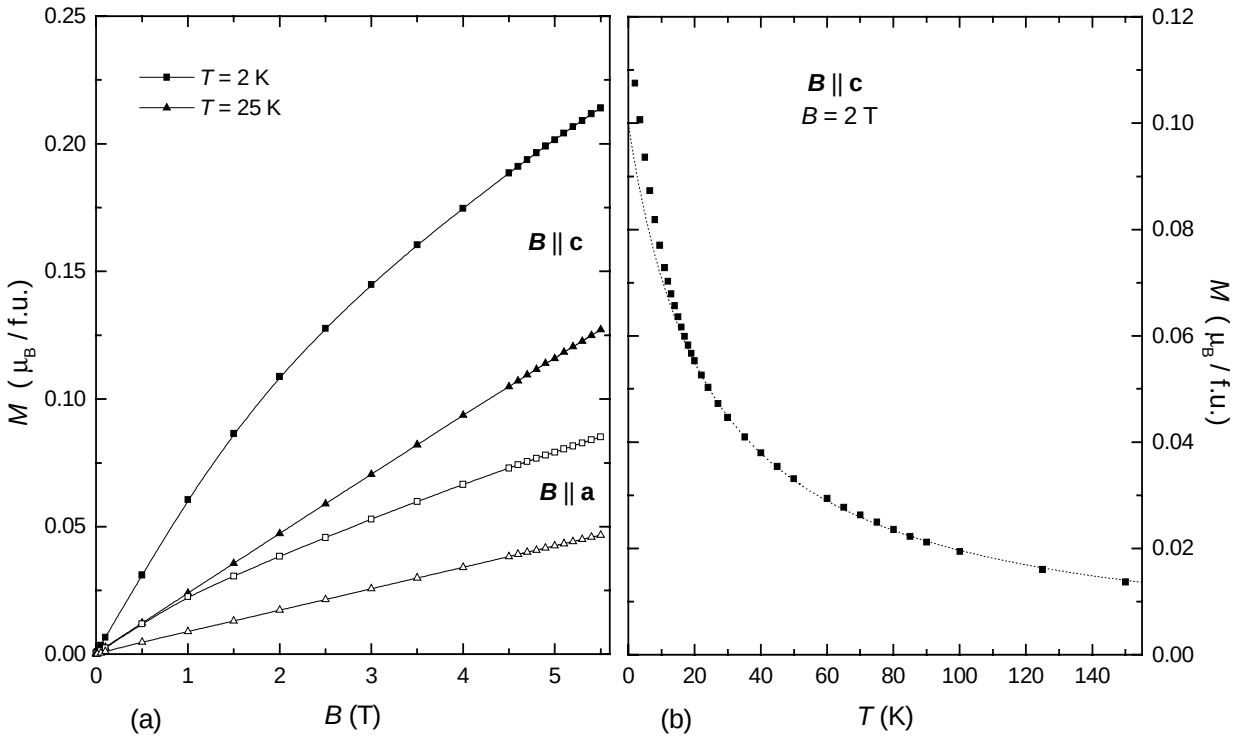

Figure 6.12 - Magnetization of U_2Co_2Sn (solid symbols: **B** ∥ **c**; open symbols: **B** ∥ **a**). a) Field dependence at $T = 2$ and 25 K. b) Temperature dependence measured in a field of 2 T applied along the c-axis. The line represents a high temperature Curie-Weiss behaviour.

In order to determine if the Co atoms carry a magnetic moment, the magnetization density distribution in the unit cell was measured at 2 K by means of polarized-neutron scattering experiments under a magnetic field of 5.5 T applied along the c-axis [17]. It was found that the major contribution to the magnetic susceptibility is located on the U atoms, $\mu_U = 0.118(3)\ \mu_B$, but a small response from the Co atoms was also present, $\mu_{Co} = 0.013(2)\ \mu_B$. At 2 K and 5.5 T, the induced magnetization along the c-axis is 0.220 μ_B/f.u. to be compared with a value of 0.262(7) μ_B/f.u. determined by neutron scattering. The difference is likely due to a negative conduction-electron polarization.

6.4.2. U_2Ru_2Sn

Experiments carried out on polycrystalline samples have shown that U_2Ru_2Sn is a weak itinerant paramagnet [18]. This is confirmed by magnetization measurements on single crystals. A linear behaviour of the magnetization is observed as a function of applied fields up to 5.5 T (Figure 6.13a). $M(T)$ shows a weak temperature dependence (Figure 6.13b) and the

magnetization curves show no difference when measured after ZFC and FC. At room temperature, the susceptibility along the a-axis reaches a value of 2.51×10^{-8} m^3/mol only. This value is further gradually reduced below 200 K to 1.98×10^{-8} m^3/mol at T = 5 K.

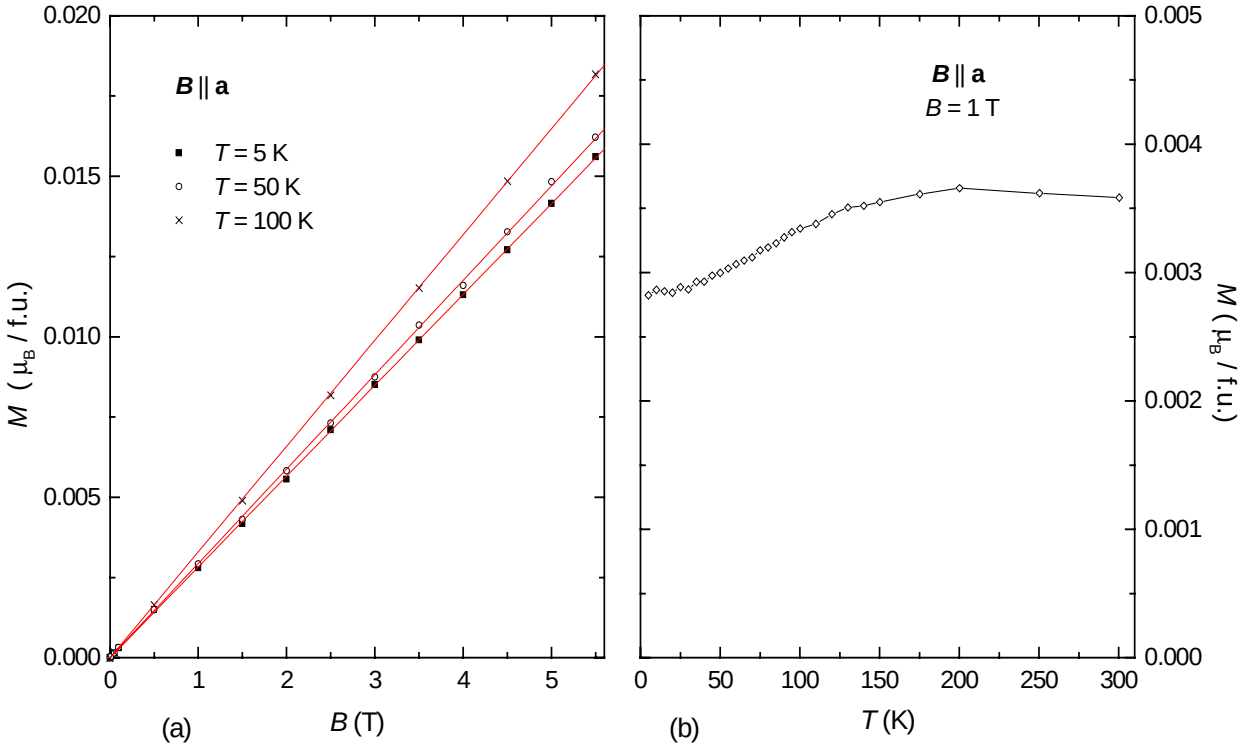

Figure 6.13 - Magnetization of U_2Ru_2Sn for fields applied along the a-axis. (a) Field dependence at temperatures as indicated. (b) Temperature dependence at B = 1 T.

Recently, resistivity data taken on polycrystalline samples were reported [19], which possibly reveal Kondo insulating behaviour. A sharp rise in the resistivity was observed at low temperatures (T < 30 K), which could be an indication of semiconducting behaviour due to gap formation in the electronic density of states with an energy gap of the order of 1 K. So far, this has not been confirmed by the single-crystal magnetization data.

6.4.3. U_2Rh_2Sn

The ZFC magnetizations, $M_a(T)$ and $M_c(T)$, of U_2Rh_2Sn are shown in Figure 6.14a for B = 0.05 T. For both field directions a well defined peak in the susceptibility is observed, which signals an antiferromagnetic transition with a Néel temperature T_N = 28(2) K.

Over the whole temperature range studied $M_a < M_c$. This shows that the unique tetragonal axis is the easy axis for magnetization. The pronounced peak observed in $M_c(T)$ indicates that the magnetic moments are aligned along the c-axis. In a simple ideal antiferromagnet, the susceptibility measured for the field direction perpendicular to the magnetic moments should be almost constant below T_N. The small peak at T_N observed in $M_a(T)$ is possibly due to a small misalignment of the crystal with respect to the magnetic field direction. In fact, if one considers a misalignment of only 5º between the field direction and the a-axis, the magnetization becomes almost constant for temperatures up to T_N and the peak is much reduced (Figure 6.14a).

The $M(B)$ curves (Figure 6.14b) show a linear behaviour for fields up to 5.5 T in both directions (***B*** || **c** and ***B*** || **a**). No hysteresis was observed for either field direction over the whole temperature range studied.

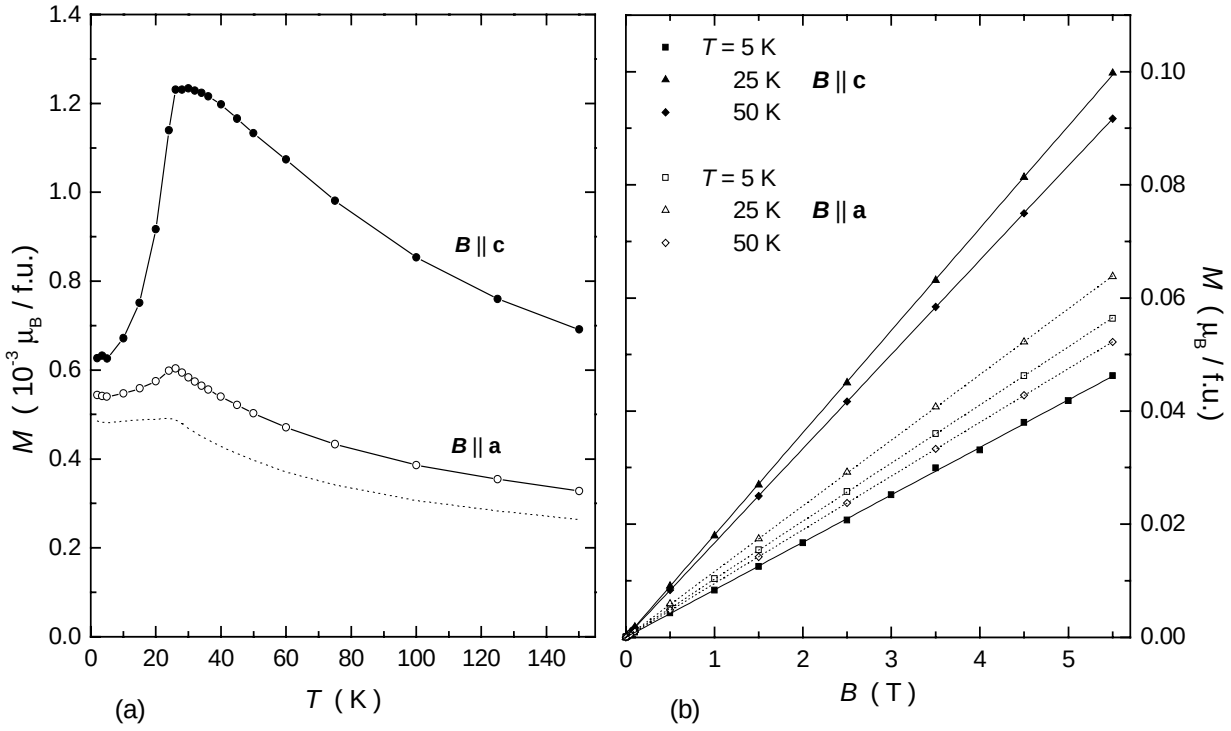

Figure 6.14 - Magnetization of U_2Rh_2Sn. a) Temperature dependence for $B = 0.05$ T (the dotted line represents the corrected magnetization curve for ***B*** || **a** assuming a misalignment of 5º - see text). b) Field dependence (open symbols: ***B*** || **a**; solid symbols: ***B*** || **c**).

The susceptibility curves show that there is an important magnetic anisotropy even in the paramagnetic region. For ***B*** || **c**, a Curie-Weiss behaviour is detected for temperatures above T_N with $\theta = -105(2)$ K and an effective moment per U atom $\mu_{eff} = 2.80\ \mu_B$/U. For ***B*** || **a**, $\chi^{-1}(T)$ shows a positive curvature for the higher temperatures in the paramagnetic region, well described by a

modified Curie-Weiss law with θ = -60(2) K, μ_{eff} = 1.34 μ_B/U and $\chi_0 = 1.9\times 10^{-8}$ m^3/mol_{fu}. This modified Curie-Weiss behaviour could be due to a small misalignment of the crystal with respect to the direction of the field, which leads to an additional contribution from the c-axis to the total magnetization measured. Therefore, the smaller value of μ_{eff} that was found for $\boldsymbol{B} \parallel \mathbf{a}$ should be treated with caution. Accurate determinations of μ_{eff} along both axes require a perfectly aligned crystal and an extension of the measurements to higher temperatures. It is likely that hybridization effects between the *f*-electrons and the ligands, as found in the UTX family of compounds [20], contribute significantly to this strong anisotropy in the paramagnetic region.

Antiferromagnetic order of the U moments was confirmed by neutron-scattering experiments on a single crystal [21]. The data reveal that U_2Rh_2Sn orders in a collinear magnetic structure along the c-axis with k = (0,0,1/2) (magnetic unit cell doubled in the **c** direction compared to the nuclear cell). The refined value of the ordered magnetic moment at the U atom is 0.53(2) μ_B.

Interestingly, U_2Rh_2Sn presents an exception to the empirical rule (obtained for the UTX compounds) that the *f*-moments should point perpendicularly to the shortest *f-f* bond distances, as in this compound the shortest interuranium distances are found to lie along the easy axis (d_{ff} = 3.63 Å).

6.4.4. U_2Ir_2Sn

The magnetization of U_2Ir_2Sn measured in fields applied along the a- and c-axis, shows the presence of a ferromagnetic phase below 50 K (Figure 6.15). Below this temperature, the M/H values strongly deviate from a Curie-Weiss behaviour. The $M(B)$ curves indicate the saturation of a minority ferromagnetic phase at low fields, although the structural analysis of the single-crystals did not reveal the presence of an impurity phase. The impurity that is likely to be present in small quantities in the samples at e.g. the grain boundaries, may be UIr, a ferromagnet with T_C = 46 K and $\mu_U \approx$ 0.5 μ_B [22]. Considering that the slope of the $M(B)$ curves at high fields is due to the U_2Ir_2Sn matrix, the saturation magnetization of the ferromagnetic impurity can be extracted. At 5 K one obtains $\mu_{UIr} \sim 0.003$ μ_B. Comparing this value with the moment of pure UIr, results in the presence of about 0.6% of UIr impurity phase in the single-crystalline samples.

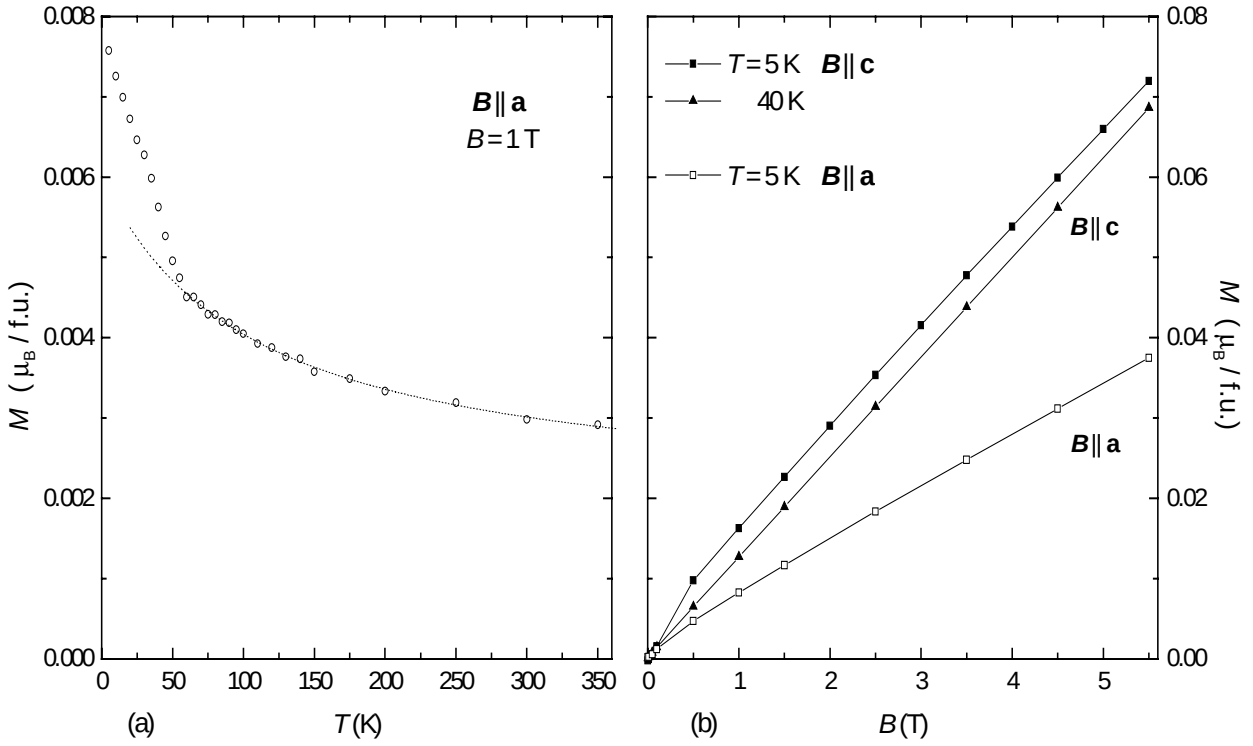

Figure 6.15 - Magnetization of U_2Ir_2Sn (solid symbols: ***B*** || **c**; open symbols: ***B*** || **a**). a) Temperature dependence for 1 T applied along the a-axis. The line is a high-temperature Curie-Weiss fit. b) Field dependence at T = 5 and 40 K.

The-high temperature (T > 50 K) susceptibility follows a modified Curie-Weiss behaviour with a high Curie-Weiss temperature and a very much reduced effective moment: $\chi_0 = 1.4\times 10^{-8}$ m^3/mol, θ = -106 K and $\mu_{eff} = 1.0\ \mu_B$/U for ***B*** || **a**. A strong anisotropy is present in the system which persists up to 300 K, typical of systems with pronounced spin fluctuations. The c-axis is the easy direction of magnetization.

Due to the presence of the ferromagnetic impurity phase, a detailed study of the magnetization of U_2Ir_2Sn was not carried out.

6.4.5. U_2Ni_2In

The magnetization of U_2Ni_2In is linear in applied fields up to 5.5 T. The ZFC $M(T)$ curves for U_2Ni_2In in a field of 0.05 T are shown in Figure 6.16. The measurements show a typical behaviour of an antiferromagnet with T_N = 15.0(5) K. In contrast with what is expected for antiferromagnets with collinear structures, an extremely small magnetic anisotropy is observed in the ordered state, as evidenced by the similarity of $M_a(T)$ and $M_c(T)$.

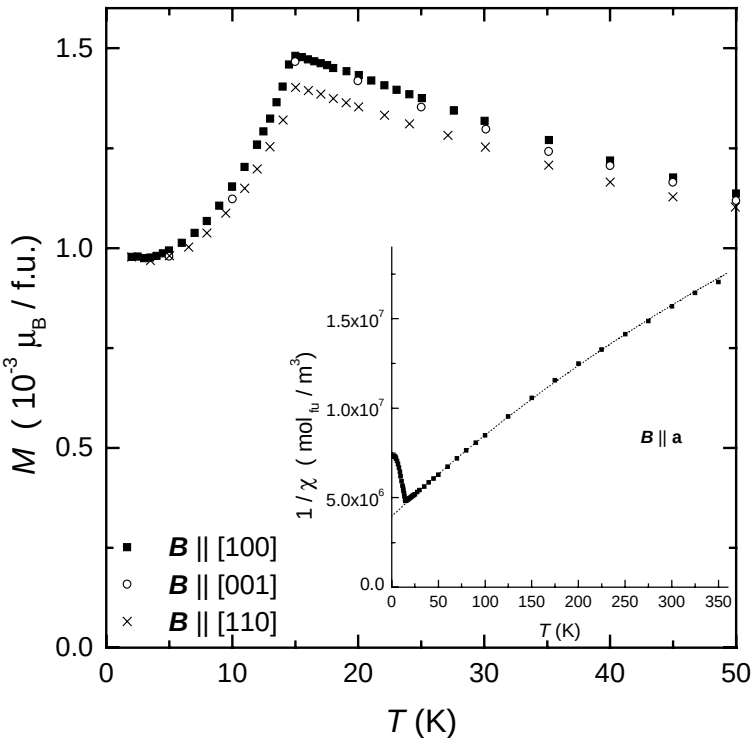

Figure 6.16 - Temperature dependence of the magnetization of U_2Ni_2In in a magnetic field of 0.05 T applied along the **a**, **c** and [110] directions. Insert: inverse susceptibility for ***B*** || **a**.

Neutron-diffraction experiments on a U_2Ni_2In single-crystal [23] indicate a non-collinear antiferromagnetic structure with the moments aligned along the [110] and $[1\bar{1}0]$ directions and a magnetic propagation vector $k = (0,0,1/2)$. The size of the ordered U moments amounts to 0.92(2) μ_B and no moments were found on the Ni sites, in contrast with what was reported in studies on polycrystalline samples [24].

Magnetization measurements were also performed with magnetic fields applied along the [110] direction. Also in this direction, $M(T)$ follows the same behaviour as M_a and M_c. High-temperature fits of the susceptibility to a modified Curie-Weiss law yield the results shown in Table 6.1. The parameters obtained are similar in all field directions.

The reason for the similarity of the $M(T)$ curves for all studied field directions remains unclear.

Table 6.1 - Results from the fits of the susceptibility of U_2Ni_2In to a modified Curie-Weiss law.

	χ_0 (10^{-8} m^3/mol)	θ (K)	μ_{eff} (μ_B/U)
B ∥ [100]	1.8	-73	2.3
B ∥ [110]	1.2	-92	2.5
B ∥ [001]	1.9	-64	2.2

6.5. Discussion

The measured resistivity of U_2Pt_2In under pressure is consistent with an increase of the control parameter J upon pressure, bringing this compound into the Fermi-liquid regime. The pressure dependence of the temperature T_{FL} below which $\rho_a \sim T^2$, is also consistent with the location of U_2Pt_2In at or close to a QCP. A highly anisotropic resistivity component mainly present for ***I*** ∥ **c** is strongly enhanced upon pressure. A minimum in $\rho_c(T)$ develops as a consequence of this enhancement. The origin of this extra component remains unclear.

The effect of Th doping can be considered, in a first approach, as being equivalent to negative hydrostatic pressure. A comparison between the unit-cell contraction upon application of pressure and the unit-cell expansion upon Th doping, yields a value of -20.4 GPa/x. This implies that $\Delta V/V_0$ for x = 0.03, 0.05, 0.08 and 0.1 corresponds to - $\Delta V/V_0$ for p = 0.6, 1.0, 1.6 and 2.0 GPa, respectively.

Therefore, magnetic order could be expected to occur for the Th-doped compounds. The ordering temperature should increase with increasing Th content. Although the preliminary μSR experiments described are consistent with this hypothesis, the specific-heat results seem to contradict it. The presence of impurity phases in the samples unfortunately hampers the proper determination of the magnetic phase diagram of $(U_{1-x}Th_x)_2Pt_2In$. Therefore, the results regarding Th doping presented in this chapter, should be considered as preliminary and taken with caution.

Assuming that the atomic coordinates do not change with pressure, the isotropic compressibility indicates that the primary effect of pressure is a uniform reduction of the interatomic distances. Therefore, the hybridization matrices can be calculated for U_2Pt_2In under pressure. The total hybridization V_{cf} increases about 2.3% from p=0 to p = 1.8 GPa. The

temperature T_{FL} below which a $\rho \sim T^2$ behaviour is observed is plotted in Figure 6.17b as a function of V_{cf}^2, where $V_{cf}^2 \propto J$.

The antiferromagnetic ordering temperature of U_2Pd_2In decreases slightly with pressure, as evidenced by the resistivity measurements. Taking for U_2Pd_2In the same compressibility value as for U_2Pt_2In, the hybridization can be calculated in the same way as before. From p=0 to p = 1.8 GPa, V_{cf} increases 2.4%. The values of T_N are also shown in Figure 6.17b.

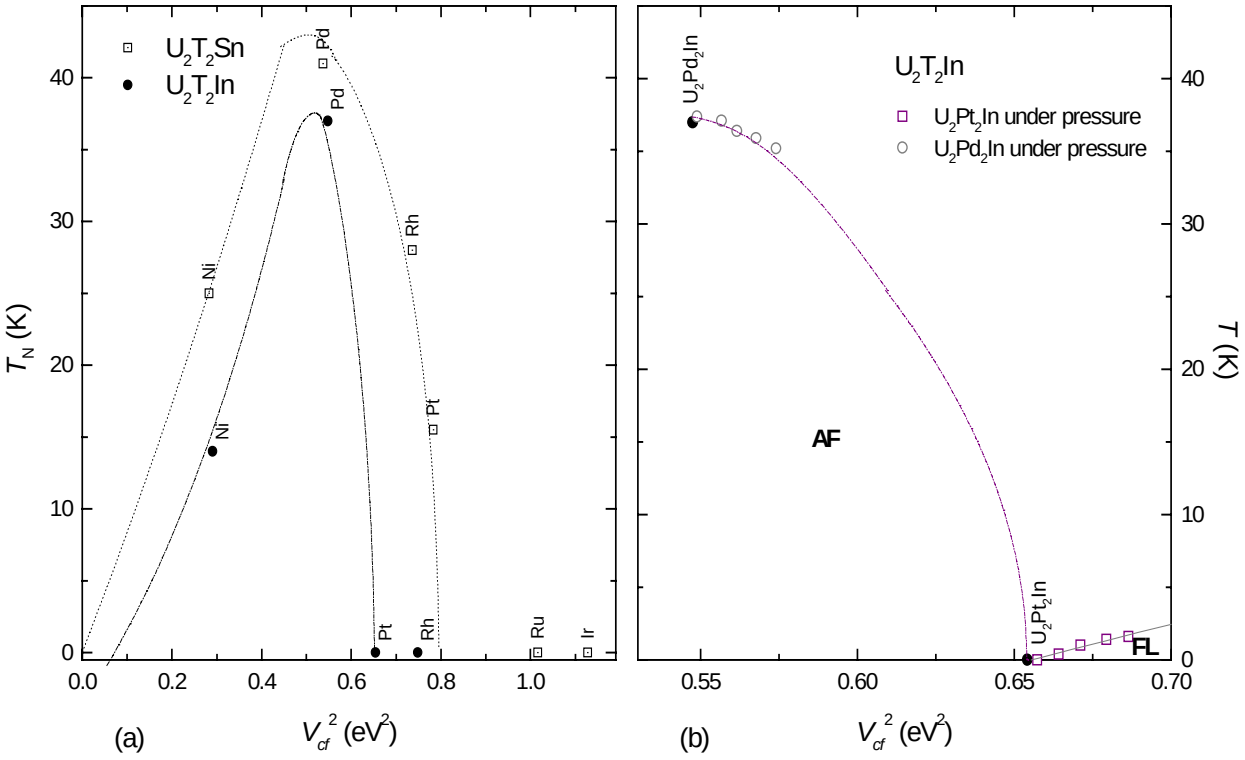

Figure 6.17 - (a) Doniach phase diagram for the U_2T_2X (X=In, Sn) family of compounds. (b) Possible phase diagram around U_2Pt_2In. The lines are guides to the eye.

Recently, magnetization, resistivity and neutron-diffraction studies on the system $U_2(Pt_{1-x}Ni_x)_2In$ have been reported [25]. No magnetic order was found down to 1.7 K for the polycrystalline samples with $x \leq 0.4$. For $x \geq 0.5$, antiferromagnetism is present with T_N increasing from ~ 11 K for x = 0.5 to ~ 14 K for x = 1. The evolution of T_N upon Ni doping is not consistent with the Doniach phase diagram for the U_2T_2In compounds (Figure 6.17a). However, there is a strong suppression of the heavy-fermion character of U_2Pt_2In upon Ni doping which might reflect a strong modification of the density of states at the Fermi surface [25].

The tentative phase diagram presented in Figure 6.17b is consistent with the location of U_2Pt_2In at or close to a quantum critical point (QCP). Whether the non-Fermi liquid behaviour is

present only at the QCP or for a finite region of J values around the QCP is a question that can only be answered by a more thorough study of the phase diagram. This could be done by investigating single-phase samples of $(U_{1-x}Th_x)_2Pt_2In$ or preferably $U_2(Pt_{1-x}Pd_x)_2In$.

References

1. T.T.M. Palstra, A.A. Menovsky and J.A. Mydosh, Phys. Rev. B 33 (1986) 6527.
2. A. de Visser, A. Menovsky and J.J.M. Franse, Physica B 147 (1987) 81.
3. L. Havela, V. Sechovský, P. Svoboda, H. Nakotte, K. Prokeš, F.R. de Boer, A. Seret, J.M. Winand, J. Rebizant, J.C. Spirlet, A. Purwanto and R.A. Robinson, J. Magn. Magn. Mater. 140-144 (1995) 1367.
4. L.C.J. Pereira, Ph.D. Thesis, University of Lisbon, 1998 (unpublished).
5. A. Rosch, Physica B 280 (2000) 341.
6. A. Yoshimori and H. Kasai, J. Magn. Magn. Mater. 31-34 (1983) 475.
7. T. Kagayama and G. Oomi, in "Transport and Thermal Properties of *f*-Electron Systems" (G. Oomi, H. Fujii and T. Fujita, eds.), Plenum Press, New York, 1993, p. 155.
8. P. Estrela, T. Naka, A. de Visser, F.R. de Boer, L.C.J. Pereira and M. Almeida, Physica B 281-282 (2000) 381.
9. A.M. Strydom and P. de V. du Plessis, Physica B 223-224 (1996) 222.
10. A.M. Strydom and P. de V. du Plessis, Physica B 230-232 (1997) 62.
11. P.H. Frings and J.J.M. Franse, J. Magn. Magn. Mater. 51 (1985) 141.
12. L.C.J. Pereira, J.C. Waerenborgh, I. Catarino, G. Bonfait, M. Godinho and M. Almeida, J. Alloys Compounds, in press.
13. H. Nakotte, Ph.D. Thesis, University of Amsterdam, 1994 (unpublished).
14. A. Schenck and F.N. Gygax, in "Handbook of Magnetic Materials" vol. 9 (K.H.J. Buschow, ed.), Elsevier, Amsterdam, 1995, p. 57.
15. A. Purwanto, R.A. Robinson, L. Havela, V. Sechovský, P. Svoboda, H. Nakotte, K. Prokeš, F.R. de Boer, A. Seret, J.M. Winand, J. Rebizant and J.C. Spirlet, Phys. Rev. B 50 (1994) 6792.
16. K. Prokeš, H. Nakotte, L. Havela, V. Sechovský, L.C.J. Pereira, C. Rijkeboer, A. Seret, J.C. Spirlet, P. Svoboda and F.R. de Boer, Physica B 223-224 (1996) 225.
17. J.A. Paixão, L.C.J. Pereira, P. Estrela, M. Godinho, M. Almeida, L. Paolasini, M. Bonnet and J. Rebizant, J. Phys.: Condens. Matter 11 (1999) 2115.
18. L. Havela, V. Sechovský, P. Svoboda, M. Diviš, H. Nakotte, K. Prokeš, F.R. de Boer, A. Purwanto, R.A. Robinson, A. Seret, J.M. Winand, J. Rebizant, J.C. Spirlet, M. Richter and H. Eschrig, J. Appl. Phys. 76 (1994) 6214.
19. L. Menon, P. de V. du Plessis and A.M. Strydom, Solid State Commun. 106 (1998) 519.

20. J.A. Paixão, G.H. Lander, P.J. Brown, H. Nakotte, F.R. de Boer and E. Brück, J. Phys.: Condens. Matter 4 (1992) 829.
21. L.C.J. Pereira, J.A. Paixão, P. Estrela, M. Godinho, F. Boudarot, M. Bonnet, J. Rebizant, J.C. Spirlet and M. Almeida, J. Phys.: Condens. Matter 8 (1996) 11167.
22. A. Domman, F. Hulliger, T. Siegrist and P. Fischer, J. Magn. Magn. Mater. 67 (1987) 323.
23. A. Martin-Martin, L.C.J. Pereira, G.H. Lander, J. Rebizant, F. Wastin, J.C. Spirlet, P. Dervenagas and P.J. Brown, Phys. Rev. B 59 (1999) 11818.
24. H. Nakotte, A. Purwanto, R.A. Robinson, K. Prokeš, J.C.P. Klaasse, P.F. de Châtel, F.R. de Boer, L. Havela, V. Sechovský, L.C. J. Pereira, A. Seret, J. Rebizant and J.C. Spirlet, Phys. Rev. B 53 (1996) 3263.
25. V.H. Tran, A. Hoser and M. Hofmann, J. Phys.: Condens. Matter 12 (2000) 1029.

7. Non-Fermi liquid behaviour in other uranium compounds

In this chapter, the results are presented of the measurements of the thermal, magnetic and transport properties of a few other uranium intermetallic compounds, which show non-Fermi liquid behaviour (NFL) and/or quantum critical points.

The first compound is a stoichiometric one: $U_3Ni_3Sn_4$. NFL behaviour is observed for 0.5 K < T < 5 K [1], while at lower temperatures the Fermi liquid (FL) state is attained [2]. Upon applying pressure, the FL regime becomes more robust, as it is observed up to higher temperatures [3]. As it will be shown, the data are consistent with the location of $U_3Ni_3Sn_4$ close to (but not *at*) an antiferromagnetic quantum critical point (QCP).

The second system is the pseudobinary series $U(Pt_{1-x}Pd_x)_3$. Pure UPt_3 is an unconventional superconductor. Upon alloying with Pd, superconductivity is suppressed and an antiferromagnetic phase with "large" ordered moments is found for $0.006 < x < 0.1$. At the critical concentration $x_c = 0.006$, both the superconducting and antiferromagnetic phase lines meet at a (T = 0 K) QCP [4].

The last material is the system $URh_{1-x}Ni_xAl$. On the Ni-rich side of the magnetic phase diagram antiferromagnetism exists, while the compounds with a low Ni content order ferromagnetically. The antiferromagnetic and ferromagnetic phases meet at $x = 2/3$, where magnetism vanishes and NFL properties are observed [5].

The experiments, of which the results are presented in this chapter, include:

- specific-heat measurements on $U_3Ni_3Sn_4$ single crystals at 0.1 K $\leq T \leq$ 5 K;
- muon spin relaxation experiments on $U_3Ni_3Sn_4$ single crystals at 2 K $\leq T \leq$ 10 K;
- resistivity measurements under hydrostatic pressures up to 1.8 GPa on $U_3Ni_3Sn_4$ single crystals at 0.3 K $\leq T \leq$ 300 K;
- muon spin rotation experiments on polycrystalline samples of $U(Pt_{1-x}Pd_x)_3$ with x = 0.007, 0.008 and 0.009 in a transverse field of 0.01 T at 0.04 K $\leq T \leq$ 2 K;
- resistivity measurements on a polycrystalline sample of $URh_{1/3}Ni_{2/3}Al$ at 0.05 K $\leq T \leq$ 300 K.

These results have been published [1,2,5] or are submitted for publication [3,4]. In this chapter, these papers are partially reproduced.

7.1. $U_3Ni_3Sn_4$

7.1.1. Non-Fermi liquid behaviour in $U_3Ni_3Sn_4$

The ternary $U_3T_3Sn_4$ compounds (where T = Ni, Cu, Pt, Au) crystallize in the cubic $Y_3Au_3Sb_4$-type structure (space group $I\bar{4}3d$) which is a filled variant of the Th_3P_4-type [6]. The key feature of this system is that the 5*f*-hybridization of the U atoms can be systematically increased by adding relatively small transition element atoms into voids in the Th_3P_4-type structure [6]. Indeed, different magnetic ground states (paramagnetism and weak magnetic order) can be found in the $U_3T_3Sn_4$ family of compounds, including several that exhibit heavy-fermion (HF) behaviour. Only the Cu variant orders magnetically (antiferromagnet at T_N = 12 K) while the other analogues are paramagnetic [7]. Of special interest are the striking departures from the standard FL theory of metals observed in nominally stoichiometric $U_3Ni_3Sn_4$ single crystals [1]. The magnetic, transport and specific-heat properties of $U_3Ni_3Sn_4$ are consistent with recent theoretical models based upon classical fluctuations near an antiferromagnetic QCP

Single crystals of $U_3Ni_3Sn_4$ and $U_3Cu_3Sn_4$ were grown by the Kyropoulos technique from the top of the melt by means of a cooled-seed crystal holder. Bulk charges were first prepared by induction melting with 3:3:4 atomic ratios of pure U (depleted), Ni or Cu, and Sn, respectively, each of at least 99.9% purity. Finally single-crystalline samples of $U_3Ni_3Sn_4$ and $U_3Cu_3Sn_4$ were

grown by slowly cooling a semi-levitated melt of the bulk charges in a cold crucible using an induction furnace. The rate of cooling was approximately 40°C/h between 1600-1400°C and 50°C/h between 1400-800°C. The obtained solid products were about 2-2.5 cm in diameter, and consisted of many crystalline grains, from which single-crystals with dimensions ranging from 0.5 to 2 mm^3 were extracted.

Single-crystal X-ray diffraction (XRD) data, collected at room temperature, are consistent with the cubic space-group $I\bar{4}3d$. The unit-cell parameters of $U_3Ni_3Sn_4$ and $U_3Cu_3Sn_4$ are 9.3524(5) Å and 9.4956(5) Å, respectively.

Previously the heat capacity of a $U_3Ni_3Sn_4$ single crystal [1] in the temperature interval 0.3-5 K was described using the expression:

$$c = (\gamma_0 - \alpha\sqrt{T})T + \beta T^3 + DT^{-2} \quad , \qquad (7.1)$$

where $c_E = (\gamma_0 - \alpha\sqrt{T})T$ is the electronic contribution, $c_L = \beta T^3$ the lattice contribution, and $c_N = D/T^2$ represents the high-temperature form of a nuclear Schottky term [10]. The best-fit coefficients obtained were $\gamma_0 = 0.124$ J/mol$_U$K^2, $\alpha = 0.0151$ J/mol$_U$K$^{2.5}$, $\beta = 2.07 \times 10^{-3}$ J/mol$_U$K^4 and $D = 4.62 \times 10^{-4}$ JK/mol$_U$. From the value of β we estimated a Debye temperature $\theta_D \approx$ 210 K [1]. This description is in agreement with a renormalization group theory [8], which predicts $\gamma \sim \gamma_0 - \alpha\sqrt{T}$ near a zero-temperature antiferromagnetic instability (NFL behaviour). A non-universal scale factor $T_0 \approx$ 10 K was estimated using the fitted value of $\alpha = (15/64)k_B N_A N[2/\pi T_0]^{3/2}\xi(5/2)$ [11]. This value of T_0 corresponds very well with the onset temperature of the non-analytic behaviour of the magnetic susceptibility and resistivity.

Alternatively, recent experimental [12] and theoretical [13] work proposes that NFL behaviour might be caused by a competition between RKKY and Kondo interactions in the presence of atomic disorder leading to a Griffiths phase (large magnetic clusters) close to a QCP. We found that the NFL behaviour of nominally stoichiometric $U_3Ni_3Sn_4$ single-crystals can also be described by a divergent power law predicted by this model, i.e., $c(T)/T \propto \chi(T) \propto T^{-1+\lambda}$ with $\lambda = 0.7$ [1]. The best-fit coefficients yielded electronic, lattice and nuclear contributions that differ by only a few percent from those obtained using the renormalization group theory form of Equation 7.1.

New heat capacity data spanning the temperature interval 0.1-300 K for a $U_3Ni_3Sn_4$ single-crystal are presented in Figure 7.1. A ^{3}He/^{4}He dilution refrigerator was used for attaining temperatures down to 0.1 K, while the high temperature data were obtained in a standard ^{4}He

cryostat using a semi-adiabatic method. The phononic contribution to the high temperature specific heat can be properly estimated for comparison to previous results. Fitting the high temperature data with a Debye function [14] we obtain the value $\theta_D = 208$ K. The solid line in Figure 7.1 is the sum of the numerical solution of the Debye integral and linear electronic contribution.

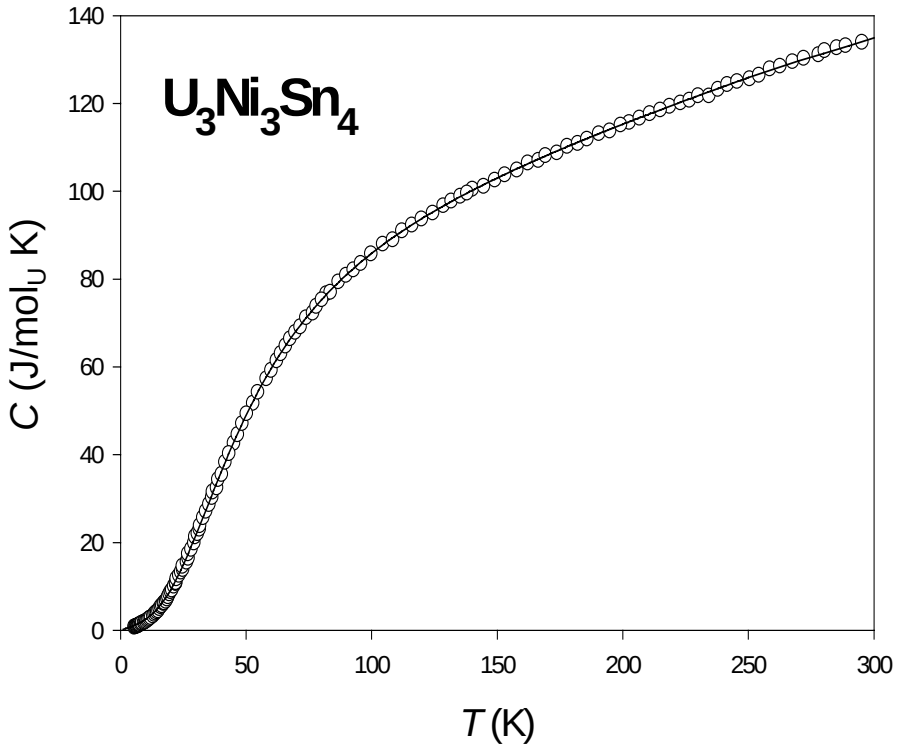

Figure 7.1 - Temperature dependence of the specific heat of single-crystalline $U_3Ni_3Sn_4$. The solid line is a fit to the data with the sum of the Debye approximation of the phonon contribution and the linear electronic term to the specific heat.

Data for c/T over the temperature range 0.1-5 K are plotted versus the logarithm of temperature in Figure 7.2. The lower temperature data make it clear that the previously calculated nuclear contribution to the specific heat was overestimated [1], since the specific heat data below 0.4 K exhibit a tendency toward saturation, in contrast with what would be expected from an important nuclear contribution to the specific heat, unless a Schottky anomaly (maximum) takes place in the temperature range 0.1–0.2 K. However, this would be very unlikely considering that: i) although quadrupolar interactions from ^{235}U and ^{62}Ni could yield a specific heat Schottky anomaly in the measured temperature range, the fact that these isotopes form very small quantities of $U_3Ni_3Sn_4$ (<1 at.% for the formula unit) makes it difficult to conceive that such contribution would be observable with the relatively large electronic background in $U_3Ni_3Sn_4$;

ii) the I = 1/2 Sn isotopes (that have no quadrupolar interactions) would be expected to give rise to a Schottky maximum only at much lower temperatures.

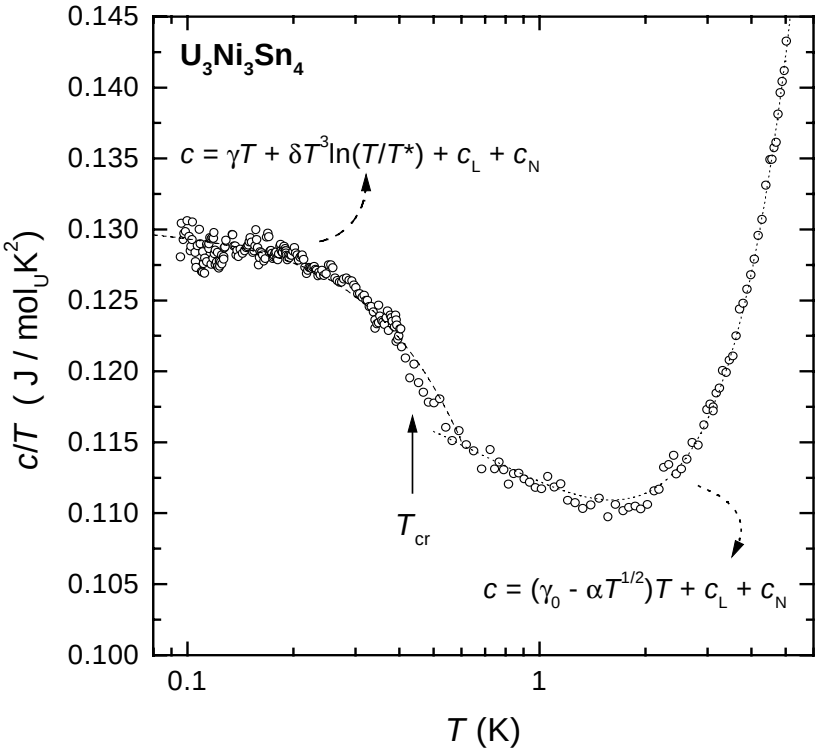

Figure 7.2 - $U_3Ni_3Sn_4$ low temperature specific heat divided by temperature versus log$T$. The lines are fits to the data with Equations 7.1 and 7.2 (see text).

Another possibility would be a crossover to a Fermi liquid regime at the lowest temperatures, which would require a saturation of c/T as $T \to 0$. In fact, the low temperature data below $T = 0.4$ K can be fitted with a modified Fermi liquid expression of the type:

$$c = \gamma T + \delta T^3 \ln(T/T^*) + c_L + c_N \quad , \tag{7.2}$$

where T^* is a characteristic spin fluctuation temperature [15-16]. The lattice contribution can be fixed using our high temperature Debye fit, while for the nuclear contribution we used $D = 6.45 \times 10^{-8}$ JK/mol$_U$, which corresponds to a typical hyperfine field of $B_{hf} = 0.5$ T for the Sn isotopes with I = 1/2, consistent with preliminary Mössbauer experiments on $U_3Ni_3Sn_4$ single crystals [17]. Using this expression we obtain a characteristic spin fluctuation temperature T^* of the order of T_0 and a Sommerfeld coefficient $\gamma = 0.130$ J/mol$_U$K^2. In Figure 7.2, we present the fits to the data using the form of Equation 7.1 for $T > 0.5$ K, and Equation 7.2 for $T < 0.4$ K, considering the same values of c_L and c_N for both temperature ranges. The saturation behaviour of the heat capacity can be interpreted as the onset of a degenerate Fermi liquid regime for

$T << 0.5$ K. Defining T_{cr} as a crossover temperature to a Fermi liquid state, i.e. the temperature below which Equation 7.2 applies, we obtain $T_{cr} = 0.40(2)$ K. With this reduced nuclear contribution Equation 7.1 only holds down to $T \sim 0.5$ K, which means that there is a crossover region in the temperature range 0.4-0.5 K separating a non-Fermi liquid to a Fermi liquid regime.

An assessment of the potential existence of a Schottky term in the specific heat can only be made by studying the effect of a magnetic field, or the acquisition of data for $T < 0.1$ K.

We have characterized the heat capacity, microstructure and crystal structure of $U_3Ni_3Sn_4$ and $U_3Cu_3Sn_4$ single-crystals. $U_3Cu_3Sn_4$ is a heavy-fermion antiferromagnet while nominally stoichiometric $U_3Ni_3Sn_4$ is a nearly magnetic NFL compound.

We find that satisfactory fits of the heat capacity data for $U_3Ni_3Sn_4$ in the temperature range 0.5-5 K always require a dominant electronic term which exhibits a near-square-root temperature dependence, consistent with a theoretical model for NFL systems near a zero-temperature quantum transition from magnetic to non-magnetic states [8] or an alternative Griffiths phase model [13]. It should be noted that the renormalization group theory treatment does not include the effects of disorder, which must be present in real systems to some degree, while the Griffiths phase model includes disorder as a crucial ingredient.

Previously we have undertaken a thorough analysis of the heat capacity and susceptibility of nominally stoichiometric $U_3Ni_3Sn_4$ [1], and conclude that several NFL models (e.g. multichannel Kondo [18] and Kondo disorder [19]) commonly considered in the contemporary literature do not describe the entire data set known for this material. All attempts to include a logarithmic heat capacity term resulted in an unphysically high characteristic temperature scale T_0 [1]. On the other hand, the scaling temperature $T_0 \approx$ 10 K, obtained from low temperature analysis based on renormalization group theory, is consistent with the onset of the non-analytic behaviour of physical properties in this material. Having extended heat capacity measurements to the lower temperatures we found a crossover to a Fermi liquid state below 0.4 K described by a $T^3 \ln T$ term to the specific heat, characteristic of spin fluctuation phenomena. The crossover to a Fermi liquid state is a characteristic of NFL materials that are imprecisely tuned to a QCP [8], due to unfavourable conditions of a control parameter such as pressure, magnetic field, composition or atomic disorder. In the case of nominally stoichiometric $U_3Ni_3Sn_4$, such a non-thermal critical parameter might be vacancy doping which governs the degree of *spd-f* hybridization leading to competition between NFL-FL states. On the other hand, a possible marginal Fermi liquid ground state can not be ruled out. The precise role of small amounts of

disorder detected by XRD analysis in nominally stoichiometric $U_3Ni_3Sn_4$ single crystals [1] must be investigated by further studies of carefully characterized samples.

The moderate size of the Sommerfeld coefficient $\gamma \sim 0.130$ J/mol$_U$K^2 and reduction of $\mu_{eff} = 2.0\ \mu_B$/U [1] from 3.62 or 3.58 μ_B expected for U^{3+} or U^{4+} free ions, respectively suggest significant hybridization between 5*f* and itinerant electron states takes place in $U_3Ni_3Sn_4$. The replacement of the Ni atoms by Cu gives rise to an increase in the number of 3*d* electrons, leading to a dehybridization of the 5*f* states with the 3*d* band. This is consistent with the observed lattice expansion on replacing Ni (a = 9.3524(5) Å) with Cu (a = 9.4956(5) Å), the increase of γ by a factor of about 3, and development of antiferromagnetism below 14 K in $U_3Cu_3Sn_4$ with an effective magnetic moment $\mu_{eff} = 3.3\ \mu_B$/U, corresponding to either a $5f^2$ or $5f^3$ uranium configuration. The apparent variation in 5*f* hybridization with transition element substitution, the crossover from a Fermi liquid ground state in $U_3Ni_3Sn_4$ to weak antiferromagnetism with $T_N = 14$ K in $U_3Cu_3Sn_4$, and the observation of NFL properties in $U_3Ni_3Sn_4$ for the temperature range 0.5-5 K, imply that a QCP should exist in this series of materials over some range of composition and/or pressure in the vicinity of stoichiometric $U_3Ni_3Sn_4$.

7.1.2. Recovery of the Fermi liquid state in $U_3Ni_3Sn_4$ under pressure

The specific heat of single-crystalline $U_3Ni_3Sn_4$ shows a temperature dependence of the type $c/T \sim \gamma_0 - \alpha T^{1/2}$ in the temperature interval 0.5-5 K [1,2]. This is consistent with theoretical models for NFL systems near a zero-temperature antiferromagnetic (AF) QCP [8,9]. Below about 0.4 K, there is a crossover to a FL state [2]. It is interesting to compare $U_3Ni_3Sn_4$ with $U_3Cu_3Sn_4$. The latter compound is an antiferromagnet with $T_N = 14$ K [2]. Replacement of Ni by Cu results in an increase of the number of 3*d* electrons, leading to a decrease of the hybridization of the 5*f*-states with the 3*d*-band. The hybridization change across the $U_3(Ni,Cu)_3Sn_4$ series, namely the crossover from a FL ground state in $U_3Ni_3Sn_4$ to weak antiferromagnetism in $U_3Cu_3Sn_4$, together with the observation of a NFL region in $U_3Ni_3Sn_4$ suggests that a QCP may exist in this series of compounds.

In order to confirm the absence of magnetic order in $U_3Ni_3Sn_4$, zero-field muon spin relaxation (μSR) experiments were carried out on single-crystalline samples at 2 K and 10 K in the general purpose spectrometer (GPS) of the Paul Scherrer Institute (Switzerland). Best fits to

the spectra were obtained by a depolarization function consisting of a single Gaussian component. The depolarization rate obtained at 10 K is $\Delta_G = 0.044(3)\ \mu s^{-1}$. This small value of Δ can be attributed to a random distribution of the Sn nuclei with spin I = ½ and magnetic moment $\mu = 1.0\ \mu_N$. At 2 K, the depolarization rate slightly increases to $\Delta_G = 0.061(2)\ \mu s^{-1}$. This small increase, if significant, could be attributed to the presence of spin fluctuations in the system associated with the NFL behaviour observed in the specific heat below 5 K. No static magnetic order has been detected in these μSR experiments.

Resistivity measurements were performed on a bar-shaped single crystal of $U_3Ni_3Sn_4$ under hydrostatic pressures up to 1.8 GPa in the temperature range 0.3-300 K. A CuBe piston clamp cell was used with Fluorinert acting as pressure transmitting medium. The pressure values here presented were corrected for an empirical efficiency of 80%. The resistivity was measured using a standard a.c. 4-probe method. Since the crystallographic structure of $U_3Ni_3Sn_4$ is cubic, the resistivity should be isotropic. Therefore, the current was applied along an arbitrary direction.

The low-temperature ($T < 10$ K) resistivity curves at $p = 0$, 0.6 GPa and 1.8 GPa are shown in Figure 7.3. At ambient pressure, the resistivity increases slowly as temperature is decreased below room temperature (RT), reaching a maximum value at $T_{max} \sim 240$ K. Below this temperature the resistivity decreases and coherent scattering sets in at lower temperatures. A low residual-resistivity value of $\rho_0 = 6\ \mu\Omega$cm is attained, indicating that the single crystal is relatively clean ($RRR \equiv \rho_{RT}/\rho_0 \approx 60$).

In order to account for possible changes in the distance between the voltage contacts upon applying pressure, ρ_{RT} was assumed to be pressure independent. This assumption is supported by the resulting negligible pressure dependence of ρ_0. Pressure has the effect of reducing the resistivity values. At the lowest temperatures, a tendency to FL-like behaviour $\rho \sim T^2$ is clearly observed (Figure 7.3)

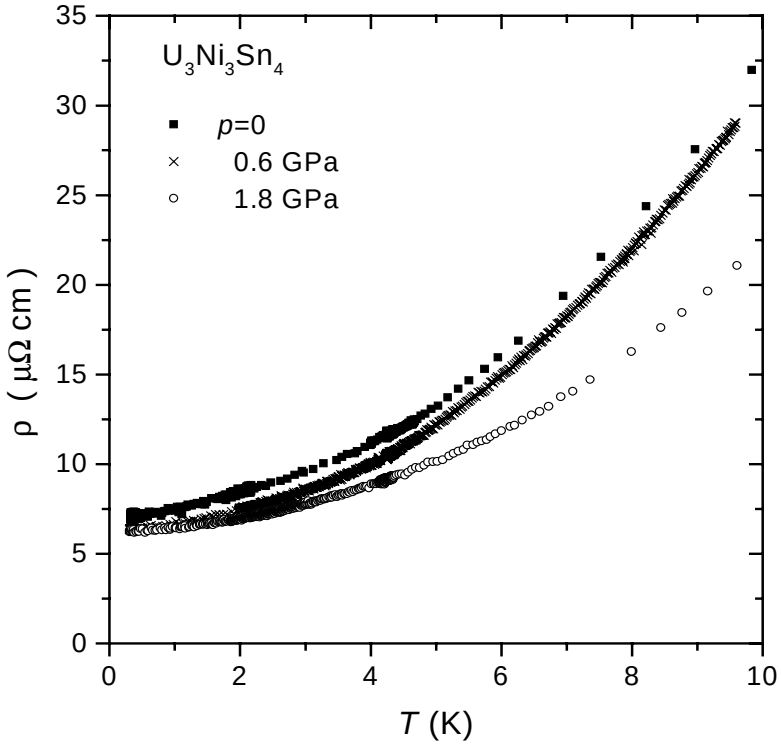

Figure 7.3 - Temperature dependence of the resistivity of single-crystalline $U_3Ni_3Sn_4$ at $p = 0$, 0.6 and 1.8 GPa. The arrows indicate $T_{\rho FL}$ for $p = 0.6$ and 1.8 GPa.

The pressure dependence of the temperature $T_{\rho FL}$ below which the resistivity follows the relationship $\rho = \rho_0 + AT^2$ is shown in Figure 7.4. $T_{\rho FL}$ follows the pressure dependence $T_{\rho FL} = a\,(p-p_c)^{\nu}$, with $p_c = -0.04(2)$ GPa, $\nu = 0.50(7)$ and $a = 2.0(1)$ KGPa$^{-\nu}$ (Figure 7.4).

At the proximity to an AF QCP, $T_{\rho FL}$ is predicted within the theory of Millis [8] to vary as $T_{\rho FL} \sim (p-p_c)$, where p_c is the critical pressure (i.e. the pressure value at which the QCP occurs). However, according to the theory of Rosch [20] for the resistivity of HF compounds close to an AF QCP, the linear behaviour of $T_{\rho FL}$ (p) depends on the amount of disorder in the system. The less disordered the material is, the narrower the region $T_{\rho FL} \sim (p-p_c)$. Above this region, $T_{\rho FL} = a\,(p-p_c)^{1/2}$. In the very clean limit, the linear behaviour of $T_{\rho FL}$ (p) is not observed.

The RRR value of 60 of $U_3Ni_3Sn_4$ implies that the range where $T_{\rho FL} \sim (p-p_c)$ should be narrow. Due to the limited number of data points at low pressures, it is not possible to clearly distinguish the range in which this linear behaviour is observed. The location of a QCP at $p_c = -0.04(2)$ GPa is in agreement with the observed NFL behaviour in the specific heat of $U_3Ni_3Sn_4$ for $0.5 < T < 5$ K.

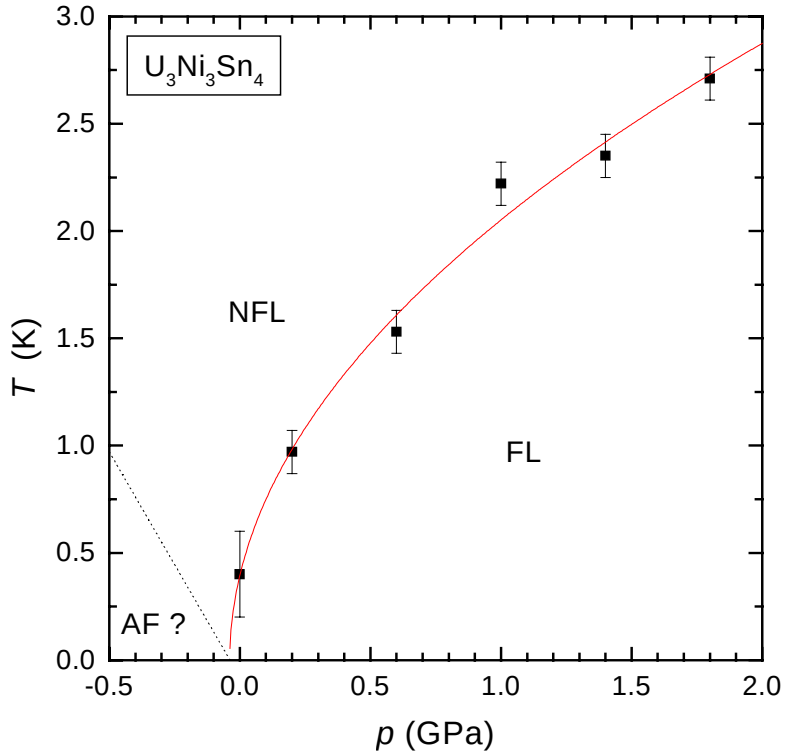

Figure 7.4 - Pressure dependence of the temperature below which a $\rho \sim T^2$ behaviour is observed in $U_3Ni_3Sn_4$. The solid line represents a $T_{\rho FL} = a(p-p_c)^{1/2}$ fit.

The FL resistivity coefficient A is related to the coherence temperature T_{coh}. In the FL regime and close to a QCP, ,T_{coh} is related to the electronic specific-heat coefficient γ by $\gamma \propto T_{coh}^{-1}$ [21]. On the other hand, $A \propto \gamma^2$ according to the Kadowaki-Woods relation for HF compounds [22]. The volume dependence of T_{coh} is given by the Grüneisen parameter Γ_{coh} defined as

$$\Gamma_{coh} = -\frac{\partial \ln T_{coh}}{\partial \ln V}\bigg|_{V=V_0} = -\left(\frac{\Delta V}{V_0}\right)^{-1} \ln \frac{T_{coh}}{T_{coh,0}} \quad , \tag{7.3}$$

where $V_0 \equiv V(p=0)$ and $T_{coh,0} \equiv T_K(p=0)$. Using $\Delta V/V_0 = -\kappa p$, where κ is the compressibility, the pressure dependence of A can be written as

$$A(p) = A(p=0)\exp(-2\kappa\Gamma_{coh}\, p) \quad . \tag{7.4}$$

The pressure dependence of A is shown in Figure 7.5. Due to the limited temperature range where $\rho = \rho_0 + AT^2$ at ambient pressure, $A(p=0)$ cannot be reliably determined. Fitting the data with Equation 7.4 yields $\kappa\Gamma_{coh} = 0.29(5)$ GPa^{-1} and $A(p=0) = 0.43(4)$ μΩcmK^{-2}. This value of $\kappa\Gamma_{coh}$ is similar to the value of 0.26 GPa^{-1} obtained for UPt_3 [23] from measurements of γ and A under pressure (see references cited in Ref. 21).

Since $\gamma \sim A^{1/2}$ and $\gamma(p=0) = 0.13$ J/mol$_U$K^2 [2], a value of $\gamma(p = 1.8$ GPa) of about 0.08 J/mol$_U$K^2 can be predicted. The reduction of γ reflects the fact that, upon pressure, the compound is driven away from the magnetic instability and that the interactions between the quasiparticles are reduced.

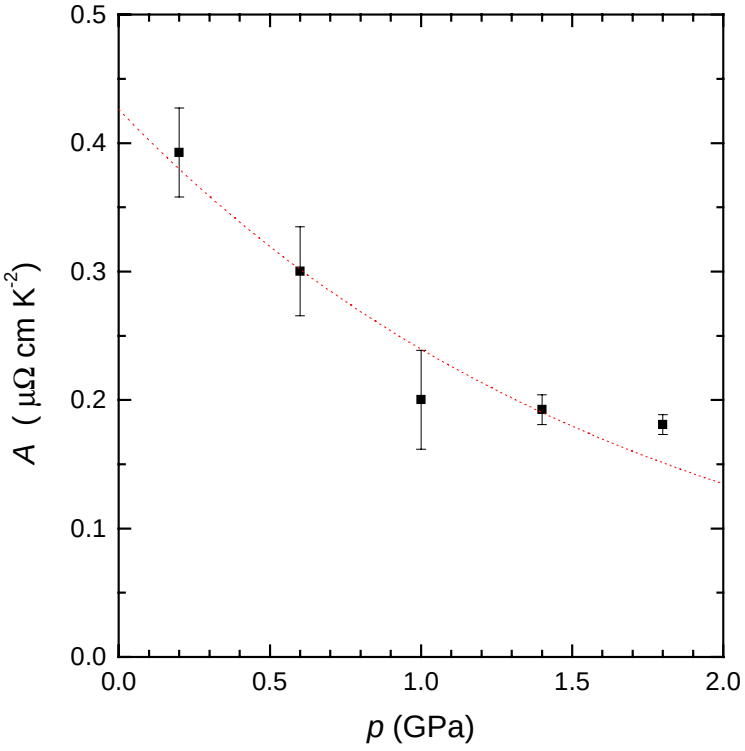

Figure 7.5 - Pressure dependence of the resistivity coefficient A of $U_3Ni_3Sn_4$. The line represents a fit to Equation 7.4.

At high temperatures, a weak maximum in $\rho(T)$ is observed at T=T_{max}, which is attributed to the Kondo effect. T_{max} increases almost linearly from 240 K at p=0 to 265 K at p = 1.8 GPa. Taking T_{max} roughly proportional to T_K [24], the increase of T_{max} reflects the increase of the characteristic temperature of the Kondo effect. Because the observed maximum is weak and the phonon contribution to the resistivity has not been determined, an analysis of $T_{max}(p)$ in terms of the Grüneisen parameter Γ_K is not possible.

In conclusion, upon application of pressure, a FL behaviour is restored in the resistivity of $U_3Ni_3Sn_4$ at temperatures below $T_{\rho FL}$, which increases with increasing p. The pressure dependence of $T_{\rho FL}$ is consistent with the presence of an AF QCP at p_c = -0.04(2) GPa. The pressure dependence of the resistivity coefficient A can be analysed in terms of the Grüneisen parameter for the coherence temperature T_{coh}. Upon pressure, the compound is driven away from

the QCP and the increase of T_{coh} is reflected in a decrease of A. Also T_K, being related to T_{coh}, increases upon pressure. The increase of T_K is seen in the increase of the temperature at which $\rho(T)$ reaches a maximum. The NFL behaviour observed at ambient pressure at temperatures above the FL regime in $U_3Ni_3Sn_4$ is a direct consequence of its proximity to a QCP.

7.2. Magnetic quantum critical point and superconductivity in $U(Pt_{1-x}Pd_x)_3$

For more than a decade now it has been recognized that superconductivity (SC) and magnetism are intimately related in strongly correlated systems, such as the high-T_c cuprates, heavy-fermion materials and organic superconductors [25]. One of the key issues is to identify the nature of the attractive interaction for Cooper pairing. In conventional s-wave superconductors Cooper pairing is mediated by phonons. In strongly correlated electron systems magnetic interactions suppress s-wave SC, and therefore it has been proposed that SC is unconventional and mediated by spin fluctuations [26,27]. Compelling evidence for spin-fluctuation mediated SC [28] has recently been obtained for the magnetically ordered heavy-fermion materials $CePd_2Si_2$ and $CeIn_3$. By tuning these materials towards a magnetic quantum critical point (the Néel temperature $T_N \rightarrow 0$ K), by the application of mechanical pressure, a SC phase appeared.

The heavy-fermion superconductor UPt_3 ($T_c \sim 0.5$ K) has become an exemplary system to study unconventional SC [25,29]. Because of the unusual coexistence of SC and ferromagnetic (FM) spin fluctuations, the latter signalled by a pronounced $T^3 \ln T$ contribution to the low-temperature specific heat [30,31], it has been argued that UPt_3 is an odd-parity spin-fluctuation mediated superconductor [31,32], in close analogy with superfluidity in ^{3}He. The thermodynamic properties and multicomponent SC phase diagram can only be explained by Ginzburg-Landau models, based on an unconventional SC order parameter [29,33-35]. Much attention has been devoted to models where a symmetry-breaking field (SBF) lifts the (spin) degeneracy of the 2D (or 1D) order parameter, which results in a splitting $\Delta T_c = T_c^+ - T_c^-$ of the SC phase transition [33-35]. Experimental evidence [36] has been put forward that the SBF is provided by *small-*

moment antiferromagnetism (SMAF) which sets in at $T_{N,SMAF} \sim 6$ K [37]. This established a clear coupling between magnetism and SC in UPt_3.

The nature of the SMAF state itself is the subject of lively debate. It has been observed convincingly through neutron [36,37] and magnetic x-ray [38] scattering only. The ordered moment, $m = 0.02$ μ_B/U-atom ($T \to 0$), is extremely small, which hampers its detection by standard bulk probes. However, NMR [39] and zero-field muon spin relaxation (μSR) experiments [40,41] also do not signal the small moment (the early μSR results of Ref. 42 have not been reproduced thereafter), which strongly suggests that the moment *fluctuates* at a rate larger than 10 MHz, but on a time scale which appears static to neutrons and X-rays. Therefore, $T_{N,SMAF}$ may be considered to represent a cross-over temperature, rather than being connected to a true phase transition. This is in line with the unusual quasi-linear increase of $m^2(T)$ below $T_{N,SMAF}$ [37].

One of the hallmarks of heavy-fermion materials is the proximity to a magnetic quantum critical point (QCP). In the case of UPt_3 pronounced antiferromagnetic (AF) phase transitions can readily be induced by chemical alloying, e.g. by substituting small amounts of Pt by Pd [43] or U by Th [44]. In the $U(Pt_{1-x}Pd_x)_3$ pseudobinaries, AF order of the spin-density wave type has been observed in the thermal, magnetic and transport properties in the concentration range $0.02 \leq x \leq 0.08$ (see Figure 7.6). Neutron-diffraction experiments [45,46] show that at optimal doping ($x = 0.05$, $T_N = 6$ K) the ordered moment of the so-termed *large-moment antiferromagnetic phase* (LMAF) is substantial, $m = 0.63 \pm 0.05$ μ_B/U-atom, and that the magnetic order parameter is conventional. The magnetic structure consists of a doubling of the nuclear unit cell (space group $P6_3/mmc$) along the a*-axis, with the moments pointing along a*. LMAF is also detected by local probe techniques, such as μSR [41] and NMR [47]. $T_N(x)$ follows a rather conventional Doniach-type phase diagram [48] (see Figure 7.6).

The SMAF phase has clearly a different signature, although the magnetic structure is identical to the one of the LMAF phase. Neutron-diffraction experiments [46] show that SMAF is robust upon alloying with Pd and persists till at least $x = 0.005$. The ordered moment grows upon alloying, but $T_{N,SMAF}(x)$ remains ~ 6 K and does not vary at these small Pd concentrations (see Figure 7.6). Notice that $T_{N,SMAF}$ is also insensitive to the application of pressure [36], unlike the LMAF T_N [49].

All these results strongly suggest that SMAF and LMAF are different phases with a distinctly different nature. As a consequence they might also couple differently to SC. Pressure [36] and alloying experiments [50] are consistent with SMAF acting as SBF. In order to fully

understand the nature of the SC phase, it is important to examine the relation (coexistence or competition) between LMAF and SC as well. Therefore, it is crucial to determine the critical Pd concentration for the emergence of the LMAF phase. In this Letter we present μSR experiments carried out on $U(Pt_{1-x}Pd_x)_3$ samples (x = 0.007, 0.008 and 0.009), which show that the Néel temperature T_N for the LMAF phase is suppressed to 0 K at a Pd concentration $x_{c,af} \approx 0.006$. Combined with our earlier results on the suppression of SC by Pd substitution [50-52], we find that $x_{c,af} \approx x_{c,sc}$ and that unconventional SC is replaced by LMAF. As we will show, these results provide strong evidence for SC mediated by *ferromagnetic* spin fluctuations.

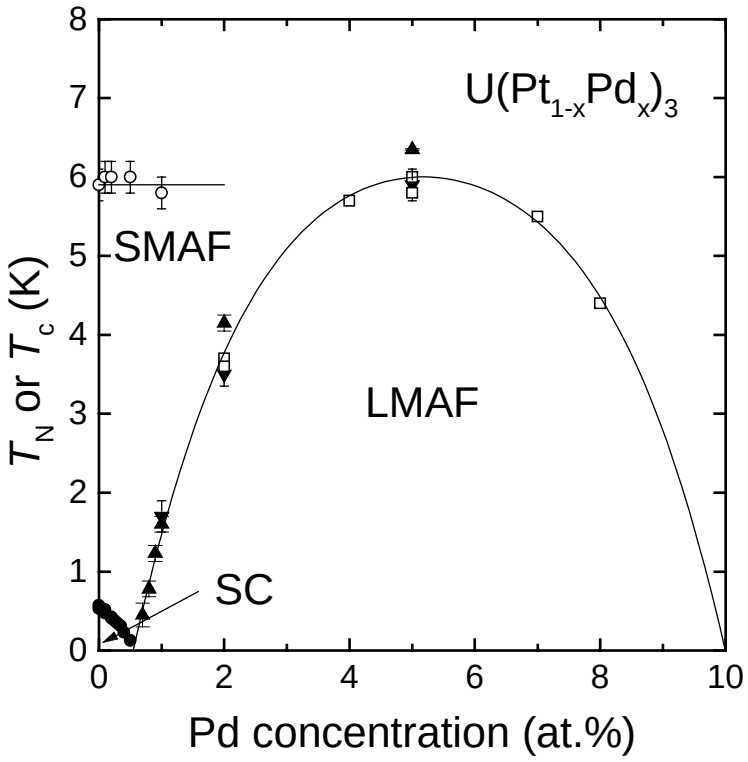

Figure 7.6 - Magnetic and superconducting phase diagram for $U(Pt_{1-x}Pd_x)_3$ alloys. SMAF = small-moment antiferromagnetic phase, LMAF = large-moment antiferromagnetic phase, SC = superconducting phase. Néel temperatures T_N are measured by neutron-diffraction (o and ▼) [46], specific heat (□) [43,46] and μSR (▲) (Ref. 41 and this work). Resistively determined superconducting transition temperatures T_c^+ (●) are taken from Refs. 51 and 52. The solid lines are to guide the eye.

Polycrystalline $U(Pt_{1-x}Pd_x)_3$ samples were prepared in a two-step process. First, master alloys of UPt_3 and $U(Pt_{0.95}Pd_{0.05})_3$ were prepared by arc-melting stoichiometric amounts U (purity 99.98%), Pt and Pd (both with purity 99.999%) on a water-cooled copper crucible in a high-purity argon atmosphere (0.5 bar). Next samples with x = 0.007, 0.008 and 0.009 were prepared by arc-melting together appropriate amounts of the master alloys. After an annealing

procedure (see Ref. 41), four thin platelets (thickness 0.8 mm, area 6×10 mm^2) were prepared by spark-erosion and glued with General Electric varnish on a silver support, in order to cover an area of 12×20 mm^2, which corresponds to the total cross-section of the muon beam. Measurements of the residual resistivity on pieces cut from the annealed buttons are consistent with previous results [51,52], which ensures that Pd dissolves homogeneously in the UPt_3 matrix.

Measurements of the positive muon (μ^+) precession in an applied transverse field of 100 G were conducted at the low temperature μSR facility (LTF) on the πM3 beam line at the Paul Scherrer Institute. The samples were mounted on the cold-finger of a top-loading dilution refrigerator with a base temperature of 0.025 K. As we shall see, the muon spin depolarization rates are very small. Accurate determination of the rates for the samples with $x = 0.007$ and 0.008 was made possible by the use of a kicker device, which ensures that only one muon at a time is present in the sample and that no other muons are present in the spectrometer [53]. This so-called MORE (Muons On REquest) mode allows to extend the μSR time window to 20 μs, with virtually no accidental background, making it possible to measure relaxation rates as small as 0.001 μs^{-1}.

When positive muons come to rest in the sample they start to precess around the local field, B_{loc}, with a precession frequency $\nu_\mu = \gamma_\mu B_{loc}$ ($\gamma_\mu/2\pi = 135.5$ MHz/T is the muon gyromagnetic ratio). The internal dipolar magnetic field distribution in general leads to de-phasing of the precession frequency and consequently the signal is damped. As a first step, we have analyzed the μSR spectra using a Gaussian-damped depolarization function $P_G(t) = A_G\cos(\omega t)\exp(-\Delta^2 t^2/2)$, where A_G is the asymmetry, $\omega = 2\pi\nu_\mu$ and Δ is the Gaussian damping rate. At the highest temperatures, Δ attains a temperature-independent value of ~ 0.06 μs^{-1}, which is consistent with depolarization due to static ^{195}Pt nuclear moments [41]. Upon lowering the temperature, Δ rises progressively, which points to the presence of an additional source of internal dipolar magnetic fields. Improved fit results were obtained using the damped-Gauss muon spin depolarization function

$$P_{DG}(t) = A_{DG}\cos(\omega t)\exp(-\lambda_E t - \Delta^2 t^2/2) \qquad (7.5)$$

with Δ fixed at the observed Pt nuclear depolarization rate ~ 0.06 μs^{-1}. In Equation 7.5 the factor $\exp(-\lambda_E t)$ accounts for damping due to the additional magnetic signal. Because of the low damping rates and the large sample size, the asymmetry A_{DG} is close to the maximum value ~0.3. In Figure 7.7 the temperature dependence of λ_E is shown for all three samples. At the highest

temperatures, λ_E is very small (about 0.003 μs^{-1}) and essentially temperature independent. Upon lowering the temperature, λ_E increases, as the additional source of magnetism emerges. The additional source of magnetism becomes stronger when the Pd concentration increases, and we associate its onset temperature with the Néel temperature T_N for LMAF.

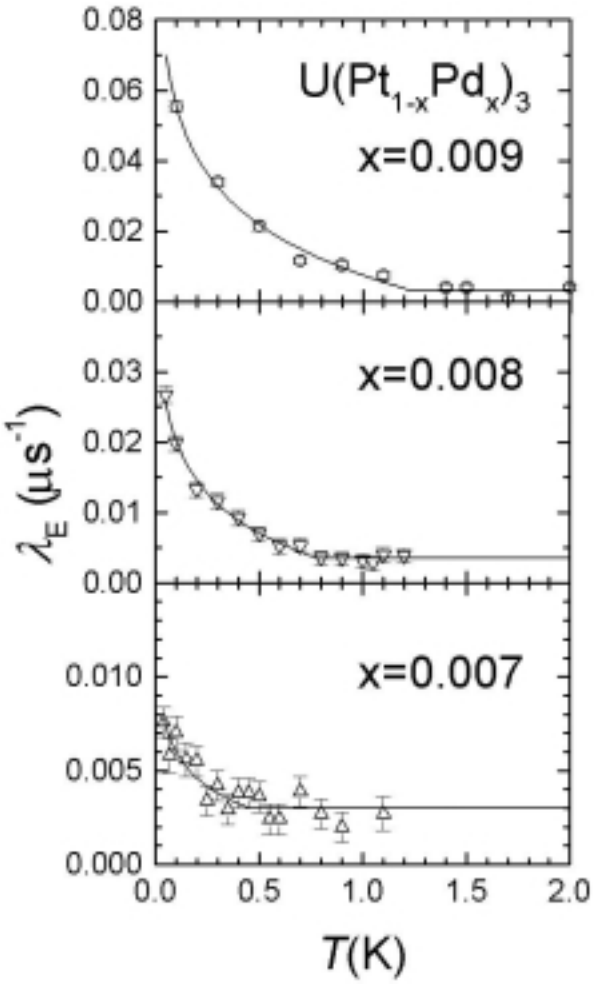

Figure 7.7 - Temperature variation of the exponential relaxation rate, extracted from transverse field (100 G) μSR spectra using Equation 7.5, for $U(Pt_{1-x}Pd_x)_3$ with $x = 0.007$, 0.008 and 0.009. The solid lines show the quasi-logarithmic increase of λ_{LMAF} below T_N and the temperature independent background λ_{BG} above T_N.

In order to extract T_N, we write the observed exponential damping rate as $\lambda_E = \lambda_{BG} + \lambda_{LMAF}$, where λ_{BG} and λ_{LMAF} are due to the background and the LMAF phase, respectively. λ_{BG} may account for small variations of the actual depolarization rate due to Pt nuclear moments, as in the fitting procedure we used the fixed value $\Delta = 0.06\ \mu s^{-1}$. The super-linear increase of λ_{LMAF} is unusual, and can be described phenomenologically, in this limited temperature interval, by a quasi-logarithmic increase $\lambda_{LMAF} \sim -\ln(T/T_N)$. Making use of this

functional dependence and imposing $\lambda_{LMAF}=0$ for $T>T_N$, we obtain T_N values of 1.23±0.10 K, 0.78±0.10 K and 0.45±0.15 K for x = 0.009, 0.008 and 0.007, respectively.

The assignment of the increase of λ_E to the onset of LMAF ordering is based on an analogy with the analysis of the zero-field μSR spectra obtained in the LMAF phase for samples with higher Pd concentrations [41]. For $x \geq 0.01$ the spectra are well described by a two-component depolarization function, consisting of the standard depolarization function of a polycrystalline antiferromagnet and a Kubo-Lorentzian (KL) term, accounting for the spectral distribution of internal fields. Within this phenomenological approach it was observed that the depolarization rate of the KL function, λ_{KL}, scales with the ordered moment as determined by neutron diffraction. Our new results indicate that below x = 0.01 the LMAF state rapidly weakens. The quasi-logarithmic temperature dependence of λ_{LMAF} below T_N shows that the internal magnetic dipolar fields measured at the μ^+ localization site [54] grow only slowly with decreasing temperature.

In Figure 7.8 we show the magnetic and SC phase diagram for $x < 0.012$, highlighting our new μSR results. For x = 0.01, a T_N value of 1.6±0.1 K has been extracted from zero-field μSR data taken on a polycrystal [41], while T_N = 1.7±0.1 K was obtained by single-crystal neutron-diffraction [46]. The SC (T_c^+) phase transition temperatures have been taken from Ref. 51. Our new data for T_N nicely follow the Doniach-diagram type behaviour. From the data in Figure 7.6 and in Figure 7.8, we can safely conclude that the LMAF phase line smoothly extrapolates to T_N=0 at $x_{c,af} \approx$ 0.006. Locating the magnetic QCP near x = 0.006 is consistent with the absence of any signal of the LMAF phase for x = 0.005, as was concluded from zero-field μSR measurements on a polycrystal down to 0.04 K [41], as well as from single-crystal neutron-diffraction data down to 0.1 K [46].

Our results show that *it is the LMAF phase which presents the magnetic instability in U(Pt,Pd)$_3$ and not SMAF*. This is consistent with recent transport measurements on polycrystalline U(Pt,Pd)$_3$ [55], which show clear deviations from Fermi-liquid behaviour in the vicinity of $x_{c,af}$, as predicted for a QCP [56].

Inspecting the phase lines $T_N(x)$ and $T_c^+(x)$ plotted in Figure 7.8, we arrive at a most important conclusion, namely *the phase diagram two quantum critical points coincide*, i.e. the critical concentration for the suppression of SC coincides with the critical concentration for the emergence of LMAF, $x_{c,s} = x_{c,af} = 0.006$. The fact that Pd substitution results in an anomalously

high rate of suppression of T_c^+ [51,52], as well as in the onset of the LMAF phase, indicates that this relationship is not coincidental. Stabilization of the LMAF phase completely suppresses unconventional SC. Recent NMR measurements [39], as well as alloying experiments [57,58], provide strong evidence that the SC wave function has odd parity. This in turn implies that Cooper pairing is driven by FM spin fluctuations, rather than by AF fluctuations [26,32]. Therefore, our experiments indicate that *doping UPt_3 with Pd leads to a shift of the spectral weight from FM to AF fluctuations*. This is not uncommon near a QCP, where the many energy scales become comparable and competition between various phases becomes important. Indeed, inelastic neutron scattering experiments carried out on pure UPt_3 [59] show that the magnetic fluctuation spectrum is complex and has both AF and FM components.

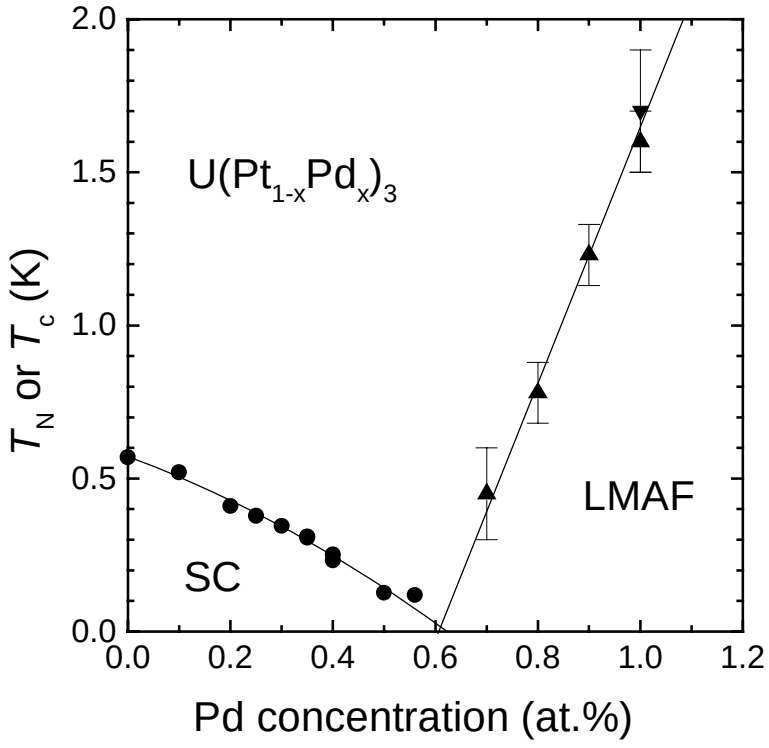

Figure 7.8 - Magnetic and superconducting phase diagram for $U(Pt_{1-x}Pd_x)_3$ alloys with $x < 0.012$. The meaning of the symbols is the same as in Figure 7.6. The solid lines serve to guide the eye.

The phase diagram shown in Figure 7.6, differs from the generic phase diagram, proposed for magnetically ordered pure heavy-fermion materials under pressure [28]. In these materials, the approach to the magnetic QCP at T=0 is circumvented by the occurrence of a SC ground state. T_c is maximum near the critical pressure $p_{c,af}$, which has been interpreted as evidence for SC mediated by AF fluctuations. In the case of $U(Pt,Pd)_3$, however, $T_c \to 0$ at the QCP. This is

naturally explained if *SC in UPt_3 is mediated by FM spin fluctuations,* which cannot coexist at any non-zero temperature with an ordered AF state. This is consistent with the notion that the SMAF state is fluctuating in time.

In conclusion, we have shown that the magnetic instability in $U(Pt,Pd)_3$ is due to the LMAF phase rather than SMAF. The $U(Pt_{1-x},Pd_x)_3$ phase diagram has a critical point at $x \approx 0.006$ where unconventional SC is suppressed and LMAF emerges. The existence of this critical point provides strong evidence for SC mediated by FM spin fluctuations. A complete understanding of the phase diagram and its quantum critical point might prove to be essential in further specifying the SC pairing mechanism. Measurements of the critical exponents of the thermal, magnetic and transport properties in the concomitant non-Fermi liquid regime are needed to identify the character of the magnetic fluctuations [56]. Moreover, the results may be relevant [60] to other strongly correlated systems, such as the high temperature superconductors, which have phase diagrams that exhibit a similar competition between SC and static AF order.

7.3. Possible non-Fermi liquid behaviour in $URh_{1/3}Ni_{2/3}Al$

Ternary intermetallic compounds with the general formula UTX (T = late transition metal, X = *p*-element) crystallizing in the hexagonal ZrNiAl-type of structure exhibit a large variety of magnetic properties [61]. This structure consists of two basal planes, one containing U and 1/3 of T atoms and the other the remaining T atoms and Al. It is well established that the magnetism, which is mainly due to U moments, is controlled by the strength of the hybridization between the *5f*- and the ligand-electronic states. On one hand, hybridization delocalizes the *5f*-states and inhibits magnetic ordering, on the other hand, however, it mediates interaction between them and promotes magnetic ordering. It is therefore not surprising that the magnetic properties of these compounds vary as a function of the constituents, which change the hybridization. Recently, we have started a systematic study of quasiternary compounds with substitutions on the transition-metal sites [62]. Here, we report on the magnetic, thermal and transport properties of $URh_{1/3}Ni_{2/3}Al$, which appears to show anomalous low-temperature behaviour.

$URh_{1/3}Ni_{2/3}Al$ was prepared in polycrystalline form by arc melting stoichiometric amounts of the constituting elements (the purity of U was 99.8%, of the other elements 99.99%). After re-melting and reversing the ingot several times to ensure homogeneity, the resulting ingot was annealed for one week at 700°C in a vacuum-sealed quartz ampoule. After crushing the annealed material under protective atmosphere, X-ray powder diffraction was carried out to verify the structure and lattice parameters. The magnetic susceptibility $\chi(T) = M/H$ was measured between 1.7 and 320 K in fields up to 5 T on a sample consisting of powder that was fixed in random orientation in a SQUID magnetometer (Quantum Design). Electrical-resistivity measurements were performed in the temperature range 0.05-300 K on a bar-shaped sample by means of a standard four-probe method. The temperature dependence of the specific heat was measured between 0.4 and 40 K by means of a semi-adiabatic heat-pulse method.

In Figure 7.9 we show the temperature dependence of (a) the magnetic susceptibility measured in 0.1 T both in zero-field cooled (ZFC) and field-cooled (FC) modes, (b) the specific heat in the absence of a magnetic field and (c) of the electrical resistivity. It is clearly seen that all the three physical properties deviate from the temperature dependencies expected for Fermi-liquid systems. At low temperatures, the FC susceptibility diverges and the ZFC curve exhibits a clear maximum at 10 K above which the FC and ZFC curves coincide. The maximum suggests the presence of AF correlations and the difference between the FC and ZFC curves reminds one of a spin-glass system (SG). For a SG system, some type of disorder in the compound is required. Indeed, recent X-ray and neutron-diffraction studies suggest a random occupation of Rh and Ni atoms of sites in the plane that does not contain U atoms [63].

The specific heat shown in Figure 7.9b exhibits a low-temperature dependence that can be described by a $-\ln(T/T_0)$ dependence with $T_0 \approx 10\,\mathrm{K} \approx -\theta_P/4$ (dashed line in Figure 7.9b), suggesting non-Fermi-liquid (NFL) behaviour. However, the data are equally well described by the expression $c/T \approx T^{\lambda-1}$ with $\lambda = 0.94$ (solid line in Figure 7.9b). To discriminate between the two descriptions, measurements at even lower temperatures would be required.

At high temperatures, as in normal metals, the electrical resistivity decreases with decreasing temperature. However in $URh_{1/3}Ni_{2/3}Al$, it exhibits a minimum near 10 K and a pronounced increase below this temperature. In other words, the aT^2 term is absent or it is very weak. The resistivity can be fitted to a $\rho_0 + a(T/T_0)^{\alpha}$ dependence with a negative a and $\alpha = 0.96$. The best fit is shown in Figure 7.9c by the full line. At an even lower temperature of 0.33 mK, a distinct step-like decrease of the resistivity is found (see inset of Figure 7.9) which we tentatively

attribute to a small amount of UNi_2Al_3[i] which may be present as impurity phase and which exhibits superconductivity around this temperature [64].

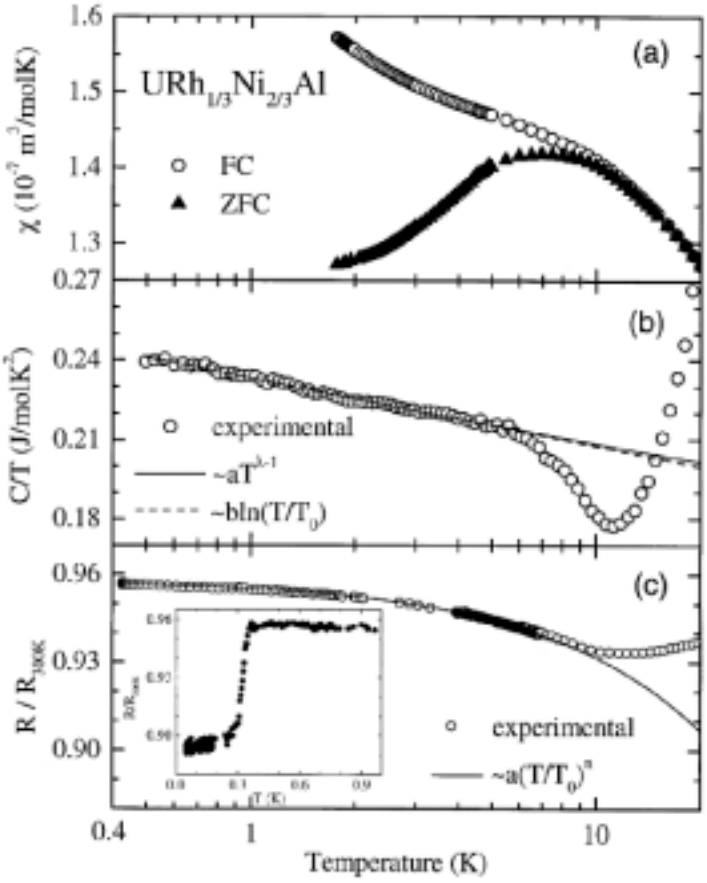

Figure 7.9 - The temperature dependence of the magnetic susceptibility (a), the specific heat (b) and the electrical resistivity of $URh_{1/3}Ni_{2/3}Al$ (c). The curves through the symbols denote the best fits to the expressions given in the text. The inset of (c) shows the low-temperature detail of the electrical resistivity.

In the limit $T \to 0$, the Fermi-liquid theory (FL) predicts a temperature-independent contribution to the specific heat, an aT^2-type of behaviour of the electrical resistivity and a substantial temperature-independent contribution to the magnetic susceptibility. Deviations from the behaviour predicted by FL theory are referred to as NFL behaviour. One of the hallmarks of NFL is divergence at low temperature of the specific heat divided by temperature, C/T, which behaves as $-\ln(T/T_0)$ or as $T^{\lambda-1}$ as found in $URh_{1/3}Ni_{2/3}Al$. It is also clear that the magnetic and transport properties of the $URh_{1/3}Ni_{2/3}Al$ compound cannot be explained solely within the FL theory.

[i] A possible off-stoichiometry of an impurity phase of UNi_2Al_3 ($T_c = 1.2$ K) might reduce its superconducting transition temperature.

References

1. L. Shlyk, J.C. Waerenborgh, P. Estrela, L.E. De Long, A. de Visser and M. Almeida, J. Phys.: Condens. Matter 11 (1999) 3525.
2. L. Shlyk, P. Estrela, J.C. Waerenborgh, L.E. De Long, A. de Visser, D.P. Rojas, F. Gandra and M. Almeida, Physica B 292 (2000) 89.
3. P. Estrela, T. Naka, A. de Visser, F.R. de Boer and L. Shlyk, in preparation
4. A. de Visser, M.J. Graf, P. Estrela, A. Amato, C. Baines, D. Andreica, F. Gygax and A. Schenck, submitted to Phys. Rev.
5. K. Prokeš, I.H. Hagmusa, P. Estrela, J.C.P. Klaasse, A.V. Andreev, V. Sechovský, E. Brück and F.R. de Boer, Physica B 281-282 (2000) 377.
6. A. E. Dwight, Acta Cryst. B 33 (1977) 1579.
7. T. Takabatake, S. Miyata, H. Fujii, Y. Aoki, T. Suzuki, T. Fujita, J. Sakurai and T. Hiraoko, J. Phys. Soc. Jpn. 59 (1993) 4412.
8. A.J. Millis, Phys. Rev. B 48 (1993) 7183.
9. U. Zülicke and A.J. Millis, Phys. Rev. B 51 (1995) 8996.
10. O.V. Lounasmaa, in "Hyperfine Interactions" (A.J. Freeman and R.B. Frankel, eds.), Academic Press, New York, 1967, p.467.
11. Proc. ITP Conference on Non-Fermi Liquid Behaviour in Metals, Santa Barbara, 1996, in J. Phys.: Condens. Matter 8 (1996) 9675 ff.
12. M.C. de Andrade, R. Chau, R.P. Dickey, N.R. Dilley, E.J. Freeman, D.A. Gajewski, M.B. Maple, R. Movshovich, A.H. Castro Neto, G.E. Castilla and B.A. Jones, Phys. Rev. Lett. 81 (1998) 5620.
13. A.H. Castro Neto, G.E. Castilla and B.A. Jones, Phys. Rev. Lett. 81 (1998) 3531.
14. R. Gopal, "Specific Heat at Low Temperatures", Plenum Press, New York, 1966.
15. W. Brenig, H.J. Mikeska and E. Riedel, Z. Phys. 206 (1967) 439.
16. E. Riedel, Z. Phys. 210 (1968) 403.
17. L. Shlyk et al. (unpublished).
18. D.L. Cox and M. Jarrell, J. Phys.: Condens. Matter 8 (1996) 9825.
19. E. Miranda, V. Dobrosavljević and G. Kotliar, J. Phys.: Condens. Matter 8 (1998) 9871.
20. A. Rosch, Physica B 280 (2000) 341.
21. M.A. Continentino, Phys. Rev. B 47 (1993) 11587.
22. K. Kadowaki and S.B. Woods, Solid State Commun. 58 (1986) 507.
23. M.A. Continentino, Phys. Rev. B 57 (1998) 5966.
24. J.S. Schilling, Adv. Phys. 28 (1979) 657.
25. R.H. Heffner and M.R. Norman, Comm. Condens. Matter Phys. 17 (1966) 361.
26. P.W. Anderson, Phys. Rev. B 30 (1984) 1549.
27. K. Miyake, S. Schmitt-Rink and C.M. Varma, Phys. Rev. B 34 (1986) 6554.

28. N.D. Mathur, F.M. Grosche, S.R. Julian, I.R. Walker, D.M. Freye, R.K.W. Haselwimmer and G.G. Lonzarich, Nature 394 (1998) 39.
29. J.A. Sauls, Adv. Phys. 43 (1994) 113.
30. P.H. Frings, J.J.M. Franse, F.R. de Boer and A. Menovsky, J. Magn. Magn. Mater. 31-34 (1983) 240.
31. G.R. Stewart, Z. Fisk, J.O. Willis and J.L. Smith, Phys. Rev. Lett. 52 (1984) 679.
32. C.J. Pethick, D. Pines, K.F. Quader, K.S. Bedell and G.E. Brown, Phys. Rev. Lett. 57 (1986) 1955.
33. D.W. Hess, T.A. Tokuyasu and J.A. Sauls, J. Phys.: Condens. Matter 1 (1989) 8135.
34. R. Joynt, V.P. Mineev, G.E. Volovik and M.E. Zhitomirsky, Phys. Rev. B 42 (1990) 2014.
35. K. Machida and M. Ozaki, Phys. Rev. Lett. 66 (1991) 3293.
36. S.M. Hayden, L. Taillefer, C. Vettier and J. Flouquet, Phys. Rev. B 46 (1992) 8675.
37. G. Aeppli, E. Bucher, C. Broholm, J.K. Kjems, J. Baumann and J. Hufnagl, Phys. Rev. Lett. 60 (1988) 615.
38. E.D. Isaacs, P. Zschack, C.L. Broholm, C. Burns, G. Aeppli, A.P. Ramirez, T.T.M. Palstra, R.W. Erwin, N. Stücheli and E. Bucher, Phys. Rev. Lett. 75 (1995) 1178.
39. H. Tou, Y. Kitaoka, K. Asayama, N. Kimura, Y. Onuki, E. Yamamoto and K. Maezawa, Phys. Rev. Lett. 77 (1996) 1374.
40. P. Dalmas de Réotier, A. Huxley, A. Yaouanc, J. Flouquet, P. Bonville, P. Imbert, P. Pari, P.C.M. Gubbens and A.M. Mulders, Phys. Lett. A 205 (1995) 239.
41. R.J. Keizer, A. de Visser, A.A. Menovsky, J.J.M. Franse, A. Amato, F.N. Gygax, M. Pinkpank and A. Schenck, J. Phys.: Condens. Matter 11 (1999) 8591.
42. R.H. Heffner, D.W. Cooke, A.L. Giorgi, R.L. Hutson, M.E. Schillaci, H.D. Rempp, J.L. Smith, J.O. Willis, D.E. MacLaughlin, C. Boekema, R.L. Lichti, J. Oostens and A.B. Denison, Phys. Rev. B 39 (1989) 11345.
43. A. de Visser, J.C.P. Klaasse, M. van Sprang, J.J.M. Franse, A. Menovsky, T.T.M. Palstra and A.J. Dirkmaat, Phys. Lett. A 113 (1986) 489.
44. A.P. Ramirez, B. Batlogg, E. Bucher and A.S. Cooper, Phys. Rev. Lett. 57 (1986) 1072.
45. P. Frings, B. Renker and C. Vettier, J. Magn. Magn. Mater. 63-64 (1987) 202.
46. R.J. Keizer, A. de Visser, A.A. Menovsky, J.J.M. Franse, B. Fåk and J.M. Mignot, Phys. Rev. B 60 (1999) 6668.
47. Y. Kohori, M. Ishii and T. Kohara, J. Magn. Magn. Mater. 177-181 (1998) 441.
48. S. Doniach, Physica B 91 (1977) 231.
49. J. Tang, A. de Visser, A. Matsushita and T. Matsumoto, J. Magn. Magn. Mater 177-181 (1998) 465.
50. R.J. Keizer, A. de Visser, M.J. Graf, A.A. Menovsky and J.J.M. Franse, Phys. Rev. B 60 (1999) 10527.
51. M.J. Graf, R.J. Keizer, A. de Visser and J.J.M. Franse, Physica B 259-261 (1999) 666.
52. M.J. Graf, R.J. Keizer, A. de Visser, A.A. Menovsky and J.J.M. Franse, Phys. Rev. B 60 (1999) 3056.

53. R. Abela, A. Amato, C. Baines, X. Donath, R. Erne, D.C. George, D. Herlach, G. Irminger, I.D. Reid, D. Renker, G. Solt, D. Suhi, M. Werner and U. Zimmermann, Hyperfine Interact. 120-121 (1999) 575.
54. A. Schenck, R.J. Keizer, A. de Visser, A. Amato, D. Andreica, F.N. Gygax, M. Pinkpank, P. Estrela, M.J. Graf, A.A. Menovsky and J.J.M. Franse, Physica B 289-290 (2000) 455.
55. M.J. Graf, R.J. Keizer, A. de Visser and S.T. Hannahs, Physica B 284-288 (2000) 1281.
56. A.J. Millis, Phys. Rev. B 48 (1993) 7183; A. Rosch, Phys. Rev. Lett. 82 (1999) 4280.
57. Y. Dalichaouch, M.C. de Andrade, D.A. Gajewski, R. Chau, P. Visani and M.B. Maple, Phys. Rev. Lett. 75 (1995) 3938.
58. H.G.M. Duijn, N.H. van Dijk, A. de Visser and J.J.M. Franse, Physica B 223-224 (1996) 44.
59. A.I. Goldman, G. Shirane, G. Aeppli, E. Bucher and J. Hufnagl, Phys. Rev. B 36 (1987) 8523.
60. C.M. Varma, Phys. World 11 (1998) 22.
61. V. Sechovský and L. Havela, in "Handbook of Magnetic Materials" vol. 11 (K.H.J. Buschow, ed.), Elsevier, Amsterdam, 1998, p. 1.
62. A.V. Andreev, R.V. Dremov, V. Sechovský, Y. Uwatoko, N.V. Mushnikov, T. Goto, K. Prokeš, Y. Shiokawa, Y. Homma, I.H. Hagmusa and J.C.P. Klaasse, J. Alloys Compounds 282 (1999) 64.
63. K. Prokeš et al. (unpublished).
64. C. Geibel, S. Thies, D. Kaczorowski, A. Mehner, A. Grauel, B. Seidel, U. Ahlheim, R. Helfrich, K. Petersen, C.D. Bredl and F. Steglich, Z. Phys. B 83 (1991) 305.

8. Concluding remarks

8.1. U_2Pt_2In

In this thesis, it has been shown that U_2Pt_2In is the first *stoichiometric* U-based compound that exhibits non-Fermi liquid (NFL) behaviour *at ambient pressure*. Research on stoichiometric compounds prepared in a single-crystalline form is highly desirable in the study of NFL behaviour because the effects of disorder may not dominate the physics. This provided a strong motivation to carry out an extensive study on U_2Pt_2In in order to determine its NFL properties. Nevertheless, the rather difficult metallurgy of U_2Pt_2In imposed its restrictions on the research carried out.

The main results obtained on U_2Pt_2In are summarized below.

- Polymorphism was found in U_2Pt_2In [1]: while polycrystalline samples form in the U_3Si_2-type of structure, single-crystals form in the Zr_3Al_2-type of structure (superstructure of the U_3Si_2 type with a doubling along the c-axis).
- When tracing the magnetic ordering temperatures of the U_2T_2X family of compounds versus the square of the conduction-electron - *f*-electron hybridization matrix element in a Doniach-like diagram, one finds that U_2Pt_2In is located at the border line between magnetic and non-magnetic compounds, which suggests that U_2Pt_2In is near a magnetic instability.

- The magnetic susceptibility of U_2Pt_2In is weakly anisotropic and follows a (modified) Curie-Weiss behaviour at high temperatures. At low temperatures, however, an anomalous behaviour is observed: χ_c goes through a maximum at 7.9 K, which is attributed to the stabilization of short-range antiferromagnetic (AF) correlations, while χ_a increases as $1\text{-}bT^{0.7}$ for 2 K $\leq T <$ 10 K. This is at variance with the standard Fermi liquid (FL) behaviour, which predicts χ to attain a constant value at low temperatures.

- The resistivity of U_2Pt_2In is highly anisotropic below about 80 K with $\rho_c > \rho_a$. At the lowest temperatures, the resistivity does not follow the FL quadratic temperature dependence, instead $\rho_a \sim T^{1.25}$ and $\rho_c \sim T^{0.9}$. The residual resistivities are unusually high: $\rho_{0,a} \approx$ 115 μΩcm and $\rho_{0,c} \approx$ 210 μΩcm. However, structure refinements from X-ray [1] and neutron-diffraction [2] experiments indicate a high sample quality. Also, the large difference between $\rho_{0,a}$ and $\rho_{0,c}$ shows that ρ_0 is largely determined by other scattering mechanisms than impurity or defect scattering. It should also be noted that the higher resistivity values are found for a current along the c-axis, which is the axis along which the AF fluctuations stabilize.

- Magnetoresistance (MR) experiments show a gradual increase of the resistivity exponent α (defined as $\rho \sim T^{\alpha}$ as $T \to 0$) with increasing magnetic field strength. At 8 T, $\alpha = 2$ as expected for a FL. There are two different contributions to the MR: a negative one (associated with spin effects) and a positive one (associated with orbital effects). At low fields, the negative contribution is dominant, except in the case $\boldsymbol{B} \parallel \boldsymbol{I} \parallel \mathbf{a}$, whereas at high fields the positive contribution becomes more and more important. The negative contribution to the MR is more important for $\boldsymbol{I} \parallel \mathbf{c}$ than for $\boldsymbol{I} \parallel \mathbf{a}$. However, no satisfactory explanation for this anisotropy can be offered at the moment. Additional evidence that the high residual resistivity in U_2Pt_2In is not determined by crystallographic disorder is provided by the strong field dependence of ρ_0.

- The specific heat of U_2Pt_2In provides solid evidence for the classification of this heavy-fermion compound as a NFL. The specific heat shows a pronounced diverging behaviour of the type $c/T \sim -\ln(T/T_0)$ over almost two decades of temperature. The low-temperature specific heat measured in a magnetic field is dominated by a strong contribution of the In nuclear moments. The same logarithmic divergency is observed in the specific heat measured on polycrystalline samples. As these crystallize in the simpler U_3Si_2-type of structure, the NFL behaviour is not directly related to the presence of two inequivalent U positions, as present in the single crystals with the Zr_3Al_2-type of structure.

- The thermal-expansion coefficient of U_2Pt_2In becomes anisotropic below about 12 K, in a way that the c-axis shrinks more rapidly than the a-axis upon formation of the heavy-fermion bands.
- Absence of weak magnetic order, at least down to 0.05 K, is confirmed by means of muon spin relaxation and rotation (μSR) experiments. Besides a static magnetic component originating from the In nuclear moments, the μSR spectra below 10 K reveal the presence of magnetic fluctuations. No evidence was found for Kondo disorder.
- Resistivity experiments under hydrostatic pressure indicate a recovery of the FL $\rho \sim T^2$ behaviour at low temperatures for $\boldsymbol{I} \parallel \mathbf{a}$. This is consistent with predictions from a transport theory for heavy-fermion compounds near an AF quantum critical point (QCP) [3]. The anisotropy in the resistivity is strongly enhanced under pressure, as follows from the increase of the ratio ρ_c/ρ_a measured for 0.3 K $\leq T <$ 300 K. Due to the enhancement of the anisotropy, the resistivity curves for $\boldsymbol{I} \parallel \mathbf{c}$ do not show a $\rho \sim T^2$ behaviour but a low-temperature minimum.

One of the main issues that arise when discussing the properties of NFL compounds is the responsible mechanism for this behaviour. Although in the current state-of-the-art NFL physics no definite answers can be provided, one most important distinction can often be made: whether the NFL behaviour is due to a single-ion or a cooperative mechanism.

The location of U_2Pt_2In at the border line between magnetic and non-magnetic compounds in the Doniach diagram for the U_2T_2In family of compounds, suggests a proximity to an AF QCP. Resistivity measurements under pressure carried out on U_2Pt_2In and U_2Pd_2In yield strong support for this hypothesis. Considering the absence of magnetic order down to 0.05 K (as evidenced from the μSR experiments) and the important finding that pressure leads to the recovery of the FL behaviour, one cannot exclude that U_2Pt_2In is even located *at* the AF QCP. In order to investigate this further, specific-heat experiments under pressure would be most welcome. As the specific-heat coefficient γ is related to the coherence temperature T_{coh} [4], the observation and evolution of the FL γ coefficient with pressure would provide valuable information on the recovery of the FL state near the QCP.

It is important to notice that the observed divergency of the specific heat, $c/T \sim -\ln(T/T_0)$ is not consistent with an AF QCP, but rather indicates a ferromagnetic (FM) QCP [5]. However, a logarithmic divergency of c/T is allowed for an AF QCP in a two-dimensional (2D) system. This appears to apply to compounds like $CeCu_{5.9}Au_{0.1}$ [6] and $CeNi_2Ge_2$ [7], where inelastic neutron

scattering (INS) experiments have provided evidence for a spectrum of strongly anisotropic magnetic fluctuations, with a quasi-2D nature. INS experiments on U_2Pt_2In could possibly elucidate the nature of the magnetic fluctuations further.

In order to investigate the evolution of magnetic order near U_2Pt_2In in the Doniach phase diagram, the study of single-phase samples of e.g. $(U_{1-x}Th_x)_2Pt_2In$ and $U_2(Pt_{1-x}Pd_x)_2In$ is helpful If Pd or Th doping results in the emergence of magnetism, strong evidence for U_2Pt_2In being at a QCP is obtained. One could then also study such doped samples under pressure, which should lead to the suppression of magnetic order and to the appearance of the FL state.

The origin of the strongly anisotropic character of the resistivity of U_2Pt_2In remains puzzling. Its enhancement under pressure indicates that the anisotropy is not inherent to the crystal structure since the compressibility is almost isotropic. Resistivity measurements on single crystals of the non-magnetic compound Th_2Pt_2In would be useful to address this issue. These could also serve to obtain an estimate for the phonon contribution to the resistivity of U_2Pt_2In. In addition, specific-heat experiments on Th_2Pt_2In should be carried out in order to estimate the phonon contribution to $c(T)$. This would enable a more precise determination of the temperature up to which a logarithmic divergency is present in the electronic specific heat of U_2Pt_2In.

The high residual resistivity of U_2Pt_2In raises the question of the role of disorder in the NFL properties. The dependence of ρ_0 on the current direction, as well as its field and pressure variations, indicate that impurity and defect scattering are not the dominant mechanisms leading to the high values of ρ_0. Even though X-ray and neutron-diffraction experiments indicate a good single-crystalline quality, the use of a local probe to measure the near-neighbour bond-length distributions, like (synchrotron radiation) X-ray absorption fine-structure (XAFS) experiments, could be helpful to determine the exact amount of disorder. For instance, neutron-diffraction experiments carried out on UCu_4Pd were inconclusive regarding the presence of disorder [8]. However, XAFS experiments on the same sample revealed the presence of Pd/Cu site interchange [9]. It was concluded that the amount of disorder observed was sufficient for the Kondo disorder model to apply.

Although there is no evidence for Kondo disorder in U_2Pt_2In, a good test for the Kondo disorder model is obtained by a comparison of the μSR and NMR line widths [10]. As shown in this work, the small frequency shifts observed in the transverse-field (TF) μSR spectra of U_2Pt_2In, require that a full analysis of the TF line widths can only be accomplished with samples with a well-defined geometry in order to account for demagnetizing effects.

A further study of the NFL behaviour of U_2Pt_2In may hopefully be carried out on a "second generation" of single crystals, with a minimum amount of disorder. Single crystals with a lower residual resistivity should be prepared. Therefore, one should look into single-crystal growth methods other than the mineralization technique, by which possibly crystals of higher quality can be produced.

8.2. Related compounds

The presence of a QCP has also been investigated for the compounds $U_3Ni_3Sn_4$ and $U(Pt_{1-x}Pd_x)_3$.

Specific-heat measurements carried out on the stoichiometric compound $U_3Ni_3Sn_4$ show the presence of a NFL regime in the temperature range 0.5-5 K and a crossover to a FL ground state below 0.4 K. The divergency of the specific heat in the NFL regime is of the type $c/T \sim \gamma_0 - \alpha T^{1/2}$, which is consistent with the proximity to an AF QCP in a 3D system [5]. Both the NFL c/T divergence and the spin-fluctuation term in the FL specific heat, have the same characteristic temperature T_0 of 10 K. The pressure dependence of the temperature below which the FL regime in the resistivity is attained, is well described in terms of a transport theory for nearly AF metals [3]. These results indicate that by a small lattice expansion, equivalent to a negative pressure of about -0.04 GPa, $U_3Ni_3Sn_4$ may be tuned to the QCP. The isostructural compound $U_3Cu_3Sn_4$ is an antiferromagnet with T_N = 13 K and its unit-cell volume is about 5% larger than that of $U_3Ni_3Sn_4$. Therefore, it would be highly interesting to check the existence of an AF QCP by studying samples in which small amounts of Ni are replaced by Cu.

μSR experiments on the system $U(Pt_{1-x}Pd_x)_3$ indicate a new type of QCP in the phase diagram: at the critical concentration $x_c = 0.006$, unconventional superconductivity is suppressed and a large-moment antiferromagnetic (LMAF) phase emerges. The fact that the superconducting wave-function has odd parity suggests that doping with Pd leads to a shift of the spectral weight from FM to AF fluctuations. The observed competition between superconductivity mediated by FM fluctuations and static AF order, is in contrast with superconductivity mediated by AF interactions in materials like $CePd_2Si_2$ close to the QCP [11]. The phase diagram of $U(Pt_{1-x}Pd_x)_3$

is similar to the phase diagrams observed for high-temperature superconductors with the peculiarity that the critical points $T_N \rightarrow 0$ and $T_c \rightarrow 0$ coincide.

Resistivity measurements carried out on $U(Pt_{1-x}Pd_x)_3$ show values of the exponent α equal to 1.8 and 1.6 for samples with $x = 0.004$ and $x = 0.007$, respectively [12]. These values are inconclusive with respect to the type of QCP in the system ($\alpha = 3/2$ and $\alpha = 5/3$ are predicted for the AF and FM QCP, respectively). A systematic study of the resistivity exponents in samples with x around 0.006 is required to clearly determine the type of magnetic fluctuations at the QCP.

The origin of the NFL behaviour observed in $URh_{1/3}Ni_{2/3}Al$ might be of the single-ion type. $URh_{1/3}Ni_{2/3}Al$ shows a diverging specific heat of the type $c/T \sim -\ln(T/T_0)$ below about 6 K. Below 10 K the resistivity increases as $\rho \sim 1-aT^{\alpha}$ with α about 1. The low-temperature resistivity increase is an indication that the mechanism responsible for the NFL behaviour is of the single-ion type. In fact, a loss of coherence is predicted to occur at low temperatures within the Kondo disorder model. This model also predicts a logarithmic divergency of c/T and the linear increase of the resistivity below T_K, as observed for $URh_{1/3}Ni_{2/3}Al$. A detailed structural analysis on single-phase samples is required to establish the amount of disorder in this compound.

References

1. P. Estrela, L.C.J. Pereira, A. de Visser, F.R. de Boer, M. Almeida, M. Godinho, J. Rebizant and J.C. Spirlet, J. Phys.: Condens. Matter 10 (1998) 9465.
2. A. Martin-Martin, L.C.J. Pereira, G.H. Lander, J. Rebizant, F. Wastin, J.C. Spirlet, P. Dervenagas and P.J. Brown, Phys. Rev. B 59 (1999) 11818.
3. A. Rosch, Physica B 280 (2000) 341.
4. M.A. Continentino, Phys. Rev. B 47 (1993) 11587.
5. A.J. Millis, Phys. Rev. B 48 (1993) 7183.
6. A. Rosch, A. Schröder, O. Stockert and H.v. Löhneysen, Phys. Rev. Lett. 79 (1997) 159.
7. B. Fåk, J. Flouquet, G. Lapertot, T. Fukuhara and H. Kadowaki, J. Phys.: Condens. Matter 12 (2000) 5423.
8. R. Chau, M.B. Maple and R.A. Robinson, Phys. Rev. B 58 (1998) 139.
9. C.H. Booth, D.E. MacLaughlin, R.H. Heffner, R. Chau, M.B. Maple and G.H. Kwei, Phys. Rev. Lett. 81 (1998) 3960.
10. D.E. MacLaughlin, O.O. Bernal and H.G. Lukefahr, J. Phys.: Condens. Matter 8 (1996) 9855.

11. N.D. Mathur, F.M. Grosche, S.R. Julian, I.R. Walker, D.M. Freye, R.K.W. Haselwimmer and G.G. Lonzarich, Nature 394 (1998) 39.
12. M.J. Graf, R.J. Keizer, A. de Visser and S.T. Hannahs, Physica B 284-288 (2000) 1281.

Summary

The *Fermi liquid* (FL) theory of Landau has been very successful in describing the low-temperature properties of metals. This description is summarized by the well-known expressions for the specific heat $c(T) = \gamma T$, the magnetic susceptibility $\chi(T) = \text{const}$, and the electrical resistivity $\rho(T) = \rho_0 + AT^2$. It has been a challenging task to also describe *heavy-fermion* (HF) materials as strongly renormalized FL's. However, quite surprisingly, in the past decade, a number of HF systems has been discovered, which does not obey the standard FL behaviour, at least not down to the lowest temperatures experimentally accessible. Detailed studies of such systems have led to the recognition that the FL framework may break down under specific conditions. This so-called *non-Fermi liquid* (NFL) state may be considered as a new type of ground state. In NFL materials, $c(T)/T$ and $\chi(T)$ diverge when $T \to 0$, while $\rho(T)$ obeys a non-quadratic temperature dependence.

In this thesis it is shown that U_2Pt_2In is the first stoichiometric uranium-based compound which exhibits NFL behaviour at ambient pressure. The specific heat of U_2Pt_2In shows a pronounced diverging behaviour of the type $c/T \sim -\ln(T/T_0)$ over almost two decades of temperature ($0.1 \leq T < 6$ K), providing solid evidence for the classification of this heavy-fermion compound as a NFL.

At low temperatures, an anomalous behaviour is observed in the magnetic susceptibility of U_2Pt_2In: χ_c goes through a maximum at 7.9 K, which is attributed to the stabilization of short-range antiferromagnetic (AF) correlations, while χ_a increases as $1\text{-}bT^{0.7}$ for $2\text{ K} \leq T < 10$ K. This is in variance with the standard FL behaviour.

The resistivity of U_2Pt_2In is highly anisotropic below about 80 K with $\rho_c > \rho_a$. At the lowest temperatures, the resistivity does not follow the FL quadratic temperature dependence,

instead $\rho \sim T^{\alpha}$ with $\alpha = 1.25$ and 0.9 for currents applied along the a- and c-axis, respectively. Magnetoresistance experiments show a gradual increase of the resistivity exponent α with increasing magnetic field strength, reaching the FL value $\alpha = 2$ at 8 T.

The residual resistivities are unusually high ($\rho_{0,a} \approx 115\ \mu\Omega$cm and $\rho_{0,c} \approx 210\ \mu\Omega$cm), even though the structure refinements from X-ray and neutron-diffraction experiments indicate a high sample quality. The large difference between $\rho_{0,a}$ and $\rho_{0,c}$ and the strong field dependence of ρ_0, shows that ρ_0 is largely determined by other scattering mechanisms than impurity or defect scattering.

Resistivity experiments under hydrostatic pressure indicate a recovery of the FL $\rho \sim T^2$ behaviour at low temperatures. This is consistent with predictions from a transport theory for heavy-fermion compounds near an AF *quantum critical point* (QCP). The anisotropy in the resistivity is strongly enhanced under pressure.

Absence of weak magnetic order, at least down to 0.05 K, is confirmed by means of muon spin relaxation and rotation (μSR) experiments. Besides a static magnetic component originating from the indium nuclear moments, the μSR spectra below 10 K reveal the presence of magnetic fluctuations. No evidence was found for Kondo disorder.

The location of U_2Pt_2In at the border line between magnetic and non-magnetic compounds in a Doniach-type of diagram for the U_2T_2X family and the recovery of the FL state in the resistivity of U_2Pt_2In under pressure, yield evidence for U_2Pt_2In being at or close to a QCP.

Other uranium-based heavy-fermion compounds exhibiting NFL behaviour have been studied in this work:

– Specific-heat experiments on the compound $U_3Ni_3Sn_4$ evidence a FL ground state. However, a NFL regime is observed for 0.5-5 K. Resistivity experiments show that the temperature range where FL behaviour is observed increases with applying pressure. The results are consistent with the location of $U_3Ni_3Sn_4$ close to an antiferromagnetic QCP (at the paramagnetic side of the phase diagram).

– A new type of QCP is found for the system $U(Pt_{1-x}Pd_x)_3$. μSR experiments show that the so-called large-moment antiferromagnetic phase appears at the same Pd concentration where superconductivity is suppressed, i.e. the QCP of both superconducting and antiferromagnetic

phases coincide. This result suggests that odd-parity superconductivity is suppressed because of a shift of the spectral weight from ferromagnetic to antiferromagnetic fluctuations upon Pd doping.

– The temperature variation of the resistivity of the pseudo-ternary compound $URh_{1/3}Ni_{2/3}Al$ is consistent with NFL behaviour due to a single-ion mechanism.

Samenvatting

Het *Fermi-vloeistof* (FV) model van Landau is uitzonderlijk succesvol gebleken in het beschrijven van metalen bij lage temperaturen. Deze beschrijving kan in het kort samengevat worden middels de overbekende uitdrukkingen voor de soortelijke warmte $c(T) = \gamma T$, de magnetische susceptibiliteit $\chi(T) = \text{const}$ en de elektrische weerstand $\rho(T) = \rho_0 + AT^2$. Niet alleen normale metalen, maar ook de zogeheten *zware-fermion* (ZF) systemen kunnen beschreven worden met behulp van het FV model, waarbij de FV parameters sterk gerenormaliseerd zijn. Echter, in de afgelopen tien jaar is een aantal sterk gecorreleerde elektronsystemen ontdekt dat sterke afwijkingen van het standaard FV gedrag vertoont. Gedetailleerde studies van zulke systemen hebben tot het inzicht geleid dat het FV model onder bepaalde condities niet toepasbaar is. Deze zogeheten *niet-Fermi-vloeistof* (NFV) toestand kan beschouwd worden als een nieuwe grondtoestand. In NFV materialen, divergeren $c(T)/T$ en $\chi(T)$ voor $T \to 0$, terwijl $\rho(T)$ een niet-kwadratische afhankelijkheid van de temperatuur vertoont.

In dit proefschrift wordt aangetoond dat de ZF verbinding U_2Pt_2In de eerste stochiometrische uranium verbinding is, die onder normale atmosferische druk NVF gedrag vertoont. De soortelijke warmte van U_2Pt_2In divergeert volgens $c/T \sim -\ln(T/T_0)$ over twee decades in temperatuur ($0.1\ \text{K} \leq T < 6\ \text{K}$), hetgeen overtuigend bewijs is dat U_2Pt_2In geclassificeerd dient te worden als een zware-fermion NFV materiaal.

Ook de magnetische susceptibiliteit vertoont anomaal gedrag bij lage temperatuur: χ_c vertoont een minimum bij 7.9 K, hetgeen toegeschreven kan worden aan de stabilisatie van antiferromagnetische (AF) interacties, terwijl χ_c toeneemt als $1\text{-}bT^{0.7}$ voor $2\ \text{K} \leq T < 10\ \text{K}$. Dit gedrag is in strijd met het normale FV gedrag.

De elektrische weerstand van U_2Pt_2In is sterk anisotroop voor temperaturen beneden 80 K, waarbij $\rho_c > \rho_a$. Bij de laagste temperaturen varieert de elektrische weerstand niet kwadratisch met de temperatuur zoals voor een FV. In plaats daarvan geldt $\rho \sim T^{\alpha}$ met $\alpha = 1.25$ en 0.9 voor een stroom langs de a- en c-as, respectievelijk. Magnetoweerstandsmetingen laten zien dat de exponent α geleidelijk toeneemt in een uitwendig magneetveld. In 8 T wordt de FV waarde $\alpha = 2$ bereikt.

De restweerstanden zijn uitzonderlijk hoog ($\rho_{0,a} \approx 115\ \mu\Omega$cm en $\rho_{0,c} \approx 210\ \mu\Omega$cm), terwijl Röntgen- en neutronendiffractie experimenten erop duiden dat de kristallen van goede kwaliteit zijn. Het grote verschil tussen $\rho_{0,a}$ en $\rho_{0,c}$ en de sterke magneetveldafhankelijkheid van ρ_0 laten zien dat ρ_0 grotendeels bepaald wordt door andere verstrooiingsmechanismen dan verstrooiing aan onzuiverheden of defecten.

Weerstandsmetingen onder uitwendige hydrostatische druk laten zien dat onder hoge druk de FV toestand hersteld wordt, aangezien $\rho \sim T^2$. Dit is consistent met een transporttheorie voor zware-fermion systemen die een antiferromagnetisch *quantum kritisch punt* (QKP) hebben voor $T \to 0$. De anisotropie in de weerstand neemt toe onder druk.

Muon spin-rotatie en relaxatie (μSR) experimenten laten zien dat U_2Pt_2In geen zwakke magnetische ordening vertoont, althans niet boven een temperatuur van 0.05 K. Naast een statische magnetische component, die toegeschreven kan worden aan de depolarisatie t.g.v. indium nucleaire momenten, bestaat het μSR signaal uit een component die op magnetische fluctuaties duidt ($T < 10$ K). Er is geen bewijs gevonden voor zogeheten Kondo wanorde.

De lokatie van U_2Pt_2In vlakbij de grens voor magnetische ordening in een Doniach-diagram zoals samengesteld voor de hele reeks van U_2T_2X verbindingen en het herwinnen van de FV grondtoestand zoals gemeten d.m.v. elektrische weerstand onder uitwendige druk, vormen overtuigend bewijs dat U_2Pt_2In op of vlakbij een magnetisch QKP ligt.

Soortelijke-warmte metingen aan de verbinding $U_3Ni_3Sn_4$ laten zien dat de grondtoestand een FV is. Echter, in het temperatuurgebied 0.5-5 K wordt NFV gedrag gevonden. Weerstandsmetingen onder uitwendige druk laten zien dat het temperatuurgebied waar FV gedrag gevonden wordt groeit met toenemende druk. De resultaten kunnen geïnterpreteerd worden als een bewijs dat $U_3Ni_3Sn_4$ vlakbij een QKP ligt (aan de paramagnetische kant).

Een nieuw type van QKP is gevonden in het systeem $U(Pt_{1-x}Pd_x)_3$. μSR experimenten laten zien dat de zogenaamde groot-moment antiferromagnetische fase ontstaat bij dezelfde Pd

concentratie als die waar supergeleiding wordt onderdrukt, d.w.z. de QKP voor supergeleiding en antiferromagnetisme vallen samen. Dit resultaat suggereert dat het spectrale gewicht van de magnetische fluctuaties in UPt_3 verschuift van ferro- naar antiferromagnetisch door legeren met Pd.

De NFV weerstand van de pseudo-ternaire verbinding $URh_{1/3}Ni_{2/3}Al$ zoals gevonden bij lage temperatuur kan toegeschreven worden aan een single ion NFV mechanisme.

Published work

Publications related to the work described in this thesis:

- P. Estrela, A. de Visser, T. Naka, F.R. de Boer and L.C.J. Pereira: *"Probing U_2Pt_2In in the Doniach Phase Diagram"*, in preparation.
- P. Estrela, A. de Visser, F.R. de Boer and L.C.J. Pereira: *"Magnetoresistance Study of the Non-Fermi Liquid Compound U_2Pt_2In"*, in preparation.
- P. Estrela, T. Naka, A. de Visser, F.R. de Boer and L. Shłyk: *"Recovery of a Fermi Liquid State in $U_3Ni_3Sn_4$"*, in preparation.
- P. Estrela, A. de Visser, G.J. Nieuwenhuys, A. Schenck, A. Amato and L.C.J. Pereira: *"μSR Study of the Non-Fermi Liquid Compound U_2Pt_2In"*, in preparation.
- A. de Visser, M.J. Graf, P. Estrela, A. Amato, C. Baines, D. Andreica, F. Gygax and A. Schenck: *"Magnetic Quantum Critical Point and Superconductivity in UPt_3 Doped with Pd"*, submitted to Phys. Rev. Lett.
- L. Shłyk, P. Estrela, J.C. Waerenborgh, L.E. De Long, A. de Visser, D.P. Rojas, F. Gandra and M. Almeida: *"Crystal Structure and Physical Properties of $U_3T_3Sn_4$ (T=Ni, Cu) Single-Crystals"*, Physica B 292 (2000) 89-96.
- A. Schenck, R.J. Keizer, A. de Visser, A. Amato, D. Andreica, F.N. Gygax, M. Pinkpank, P. Estrela, M.J. Graf, A.A. Menovsky and J.J.M. Franse: *"Muon Localization Site in $U(Pt,Pd)_3$"*, Physica B 289-290 (2000) 455-458.
- P. Estrela, T. Naka, A. de Visser, F.R. de Boer, L.C.J. Pereira and M. Almeida: *"Resistivity of Non-Fermi Liquid U_2Pt_2In Under Pressure"*, Physica B 281-282 (2000) 381-383.
- K. Prokeš, I.H. Hagmusa, P. Estrela, J.C.P. Klaasse, A.V. Andreev, V. Sechovský, E.H. Brück and F.R. de Boer: *"Possible Non-Fermi-Liquid Behaviour in $URh_{1/3}Ni_{2/3}Al$"*, Physica B 281-282 (2000) 377-378.
- L.C.J. Pereira, M. Almeida, P. Estrela, M. Godinho, J. Rebizant, J.C. Spirlet, R.P. Pinto, M.M. Amado, M.E. Braga and J.B. Sousa: *"Magnetic and Transport Properties of U_2Pt_2In Single Crystals"*, J. Magn. Magn. Mater. 196-197 (1999) 885-887.

- L. Shłyk, J.C. Waerenborgh, P. Estrela, L.E. De Long, A. de Visser and M. Almeida: *"Non-Fermi-Liquid Behaviour of $U_{3-x}Ni_3Sn_{4-y}$ Single Crystals"*, J. Phys.: Condens. Matter 11 (1999) 3525-3534.
- P. Estrela, A. de Visser, F.R. de Boer, G.J. Nieuwenhuys, L.C.J. Pereira and M. Almeida: *"Non-Fermi-Liquid Behaviour in U_2Pt_2In"*, Physica B 259-261 (1999) 409-411.
- L. Shłyk, J.C. Waerenborgh, P. Estrela, A. de Visser, L.E. De Long, A.M. Gurevich and M. Almeida: *"Non-Fermi Liquid Behavior in $U_{3-x}Ni_3Sn_{4-y}$ Single Crystals"*, Physica B 259-261 (1999) 423-425.
- J.A. Paixão, L.C.J. Pereira, P. Estrela, M. Godinho, M. Almeida, L. Paolasini, M. Bonnet, J. Rebizant and J.C. Spirlet: *"Magnetization Density Distribution in U_2Co_2Sn"*, J. Phys.: Condens. Matter 11 (1999) 2115-2125.
- P. Estrela, L.C.J. Pereira, A. de Visser, F.R. de Boer, M. Almeida, M. Godinho, J. Rebizant and J.C. Spirlet: *"Structural, Magnetic and Transport Properties of Single-Crystalline U_2Pt_2In"*, J. Phys.: Condens. Matter 10 (1998) 9465-9475.
- L.C.J. Pereira, J.A. Paixão, P. Estrela, M. Godinho, F. Boudarot, M. Bonnet, J. Rebizant, J.C. Spirlet and M. Almeida: *"A Single-Crystal Magnetization and Neutron Scattering Investigation of the Magnetic Structure of U_2Rh_2Sn"*, J. Phys.: Condens. Matter 8 (1996) 11167-11179.

Other publications:

° A.P. Gonçalves, P. Estrela, J.C. Waerenborgh, J.A. Paixão, M. Bonnet, J.C. Spirlet, M. Godinho and M. Almeida: *"Crystallographic and Magnetic Properties of $UFe_{5.8}Al_{6.2}$ Single Crystals"*, J. Magn. Magn. Mater. 189 (1998) 283-292.

° P. Estrela, A.P. Gonçalves, M. Godinho, M. Almeida and J.C. Spirlet: *"Single Crystal Magnetisation of $UFe_{10}Mo_2$"*, J. Magn. Magn. Mater. 167 (1997) L185-L188.

° J. Ayres de Campos, J.M. Gil, P.J. Mendes, L.P. Ferreira, I.C. Ferreira, N. Ayres de Campos, P. Estrela, M. Godinho, M. Bououdina, A. Collomb, D. Fruchart, J.L. Soubeyroux, S. Takele, J. Pelloth and R.A. Brand: *"Magnetic Phase Transitions in $RFe_{9.5}Mo_{2.5}$ Intermetallics Studied by ^{57}Fe Mössbauer Spectroscopy, Magnetisation and μ^+SR"*, J. Magn. Magn. Mater. 164 (1996) 305-318.

° M. Godinho, P. Estrela, A.P. Gonçalves, M. Almeida, J.C. Spirlet and G. Bonfait: *"Anomalous Magnetisation Process in UFe_4Al_8 Probed by Magnetisation and Magnetoresistance"*, J. Magn. Magn. Mater. 157-158 (1996) 690-691.

° G. Bonfait, M. Godinho, P. Estrela, A.P. Gonçalves, M. Almeida and J.C. Spirlet: *"Giant Magnetoresistance Anomaly Associated with a New Magnetisation Process in UFe_4Al_8"*, Phys. Rev. B 53 (1996) R480-R483.

- P. Estrela, M. Godinho, A.P. Gonçalves, M. Almeida and J.C. Spirlet: *"Magnetic Properties of $UFe_{10}Si_2$ Single Crystal"*, J. Alloys Compounds 230 (1995) 35-41.
- A.P. Gonçalves, G. Bonfait, M. Almeida, P. Estrela, M. Godinho and J.C. Spirlet: *"Structural and Magnetic Properties of UFe_xM_{12-x} (M=Al, Mo and Si) Intermetallic Compounds"*, J. Magn. Magn. Mater. 140-144 (1995) 1419-1420.
- A.P. Gonçalves, P. Estrela, J.C. Waerenborgh, M. Godinho, M. Almeida and J.C. Spirlet: *"Structural and Physical Properties of $UFe_{10}Mo_2$"*, J. Alloys Compounds 218 (1995) 183-189.
- P. Estrela, C. Abílio, M. Godinho, J.L. Tholence and J.J. Capponi: *"The Irreversibility Line of the Superconducting Compound $HgBa_2Ca_3Cu_4O_{10+\delta}$"*, Physica C 235-240 (1994) 2731-2732.

Acknowledgements

I would like to thank the European Commission for a Marie Curie Fellowship within the Training and Mobility of Researchers programme (contract ERBFMBICT961763). I also acknowledge the Fundação Calouste Gulbenkian (Portugal) for partially financing my initial period in Amsterdam through a "Bolsa de Doutoramento". Further logistic support was given by the Universiteit van Amsterdam.

I'm much obliged to my supervisors for accepting me as a Ph.D. student. The positive outcome of this work would not have been possible without the continuous scientific guidance, incentive and friendship of Anne de Visser. I learned a lot from him and I thank him for everything he has done for me. Frank de Boer always accompanied, discussed and commented on my work in a very constructive way. I thank him for his kind and competent supervision.

I am grateful to my Portuguese co-workers and sample providers for a fruitful collaboration: Laura Pereira (ITN), António Gonçalves (ITN), Manuel Almeida (ITN) and Margarida Godinho (FCUL). Also Larisa Shłyk (NAS Ukraine) is acknowledged for providing the single crystals of $U_3Ni_3Sn_4$.

Special thanks are given to Ronald Keizer and Rob van Schaijk. Their precious help (and patience) strongly contributed to a successful experimental work. The pressure experiments were carried out together with Takashi Naka (NRIM Tsukuba). I thank him for a fun collaboration.

I had the pleasure to collaborate and discuss problems related to the μSR experiments with Ge Nieuwenhuys (RUL), Alex Schenck (ETH Zürich) and Alex Amato (PSI). I thank them for their valuable input. I also would like to thank Mike Graf (Boston College), Chris Baines (PSI), Daniel Andreica (ETH Zürich), Markus Pinkpank (ETH Zürich), Bob Heffner (LANL) and Fred Gygax (ETH Zürich) for assistance during the experiments and useful discussions. The European

Science Foundation is acknowledged for supporting some of the visits to the Paul Scherrer Institute within the FERLIN programme.

I thank Alois Menovsky for teaching me crystal growth methods and procedures. Many discussions with him gave me a better understanding of the problematic of sample preparation. Agung Nugroho, Nitin Patil and Marian Mihalik are also acknowledged for giving me assistance on the crystal growth attempts. I would like to thank Ton Gortenmulder (RUL) for the EPMA analysis on many of the samples.

A special acknowledgement is made to Jaap Franse for his constant interest in my work and the many group discussions. I also would like to thank Peter de Châtel and Ekkes Brück for accepting to be part of my thesis committee and for valuable remarks on my work.

Many colleagues and friends have contributed for a pleasant four-year period in the Van der Waals - Zeeman Institute. Besides the names already mentioned, I should also mention Vincent Duijn, Michiel Hilbers, Dennis de Lang, Harry Duijn, Frank Kayzel, Yuri Janssen, Isam Hagmusa, Leonid Ponomarenko, Cyril Opeil, Joost Peters, Michel Zwanenburg, Jeroen Bongaerts and Mohamed Nazih.

I also acknowledge the technical and administrative staff of the Institute/University who, at one moment or another, gave me some assistance, namely: Jenny Batson, Harry Beukers, Mariet Bos, Derk Bouhuijs, Henk Gelders, Eddy Inoeng, Dick Jensen, Willem Moolhuijzen, Ton Riemersma, Rene Rik, Marianne Roos, Piet Sannes, Hugo Schlatter and Bert Zwart.

I am deeply indebted to my parents and the rest of the family, who always supported me and encouraged me in many ways. Thanks also to the friends (some closer than others), who were always there for me.

I apologize if I forgot to mention someone. My only excuse is my policy of "democratic forgetfulness", i.e. the tendency to forget things regardless of their level of importance, spatial and temporal localization, race, sexual gender and orientation, religion or social status.